Reardon, Hazel (2014) Synthesis, structure and characterisation of novel lightweight energy materials based on group I & II metal compounds

http://theses.gla.ac.uk/5372/

Copyright and moral rights for this thesis are retained by the author

A copy can be downloaded for personal non-commercial research or study, without prior permission or charge

This thesis cannot be reproduced or quoted extensively from without first obtaining permission in writing from the Author

The content must not be changed in any way or sold commercially in any format or medium without the formal permission of the Author

When referring to this work, full bibliographic details including the author, title, awarding institution and date of the thesis must be given.

Glasgow Theses Service
http://theses.gla.ac.uk/
theses@gla.ac.uk

Synthesis, Structure and Characterisation of Novel Lightweight Energy Materials Based on Group I & II Metal Compounds

A thesis submitted to the University of Glasgow for the degree of Doctor of Philosophy

Hazel Reardon

School of Chemistry

College of Science and Engineering

University of Glasgow

May 2014

Abstract

The need for light-weight, high capacity energy stores is driven by the necessity for a more sustainable approach to reducing the global dependency on fossil fuels. Storing hydrogen in the solid state is an attractive method in which the safety, sustainability and performance requirements for the automotive and aviation sectors may be met.

Mechanochemical methods have been exploited in this work to modify and synthesise inorganic materials for hydrogen storage based on Group I and Group II metal compounds. The properties of un-milled and milled commercial MgH_2 have been examined and milling conditions optimised to obtain desirable hydrogen desorption characteristics. Subsequently, inexpensive, non-toxic, non-oxide catalyst materials were considered for enhancing the hydrogen release properties and three catalysed hydride systems were examined; MgH_2-*x*SiC, MgH_2-*x*graphite and MgH_2-*x*SiC:graphite (*x* = 1-20 wt%). The hydrogen desorption properties of the 1:1 molar SiC:graphite doped MgH_2 system are shown to exhibit improved hydrogen release properties relative to the carbide and graphite systems alone, suggesting a synergistic effect. The E_a for hydrogen desorption from MgH_2 could be decreased from 144±5 kJ/mol to 84±5 kJ/mol in the MgH_2-10 wt% SiC:graphite system, maintaining a desirable hydrogen capacity >5 wt%. A recurring artefact of thermal analysis profiles for MgH_2, in this work and in literature, indicates a two-step decomposition process under relatively mild milling conditions. Therefore, beyond the investigations described for optimisation of hydrogen release conditions, the effect that the aforementioned catalysts have on the two-step desorption anomaly using milder milling has also been investigated. This has given insight in to how the tuning of MgH_2 may be made possible by selection of catalysts which have a more prominent effect on the low temperature desorption step relative to the higher temperature feature.

Direct synthesis of ternary hydrides from their corresponding binary hydrides has been investigated by mechanical alloying of stoichiometric and non-stoichiometric binary hydride mixtures. High purity $NaMgH_3$ powder (Orthorhombic space group *Pnma*, *a* = 5.437(2) Å, *b* = 7.705(5) Å, *c* = 5.477(2) Å; *Z* = 4) was prepared in 5 h at high ball:powder ratios using a stoichiometric mixture of the respective binary hydrides. The dehydrogenation behaviour of the sub-micron (crystallites typically 200 – 400 nm in size) ternary hydride was investigated by thermal analysis. The nanostructured hydride releases hydrogen in two-steps with an onset temperature for the first step of 240 °C.

Using a range of initial binary hydride stoichiometries, a series of potentially new cubic ternary $(Ca_{1-x}Mg_xH_2)_n$ hydride phases has been proposed, such that the initial stoichiometry of Ca:Mg results in (non-)stoichiometric Ca-Mg-H phases relative to the known $Ca_{19}Mg_8H_{54}$ phase. The crystallographic properties of the $(Ca_{1-x}Mg_xH_2)_n$ series have been examined by both lab and *in-situ* synchrotron X-ray diffraction experiments, and the Rietveld method employed to establish detailed structure information. The thermal properties of the $(Ca_{1-x}Mg_xH_2)_n$ hydrides have also been determined and their relative hydrogen desorption and gravimetric capacities compared. This work demonstrates that as the proportion of Mg increases, the thermal stability of the Ca-Mg-H system is lowered and higher hydrogen capacities are obtained. The effect of small alkali metal *vs.* larger alkaline earth metal inclusion on the Mg-H system is explored through this work.

With a focus on new solid state synthesis routes to hydrides, mechanochemical metathesis reactions have been examined. Complex and ternary halides were selected as halide precursors, towards the synthesis of complex and ternary hydrides. The halides; $LiAlCl_4$, $NaMgCl_3$ and $NaAlCl_4$, were synthesised using mechanochemical alloying of stoichiometric mixtures their respective binary metal halides. Their structures and thermal properties were determined and comparisons drawn between conventional synthesis in literature and the mechanochemical method employed in this work. The halides were then milled in appropriate stoichiometric ratios with alkali metal hydrides to determine whether a proposed metathesis reaction may result in the formation of the respective ternary/complex hydride. The products of the mechanochemical metathesis reactions were evaluated using powder diffraction and then thermal analysis, where low temperature hydrogen release corresponding to the desired hydride product was found. One metathesis route in particular highlights the potential of this approach, where analysis of the product suggests that the elusive "$LiMgH_3$" hydride has been formed with hydrogen release at 316.6 ºC. This work illustrates that the solid state metathesis route is a suitable means for materials synthesis and design, where tailored reactions can yield exciting results.

Table of Contents

TABLE OF CONTENTS ..... **III**

LIST OF TABLES ..... **VI**

LIST OF FIGURES ..... **VIII**

ACKNOWLEDGMENTS ..... **XVII**

DEFINITIONS AND ABBREVIATIONS ..... **XIX**

1. INTRODUCTION **21**

1.1. THE ENERGY DEFICIT & ENERGY STORAGE 21

1.2. HYDROGEN: A PROMISING ENERGY STORE 22

1.2.1. Solid State Hydrogen Storage *25*

1.3. CONCLUSION 39

2. EXPERIMENTAL **46**

2.1. SAMPLE HANDLING 46

2.1.1. Gloveboxes *46*

2.2. PREPARATIVE METHODS & TECHNIQUES 47

2.2.1. Mechanochemistry *47*

2.2.2. Glassblowing & Furnaces *51*

2.3. CHARACTERISATION TECHNIQUES 52

2.3.1. Crystallography and Diffraction *53*

2.3.2. The Scherrer Method *61*

2.3.3. Structure Refinement & The Rietveld Method *62*

2.3.4. Spectroscopy *66*

2.3.5. Thermal Analysis *73*

2.4. ERRORS & STATISTICAL ANALYSIS 78

2.5. SUMMARY 79

3. OPTIMISATION OF MgH_2 DEHYDROGENATION PROPERTIES BY MILLING WITH/WITHOUT NON-OXIDE ADDITIVES **82**

3.1. INTRODUCTION 82

3.1.1. Structures of MgH_2 Polytypes *82*

3.1.2. Spectroscopic Properties of Commercial MgH_2 ..... *87*

3.1.3. Thermal Behaviour of Commercial MgH_2 ..... *88*

3.2. AIMS OF THE WORK DESCRIBED IN THIS CHAPTER 96
3.3. RESULTS & DISCUSSION 97
3.3.1. Commercial MgH_2 97
3.3.2. Milling MgH_2 102
3.4. ADDITIVE STUDY 119
3.4.1. MgH_2-x wt% Graphite (x = 1-20 wt%) 120
3.4.2. MgH_2-x wt% Silicon Carbide (x = 1-20 wt%) 128
3.4.3. MgH_2-x wt% Silicon Carbide:Graphite (x = 1-20 wt%) 136
3.4.4. Conclusions 148

4. FACILE SYNTHESIS OF TERNARY METAL HYDRIDES *VIA* MECHANOCHEMISTRY 152

4.1. INTRODUCTION 152
4.2. EXPERIMENTAL 158
4.3. RESULTS & DISCUSSION 161
4.3.1. Synthesis and Characterisation of Nanosized Sodium Magnesium Hydride, $NaMgH_3$ 161
4.3.2. New Ternary Alkaline Earth Metal Hydrides $(Ca_{1-x}Mg_xH_2)_n$; synthesis, structure and thermal properties 173
4.4. CONCLUSIONS 198

5. SYNTHESIS AND STRUCTURE OF HALIDE PRECURSORS FOR TAILORED HYDRIDE SYNTHESIS *VIA* SOLID STATE METATHESIS REACTIONS 202

5.1. INTRODUCTION 202
5.2. EXPERIMENTAL 204
5.3. MECHANOCHEMICAL SYNTHESIS OF $LiAlX_4$ (X = Cl, H). 206
5.3.1. Introduction 206
5.3.2. Results & Discussion 207
5.4. MECHANOCHEMICAL SYNTHESIS OF $NaMgX_3$ (X = Cl, H). 216
5.4.1. Introduction 216
5.4.2. Results & Discussion 217
5.5. MECHANOCHEMICAL SYNTHESIS OF $NaAlX_4$ (X = Cl, H). 236
5.5.1. Introduction 236
5.5.2. Results & Discussion 237

6. CONCLUSIONS 247

7. FURTHER WORK 248

APPENDIX A. 250

APPENDIX B. 257

APPENDIX C. 270

APPENDIX D. 274

APPENDIX E. 280

APPENDIX F. 285

List of Tables

Table 1-1 Key properties of the lightest known metal hydrides; LiH and NaH. 27
Table 1-2 Thermodynamic and relevant data for light metal alanates. 33
Table 2-1 Summary of crystallography notation and symmetry information for the seven crystal systems. 56
Table 2-2 Primary Rietveld refinement parameters. 64
Table 3-1 Experimentally determined polymorphs of MgH_2; blue and red spheres represent Mg and H atoms, respectively. 83
Table 3-2 Comparison of lattice parameters quoted for α-MgH_2. 84
Table 3-3 Comparison of lattice parameters quoted for β-MgH_2. 85
Table 3-4 Comparison of lattice parameters quoted for δ-MgH_2 and δ'-MgH_2. 85
Table 3-5 Comparison of lattice parameters quoted for γ-MgH_2. 87
Table 3-6 Comparison of lattice parameters quoted for ε-MgH_2. 87
Table 3-7 Summary of milled Mg-MgH_2 studies showing DSC/DTA doublet. 91
Table 3-8 Important properties of carbon and refractory carbide materials used as additives for the Mg-H system. 95
Table 3-9 Refinement data for commercial MgH_2. 99
Table 3-10 Comparison of Raman shift information for MgH_2. 101
Table 3-11 Samples of milled commercial MgH_2 investigated in this work, all milling conducted at 450 rpm. 103
Table 3-12 Rietveld refinement data for Sample 1. 106
Table 3-13 DTA-TG data collected for un-doped, milled MgH_2 (Samples 1-12). 109
Table 3-14 MgH_2-x wt% graphite samples (x = 1-20). 120
Table 3-15 Thermal analysis data for MgH_2-x wt% graphite (Samples 13-18). 125
Table 3-16 Relative Raman intensity ratios, I_D/I_G, for Samples 13-16. 126
Table 3-17 MgH_2-x wt% SiC samples (x = 1-20 wt%). 128
Table 3-18 Thermal analysis data for Samples 19-24. 134
Table 3-19 Sample data for MgH_2-x wt% SiC-graphite. 136
Table 3-20 DTA-TG data for Samples 25-28. 140
Table 3-21 DTA-TG data for Samples 29-32. 144
Table 4-1 Crystallographic properties of CaH_2 and known ternary Ca-Mg hydrides at room temperature. 156
Table 4-2 List of samples prepared in the NaH-MgH_2 study. 158
Table 4-3 List of samples used in the MgH_2-CaH_2 study. 158

Table 4-4 Diffraction data for Sample 36. 164
Table 4-5 Atomic parameters for Sample 36. 164
Table 4-6 Assignment of the Raman spectrum for Sample 36. 167
Table 4-7 TGA-DTA-MS results for Sample 36 compared with literature data. 169
Table 4-8 Kissinger plot linear trendline data and statistics for Sample 36. 171
Table 4-9 Experimentally determined enthalpy and entropy for dehydrogenation of $NaMgH_3$. (Modified from supplementary material in Reference 25.) 172
Table 4-10 CELREF estimation of ternary phase unit cell parameters and volumes compared with known ternary hydride, $Ca_{19}Mg_8H_{54}$. 175
Table 4-11 Rietveld refinement data for the cubic ternary phase in Samples 39-43. 176
Table 4-12 Crystal structure data for samples analysed by SXD. 178
Table 4-13 Interatomic distances for $Ca_{15.6(3)}Mg_{11.4(3)}H_{54}$ (Sample 41). 180
Table 4-14 Atomic parameters for $Ca_{15.6(3)}Mg_{11.4(3)}H_{54}$ (Sample 41) 180
Table 4-15 Decomposition properties of Sample 39-43. 186
Table 4-16 Kissinger plot data for Samples 39-43. 187
Table 4-17 Phase fractions of CaH_2 and Mg from Rietveld refinement of Samples 39-43 collected after heating to 773 K. 188
Table 4-18 Exemplar Rietveld refinement data for samples collected after heating to 773 K and 973 K (data is given for Sample 39). 189
Table 4-19 Phase fractions of CaH_2 and Mg from Rietveld refinement of samples collected after heating to 973 K. 190
Table 4-20 Rietveld refinement data collected using *in-situ* Synchrotron X-ray Diffraction (623 K) for Sample 42. 193
Table 4-21 Atomic parameters for $Ca_{3.93(2)}Mg_{3.07(3)}H_{14}$. 193
Table 4-22 Rietveld refinement data collected using *in-situ* Synchrotron X-ray Diffraction (673 K) for Sample 42. 195
Table 5-1 Sample ID and reaction conditions for ternary halide synthesis and halide-hydride metathesis reactions. 204
Table 5-2 Crystallographic data from Rietveld refinement. 209
Table 5-3 Rietveld refinement data for $NaMgCl_3$ and impurity phase (Sample 50). 218
Table 5-4 Rietveld refinement data for product of Sample 51 heated to 300 ºC. 224
Table 5-5 Rietveld data for sample collected after heating Sample 54 to 500 ºC. 234
Table 5-6 Comparison of theoretical values for the $LiMgH_3$ structure (R3c (167), Z = 6) and formation thermodynamics based on Equation 5-12. 235

Table 5-7 Crystallographic data from Rietveld refinement for mechanochemically synthesised $NaAlCl_4$, Sample 56, compared with literature data (ICSD-30611). 238

List of Figures

Figure 1-1 a) Energy use projections from US DOE[1], and b) European energy supply-demand profile.[3] 21
Figure 1-2 Schematic of a sustainable hydrogen energy cycle.[23] 22
Figure 1-3 Parameters and operating margins to be met by commercially viable solid state hydrogen storage materials.[31] 24
Figure 1-4 Novel "proton flow battery", where M represents the metal component of the hydrogen storage material.[40] 24
Figure 1-5 Position of hydrogen on the periodic table and table of metals which form solid binary hydrides (adapted from Reference 49). 26
Figure 1-6 Comparison of the volumetric and gravimetric hydrogen storage properties of some potential solid state hydrogen storage materials. 27
Figure 1-7 Summary of transition metal catalysts (highlighted in bold) used to enhance the Mg-H system. 30
Figure 1-8 Unit cell of a-c) $M(AlH_4)_n$ (M=Li, Na, Mg, and n=1, 2) alanates showing the tetrahedral orientation of the $[AlH_4]^-$ anions using purple polyhedra, and the coordination orientation of the metal cations using grey (Li), green (Na) and blue (Mg) polyhedra. (Atom key: Li = white, Na = grey, Mg = blue, Al = purple, and H = red.) 34
Figure 2-1 Images of the a) Alpha and b) Omega models of Saffron Scientific gloveboxes employed for sample preparation in this thesis, and c) UniLab mBraun glovebox employed as STA housing (see section 2.3.5.1). 47
Figure 2-2 Illustration of the increasingly complex processes that occur across scales during milling. (Adapted from Reference 19.).....49
Figure 2-3 Configuration of the milling jar in the Retsch PM100 planetary ball mill. ..50
Figure 2-4 Bespoke bench-top furnace. 52
Figure 2-5 Simplified representation of the electromagnetic spectrum. 53
Figure 2-6 Basic cubic unit cell showing cell lengths and angles. 53
Figure 2-7 Representation of diffraction in a crystal where black solid lines indicate lattice planes, k_o and k_h are the incident and reflected wave vectors, d is the lattice spacing and θ is the angle between the lattice plane and k_o, where the incident and reflected angles are equivalent. 54

Figure 2-8 Configuration of the synchrotron source at NSRRC. [39] 58
Figure 2-9 a) Configuration of capillary PXD analysis in Debye-Scherrer transmission geometry, and b) magnification of capillary orientation for both D8 and X'Pert diffractometer instruments. 59
Figure 2-10 Low temperature furnace configuration on BL01C2.....59
Figure 2-11 Bragg-Brentano reflection geometry used in X'Pert and D5000 measurements. 60
Figure 2-12 Simplified representation of an energy transition in a molecule. 67
Figure 2-13 Optical schematic of a Michelson interferometer Fourier Transformer InfraRed spectrometer (reproduced from Reference 54). 68
Figure 2-14 Typical Raman spectroscopy instrument optical configuration. (Reproduced from reference 36). 69
Figure 2-15 Schematic of energy changes associated with Raman scattering. 70
Figure 2-16 Signal scattering from a sample in SEM, where the energies of the scattered species are given relative to the primary beam. (Reproduced from reference 57.) 72
Figure 2-17 Diagram of Simultaneous Thermal Analysis crucible arrangement and principle behind the temperature difference being measured. (Modified from Netzsch STA 409 user information.) 74
Figure 2-18 Schematic of the STA instrument employed in this work, indicating the main components of the analyser. (Modified from Netzsch STA 409 user information.)...75
Figure 2-19 a) Faraday Cup detector and b) secondary electron multiplier (SEM) detector used in this work. (Reproduced from reference 67).....77
Figure 3-1 *Pbca* structure of metastable δ'-MgH_2 phase observed above 10 GPa; blue and red spheres represent Mg and H, respectively.[2] 86
Figure 3-2 α- and γ-MgH_2 synthesised by reactive milling of Mg under 2 bar H_2. (Note: β-MgH_2 in the figure refers to rutile-type MgH_2, denoted α-MgH_2 in this work.)[16] 86
Figure 3-3 DSC profile of MgH_2 synthesised by reactive milling showing a two-step endothermic decomposition, and PXD of the decomposition products at 380 °C, 385 °C and 390 °C (γ-phase indicated by arrows). [31] 90
Figure 3-4 DTA of a) milled MgH_2, b) Co_3O_4-doped, c) $NiCo_2O_4$-doped and d) NiO-doped MgH_2 samples.[43].....92
Figure 3-5 Suggested non-stoichiometric phases of MgH_2 and interactions with MgO as one possible solution to the two-step decomposition phenomenon.[45] 93

Figure 3-6 a) SEM image of commercial MgH_2 as-purchased, and b) PXD of commercial MgH_2 as-received (*hkl* values given for each α-MgH_2 reflection, and ★ indicates Mg reflections).....98
Figure 3-7 Rietveld plot for commercial MgH_2; observed and calculated data are shown by red crosses and the green continuous plot, respectively. Black and red tick marks indicate MgH_2 and Mg phases, respectively. The lower continuous pink line is the difference plot. 99
Figure 3-8 FTIR spectrum of commercial MgH_2. 100
Figure 3-9 Experimental Raman spectrum for commercial MgH_2.....100
Figure 3-10 a) DTA traces and b) Kissinger plot of commercial MgH_2 used in this work, where each point is the T_{peak} for decomposition taken from the DTA plots. 102
Figure 3-11 a) TG and b) MS (*m/z* = 2) data collected for commercial MgH_2 at the four heating rates employed.....102
Figure 3-12 Low (a) and high (b) magnification images showing flattened particles of Sample 3 milled for 5 h. Low (c) and high (d) magnification images showing plate-type large particles remain after 20 h milling (Sample 5).....104
Figure 3-13 SEM images of milled-MgH_2; Sample 11 at a) 20 μm and b) 5 μm scale, and Sample 12 at c) 20 μm and d) 5 μm scale. 105
Figure 3-14 Rietveld plot for Sample 1; measured and calculated data given by red crosses and the green continuous plot, respectively. Red and black tick marks indicate reflections from Mg and α-MgH_2, respectively. The difference plot is given by the continuous pink plot.....106
Figure 3-15 PXD showing the emergence of γ-MgH_2 after only 2 h of milling (red pattern) compared with 0.5 h milled sample (blue). 107
Figure 3-16 PXD of commercial MgH_2 milled for a) 0.5 h (Samples 1 and 7), b) 2 h (Samples 2 and 8) and c) 5 h (Samples 3 and 9).....108
Figure 3-17 DTA-MS data collected at 5°C/min for MgH_2 for a) Samples 1 and 2 and b) Samples 3 and 4. 110
Figure 3-18 Trend in estimated total enthalpy of decomposition data collected for commercial, un-milled MgH_2 and MgH_2 milled for different durations (Samples 1-6)....111
Figure 3-19 a) DTA profiles, b) MS data (*m/z* = 2) and c) Kissinger plots for Sample 3 collected by STA at 2, 5, 10 and 20 ^{o}C/min. (Ozawa plots given in Appendix A; A.5.)...112
Figure 3-20 X-ray diffraction patterns of post STA products collected for Sample 3 after heating at each ramp rate used. 113

Figure 3-21 Comparison of DTA and TG traces for samples milled using 2 balls (solid line) or 8 balls (dashed line) as indicated for a) & b) Samples 1 and 7, c) & d) Samples 2 and 8, and e) & f) Samples 3 and 9. 114
Figure 3-22 Time resolved PXD for sample milled Sample 11. 115
Figure 3-23 a) EDX spectrum of Sample 11 and b) SEM image of area from which the spectrum was collected (50 μm scale). 116
Figure 3-24 Comparison of FTIR spectra collected for commercial, un-milled MgH_2 and Samples a) 11 and b) 12. 117
Figure 3-25 DTA and MS (*m/z* = 2) traces obtained used to obtain Kissinger plots for Sample 11 milled for 2 h (a & b) and Sample 12 milled for 5 h (c & d). e) Overlay of Kissinger plots for one step decomposition observed in Samples 11 and 12 compared with commercial, un-milled MgH_2 (Ozawa plot overlay given in Appendix A). 118
Figure 3-26 SEM image of a) as-received graphite (100 μm scale), b) Sample 15, c & d) Sample 17, and e & f) Sample 18. 121
Figure 3-27 PXD of MgH_2 Samples 13-16. 122
Figure 3-28 PXD of MgH_2 samples 17 (red) and 18 (blue). 123
Figure 3-29 a & b) DTA and TG data respectively for Samples 13-16. c & d) DTA and TG data respectively for Samples 17 (dashed line) and 18 (solid line). 124
Figure 3-30 Raman spectra of Sample 14 a) as-milled and b) post STA product. 127
Figure 3-31 SEM micrographs of (a & b) Sample 21, (c and d) Sample 23 and (e & f) Sample 24 using low and high magnification. 129
Figure 3-32 Exemplar PXD patterns of MgH_2 milled Samples 20 and 21. (Downward arrow indicates Fe reflection from stainless steel milling tools.).....130
Figure 3-33 PXD of Sample 23 and Sample 24. 131
Figure 3-34 Raman spectrum collected for Sample 19. 132
Figure 3-35 a & b) DTA and TG traces respectively for Samples 19-22, c & d) Comparison of DTA-TG traces for Sample 23 (dashed line) and Sample 24 (solid line). 133
Figure 3-36 Post STA PXD analysis of samples milled for 2 h (Sample 23, red) and 5 h (Sample 24, blue). 135
Figure 3-37 SEM images comparing commercial MgH_2 milled under mild conditions a) without additive (20 μm) and b) Sample 28 (10 μm). Images of Sample 28 at higher magnification using c) secondary electron and d) back scattering electron imaging. SEM images for e) Sample 29 and f) Sample 32 (20 μm). 137
Figure 3-38 PXD data for Samples 25-28. 138

Figure 3-39 a) Map of elemental Si (red) and C (green) dispersion (40 μm) and b) EDX spectrum for Sample 30. 139
Figure 3-40 DTA & TG data collected using 5 ^{o}/min heating rate for Samples 25-28. .140
Figure 3-41 Time resolved PXD of Sample 29. 141
Figure 3-42 Exemplar Raman spectra for SiC-graphite doped MgH_2 milled under harsh conditions; Sample 31 a) as-milled and b) post STA.....142
Figure 3-43 Thermal analysis data for Samples 29-32. a) DTA, b) TG and c) MS (*m/z* = 2) plots (including comparison with milled un-doped MgH_2) collected at 5 ^{o}/min. d) Kissinger plots obtained by heating at 2, 5, 10 and 20 °C including comparison with milled un-doped MgH_2. (Error bars omitted for clarity; see Appendix A, A.9 for individual Kissinger plots of Samples 29-32 including error bars.) 143
Figure 3-44 X-ray diffraction patterns for MgH_2-x wt% SiC:graphite (x = 1, 5, 10, 20) samples collected post STA. 145
Figure 3-45 Images of Sample 30 prepared as a 5 mm (diameter) pellet shown a) before and b) after heating to 500 ^{o}C under $Ar_{(g)}$. 146
Figure 4-1 a) Unit cell of CaH_2 and the ternary phases b) $Ca_{19}Mg_8D_{54}$ and c) $Ca_4Mg_3D_{14}$. (Grey, blue and green spheres represent H, Mg and Ca, respectively.).....155
Figure 4-2 X-ray diffraction patterns of 1:1 molar mixtures of NaH and MgH_2 milled for 1 h (Sample 33, blue) and 5 h (Sample 36, red). 161
Figure 4-3 SEM image of as-synthesised $NaMgH_3$ (Sample 36) at (a) low magnification and (b) high magnification, and (c & d) morphology and elemental mapping of Na (red) and Mg (green) in Sample 37. 162
Figure 4-4 (a) Rietveld refinement profile for Sample 36. (Observed data are shown by red crosses, the calculated plot is shown as a green continuous line, the tick marks indicate the reflection positions for orthorhombic $NaMgH_3$ and the difference plot is shown below in pink); (b) Unit cell of $NaMgH_3$, where gold, red and light grey spheres represent Na, Mg and H, respectively; (c) Extended structure of $NaMgH_3$ as a polyhedral representation viewed along the [010] direction.....165
Figure 4-5 a) Raman spectrum of Sample 36 collected using the UV laser (325.1 nm). b) Comparison of Raman spectra for Samples 34 and 36 given by black and blue lines respectively, and the red and green lines show the spectra of Samples 37 and 38. 166
Figure 4-6 a) DTA and b) TG data comparison for un-milled binary hydrides NaH and MgH_2 and ternary hydride, Sample 36. Values shown on DTA profiles indicate onset and peak H_2 desorption temperatures, T_{onset} and T_{peak} (italics), respectively. c) MS data for Sample 36 where the corresponding T_{peak} values are indicated on the plot. 168

Figure 4-7 Comparison of the Kissinger plots for the two endothermic decomposition processes observed for Sample 36. 171
Figure 4-8 Typical morphologies of a) as-synthesised Ca-Mg-H Sample 39 (40 μm) and b) air exposed Ca-Mg-H Sample 39 (20 μm). EDX analysis shown in c) for as-prepared Ca-Mg-H Sample 42. 173
Figure 4-9 Time resolved PXD analysis of Sample 39 under ambient conditions (red stars indicate the broad reflections for $Ca(OH)_2$).....174
Figure 4-10 Ternary phase unit cell a) *a* parameter, and b) cell volume derived from Rietveld refinement of lab PXD data plotted relative to initial CaH_2:MgH_2 ratio employed (Samples 39-43). 177
Figure 4-11 Rietveld plot for Sample 41 analysed by SXD showing a highly resolved diffraction profile for the ternary phase only (black tick marks). Red crosses indicate observed data, the green line shows the calculated pattern and the magenta line indicates the difference plot. 179
Figure 4-12 Ternary phase unit cell a) *a* parameter, and b) cell volume derived from Rietveld refinement of SXD data plotted relative to initial CaH_2:MgH_2 ratio employed..181
Figure 4-13 a) Unit cell representation of Sample 39; $Ca_{21.4(3)}Mg_{5.6(3)}H_{54}$, and b) coordination of its Ca/Mg-centred 16*f* site. c) Unit cell representation of Sample 40; $Ca_{21.6(1)}Mg_{5.1(1)}H_{54}$, and d) coordination of its Ca/Mg-centred 16*f* site. (Ca = green, Mg = blue, Ca/Mg = red, H = grey.).....182
Figure 4-14 Unit cell representation of a) Sample 41; $Ca_{15.6(3)}Mg_{11.4(3)}H_{54}$, and b-e) the coordination orientations of the 24*g*, 12*d*, 2*a* and 16*f* metal sites, respectively. (Ca = green, Mg = blue, Ca-Mg = red, H = grey.).....183
Figure 4-15 a) Unit cell representation of Sample 42; $Ca_{15.2(2)}Mg_{11.8(2)}H_{54}$, and b) coordination of its 24*g* site. c) Unit cell representation of Sample 43; $Ca_{13.3(8)}Mg_{13.8(8)}H_{54}$, and d) coordination of its 24*g* site. (Ca = green, Mg = blue, Ca-Mg = red, H = grey.).....184
Figure 4-16 a) DTA and b) TG collected at 5 ^{o}C/min for samples 39-43, where the CaH_2:MgH_2 ratios are given in the legends. Corresponding MS data for the same samples showing c) full H_2 desorption profile and d) high temperature MS (*m/z* = 2) data. 185
Figure 4-17 Comparison of Kissinger plots of Samples 39-43 where the CaH_2:MgH_2 stoichiometries for each sample are indicated. 186
Figure 4-18 Typical PXD pattern collected for samples retrieved after heating to 773 K (Sample 39). (CaH_2 indicated by black tick marks, and Mg indicated by red tick marks). Red crosses show experimental data, the green line is the calculated data and the magenta line is the difference plot.....187

Figure 4-19 Typical PXD pattern collected for sample collected after STA after heating to 973 K (Sample 39). (CaH_2 indicated by black tick marks and $CaMg_2$ indicated by red tick marks). Red crosses show experimental data, the green line is the calculated data and the magenta line is the difference plot. 189
Figure 4-20 SXD patterns collected *in-situ* between 298-673 K for Sample 42. 191
Figure 4-21 Plots of a) *a* cell parameter and b) cell volume for the ternary phase between 298-573 K for Sample 42. 191
Figure 4-22 SXD pattern of Sample 42 collected after heating *in-situ* 623 K, where the black tick marks represent the "$Ca_{3.93(2)}Mg_{3.07(3)}H_{14}$" phase. Red crosses show experimental data, the green line is the calculated data and the magenta line is the difference plot.....192
Figure 4-23 Polyhedral representation of the unit cell structure of "$Ca_{3.93(2)}Mg_{3.07(3)}H_{14}$". The green, blue and small light grey spheres represent Ca, Mg, and H atoms respectively. The red spheres represent the shared Ca/Mg 2*e* site. 194
Figure 4-24 SXD pattern of Sample 42 collected after heating *in-situ* 673 K, where the black, red blue and green tick marks represent the $Ca_4Mg_3H_{14}$, CaH_2, MgH_2 and Mg phases, respectively. Red crosses show experimental data, the green line is the calculated data and the magenta line is the difference plot. 194
Figure 4-25 a) SXD patterns of Sample 40 collected after heating *in-situ* from 298-673 K. b) Rietveld refinement plot of SXD pattern collected at 623 K. The cubic ternary phase is indicated by black tick marks and CaH_2 is indicated by red tick marks; χ^2 = 1.343 R_p = 3.61 %, R_{wp} = 4.85 %. Red crosses show experimental data, the green line is the calculated data and the magenta line is the difference plot. 196
Figure 4-26 Plots of a) a cell parameter *vs.* temperature and b) volume *vs.* temperature for Sample 40 obtained from Rietveld refinement of diffraction data collected by *in-situ* SXD between 298-673 K. 197
Figure 5-1 Rietveld refinement plot of PXD data for Sample 46. Black tick marks represent the $LiAlCl_4$ phase and the red tick marks indicate the LiCl phase. Red crosses indicate observed data, the green line shows the calculated pattern and the magenta line indicates the difference plot. 208
Figure 5-2 a) Expanded structure of mechanochemically synthesised $LiAlCl_4$ (unit cell edges indicated) with tetrahedral representation of $[AlCl_4]^-$ anions given by the blue polyhedra (Li = grey spheres, Al = purple spheres, Cl = green spheres), b) octahedral coordination sphere of Li atoms, and c) tetrahedral coordination sphere of Al atom.....210
Figure 5-3 Thermal analysis of Sample 44 (dashed line) *vs*. Sample 46 (solid line). ..211

Figure 5-4 SEM images of a) mechanochemical metathesis product (Sample 48, 100 μm) and b) product collected after heating Sample 48 to 300 ºC (20 μm). 212
Figure 5-5 PXD pattern of Sample 48. 212
Figure 5-6 a) DTA, b) TG and c) MS data (*m/z* = 2) for Sample 48 heated to 500 ºC using a heating rate of 5 ºC/min. 213
Figure 5-7 X-ray diffraction patterns of samples collected post STA of Sample 48 to a) 300 ºC and b) 500 ºC. 215
Figure 5-8 SEM micrographs of as prepared $NaMgCl_3$ (Sample 50) using a) low and b) high magnification. 217
Figure 5-9 Refinement plot of data collected for Sample 50, where black tick marks indicate $NaMgCl_3$, and NaCl impurity are indicated by red tick marks. Red crosses indicate experimental data, and green line indicates the calculated pattern. The magenta line indicates difference plot. 219
Figure 5-10 a) Structure of $NaMgCl_3$ (Sample 50) showing alternating layers of Na centred octahedra (green) and Mg centred octahedral (pink). Coordination orientation of the b) Na octahedral and c) Mg octahedral. (Mg = blue spheres, Na = grey spheres, Cl = green spheres.).....220
Figure 5-11 Effect of milling time on the synthesis of $NaMgCl_3$ from a stoichiometric 1:1 mixture of NaCl and $MgCl_2$ (Sample 51). 221
Figure 5-12 STA data comparison for Samples 49 and 51, showing a) DTA and b) TG data, respectively. 222
Figure 5-13 X-ray diffraction pattern of product collected after heating Sample 51 to 300 °C (5 °C/min in a flow of $Ar_{(g)}$). 223
Figure 5-14 Rietveld plot for product of Sample 51 heated to 300 ºC. Black tick marks represent the $Na_2Mg_3Cl_8$ phase and red tick marks represent NaCl. Red crosses indicate experimental data, and the green line indicates the calculated pattern. The magenta line indicates difference plot. 223
Figure 5-15 a) Structure of $Na_2Mg_3Cl_8$ (Sample 51 heated to 300 °C) showing alternating layers of Na centred trigonal prisms (beige) and Mg centred octahedra (blue). Coordination orientation between Cl anions and the b) Na cation and c) Mg cation. (Mg = blue spheres, Na = grey spheres, Cl = green spheres.).....225
Figure 5-16 Comparison of diffraction patterns collected by *in-situ* PXD analysis between room temperature and 300 ºC (Sample 51).....226
Figure 5-17 PXD pattern of Sample 52. 227

Figure 5-18 STA data for Sample 52 heated from room temperature to 500 ^{o}C at 5 ^{o}/min; a) DTA, b) TG and c) MS (*m/z* = 2).....228
Figure 5-19 PXD pattern of sample collected after STA. 229
Figure 5-20 PXD of post milled metathesis product (Sample 53). 229
Figure 5-21 STA data for the Sample 53 heated to 500 ^{o}C at 5 ^{o}/min; a) DTA, b) TG and c) MS (*m/z* = 2). 230
Figure 5-22 SEM images of Sample 54; a) low (20 μm) and b) high (10 μm) magnifications. 231
Figure 5-23 PXD pattern of post metathesis product; Sample 54. 231
Figure 5-24 STA data collected Sample 54; a) DTA, b) TG and c) MS (*m/z* = 2).....232
Figure 5-25 Rietveld refined of the post STA product collected for Sample 54 showing the LiMg alloy phase indicated by blue tick marks (Phase 1), NaCl in red tick marks (Phase 2) and LiCl in black tick marks (Phase 3). Experimental and calculated data are indicated by red crosses and the green continuous line, respectively. The lower magenta line indicates the difference plot. 233
Figure 5-26 Rietveld plot of mechanochemically prepared $NaAlCl_4$ (Sample 56); black tick marks indicate the $NaAlCl_4$ phase. Red crosses indicate experimental data, and green line indicates the calculated pattern. The magenta line indicates the difference plot. 237
Figure 5-27 a) Extended structure of mechanochemically synthesized $NaAlCl_4$ (Sample 56) and the coordination orientations of Cl anions to the b) seven coordinate Na cations (yellow polyhedra) and c) Al tetrahedra (purple polyhedra). (Al = purple spheres, Na = grey spheres, Cl = green spheres.) 239
Figure 5-28 DTA profiles of Sample 55 (dashed line) *vs.* Sample 56 (solid line). 240
Figure 5-29 PXD pattern or sample collected after metathesis reaction between $NaAlCl_4$ and LiH (Sample 57). 240
Figure 5-30 STA data for Sample 57; a) DTA, b) TG and c) MS (*m/z* = 2). 241
Figure 5-31 PXD patterns of the samples collected post STA for Sample 57 to a) 300 °C and b) 500 °C. 242

Acknowledgments

I am extremely grateful for the education that I have received. Without educators my achievements to date, including this thesis, would not have been possible. My first acknowledgement, therefore, is to the enthusiastic teachers, lecturers and technicians who, throughout my education, have helped and encouraged me to achieve my best.

The opportunity to undertake this PhD was opened up after a brave e-mail to Prof. Duncan Gregory, and without him and collaborators at Airbus (namely Dr. Agata Godula-Jopek) and the EPSRC, this project would not exist. I am thankful for the opportunity they have afforded me and for the support that has been provided during my research project.

Working in the Gregory group has been an experience, to say the least! The ups and downs of the technical (and not-so-technical) issues that arose during my studies were all shared, and I have met and worked alongside some brilliant minds including undergraduates (Berkay Ersengun, Elsa Giraud, Natalia Mazur and Niall Kirkaldy), fellow PhD students and postdoctoral researchers (Dr. Bob Hughes, Dr. Tuan Huang and Dr. Li Yang), and incredible technical staff (Jim Gallagher, Andy Monaghan and Ron Spence). I would like to acknowledge Dr. Nuria Tapia-Ruiz, Dr. Natalie Sorbie and Dr. Saleem Denholme specifically for their help in the initial stages of my research, they passed on their skills and knowledge that kick-started my experimental work and for that I am very grateful. For the office laughs, I would like to thank Helen Kitchen, Jamie Gallagher, Dr. Stephanie Kelly, Jennifer Kennedy, Dr. James Hanlon, Marc Segales-Ruiz, Alan Wiseman and Espen Drath Bøjesen. In many scenarios, individually and collectively, you have made the difficult days that bit more bearable and the awesome ones even better. Although, I don’t think we’ll ever agree on the correct way to eat a kiwi fruit.

I cannot thank the Prentice and Gillespie families enough for transforming Sunday dinners in to *the* entertainment event of the week. I dread the day that I have to make (and sieve) custard for you all! You have all made me feel like part of the family, and your warmth and kindness towards me is cherished.

My parents, Alan and Morag, are a real inspiration to me. I could not have been given a better start in life, and it is only through your efforts and sacrifices that I may lead such a privileged life. Your continued support, guidance and love are what motivate and encourage me to do my best, succeed and seek out my next challenge! I will always aspire to being as good and kind and generous as you both are. My sister, Fiona, and I have shared so much laughter and tears (and hangovers) over the years, and I’d like to thank you for being my best friend. I wish my brother, Calum, lived closer so that we could share more laughs and celebrate all of our achievements together.

Colin, you are literally the very best thing to have ever happened to me. You continue to encourage, support and motivate me through all the challenges that life throws, and I cannot thank you enough for your patience and love. We have already been on so many adventures together, and I look forward to the next. I could not have done this without you. So there ye are.

“Those who matter don’t mind, and those who mind don’t matter.”

– Bernard Mannes Baruch

Definitions and Abbreviations

Abbreviation	Definition
CCD	Charge-Coupled Device
CELREF	Unit Cell refinement software package
COF	Covalent Organic Framework
DOE	Department of Energy
DSC	Differential Scanning Calorimetry
DTA	Differential Thermal Analysis
EDX	Energy Dispersive X-ray spectroscopy
EGA	Evolved Gas Analysis
ESD	Estimated Standard Deviation
ESEM	Environmental Scanning Electron Microscope
FTIR	Fourier Transform InfraRed spectroscopy
FWHM	Full Width Half Maximum
GNS	Graphene Nano-Sheets
GSAS-EXPGUI	General Structural Analysis System – EXP Graphical User Interface
HP-DSC	High Pressure - Differential Scanning Calorimetry
HT	High Temperature
ICDD	International Centre for Diffraction Data
ICSD	Inorganic Crystal Structure Database
ID	Identification
IAESTE	International Association for the Exchange of Students for Technical Experience
IGA	Intelligent Gravimetric Analyser
INCA	INCAEnergy EDX analysis software package
IR	InfraRed
ISIS	ISIS Neutron and Muon Source
LAPW	Linear Augmented-Plane Wave
LINEST	Microsoft Excel Function - calculates the statistics for a line by using the "least squares" method to calculate a straight line that best fits a dataset
LO	Longitudal Optical phonon mode
LT	Low Temperature
MOF	Metal Organic Framework
MPD	Multi-Purpose Diffractometer
MS	Mass Spectrometry
MWCNT	Multi-Walled Carbon Nanotubes
NIMROD	Near and InterMediate Range Order Diffractometer
NMR	Nuclear Magnetic Resonance
NSRRC	National Synchrotron Radiation Research Center

Abbreviation	Definition
NTNU	Norwegian University of Science and Technology
PEM	Proton Exchange Membrane
PCT	Pressure-Composition-Temperature
PND	Powder Neutron Diffraction
POLARIS	Powder Neutron Diffraction Beam line at ISIS
PXD	Powder X-ray Diffraction
RT	Room Temperature
SAED	Selected Area Electron Diffraction
SANS	Small Angle Neutron Scattering
SDD	Silicon Drift Detector
SEM	Scanning Electron Microscope
SHS	Self propagating High temperature Synthesis
SOF	Site Occupancy Factor
SSM	Solid State Metathesis
STA	Simultaneous Thermal Analysis
STFC	Science & Technology Facilities Council
SWLS	Superconducting Wave Length Shifter
SXD	Synchrotron X-ray Diffraction
TEM	Transmission Electron Microscopy
TG	ThermoGravimetry
THF	TetraHydroFuran
TM	Transition Metal
TO	Transverse Optical phonon mode
TPD	Temperature Programmed Desorption
UV	Ultra Violet
XANES	X-ray Absorption Near Edge Structure
XPS	X-ray Photoelectron Spectroscopy
XRD	X-Ray Diffraction

1. Introduction

1.1. The Energy Deficit & Energy Storage

Global energy consumption forecasts predict a 56 % increase in energy consumption between 2010 and 2040.[1] The growth in world population over this period, particularly in developing countries, will play a major role in determining how the increasing energy requirements of society will be met.[2, 3] Thus, sustainable energy production, storage, delivery, and consumption are among the major global development challenges (including poverty, health and disease prevention, food production, climate change, education and inequality) that must be tackled to achieve global prosperity.

Finite energy resources, including coal, oil and gas are expected to remain providing the majority of energy consumed globally over the next three decades, although renewable energy sources are set to increase significantly over this period (Figure 1-1). The reserves of non-renewable energy sources are diminishing and it is inevitable that they will one day be depleted and become obsolete. Therefore, the ideal scenario is for usage of renewable energy sources to replace fossil fuels, and research into safe, environmentally benign alternatives has been under way for many decades.[4]

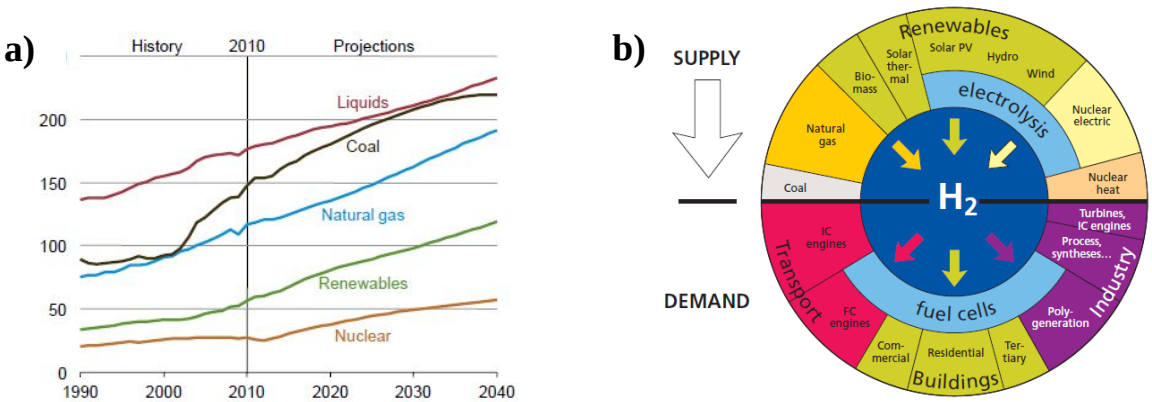

Figure 1-1 a) Energy use projections from US DOE[1], and b) European energy supply-demand profile.[3]

It is possible to store the surplus electrical energy generated by current sustainable energy sources, *i.e.*, wind, hydro, solar, wave and tidal power, by means of hybrid power generation-storage systems. State-of-the-art energy storage methods for this approach are developing rapidly, and include hybrid fuel cell or battery systems, where production of hydrogen (former) or storing electrical potential (latter) ensure energy waste is minimised.[5, 6, 7] Efficient energy storage is therefore critical in ensuring sufficient,

sustainable energy supplies are produced and are available on demand for the target application.[8]

From thermal storage in phase change materials to electrical storage in ionic conductors, developments in solid state inorganic materials chemistry play a pivotal role in the progression of modern energy storage technology. The introductory chapter of this thesis will focus on inorganic materials which have made the most significant progress in energy storage and harnessing in recent years.

1.2. Hydrogen: A Promising Energy Store

Effective storage of hydrogen has played a significant role in realising accessible clean energy for all, and many static and automotive projects worldwide are already utilising hydrogen as an energy carrier either as a (compressed) gas, liquid or within solids. Based on production *via* renewable energy sources, hydrogen (H_2) may be considered a convenient sustainable energy reservoir with an energy density significantly greater than current fossil fuel derived fuels.[9, 10] Hydrogen is conveniently the most abundant element on Earth, although inconveniently it is usually combined in molecules from which it must be extracted. A future hydrogen economy is based on a sustainable hydrogen energy cycle.[11] Complete consideration of the hydrogen energy lifecycle, from production to utilisation, is highlighted in the ongoing research being conducted by the U. S. Department of Energy "Hydrogen and Fuel Cells Program".[12]

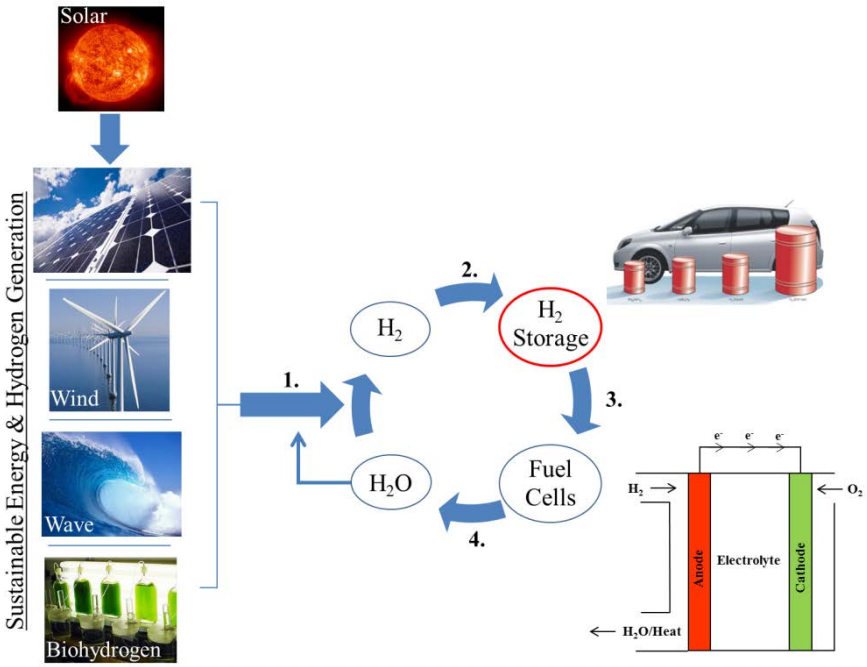

Figure 1-2 Schematic of a sustainable hydrogen energy cycle.[23]

The key processes of a sustainable hydrogen energy cycle are highlighted in Figure 1-2, and will now be discussed.

1. Sustainable energy sources, solar, wind, *etc*., mentioned previously, may be used to produce hydrogen with minimum environmental impact. Biohydrogen technology is a rapidly developing field, and provides another sustainable hydrogen production route.[13, 14, 15] Use of organic municipal waste in the biohydrogen production process creates further arguments for developing this as an environmentally and economically viable hydrogen production route.[16]

2. Hydrogen exists as a gas under standard conditions and is normally used in industry as a compressed gas or as a liquid.[17] The potential for hydrogen to be a widespread energy carrier for mobile applications is dependent upon the discovery of adequate storage solutions. These must be capable of supplying sufficient quantities of hydrogen to meet the operating demands of the application. Solid state hydrogen storage presents a safer alternative to compressed gas, with most research focussing on high energy density materials with tuneable thermodynamic and kinetic properties.[18, 19, 20] Consideration of the thermodynamics and kinetics of the hydrogen sorption processes, and optimisation of the gravimetric and volumetric capacities of hydrogen storage matrices have thus been at the forefront of hydrogen storage research. The use of hydrogen for mobile vehicular applications is already globally apparent, but currently technology relies on compressed hydrogen gas stored in high pressure tanks.[21, 22] A number of factors related to the use of high pressure hydrogen gas, including safety implications and volume restrictions, are limiting the introduction of hydrogen to the wider vehicular market.[23, 24] Recent literature on tank designs have emerged, and experimental assessments indicate significant steps are being made towards realising metal hydrides as an alternative to compressed hydrogen gas for on-board hydrogen storage for mobile applications. [25, 26, 27, 28, 29, 30] It is clear that a complex balance of material properties must be met in order for the ideal solid state hydrogen storage conditions to be realised (Figure 1-3).[24, 31, 32] Hydrogen storage materials are the focus of this research, as will become evident.

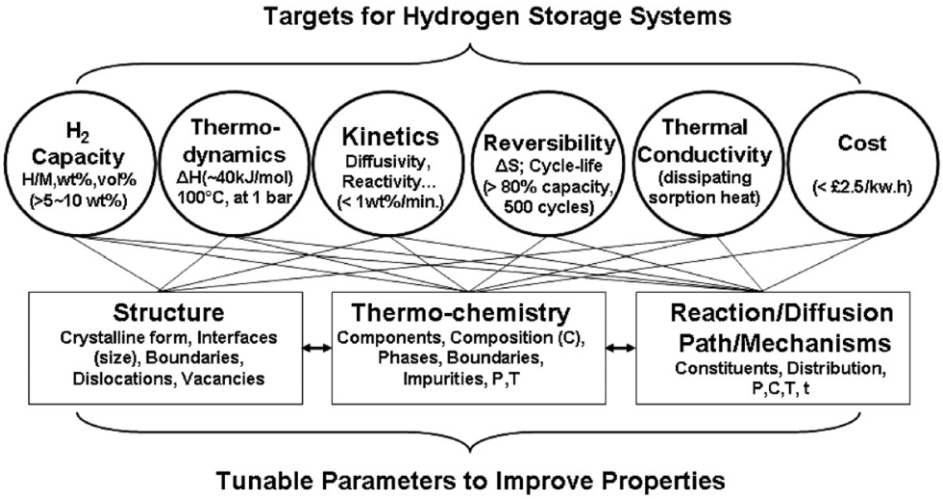

Figure 1-3 Parameters and operating margins to be met by commercially viable solid state hydrogen storage materials.[31]

3. Utilization of hydrogen for energy is typically in fuel cell systems.[33] From detailed scrutiny of the composition of anode, cathode and electrolyte components, to the chemical processes involved therein, fuel cell design and optimization requires complex theoretical and experimental research to breed commercially viable systems.[34, 35] The compatibility of metal hydrides for fuel cells is of specific interest in this work, and developments *via* experiment and simulation over the past few years in hydride tank design and fuel delivery systems emphasise the need for more effective hydrogen storage materials if the performance demands of mobile applications are to be met. [28, 36, 37, 38, 39] Most recently, a reversible proton exchange membrane (PEM) fuel cell system ("proton flow battery") has been devised in which the role of a reversible metal hydride is fundamental to the *in-situ* charge-discharge system (Figure 1-4).[40]

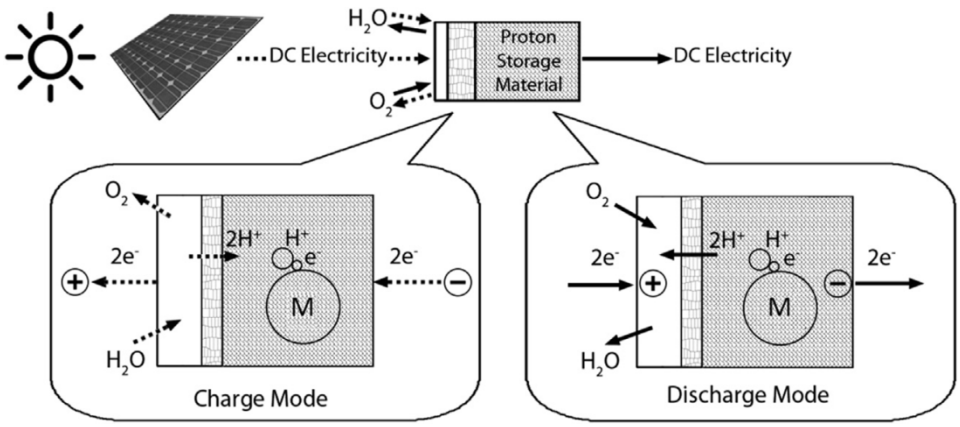

Figure 1-4 Novel "proton flow battery", where M represents the metal component of the hydrogen storage material.[40]

4. The waste products from fuel cell systems are primarily water, heat and un-reacted feedstock. These environmentally benign products are in stark contrast to the harmful effluents of fossil fuel derived energy systems, which contribute to climate change and thus the quality of life of all species on Earth.[41] Regeneration of hydrogen from the waste products by water splitting and utilisation of heat exchangers to capture the excess heat for other processes completes the hydrogen cycle.

Multi-disciplinary collaborations in academia and industry are crucial for developing a concerted approach to high performance hydrogen production, storage and delivery systems for the commercial market, and interest in those based on solid state hydrogen storage methods is gaining momentum.[42, 43]

1.2.1. Solid State Hydrogen Storage

An abundance of literature is available on the development of solid state hydrogen storage materials.[18] The storage of hydrogen in solid state materials may be classified broadly as *chemical storage* or *physical storage*. The research conducted in this work focuses on hydrogen stored in metallic materials, which lies in the domain of the former category. (A wealth of information on the latter may be found in recent literature, covering clathrate hydrates, MOFs (Metal Organic Frameworks), COFs (Covalent Organic Frameworks), polymers, various carbon structures and beyond, but will not be covered further in this work for brevity.[44, 45, 46, 47, 48])

1.2.1.1. Metal Hydrides

Solid state storage of hydrogen in alkali metal hydrides is appealing because of their inherent light weight.[49, 50, 51] It is evident from Figure 1-5 that there are a large number of known binary hydrides of both the alkali metals, transition metals and *f*-block elements, although use of the majority of the latter two systems is limited by cost or their harmful properties. This is also related to abundance of the metal component, and hydride synthesis requirements, *i.e.*, harsh pressure and temperature conditions. Thus, the main focus of hydrogen storage research based on metal hydrides has been on those which are relatively easy to synthesise at a lab and industrial scale, are derived from abundant metals and meet (or are closest to) the margins for practical hydrogen storage.

IA	IIA											IIIA	
H													
Li	Be												
Na	Mg	IIIB	IVB	VB	VIB	VIIB		VIIIB		IB	IIB	Al	
K	Ca	Sc	Ti	V	Cr*	Mn*	Fe*	Co*	Ni*	Cu	Zn	Ga	IVA
Rb	Sr	Y	Zr	Nb	Mo*	Tc*		Rh*	Pd		Cd	In	Sn
Cs	Ba	La	Hf	Ta								Tl	Pb
		Ac											

Ce	Pr	Nd		Sm	Eu	Gd	Tb	Dy	Ho	Er	Tm	Yb	Lu
Th	Pa	U	Np	Pu	Am	Cm	Bk						

Key: red = hydrogen, blue = ionic hydrides, yellow = covalent hydrides, grey = metallic hydrides, pink = both covalent and ionic, green = both ionic and metallic. *Hydride formation requires >0.1 MPa H_2 pressure.

Figure 1-5 Position of hydrogen on the periodic table and table of metals which form solid binary hydrides (adapted from Reference 49).

Hydrogen release from solid state hydride systems has been studied extensively through experimental and theoretical research, and an overview of the current metal-hydride materials is provided in this chapter.

As previously mentioned, gravimetric and volumetric capacity is of significant importance in the determination of the suitability of a solid state hydrogen storage material. Accordingly, the lightest metal hydrides have been given significant consideration in this field. The theoretical hydrogen storage capacities of these materials are promising, with an overall decrease in gravimetric hydrogen capacity upon descending Group I (12.68 wt% and 0.75 wt% for LiH and CsH respectively) and Group II (18.28 wt% and 1.44 wt% for BeH_2 and BaH_2 respectively), and a relative increase in gravimetric capacity from Group I to Group II. Much work has covered the synthesis and characterisation of light-weight alkali and alkaline earth metal hydrides for hydrogen storage, as will be described. Furthermore, some of these metal hydrides have been combined with Group XIII elements, *e.g.*, aluminium and boron, to form complex hydrides that have a higher theoretical hydrogen capacity than the light metal hydrides (Figure 1-6). Nanostructured hydride materials have highlighted how the criteria for vehicular applications may be met by metal hydrides at this scale, and various methods have been applied to understand the properties

of such structures.[52] First, in order to determine how light metal hydride materials may be modified or enhanced, a systematic review of the current technologies will be made.

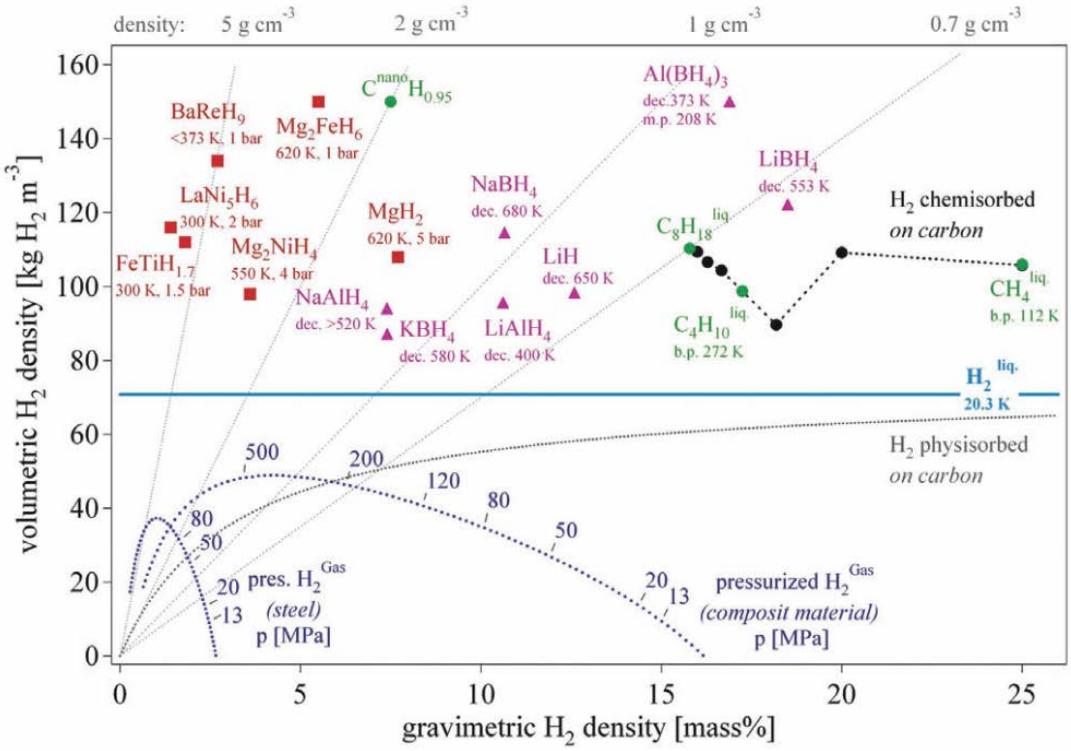

Figure 1-6 Comparison of the volumetric and gravimetric hydrogen storage properties of some potential solid state hydrogen storage materials. [53]

LiH and NaH are useful hydrides for light-weight hydrogen storage (Table 1-1), but they are extremely sensitive to air and moisture exposure, which makes them difficult to handle and store. As a result, their use as hydrogen storage materials in isolation is limited but they have found use in a range of composite systems in this field of research, which will be described later.

Table 1-1 Key properties of the lightest known metal hydrides; LiH and NaH.[54]

	Lithium Hydride	**Sodium Hydride**
Molecular Formula	LiH	NaH
Molar Mass, *g*	7.95	23.99
Theoretical Wt% H	12.7	4.21
Density, *g/cm³*	0.78	1.396
Melting Point, *°C*	688.7	800
$\Delta_f H^o_{solid}$, kJ/mol	-90.63	-56.44
Crystal System/ Space Group	Cubic / $Fm\bar{3}m$ (225)	

1.2.1.2. Magnesium Hydride

Magnesium is an abundant and inexpensive metal and plays a key role in the development of safe, lightweight, high hydrogen capacity storage materials. Figure 1-5 highlights MgH_2 as the transition point between the ionic hydrides (LiH, NaH and CaH_2) and the covalent hydrides. The hindrance for the high hydrogen capacity (7.6 wt%) Mg-H system, however, is that it suffers from poor thermodynamics and slow kinetics; high hydrogen desorption temperature and slow hydrogen absorption (Equation 1-1).[54]

Equation 1-1 $$Mg + H_2 \leftrightarrow MgH_2 \qquad \Delta_f H^\circ_{solid} = -76.15 kJ/mol$$

A number of theoretical and experimental approaches have been examined to optimise the properties of the Mg-H system. Two main approaches are used to drive down the hydrogen desorption temperature of MgH_2; nanoscaling and inclusion of catalysts/additives. These concepts have been explored *via* a number of methods, and the progress made in nanoscaling and the most successful additives/catalysts employed to date will now be discussed.

1.2.1.2.1. Nanoscaling of MgH_2

A range of Mg and MgH_2 morphologies, particularly at the nanoscale, have emerged by preparation using novel synthesis methods to optimise (de-)hydrogenation behaviour, and thorough characterisation has allowed the performance of such materials to be described in detail.[55, 56, 57] Synthesis and developments in nanostructured Mg-H materials have been possible by a number of methods, including milling/mechanochemistry, chemical vapour deposition/transport, solvated metal atom dispersion, laser ablation, and confinement.[58, 59] In the early 1980s, pure magnesium powder was hydrided to investigate whether smaller particle sizes, and hence larger surface areas, may enhance the performance of magnesium as a hydrogen store.[60] The results published by Vigeholm *et al.* showed that when commercially sourced magnesium powders below 100 μm in size were hydrided, the metal was converted entirely to the metal hydride. After further studies into the effects of hydrogen cycling in small particles (< 75 microns) of pure magnesium, interesting structural changes were revealed.[61, 62] Magnesium "whiskers" with a diameter of 500 nm were identified; a phenomenon that had not been observed in previous studies. After an increased number of hydrogen cycles further structural changes in the magnesium were visible; as the number of cycles increased, a significant agglomeration of the particles was observed, and this led to a decrease in wt% adsorption-desorption of hydrogen by the metal.[63] Theoretical studies have now shown that Mg nanoparticles must be reduced to

much less than 20 nm to produce the desirable thermal and kinetic behaviour to be practical for reversible hydrogen storage.[64] A number of experimental methods have been studied over decades to optimize the properties of the Mg-MgH_2 system for practical hydrogen storage at the nano-scale, and these have been supported by comprehensive theoretical evaluations.[65, 66, 67] Much of this work focuses on the use of milling as a suitable MgH_2 synthesis method *via* reactive milling under a hydrogen atmosphere. Furthermore, using commercial MgH_2 in the milling procedure provides a facile method of particle size reduction that is viable for translation into an industrial-scale manufacturing process.[68, 69, 70]

The main parameters for ball milling for the Mg-H system include milling time, ball:powder mass ratio, milling atmosphere, *i.e.*, pressures of hydrogen or argon, milling apparatus, and mill rotation speed.[71] The milling rotation speed is often not stated in the literature and as a result it is difficult to optimise rotation speed, and hence energy, which has implications for the consistency of results from one milling experiment to the next. There are numerous studies in the literature describing the processing of MgH_2 *via* ball milling, many of those having been discussed earlier in this work, and the reader is directed to recent reviews and literature on the synthesis and processing of MgH_2 nanoparticles by this method.[72, 73, 74]

1.2.1.2.2. Additives for Enhancing the Mg-H System

The choice of additive plays a crucial role in lowering the desorption temperature; depending on the physical properties of the additive it is likely to have a direct impact on the milling process which will in turn modify the physical properties of the milled hydride. Furthermore, certain additives may also act to catalyse hydrogen sorption in the Mg-H system. Transition metals and their compounds and multi-component systems are all contributing towards the developed understanding of how the hydrogen storage properties of MgH_2 may be understood and tuned towards real applications. (The effect of non-oxide additives will be described further in Chapter 3.)

Transition Metal Additives

The electronic structure of transition metals and their ability to readily exist in a variety of oxidation states allows them to act as catalysts. A brief summary of transition metals used in the Mg-H system will be given here and reference to relevant literature provided for further reading (Figure 1-7).[44, 75, 76, 77, 78, 79, 80, 81, 82, 83] Being the lightest transition metals, significant attention has been given to the *3d* metals, where Ti[84, 85, 86, 87], V[88, 89, 90, 91, 92] and

Ni[93, 94, 95, 96, 97] have received the greatest interest. Nb[98, 99, 100] and Pd[101] are the most developed *4d* transition metal catalysts for use in the Mg-H system.

	IIIB	IVB	VB	VIB	VIIB	VIIB			IB	IIB
3d	**Sc**	**Ti**	**V**	**Cr**	**Mn**	**Fe**	**Co**	**Ni**	**Cu**	Zn
4d	Y	**Zr**	**Nb**	**Mo**	Tc	Ru	Rh	**Pd**	Ag	Cd
5d	La	Hf	Ta	W	Re	Os	Ir	Pt	Au	Hg

Figure 1-7 Summary of transition metal catalysts (highlighted in bold) used to enhance the Mg-H system.

Co-catalysed composites have also been prepared, comprising Mg and two or more metal additives.[102, 103, 104] Bi- and multi-metallic alloys have received significant attention.[105, 106, 107, 108, 109, 110, 111, 112] Mischmetal catalysts and their potential to form nano-composites for hydrogen storage have also been explored.[113]

Numerous *nanosized* transition metal additives have been investigated with MgH_2 in order to establish if the size of the additional metal component can have an effect on the hydride performance.[81, 114] The dispersion of these nano-materials throughout the hydrogen storage material by, *e.g.*, sputtering or milling, *etc.*, is said to induce a catalytic effect, and also promote nucleation. Hanada *et al.* investigated the morphological differences observed when nickel nanoparticles and niobium (V) oxide were investigated as catalysts by milling with MgH_2 under hydrogen, since previous results had shown enhanced hydrogen sorption characteristics in comparison to magnesium hydride alone.[115] Non-agglomerated Ni nanoparticles were observed to exist only on the surface of MgH_2 particles and were uniformly distributed. By contrast, nanoparticles (<10 nm) of niobium oxide were dispersed throughout the metal hydride, both on the surface of the bulk hydride and throughout the crystallites. This was observed using TEM (Transmission Electron Microscopy) analysis and a similar scenario was found in the work by Friedrichs *et al.* on Nb_2O_5 catalysed MgH_2.[116] In both the Ni and Nb_2O_5 investigations, the nano-catalyst was found to remain on/in the hydride after dehydrogenation under vacuum at 200 °C for 8 h, which is promising since it would imply that retention of the catalytic action was possible throughout the lifetime of the hydride.

Oxides

The most studied and therefore "benchmark" catalyst for MgH_2 is Nb_2O_5.[39, 41, 117, 118, 119, 120] The remarkable work of Hanada *et al.* in 2006 demonstrated that Nb_2O_5 (1 mol%) exhibited significant catalytic activity in the Mg-H system after milling, where the hydrogen desorption activation energy determined from Kissinger plot analysis was shown to be reduced to 71 kJ/mol H_2.[121] After the first dehydrogenation conducted at 200 °C, Hanada and colleagues demonstrated that hydrogen uptake (>5 wt%) in the dehydrogenated sample was possible at room temperature under <1 MPa, where hydrogenation of un-catalysed, un-milled Mg typically requires temperatures >300 °C under similar pressure conditions. Hydrogen desorption (~6 wt%) from the re-hydrogenated sample occurred at 160 °C and although this is still higher than the temperatures typically required for a fuel cell operating system it is significantly reduced relative to that of unmodified MgH_2. With such promising sorption characteristics demonstrated experimentally by Hanada *et al.*, much work has focussed on understanding the mechanism of the Nb_2O_5 catalytic effect on MgH_2.[116, 122, 123, 124, 125, 126] A recent study by Neilsen and Jensen using SXD (Synchrotron X-ray Diffraction) confirmed that an oxide ($Mg_xNb_{1-x}O$) forms upon cycling of the milled composite comprising 8 mol% Nb_2O_5 milled with MgH_2 for 2.5 h at 300 rpm.[127] It should be highlighted that the additive proportion in this case is significantly greater than in earlier work (typically a catalytic quantity of 0.5 mol% Nb_2O_5 is added).[128]

In 2007, a study investigating the thermal properties of a 17 wt% Nb_2O_5 in MgH_2 composite showed that after 200 h milling the decomposition profile determined by DSC (Differential Scanning Calorimetry) analysis showed two curves.[129] The low temperature curve (T_{peak} = 264 °C) was more prominent than the higher temperature curve (T_{peak} = 316 °C). No reasoning was given to explain the difference between the two peaks, but Nb_2O_5 was described as acting as a lubricant to facilitate the reduction of MgH_2 particle size whilst preventing cold welding and agglomeration effects. Recent work also showed that Nb_2O_5 decreased the T_{peak} of both the low and high temperature DTA (Differential Thermal Analysis) peaks, with increasing proportions (5 wt%) of the catalyst exhibiting a pronounced effect relative to low catalyst loading (1 wt%). Again, the two peaks were described as being solely a result of the decomposition of the α- and γ-MgH_2 phases, at the lower and higher temperature respectively.[130]

Many other transition metal oxides have provided H_2 sorption results in the Mg-H system where performance is improved relative to MgH_2 alone.[131, 132, 133] Oelerich *et al.* showed

that even a small incorporation of an oxide; Sc_2O_3, TiO_2, V_2O_5 , Cr_2O_3, Mn_2O_3, Fe_3O_4, CuO, Al_2O_3, is capable of producing a positive effect on the sorption profiles of MgH_2.[134, 135] Chromium oxide had the most pronounced effect on the adsorption profile, and the iron and vanadium oxides were most efficient in decreasing the time for desorption, but no hypotheses were proposed as to why *both* the adsorption profiles and desorption profiles were not enhanced in each case.

Developments in the use of ball milling and non-oxide catalysts to enhance the performance of MgH_2 will be described in more detail in Chapter 3. Therein, the thermal behaviour of the commercial hydride as-received and after milling under different conditions is probed, and a novel catalysed MgH_2 composite will be examined.

1.2.1.3. Calcium Hydride

Calcium hydride, CaH_2, is a stable ionic hydride and there are relatively few studies solely dedicated to the use of CaH_2 as a hydrogen storage medium. This is most likely to be direct consequence of the higher thermal stability of CaH_2 when compared with MgH_2, where H_2 release from bulk CaH_2 does not occur until ~600 °C. Similarly to the Mg-H system, hydrogen uptake and release in the Ca-H system is reversible. Typically, CaH_2 is formed by reaction of Ca metal with high pressure hydrogen at high temperature.[136] A novel mechanochemical synthesis route to CaH_2 was studied by Ney and colleagues recently, however, and it was shown that nanoparticles of the hydride could be synthesised from phenylphosphonic acid and Ca metal *via* a purely solid state method.[137] The study on the Ca-H system by Dixit *et al.* indicates that CaH_2 is a less viable option than MgH_2 when compared in bulk and from their computational work on M_nH_{2n} (M = Ca, Mg) clusters.[138] Nonetheless, CaH_2 has been studied as a hydrogen storage component and has found use in a variety of composite systems, *e.g.*, in amide, borohydride and ammonia borane systems.[139, 140, 141] Milling of CaH_2 with MgH_2 has been conducted in this research, and the developments made through this work will be described in Chapter 4.

1.2.1.4. Complex Hydrides

Significant research has been conducted to evaluate the feasibility of complex hydrides, *i.e.*, alanates and borohydrides, for hydrogen storage.[142, 143] Despite their relatively low hydrogen release temperatures, much work has been focussed on the improvement of their reversibility and hydrogen release mechanisms.

Alanates

A wealth of information is available for the synthesis, structures and hydrogen storage properties of the alanates, and a summary of the Group I and Group II metal alanate dehydrogenation mechanisms are given in Table 1-2.

Table 1-2 Thermodynamic and relevant data for light metal alanates.

M^+	H_2 Release Mechanism	Theory wt% H_2	T_{des} / °C	ΔH_{des} / kJ/mol	Ref.
Li^+	(1) $3\ LiAlH_4 \longrightarrow Li_3AlH_6 + 2\ Al + 3\ H_2$ (2) $Li_3AlH_6 \longrightarrow 3\ LiH + Al + 3/2\ H_2$ (3) $3\ LiH + 3\ Al \longrightarrow 3\ LiAl + 3/2\ H_2$	5.3 2.6 2.6	150-175 180-220 400	-10 +25	144, 145, 146
Na^+	(1) $NaAlH_4 \leftrightarrow 1/3\ Na_3AlH_6 + 2/3\ Al + H_2$ (2) $Na_3AlH_6 \leftrightarrow 3\ NaH + Al + 3/2\ H_2$	3.7 1.9	120[a] 180[a]	+37 +47	161, 147
Mg^{2+}	(1) $Mg(AlH_4)_2 \longrightarrow MgH_2 + 2\ Al + 3\ H_2$ (2) $MgH_2 + 2\ Al \longrightarrow ½\ Al_3Mg_2 + ½\ Al + H_2$	9.36	150 310	+1.7 +48.8	148, 179
Ca^{2+}	(1) $Ca(AlH_4)_2 \longrightarrow CaAlH_5 + Al + 3/2\ H_2$ (2) $CaAlH_5 \longrightarrow CaH_2 + Al + 3/2\ H_2$ (3) $CaH_2 + Al \longrightarrow Ca_4Al + H_2$	7.8 4.2	127 260-550 600-700	-7 +31	174

[a] Includes Ti dopant.

The lightest complex hydride, $LiAlH_4$, has significant appeal for hydrogen storage applications (Figure 1-8 a).[51, 149] With theoretical volumetric and gravimetric capacities of 74.02 kg/m^3 and 10.5 wt%H respectively, it is clear that this alanate is within the hydrogen storage targets for mobile applications. In addition, it does not spontaneously decompose in air nor does it produce toxic by-products or emissions, emphasising its appeal as a safe hydrogen store. The crystal structure of $LiAlH_4$ was first determined from a single crystal study by Sklar and Post.[149] In the mid-1980s, the Raman spectrum of $LiAlH_4$, and its deuterated form, was collected and the bonding modes assigned.[150]

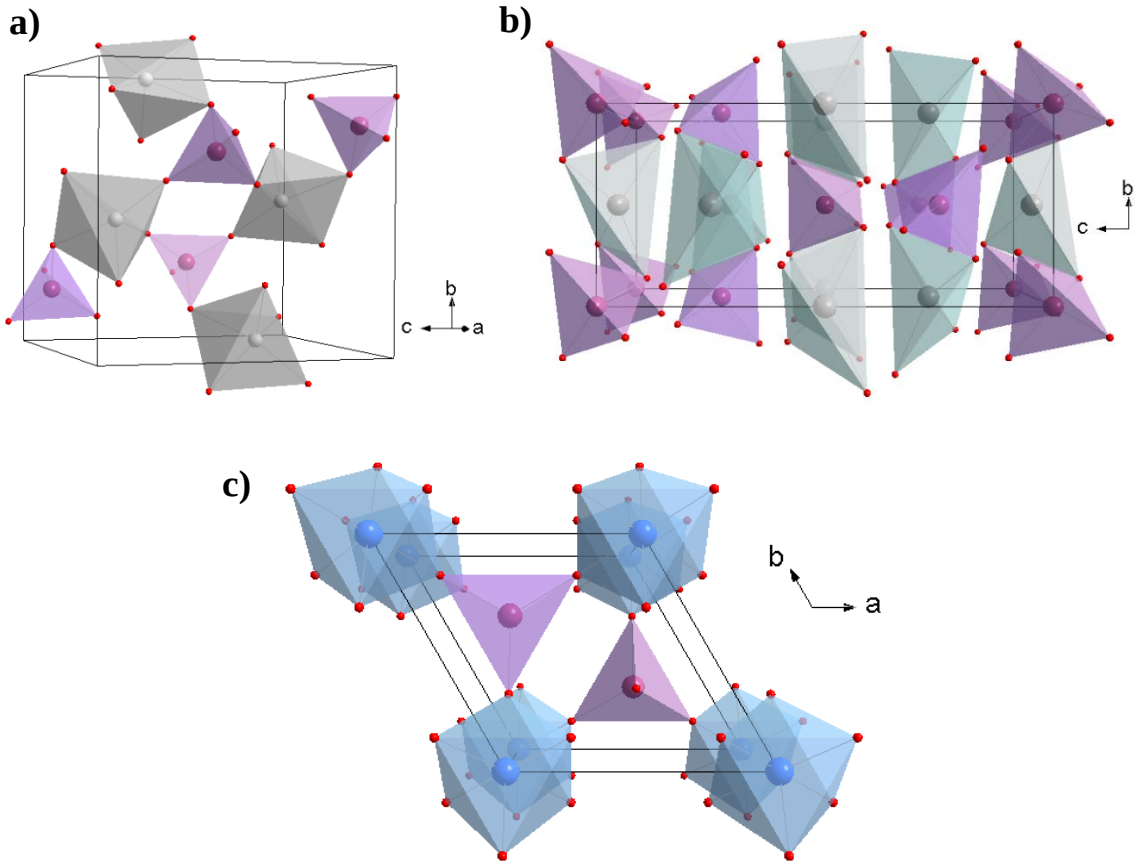

Figure 1-8 Unit cell of a-c) $M(AlH_4)_n$ (M=Li, Na, Mg, and n=1, 2) alanates showing the tetrahedral orientation of the $[AlH_4]^-$ anions using purple polyhedra, and the coordination orientation of the metal cations using grey (Li), green (Na) and blue (Mg) polyhedra. (Atom key: Li = white, Na = grey, Mg = blue, Al = purple, and H = red.)

Synthesis of $LiAlH_4$ has recently been studied by milling of LiH and Al under H_2.[151, 152] More recent work looks more intensively at the properties of milled $LiAlH_4$ with respect to the unmilled material and the effects of exposure to air and moisture.[153] The decomposition process, reaction intermediates and associated thermodynamics of hydrogen evolution from $LiAlH_4$ have been probed by a variety of techniques.[146, 154, 155, 156] The first and second hydrogenation steps are the only reversible ones, and the third and final release step has a large thermodynamic barrier which must be overcome. Much effort has been exerted to determine ways to reduce the thermodynamic barrier and thus improve reversibility. For example, catalysts have been used in $LiAlH_4$ studies where Ti compounds dominate this research.[157, 158, 159, 160]

The gravimetric capacity (7.4 wt%H) of $NaAlH_4$ is slightly diminished with respect to $LiAlH_4$, but the volumetric capacity is larger (97.41 kg/m^3, Figure 1-8 b).[161, 162] Analysis of $NaAlH_4$ and its decomposition product, Na_3AlH_6, by single crystal diffraction and Raman spectroscopy have been important for understanding the Na-Al-H system.[163, 164] A solvent free route to $NaAlH_4$ involves reactive milling of NaH/Al under $H_{2(g)}$. Additives have been

incorporated as part of the synthesis process after Bogdanovic and Schwickardi successfully demonstrated the reversibility of $NaAlH_4$ using only 2 mol% $TiCl_3$.[165, 166, 167] Thus, similarly to $LiAlH_4$, Ti based dopants dominate research towards optimization of the $NaAlH_4$ hydrogen storage characteristics.[168, 169, 170, 171, 172] Nanosized TiO_2 has been found to reduce the hydrogen release temperature of $NaAlH_4$ to 100 ºC by TPD (Temperature Programmed Desorption) experiments.[173] Furthermore, the alanate doped with 2 mol% of 25 nm TiO_2 particles was found to reversibly store up to 4 wt% hydrogen over 35 cycles.

Milling of a Group II metal halides, *e.g.*, $MgCl_2$, or $CaCl_2$, with the Group I alanates described above has been used to generate nanoscale particles of the respective Group II alanates, *i.e.*, $Mg(AlH_4)_2$ and $Ca(AlH_4)_2$, and hence evaluate their structure and decomposition (Figure 1-8 c).[174, 175, 176, 177, 178] Fichtner *et al.* produced magnesium alanate *via* a wet synthesis method, with particles in the 30-40 nm range.[179, 180] Direct synthesis of $Mg(AlH_4)_2$ from Mg and Al by reactive milling has been attempted, but was not successful.[181] The preparation of these alanates has allowed the thermal decomposition behaviour of nanoparticles of $Mg(AlH_4)_2$, $Ca(AlH_4)_2$ and $LiMg(AlH_4)_2$ to be determined.[182] This showed maximum hydrogen desorption values of up to 5 wt% for magnesium and calcium alanates, and 4 wt% for the quaternary lithium magnesium alanate.

Novel mechanochemical metathesis routes to complex metal hydrides, $LiAlH_4$ and $NaAlH_4$, *via* complex halide precursors will be explored in Chapter 5.

Borohydrides

Borohydrides have been proposed as interesting systems with high hydrogen capacities (18.54 wt%H for $LiBH_4$, and 10.68 wt%H $NaBH_4$) for hydrogen storage, and much research has focussed on their synthesis, structure and hydrogen sorption characteristics.[183, 184, 185, 186] Magnesium borohydride ($Mg(BH_4)_2$) is a particularly promising hydrogen store, with a capacity of 14.96 wt%, and may be synthesised directly through solution chemistry or indirectly through mechanochemical metathesis reactions, where the latter involves isolation of the borohydride from a by-product.[187, 188, 189, 190, 191] Zhang and co-workers, however, synthesised the borohydride directly from Mg and B powders using a reactive milling process using an H_2 environment as an alternative synthesis route.[192] The structure of this borohydride has been studied and shown to exist in a hexagonal structure at ambient conditions and undergoes phase changes upon variation of temperature and pressure, while variation of the synthesis conditions has also indicated porous configurations.[193, 194, 195, 196, 197] Decomposition characteristics of $Mg(BH_4)_2$ have been determined using a variety of

experimental and theoretical techniques to determine the thermodynamic, kinetics and reversibility kinetics, whilst identifying potential by-products and intermediates.[198, 199, 200, 201, 202] Various additives have also been used to improve the properties of $Mg(BH_4)_2$, with a focus on halide additives.[203, 204] Nanoconfinement of $Mg(BH_4)_2$ in a carbon scaffold was investigated in 2010, where the integrity of the nanoparticles of the borohydride was maintained upon dehydrogenation, which meets one of the major challenges of using nanoscale materials.[205] Beyond $Mg(BH_4)_2$ in isolation, borohydride combinations and mixed borohydride-hydride systems have been studied to establish synergistic effects.[206, 207, 208] Relevant literature has been cited in this brief overview, and discussion on borohydride systems will not be covered further in this work.

1.2.1.5. Intermetallic Mg Alloy Hydrides

Hydrogen storage alloys comprising two or more metallic components allow tailoring of the hydride properties by variation of the metal combinations and proportions.[209] Aside from hydrogen storage, Mg alloys are also aiding the advancement of battery technology, where developments in highly conducting electrode materials are vital for optimising battery performance.[210, 211, 212, 213, 214, 215, 216] A wealth of promising Mg alloys have been discovered over the past few decades as the field of hydrogen storage has gained momentum.[217, 218, 219] Most efforts have concentrated on transition metal alloys although *s*- and *p*-block alloys are also known.[220, 221] Mg alloys with Ti[222], V[223], Fe[224, 225, 226, 227], Co[228] and Ni[229, 230, 231, 232, 233] have been heavily studied. Alloys have also shown improved hydrogen storage properties when prepared by milling, indicating that particle size effects are also important in this class of hydrogen storage materials.[234, 235] Mechanochemistry has enabled the synthesis of a number of new intermetallic hydrides and exploitation of this method towards lightweight ternary hydrides will be explored further through this research in Chapter 4 and Chapter 5.[236, 237, 238]

1.2.1.6. Metal Hydride Composites

Hydride composites are emerging constantly. These comprise combinations of hydrogen storage materials and reagents/catalysts which exhibit superior properties compared to those of the respective components in isolation. This approach has been building momentum in hydrogen energy research due to the thermodynamic, kinetic and cyclability limitations of metal hydrides alone.

Complex hydride composites have been studied fervently in order to optimise hydrogen yields, and include alanate-hydride, borohydride-hydride, alanate-alanate[178] and alanate-borohydride[239] systems.

1.2.1.7. Hydrolytic Hydrogen Release Systems

Hydrolysis reactions involving hydrides are alternative hydrogen storage-release systems that involve the use of water to release the hydrogen held within the metal matrix.[240] These may be described as single-use systems, since reversibility is not possible without reformation of the hydride from the hydroxide hydrolysis product, which is thermodynamically challenging. As a result, the significant limitation of this approach for mobile vehicular applications is that the materials must be regenerated "off-board", *i.e.*, outside of the vehicle.

Magnesium hydride may be used in this way *via* the following mechanism and is particularly promising since it has a theoretical hydrogen capacity of 15.2 wt% H_2 (Equation 1-2).

Equation 1-2 $$MgH_2 + H_2O \rightarrow Mg(OH)_2 + H_2 \qquad \Delta H_{298\,K} = -\,277\ \text{kJ/mol}$$

Many of the systems are based on combinations of light metal hydrides and hydroxides, *i.e.*, alkali metal hydroxide-alkaline earth metal hydride, or light metal hydride/complex metal hydride-hydroxide composites. Hydrolysis reactions involving MgH_2-Ca/CaH_2 mixtures were studied in 2004, by Tessier *et al.*, which showed hydrolysis to be up to 80% complete after only 30 minutes.[241] Ultrasonic irradiation has been used with magnesium hydroxide to determine the enhancing effects it may have on the release of hydrogen from the hydrolysis reaction.[242] Hiroi *et al.* used nanowires as well as microstructured Mg in this investigation and found enhanced hydrogen release from the former at an ultrasonic frequency of 28 kHz. More recent work to develop this system uses acids to overcome the formation of the $Mg(OH)_2$ phase on the surface of the hydride, which hinders its complete hydrolysis.[243, 244] Recently, use of catalytic quantities of hydroxides with MgH_2 have indicated improved performance of the hydride, where the kinetics of NaOH and KOH doped composites were significantly altered by the formation of ternary Perovskite hydrides, $NaMgH_3$ and $KMgH_3$ respectively.[245] Mg-derived systems dominate this emerging energy storage domain.[246, 247, 248, 249, 250, 251]

1.2.1.8. Nitrogen-Hydrogen Systems

Interest in metal-N-H systems has been gaining momentum in the past decade, owing to the synthesis and stabilisation of light-weight, high capacity storage materials (including amides, imides and nitrides) and a developing knowledge of their decomposition pathways.[252, 253, 254] Hu and Ruckestein studied interactions of LiH with ammonia in 2002, although ammoniation of light metal halides has been known since the early 20th century.[255, 256] Ammoniation of MgH_2 has been studied by Li and Hurley, who used both purge and vacuum procedures between 75-150 °C, with and without halide-based dopants for promotion of hydrogen release.[257] Hydrogen release was expected to be *via* the following reaction:

Equation 1-3

$$2\ NH_3 + 3\ MgH_2 \leftrightarrow Mg_3N_2 + 6\ H_2 \qquad \Delta H = -\ 33.52\ \text{kcal}$$

Their results indicated that ammoniation of the hydride was possible and hydrogen release from the doped systems was possible at near ambient conditions, although a wt% H_2 penalty would have been paid for inclusion of the dopants and only partial dehydrogenation was possible. At room temperature, ammoniation of various alkali metal hydrides has been conducted, and shown to form the corresponding metal amides after 24 hours of ammonia exposure (0.5 MPa).[258] They showed significantly low hydrogen release temperatures for these systems upon decomposition of the amide, as expected from their decomposition temperatures. They demonstrated the reversibility of the reactions by exposing the resultant amide to hydrogen at elevated temperatures, achieving partial conversion in the $NaNH_2$ and KNH_2 systems at as low as 50 °C, and full conversion back to ammonia and the metal hydride using KNH_2 at 300 °C. The same research group also published developed work on these amide hydrogen release systems.[259] Decomposition and synthesis of amides by ball milling methods has also been developed, and knowledge of their individual characteristics will be key to understanding developed decomposition pathways of mixtures of amides and hydrides.[260] These materials form an entirely new category of hydrogen storage materials since they may also involve ammonia sorption, which will not be discussed further in this work and the reader is directed to relevant literature.[261] However, it is worth noting that they commonly employ metal hydrides in composite systems for hydrogen release, which is of interest to the developments made in this work. Amide-hydride mixtures have been studied which form either new ternary amide phases or intermediates with associated low temperature hydrogen release.[259, 262, 263]

1.3. Conclusion

The various materials classifications employed for hydrogen storage have been summarized in the above literature review. Due to the wealth of literature available on the subject of hydrogen storage materials, however, this is not an exhaustive review and the reader is directed to the literature reviews cited in this work.

It should be clear that metal hydrides are the primary subject of this work, with a focus on Mg based materials. Although hydrogen release from the borohydride, hydrolytic and N-H type systems will not be covered further in this work, development of new lightweight hydrides for promising new composite systems involving such materials is of significant importance in energy materials research with the potential for new low temperature hydrogen desorption systems.

The main aims of this research are:

1. to investigate the hydrogen release properties of MgH_2 and enhance them by optimization of mechanochemical nanostructuring and inclusion of appropriate catalysts and/or additives, and
2. determine new routes to promising Mg-based hydride materials at the nanoscale and determine their structure and thermal properties.

---

[1] "*International Energy Outlook 2013*", July 2013, U.S. International Energy Agency
[2] "*World Population to 2300*", 2012 rev., United Nations
[3] "*Hydrogen Energy and Fuel Cells*", EUR 20719 EN, European Commission
[4] M. S. Dresselhaus and I. L. Thomas, *Nature*, 2001, **414**, 332
[5] B. D. Shakya, L. Aye and P. Musgrave, *International Journal of Hydrogen Energy*, 2005, **30**, 9
[6] W. Li, G. Joos and J. Belanger, *IEEE Transactions on Industrial Electronics*, 2010, **57**, 1137
[7] A. Ozbilen, I. Dincer and M. A. Rosen, *Environmental Impact Assessment Review*, 2013, **42**, 1
[8] R. M. Dell and D. A. J. Rand, *Journal of Power Sources*, 2001, **100**, 2
[9] A. Züttel, *Naturwissenschaften*, 2004, **91**, 157
[10] W. Lubitz and B. Tumas, *Chemical Reviews Editorial*, 2007, **107**, 3900
[11] A. Züttel, A. Remhof, A. Borgschulte and O. Friedrichs, *Philosphical Transactions of the Royal Society A*, 2010, **368**, 3329
[12] http://www.hydrogen.energy.gov/; accessed 08/05/201
[13] D. Das and T. N. Veziroğlu, *International Journey of Hydrogen Energy*, 2001, **26**, 13
[14] O. Elsharnouby, H. Hafez, G. Nakhla and M. H. El Naggar, *International Journal of Hydrogen Energy*, 2013, **38**, 4945
[15] M. Y. Azwar, M. A. Hussain, A. K. Abdul-Wahab, *Renewable and Sustainable Energy Review*, 2014, **31**, 158
[16] N. H. M. Yasin, T. Mumtaz, M. A. Hassan and N. A. Rahman, *Journal of Environmental Management*, 2013, **130**, 375
[17] R. T. Jacobsen, J. W. Leachman, S. G. Penoncello and E. W. Lemmon, *International Journal of Thermophysics*, 2007, **28**, 758
[18] T. K. Mandal and D. H. Gregory, *Annual Reports on the Progress of Chemistry: Section A*, 2009, **105**, 21
[19] U. Eberle, M. Felderhoff and F. Schüth, *Angewandte Chemie*, 2009, **48**, 6608
[20] K. L. Lim, H. Kazemian, Z. Yaakob and W. R. W. Daud, *Chemical Engineering and Technology*, 2010, **33**, 213

[21] http://www.hyundai.co.uk/about-us/environment/hydrogen-fuel-cell; accessed 08/05/2014
[22] http://www.toyota.com/fuelcell/; accessed 08/05/2014
[23] L. Schlapbach and A. Züttel, *Nature*, 2001, **414**, 353
[24] S. Satyapal, J. Petrovic, C. Read, G. Thomas and G. Ordaz, *Catalysis Today*, 2007, **120**, 246
[25] A. Chaise, P. de Rango, Ph. Marty and D. Fruchart, *International Journal of Hydrogen Energy*, 2010, **35**, 6311
[26] S. Garrier, A. Chaise, P. de Rango, P. Marty, B. Denholmme, D. Fruchart and S. Miraglia, *International Journal of Hydrogen Energy*, 2011, **36**, 9719
[27] J. M. Bellosta von Colbe, O. Metz, G. A. Lozano, P. K. Pranzas, H. W. Schmidt, F. Beckmann, A. Schreyer, T. Klassen and M. Dornheim, *International Journal of Hydrogen Energy*, 2011, **37**, 2807
[28] G. A. Lozano, C. N. Ranong, J. M. Bellosta von Colbe,R. Bormann, J. Hapke, G. Fieg, T. Klassen and M. Dornheim, *International Journal of Hydrogen Energy*, 2012, **37**, 2825
[29] T. A. Johnson, M. P. Kanouff, D. E. Dedrick, G. H. Evans and S. W. Jorgensen, *International Journal of Hydrogen Energy*, 2012, **37**, 2835
[30] C. Corgnale, B. J. Hardy, D. A. Tamburello, S. L. Garrison and D. L. Anton *International Journal of Hydrogen Energy*, 2012, **37**, 2812
[31] Z. X. Guo, C. Shang and K. F. Aguey-Zinsou, *Journal of the European Ceramic Society*, 2008, **28**, 1467
[32] J. M. Pasini, C. Corgnale, B. A. van Hassel, T. Motyka, S. Kumar and K. L. Simmons, *International Journal of Hydrogen Energy*, 2013, **38**, 9755
[33] M. Winter and R. J.*International Journal of Hydrogen Energy* Brodd, *Chemical Reviews*, 2004, **104**, 4245
[34] P. Colomban, *Fuel Cells*, 2013, **13**, 6
[35] P. Pei and H. Chen, *Applied Energy*, 2014, **125**, 60
[36] S. Mellouli, F. Askri, H. Dhaou, A. Jemni and S. B. Nasrallah, *International Journal of Hydrogen Energy*, 2010, **35**, 1693
[37] A. D'Orazio, A. Dell'Era, P. Artuso and M. Pasquali, *International Journal of Hydrogen Energy*, 2011, **36**, 7902
[38] J. M. Bellosta von Colbe, O. Metz, G. A. Lozano, P. K. Pranzas, H. Schmidt, F. Beckman, A. Schreyer, T. Klassen and M. Dornheim, *International Journal of Hydrogen Energy*, 2012, **37**, 2807
[39] C. Corgnale, T. Motyka, S. Greenway, J. M. Perez-Berrios, A. Nakano, H. Ito and T. Maeda, *Journal of Alloys and Compounds*, 2013, **380**, S406
[40] J. Andrews and S. S. Mohammadi, *International Journal of Hydrogen Energy*, 2014, **39**, 1740
[41]World Wide Fund for Nature;
http://www.wwf.org.uk/what_we_do/tackling_climate_change/impacts_of_climate_change/; accessed 09/10/2014
[42] S. W. Jorgensen, *Current Opinion in Solid State and Materials Science*, 2011, **15**, 39
[43] A. Nakano, H. Ito, T. Maeda, T. Munakata, T. Motyka, C. Corgnale, S. Greenway and J. M. Perez-Berrios, *Journal of Alloys and Compounds*, 2013, **580**, S418
[44] R. Dawson, A. I. Cooper and D. J. Adams, *Progress in Polymer Science*, 2012, **37**, 530
[45] D. Lozano-Castelló, F. Suárez-García, Á. Linares-Solano, D. Cazorla-Amorós, *Renewable Hydrogen Technologies*, Chapter 12, 2013, *pp*. 269-291
[46] L. Wang, R. T. Yang, J. Yang, *New and Future Developments in Catalysis*, Chapter 6, 2013, pp. 137-164
[47] H. P. Veluswamy, R. Kumar and P. Linga, *Applied Energy*, 2014, **122**, 112
[48] L. M. Kustov, A. L., Tarasov, J. Sung and D. Y. Godovsky, *Mendeleev Communications*, 2014, **24**, 1
[49] G. G. Libowitz, *Journal of Physics and Chemistry of Solids*, 1994, **55**, 1461
[50] B. Sakintuna, F. Lamari-Darkrim and M. Hirscher, *International Journal of Hydrogen Energy*, 2007, **32**, 1121
[51] L. George and S. K. Saxena, *International Journal of Hydrogen Energy*, 2010, **35**, 5454
[52] K. C. Kim, B. Dai, J. K. Johnson and D. S. Scholl, *Nanotechnology*, 2009, **20**, 204001
[53] A. Züttel, *Materials Today*, 2003, **6**, 24
[54] *National Institute of Standards and Technology*; http://webbook.nist.gov/; accessed 07/05/2014
[55] B. Peng, J. Liang, Z. Tao and J. Chen, *Journal of Materials Chemistry*, 2009, **19**, 2877
[56] K. F. Aguey-Zinsou, J.-R. Ares-Fernández, *Energy and Environmental Science*, 2010, **3**, 526
[57] F. Cheng, Z. Tao, J. Liang and J. Chen, *Chemical Communications*, 2012, **48**, 7334
[58] H. Reardon, J. M. Hanlon, R. W. Hughes, A. Godula-Jopek, T. K. Mandal and D. H. Gregory, *Energy and Environmental Science*, 2012, **5**, 5951
[59] J. J. Vajo, *Current Opinion in Solid State Chemistry*, 2011, **15**, 52
[60] B. Vigeholm, J. Kjøller and B. Larsen, *Journal of the Less-Common Metals*, 1980, **74**, 341
[61] B. Vigeholm, J. Kjøller, B. Larsen and A. Schroder Pedersen, *International Journal of Hydrogen Energy*, 1983, **8**, 809
[62] B. Vigeholm, J. Kjøller, B. Larsen and A. Schroder Pedersen, *Journal of the Less-Common Metals*, 1983, **89**, 135
[63] P.J. Herley, W. Jones and B. Vigeholm, *Journal of Applied Physics*, 1985, **58**, 292

[64] S. Cheung, W.-Q. Deng, A.C.T. van Duin and W.A. Goddard III, *Journal of Physical Chemistry A*, 2005, **109**, 851
[65] J. J. Liang, *Applied Physics A*, 2005, **80**, 173
[66] K.-F. Aguey-Zinsou and J.-R. Ares-Fernandez, *Energy and Environmental Science*, 2010, **3**, 526
[67] F. Cheng, Z. Tao, J. Liang and J. Chen, *Chemical Communications*, 2012, **48**, 7334
[68] G. Wu, J. Zhang, Q. Li, Y. Wu, K. Chou and X. Bao, *Computational Materials Science*, 2010, **49**, S144
[69] N. Hanada, T. Ichikawa, S.-I. Orimo and H. Fujii, *Journal of Alloys and Compounds*, 2004, **366**, 269
[70] N. Hanada, T. Ichikawa, S. Hino and H. Fujii, *Journal of Alloys and Compounds*, 2006, **420**, 46
[71] J.R. Ares, K.-F. Aguey-Zinsou, T. Klassen and R. Bormann, *Journal of Alloys and Compounds*, 2007, 434-**435**, 729
[72] J. Huot, D. B. Ravnsbæk, J. Zhang, F. Cuevas, M. Latroche and T. R. Jensen, *Progress in Material Science*, 2013, **58**, 30
[73] C. Suryanarayana and N. Al-Aqeeli, *Progress in Materials Science*, 2013, **58**, 383
[74] V. Fahimpour and S. K. Sadrnezhaad, *Materials Letters*, 2012, **85**, 128
[75] G. Liang, J. Huot, S. Boily, A. Van Neste and R. Schulz, *Journal of Alloys and Compounds*, 1999, **292**, 247
[76] J.-L. Bobet, C. Even, Y. Nakamura, E. Akiba and B. Darriet, *Journal of Alloys and Compounds*, 2000, **298**, 279
[77] C. X. Shang, M. Bououdina, Y. Song and Z. X. Guo, *International Journal of Hydrogen Energy*, 2004, **29**, 73
[78] N. Hanada, T. Ichikawa and H. Fukii, *Journal of Physical Chemistry B*, 2005, **109**, 7188
[79] M. Tsuda, W. A. Dino, H. Kasai, H. Nakanishi and H. Aikawa, *Thin Solid Films*, 2006, **509**, 157
[80] A. Denis, E. Sellier, C. Aymonier and J.-L. Bobet, *Journal of Alloys and Compounds*, 2009, **476**, 152
[81] N. Bazzanella, R. Checchetto and A. Miotello, *Journal of Nanomaterials*, 2011, **2011**, 865969
[82] H. Gasan, O. N. Celik, N. Aydinbeyli and Y. M. Yaman, *International Journal of Hydrogen Energy*, 2012, **37**, 1912
[83] S. D. Vincent, J. Lang and J. Huot, *Journal of Alloys and Compounds*, 2012, **512**, 290
[84] Y. Song, Z. X. Guo and R. Yang, *Materials Science and Engineering A*, 2004, **365**, 73
[85] A. J. Du, S. C. Smith, X. D. Yao and G. Q. Lu, *Journal of Physical Chemistry B*, 2005, **109**, 18037
[86] L.-P. Ma, P. Wang and H.-M. Cheng, *International Journal of Hydrogen Energy*, 2010, **35**, 3046
[87] M. P. Pitt, M. Paskevicius, C. J. Webb, D. A. Sheppard, C. E. Buckley and E. MacA. Gray, *International Journal of Hydrogen Energy*, 2012, **37**, 4227
[88] G. Liang, J. Huot, S. Boily, A. Van Neste, R. Schulz, *Journal of Alloys and Compounds*, 1999, **291**, 295
[89] G. Liang, J. Huot, S. Boily and R. Shulz, *Journal of Alloys and Compounds*, 2000, **305**, 239
[90] W. Oelrich, T. Klassen and R. Bormann, *Journal of Alloys and Compounds*, 2001, **322**, L5
[91] Z. Dehouche, J. Goyette, T. K. Bose, J. Huot and R. Shulz, *Nano Letters*, 2001, **1**, 175
[92] L. E. A. Berlouis, R. Perez Aguado, P. J. Hall, S. Morris, L. Chandrasekaran, S. B. Dodd, *Journal of Alloys and Compounds*, 2003, **356-357**, 584
[93] B. Bogdanovic, H. Hofman, A. Neuy, A. Reiser, K. Schlichte, B. Spliethoff and S. Wessel, *Journal of Alloys and Compounds*, 1999, **292**,57
[94] R. A. Varin, T. Czujko, E. B. Wasmund and Z. S. Wronski, *Journal of Alloys and Compounds*, 2007, **432**, 217
[95] L. Xie, Y. Liu, X. Zhang, j. Qu, Y. Wang and X. Li, *Journal of Alloys and Compounds*, 2009, **482**, 388
[96] Z. S. Wronski, G. J. C. Carpenter, T. Czujko and R. A. Varin, *International Journal of Hydrogen Energy*, 2011, **36**, 1159
[97] W. N. Yang, C. X. Shang and Z. X. Guo, *International Journal of Hydrogen Energy*, 2010, **35**, 4534
[98] J. F. Pelletier, J. Huot, R. Schulz, A. R. Sandy, L. B. Lurio and S. G. Mochrie, *Physical Review B*, 2001, **63**, 052103
[99] J. Huot, J. F. Pelletier, G. Liang, M. Sutton and R. Schulz, *Journal of Alloys and Compounds*, 2002, **330-332**, 727
[100] C. R. Luna, C. E. Macchi, A. Juan and A. Somoza, *International Journal of Hydrogen Energy*, 2010, **35**, 12421
[101] A. Zaluska, L. Zaluska and J. O. Strom-Olsen, *Journal of Alloys and Compounds*, 1999, **288**, 217
[102] J. Liu, X. P. Song, P. Pei and G.L. Chen, *Journal of Alloys and Compounds*, 2009, **486**, 338
[103] M. Y. Song, S. H. Baek, J.-L. Bobet and S.-H. Hong, *International Journal of Hydrogen Energy*, 2010, **35**, 10366
[104] R. R. Shahi, A. P. Tiwari, M. A. Shaz and O. N. Srivastava, *International Journal of Hydrogen Energy*, 2013, **38**, 2778
[105] H. Reule, M. Hirscher, A. Weiβhardt and H. Kronmuller, *Journal of Alloys and Compounds*, 2000, **305**, 246
[106] B. Molinas, A. A. Ghilarducci, M. Melnichuk, H. L. Corso, H. A. Peretti, F. Agresti, A. Bianchin, S. Lo Russo, A. Maddalena and G. Principi, *International Journal of Hydrogen Energy*, 2009, **34**, 4597.

[107] J.-H. Kim, J.-H. Kim, K.-T. Hwang and Y.-M. Kang, *International Journal of Hydrogen Energy*, 2010, **35**, 9641
[108] S. T. Sabitu, G. Gallo and A. J. Goudy, *Journal of Alloys and Compounds*, 2010, **499**, 35
[109] B. Zahiri, B. S. Amirkhiz and S. Mitlin, *Applied Physics Letters*, 2010, **97**, 083106
[110] J. Cermak and B. David, *International Journal of Hydrogen Energy*, 2011, **36**, 13614
[111] B. Zahiri, M. Danaie, X. H. Tan, B. S. Amirkhiz, G. A. Botton and D. Mitlin, *Journal of Physical Chemistry C*, 2012, **116**, 3188
[112] M. Pourabdoli, S. Raygan, H. Abdizadeh and D. Uner, *International Journal of Hydrogen Energy*, 2013, **38**, 11910
[113] R. Vijay, R. Sundaresan, M. P. Maiya and S. Srinivasa Murthy, *International Journal of Hydrogen Energy*, 2007, **32**, 2390
[114] N. Hanada, T. Ichikawa and H. Fujii, *Journal of Physical Chemistry B*, 2005, **109**, 7188
[115] N. Hanada, E. Hirotoshi, T. Ichikawa, E. Akiba and H. Fujii, *Journal of Alloys and Compounds*, 2008, **450**, 395
[116] O. Friedrichs, J. C. Sanchez-Lopez, C. Lopez-Cartes, T. Klassen, R. Bormann and A. Fernandez, *Journal of Physical Chemistry B*, 2006, **110**, 7845
[117] G. Barkhordarian, T. Klassen and R. Bormann, *Scripta Materialia*, 2003, **49**, 213
[118] N. Hanada, E. Hirotoshi, T. Ichikawa, E. Akiba and H. Fujii, *Journal of Alloys and Compounds*, 2008, **450**, 395
[119] M. O. T. da Conceicao, M. C. Brum, D. S. dos Santos and M. L. Dias, *Journal of Alloys and Compounds*, 2013, **550**, 179
[120] K. Takahashi, S. Isobe, S. Ohnuki, *Journal of Alloys and Compounds*, 2013, **580**, S25
[121] N. Hanada, T. Ichikawa, S. Hino and H. Fujii, *Journal of Alloys and Compounds*, 2006, **420**, 46
[122] H. Hirate, H. Sawai, H. Yukawa and M. Morinaga, *International Journal of Quantum Chemistry*, 2010, **111**, 2251.
[123] O. Friedrichs, T. Klassen, J. C. Sanchez-Lopez, R. Bormann and A. Fernandez, *Scripta Materialia*, 2006, **54**, 1293
[124] D. Zander, L. Lyubenova, U. Koster, T. Klassen and M. Dornheim, *Journal of Alloys and Compounds*, 2007, **434-435**, 753
[125] M. Porcu, A. K. Petford-Long and J. M. Sykes, *Journal of Alloys and Compounds*, 2008, **453**, 341
[126] T. Ma, S. Isobe, E. Morita, Y. Wang, N. Hashimoto, S. Ohnuki, T. Kimura, T. Ichikawa and Y. Kojima, *International Journal of Hydrogen Energy*, 2011, **36**, 12319
[127] T. K. Nielsen and T. R. Jensen, *International Journal of Hydrogen Energy*, 2012, **37**, 13409
[128] O. Friedrichs, F. Aguey-Zinsou, J. R. Ares Fernandez, J. C. Sanchez-Lopez, A. Justo, T. Klassen, R. Bormann, A. Fernandez, *Acta Materialia*, 2006, **54**, 105
[129] K.-F. Aguey-Zinsou, J. R. Ares Fernandez, T. Klassen and R. Bormann, *International Journal of Hydrogen Energy*, 2007, **32**, 2400
[130] M. O. T. da Conceicao, M. C. Brum, D. S. dos Santos and M. L. Dias, *Journal of Alloys and Compounds*, 2013, **550**, 179
[131] K. S. Jung, E. Y. Lee and K. S. Lee, *Journal of Alloys and Compounds*, 2006, **421**, 179
[132] M. Polanski and J. Bystrzycki, *Journal of Alloys and Compounds*, 2009, **486**, 697
[133] J. Bellemare and J. Huot, *Journal of Alloys and Compounds*, 2012, **512**, 33
[134] W. Oelerich, T. Klassen and R. Bormann, *Advanced Engineering Materials*, 2001, **7**, 487
[135] W. Oelerich, T. Klassen and R. Bormann, *Journal of Alloys and Compounds*, 2001, **315**, 237
[136] A. D. Bulanov, O. Y. Troshin and V. V. Balabanov, *Russian Journal of Applied Chemistry*, 2004, **77**, 875
[137] C. Ney, H. Kohlmann and G. Kickelbick, *International Journal of Hydrogen Energy*, 2011, **36**, 9086
[138] D. K. Dixit, K. Gandhi and B. K. Dixit, *International Journal of Hydrogen Energy*, 2012, **37**, 3767
[139] H. Chu, Z. Xiong, G. Wu, T. He, C. Wu and P. Chen, *International Journal of Hydrogen Energy*, 2010, **35**, 8317
[140] F. E. Pinkerton and M. S. Meyer, *Journal of Alloys and Compounds*, 2008, **464**, L1
[141] Y. Zhang, K. Shimoda, H. Miyaoka, T. Ichikawa and Y. Kojima, *International Journal of Hydrogen Energy*, 2010, **35**, 12405
[142] S. Orimo, Y. Nakamori, J. R. Eliseo, A. Züttel and C. M. Jensen, *Chemical Reviews*, 2007, **107**, 4111
[143] J. Jepsen, J. M. Bellosta con Colbe, T. Klassen and M. Dornheim, *International Journal of Hydrogen Energy*, 2012, **37**, 4202
[144] D. S. Easton, J. H. Schneibel and S. S. Speakman, *Journal of Alloys and Compounds*, 2005, **398**, 245
[145] C. M. Andrei, J. Walsmsley, D. Blanchard, H. W. Brinks, R. Holmestad and B. C. Hauback, *Journal of Alloys and Compounds*, 2005, **395**, 307
[146] Z. Xueping, L. Ping and Q. Xuanhui, *Rare Metal Materials and Engineering*, 2009, **38**, 766
[147] S. McWhorter, C. Read, G. Ordaz and N. Stetson, *Current Opinion in Solid Sate and Materials Science*, 2011, **15**, 29

[148] Y. Kim, E.-K. Lee, J.-H. Shim, Y. W. Cho and K. B. Yoon, *Journal of Alloys and Compounds*, 2006, **422**, 283
[149] N. Sklar and B. Post, *Inorganic Chemistry*, 1967, **6**, 669.
150 J.-C. Buraeu, B. Bonnetot, P. Claudy and H. Eddaoudi, *Materials Research Bulletin*, 1985, **20**, 1147
[151] Y. Kojima, Y. Kawai, T. Haga, M. Matsumoto and A. Koiwai, *Journal of Alloys and Compounds*, 2007, **441**, 189
[152] X. Liu, H. W. Langmi, S. D. Beattie, F. F. Azenwi, G. S. McGrady and C. M. Jensen, *Journal of the American Chemical Society*, 2011, **133**, 15593
[153] R. A. Varin and L. Zbroniec, *Journal of Alloys Compounds*, 2010, **504**, 89
[154] C. M. Andrei, J. Walmsley, D. Blanchard, H. W. Brinks, R. Holmestad and B. C. Hauback, *Journal of Alloys Compounds*, 2005, **395**, 307.
[155] I. P. Jain, P. Jain and A. Jain, *Journal of Alloys and Compounds*, 2010, **503**, 303
[156] J. R. Ares, K.-F. Aguey-Zinsou, M. Porcu, J. M. Sykes, M. Dornheim, T. Klassen and R. Bormann, *Materials Research Bulletin*, 2008, **43**, 1263
[157] X. Liu, S. D. Beattie, H. W. Langmi, G. S. McGrady and C. M. Jensen, *International Journal of Hydrogen Energy*, 2012, **37**, 10215
[158] R.-ud-din, L. Zhang, L. Ping and Q. Xuanhui, *Journal of Alloys Compounds*, 2010, **508**, 119
[159] L. Li, F. Qiu, Y. Wang, Y. Xu, C. An, G. Liu, L. Jiao and H. Yuan, *International Journal of Hydrogen Energy*, 2013, **38**, 3695
[160] M. Ismail, Y. Zhao, X. B. Yu, I. P. Nevirkovets and S. X. Dou, *International Journal of Hydrogen Energy*, 2011, **36**, 8327
[161] J. W. Lauher, D. Dougherty and P. J. Herley, *Acta Crystallographica B*, 1979, **35**, 1454
[162] A. Zaluska, L. Zaluski and J. O. Strom-Olsen, *Journal of Alloys and Compounds*, 2000, **298**, 125
[163] J. W. Lauher, *Acta Crystallographica B-Structural Science*, 1979, **B35**, 1454
[164] H. Yukawa, N. Morisaku, Y. Li, K. Koyima, R. Rong, Y. Shinzato, R. Sekine and M. Morinaga, *Journal of Alloys and Compounds*, 2007, **446-447**, 242
[165] B. Bogdanovic and M. Schwickardi, *Journal of Alloys and Compounds*, 1997, **253-254**, 1
[166] C. Rongeat, I. L. Jansa, S. Oswald, L. Schultz and O. Gutfleisch, *Acta Materialia*, 2009, **57**, 5563
[167] X. Xiao, K. Yu, X. Fan, Z. Wu, X. Wang, C. Chen, Q. Wang and L. Chen, *International Journal of Hydrogen Energy*, 2011, **36**, 539
[168] C. M. Jensen, K. J. Gross, *Applied Physics A-Materials Science and Processing*, 2001, **72**, 213
[169] M. Fichtner, P. Canton, O. Kircher, A. Leon, *Journal of Alloys and Compounds*, 2005, **404-406**,732
[170] J. Graetz, J. J. Reilly, J. Johnson, A. Y. Ignatov and T. A. Tyson, *Applied Physics Letters*, 2004, **85(3)**, 500
[171] J. M. Bellosta von Colbe, B. Bogdanovic, M. Felderhoff, A. Pommerin and F. Schüth, *Journal of Alloys and Compounds*, 2004, **370**, 104
[172] C. P. Balde, B. P. C. Hereijgers, J. H. Bitter and K. P. de Jong, *Journal of the American Chemical Society*, 2008, **130**, 6761
[173] D. Pukazhselvan, M. S. L. Hudson, A. S. K. Sinha and O. N. Srivastava, *Energy*, 2010, **35**, 5037
[174] A. Fossdal, H. W. Brinks, M. Fichtner and B. C. Hauback, *Journal of Alloys and Compounds*, 2005, **387**, 47
[175] A. Fossdal, H. W. Brinks, M. Fichtner and B. C. Hauback, *Journal of Alloys and Compounds*, 2005, **404-406**, 752
[176] M. Mamatha, B. Bogdanović, M. Felderhoff, A. Pommerin, W. Schmidt, F. Schüth and C. Weidenthaler, *Journal of Alloys and Compounds*, 2006, **407**, 78
[177] R. A. Varin, C. Chiu, T. Czujko and Z. Wronski, *Journal of Alloys and Compounds*, 2007, **439**, 302
[178] M. S. L. Hudson, D. Pukazhselvan, G. Irene Sheeja and O. N. Srivistava, *International Journal of Hydrogen Energy*, 2007, **32**, 4933
[179] M. Fichtner, J. Engel, O. Fuhr,A. Glöss, O. Rubner and R. Alrichs, *Inorganic Chemistry*, 2003, *42*, 7060
[180] M. Fichtner, J. Engel, O. Fuhr, O. Kircher and O. Rubner, *Materials Science and Engineering B-Solid State Materials for Advanced Technology*, 2004, **108**, 42
[181] R. A. Varin, C. Chiu, T. Czujko an d Z. Wronski, *Nanotechnology*, 2005, **16**, 2261
182 M. S. L. Hudson, H. Raghubanshi, D. Pukazhselvan and O. N. Srivastava, *International Journal of Hydrogen Energy*, 2010, **35**, 2083
[183] T. Umegaki, J.-M. Yan, X.-B. Zhang, H. Shioyama, N. Kuriyama and Q. Xu, *International Journal of Hydrogen Energy*, 2009, **34**, 2303
[184] H. Hagemann and R. Černý, *Dalton Transactions*, 2010, **39**, 6006
[185] E. Rönnebro, *Current Opinion in Solid Stae and Materials Science*, 2011, **15**, 44
[186] L. H. Rude, T. K. Nielsen, D. B. Ravnsbæk, U. Bösenberg, M. B. Ley, B. Richter, L. M. Arbnjerg, M. Dornheim, Y. Filinchuk, F. Besenbacher and T. R. Jensen, *Physica Status Solidi A-Applied Research*, 2011, **208(8)**, 1754
[187] K. Chłopek, C. Frommen, A. Léon, O. Zabara and M. Fichtner, *Journal of Materials Chemistry*, 2007, **17**, 3496

[188] P. Zanella, L. Crociani, N. Masciocchi and G. Giunchi, *Inorganic Chemistry*, 2007, **46**, 9039
[189] T. Matsunaga, F. Buchter, K. Miwa, S. Towata, S. Orimo and A. Züttel, *Renewable Energy*, 2008, **33**, 193
[190] R. A. Varin, Ch. Chiu and Z. S. Wronski, *Journal of Alloys and Compounds*, 2008, **462**, 201
[191] G. L. Soloveichik, M. Andrus, Y. Gao, J.C. Zhao and S. Kniajanski, *International Journal of Hydrogen Energy*, 2009, **34**, 2144
[192] Z. G. Zhang, S. F. Zhang, H., Wang, J. W. Liu and M. Zhu, *Journal of Alloys and Compounds*, 2010, **505**, 717
[193] P. Vajeeston, P. Ravindran, A. Kjekshus and H. Fjellvåg, *Applied Physics Letters*, 2006, **89**, 071906
[194] V. Ozolins, E. H. Majzoub and C. Wolverton, *Physical Review Letters*, 2008, **100**, 135501
[195] L. George, V. Drozd, S. K. Saxena, E. G. Bardaji and M. Fichtner, *Journal of Physical Chemistry C*, 2009, **113**, 486
[196] A. Giannasi, D. Colognesi, L. Ulivi, M. Zoppi, A. J. Ramirez-Cuesta, E. G. Barjadi, E. Roehm and M. Fichtner, *Journal of Physical Chemistry A*, 2010, **114**, 2788
[197] Y. Filinchuk, B. Richter, T. R. Jensen, V. Dmitriev, D. Chernyshov and H. Hagemann, *Angewandte Chemie International Edition*, 2011, **50**, 11162
[198] Y. Nakamori, K. Miwa, A. Ninomiya, H. Li, N. Ohba, S. Towata, A. Züttel and S. Orimo, *Physical Review B-Condensed Matter*, 2006, **74**, 045126
[199] M. J. van Setten, W. Lohstroh and M. Fichtner, *Journal of Materials Chemistry*, 2009, **19**, 7081
[200] G. L. Soloveichik, Y. Gao, J. Rijssenbeek, M. Andrus, S. Kniajanski, R. C. Bowman Jr., S.-J. Hwang and J.-C. Zhao, *International Journal of Hydrogen Energy*, 2009, **34**, 916
[201] M. Chong, A. Karkamkar, T. Autrey, S. Orimo, S. Jalisatgi and C. M. Jensen, Chem. Commun., **47** (2011) 1330
[202] D. T. Shane, L. H. Rayhel, Z. Huang, J.-C. Zhao, X. Tang, V. Stavila and M. S. Conradi, J. Phys. Chem. C, **115** (2011) 3172
[203] R. J. Newhouse, V. Stavila, S.-J. Hwang, L. E. Klabanoff and J. Z. Zhang, *Journal of Physical Chemistry C*, **114** (2010) 5224
[204] E. G. Bardaji, N. Hanada, O. Zabara and M. Fichtner, *International Journal of Hydrogen Energy*, 2011, **36**, 12313
[205] S. Sartori, K. D. Knudsen, Z. Zhao-Karger, E. G. Bardaji, J. Muller, M. Fichtner and B. C. Hauback, *Journal of Physical Chemistry C*, 2010, **114**, 18785
[206] T. Durojaiye, A. Ibikunle and A. J. Goudy, *International Journal of Hydrogen Energy*, 2010, **35**, 10329
[207] Z.z. Fang, X.-D. Kang, P. Wang, H.-W. Li and S. Orimom *Journal of Alloys and Compounds*, 2010, **491**, L1
[208] E. G. Bardaji, Z. Zhao-Karger, N. Boucharat, A. Nale, M. J. van Setten, W. Lohstroh, E. Röhm, M. Catti and M. Fichtner, *Journal of Physical Chemistry C*, 2011, **115**, 6095
[209] G. Sandrock, *Journal of Alloys and Compounds*, 1999, **293-295**, 877
[210] C. Iwakura, Y. Fukumoto, M. Matsuoka, T. Kohno and K. Shinmou, *Journal of Alloys and Compounds*, 1993, **192**, 152
[211] N. Cui, P. He and J. L. Luo, *Electrochimica Acta*, 1999, **44**, 3549
[212] T. Kohno, M. Yamamoto and M. Kanda, *Journal of Alloys and Compounds*, 1999, **293-295**, 643
[213] L. O. Valøen, A. Zaluska, L. Zaluska, H. Tanaka, N. Kuriyama, J. O. Ström-Olsen and R. Tunold, *Journal of Alloys and Compounds*, 2000, **306**, 235
[214] H. Zhang, P. Bian and D. Ju, *Journal of Environmental Sciences Supplement*, 2009, S88
[215] M. Anik, F. Karanfil and N. Küçükdeveci, *International Journal of Hydrogen Energy*, 2012, **37**, 299
[216] C. C. Nwakwuo, T. Holm, R. V. Denys, W. Hu, J. P. Maelen, J. K. Solberg and V. A. Yartys, *Journal of Alloys and Compounds*, 2013, **555**, 201
[217] E. Rönnebro, Journal of Physics and Chemistry of Solids, 2010, **71**, 1154
[218] I. P Jain, C. Lal and A. Jain, *International Journal of Hydrogen Energy*, 2010, **35**, 5133
[219] H. Kohlmann, *Zeitschrift für Kristallographie*, 2010, **225**, 195
[220] E. Andreasen, M. B. Sørensen, R. Burkarl, B. Møller, A. M. Molenbroek, A. S. Pedersen, J. W. Andreasen, M. M. Nielsen and T. R. Jensen, *Journal of Alloys and Compounds*, 2005, **404-406**, 323
[221] G. Liang, *Journal of Alloys and Compounds*, 2004, **370**, 123
222 S. Srinivasan, P. C. M. M. Mgusin, R. A. van Santen, P. H. L. Notten, H. Schreuders and B. Dam, *Journal of Physical Chemistry C*, 2011, **115**, 288
[223] D. Kyoi, T, Sato, E. Rönnebro, Y. Tsuji, N. Kitamura, A. Ueda, M. Ito, S. Katsuyama, S. Hara, D. Noréus, T. Sakai, *Journal of Alloys and Compounds*, 2004, **375**, 253
[224] M. Herrich, N. Ismail, J. Lyubina, A. Handstein, A. Pratt and O. Gutfleisch, *Materials Science and Engineering B-Solid State Materials for Advanced Technology*, 2004, **108**, 28
[225] R. A. Varin, S. Li, A. Calka and D. Wexler, *Journal of Alloys and Compounds*, 2004, **373**, 270
[226] Z. Wronski, R. A. Varin, C. Chiu, T. Czujko and A. Calka, *Journal of Alloys and Compounds*, 2007, **434-435**, 743
[227] Y. Wang, F. Cheng, C. Li, Z. Tao and J. Chen, *Journal of Alloys and Compounds*, 2010, **508**, 554

[228] J.-L. Bobet, S. Pechev, B. Chevalier and B. Darriet, *Journal of Materials Chemistry*, 1999, **9**, 315
[229] M. Y. Song, M. Pezat, B Darriet and P. Hagenmuller, *Journal of Solid State Chemistry*, 1985, **56**, 191
[230] J. Yang, M. Ciureanu and R. Roberge, *Journal of Alloys and Compounds*, 1999, **287**, 251
[231] T. Akiyama, K. Saito and I. Saita, *Journal of the Electrochemical Society*, 2003, **150**, 3450
[232] R. Kataoka, Y. Goto, A. Kamegawa, H. Takamura and M. Okada, *Journal of Alloys and Compounds*, 2007, **446-447**, 142
[233] J. Zhang, D. W. Zhou, L. P. He, P. Peng and J. S. Liu, *Journal of Physics and Chemistry of Solids*, 2009, **70**, 32
[234] L. Zaluski, A. Zaluskam J. O. Störm-Olsen, *Journal of Alloys and Compounds*, 1995, **217**, 245
[235] S. Orimo, H. Fujii and K. Ikeda, *Acta Materialia*, 1997, **45**, 331
[236] I. G. Konstanchuk, E. Y. Ivanov, V. V. Boldyrev, *Russian Chemical Reviews*, 1998, **67**, 69
[237] M. D. S. Pirzada, S. N. Ptankar, and F. H. Froes, *Metallurgical and Materials Transactions A*, 2004, **35**, 1899
[238] C. Suryanarayana and N. Al-Aqeeli, *Progress in Materials Science*, 2013, **58**, 383
[239] R. Mohtadi, P. Sivasubramanian, S.-J. Hwang, A. Stowe, J. Gray, T. Matsunaga and R. Zidan, *International Journal of Hydrogen Energy*, 2012, **37**, 2388
[240] V. C. Y. Kong, F. R. Foulkes, D. W. Kirk and J. T. Hinatsu, *International Journal of Hydrogen Energy*, 1999, **24**, 665
[241] J. P. Tessier, P. Palau, J. Huot, R. Shulz and D. Guay, *Journal of Alloys and Compounds*, 2004, **376**, 180
[242] S. Hiroi, S. Hosokai and T. Akiyama, *International Journal of Hydrogen Energy*, 2011, **36**, 1442
[243] T. Hiraki, S. Hiroi, T. Akashi, N. Okinaka and T. Akiyama, *International Journal of Hydrogen Energy*, 2012, **37**, 12114
[244] H. Uesugi, T. Sugiyama, H. Nii and I. Nakatsugawa, *Journal of Alloys and Compounds*, 2011, **509S**, S650
[245] H. Wang, J. Zhang, J. W. Liu, L. Z. Ouyang and M. Zhu, *International Journal of Hydrogen Energy*, 2013, **38**, 10932
[246] V. C. Y. Kong, D. W. Kirk, F. R. Foulkes and J. T. Hinatsu, *International Journal of Hydrogen Energy*, 2003, **28**, 205
[247] J. Huot, G. Liang and R. Schulz, *Journal of Alloys Compounds*, 2003, **353**, L12
[248] R. A. Varin, S. Li and A. Calka, *Journal of Alloys and Compounds*, 2004, **376**, 222.
[249] S. D. Kushch, N. S. Kuyunko, R. S. Nazarov and B. P. Tarasov, *International Journal of Hydrogen Energy*, 2011, **36**, 1321
[250] L. Z. Ouyang, J. M. Huang, C. J. Fang, Q. A. Zhang, D. L. Sun and M. Zhu, *International Journal of Hydrogen Energy*, 2012, **37**, 12358
[251] S.-H. Hong, H.-J. Kim and M. Y. Song, *Journal of Industrial and Engineering Chemistry*, 2012, **18**, 405
[252] H. Yamamoto, H. Miyaoka, S. Hino, H. Nakanishi, T. Ichikawa and Y. Kojima, *International Journal of Hydrogen Energy*, 2009, **34**, 9760
[253] C. Liang, Y. Liu, H. Fu, Y. Ding, M. Gao and H. Pan, *Journal of Alloys and Compounds*, 2011, **509**, 7844
[254] "*Synthesis and Structure of Group I and II Nitrides as Potential Hydrogen Stores.*" Natalie Sorbie, PhD Thesis, University of Glasgow, 2011
[255] Y. H. Hu and E. Ruckenstein, *Journal of Physical Chemistry A*, 2003, **107(46)**, 9737
[256] S.C. Collins and F. K. Camerson, *Journal of Physical Chemistry*, 1928, **32**, 1705
[257] L. Li and J. A. Hurley, *International Journal of Hydrogen Energy*, 2007, **32**, 6
[258] H. Yamamoto, H. Kiyaoka, S. Hino, H. Nakanishi, T. Ichikawa, and Y. Kojima, *International Journal of Hydrogen Energy*, 2009, **34**, 9760
[259] Y. Kojima, K. Tange, S. Hino, S. Isobe, M. Tsubota, K. Nakamura, M. Nakatake, H. Mikaoka, H. Yamamoto and T. Ichikawa, *Journal of Materials Research*, 2009, **24(7)**, 2185
[260] H. Y. Leng, T. Ichikawa, S. Isobe, S. Hino, N. Hanada and H. Fujii, *Journal of Alloys and Compounds*, 2005, **404-406**, 443
[261] R. Lan, J. T. S. Irvine and S. Tao, *International Journal of Hydrogen Energy*, 2012, **37**, 1482
[262] H. Yamamoto, H. Miyaoka, S. Hino, H. Nakanishi, T. Ichikawa and Y. Kojima, *International Journal of Hydrogen Energy*, 2009, **34**, 9760
[263] Z. Xiong, G. Wu, J. Hu and P. Chen, *Advanced Materials*, 2004, **16**, 1522

2. Experimental

The domain of solid state chemistry is concerned with the properties and characteristics of solid materials. Philips assigns solids to five categories; simple metals, transition metals, ionic crystals, semiconductors, and molecular crystals.[1] In this work, investigation of materials in the simple metal and ionic crystal classifications are covered. To describe these materials a number of different yet complementary analytical methods may be used; crystallography, spectroscopy, thermodynamic and kinetic measurements and imaging. The purpose of this chapter is to provide the reader with the theoretical and technical information about the techniques employed in this work. Furthermore, synthesis and analysis variables are also provided to illustrate how conditions were modified to prepare and characterise the materials described in subsequent results chapters.

2.1. Sample Handling

2.1.1. Gloveboxes

Use of gloveboxes in chemistry preparations is a suitable means of minimising the oxidation or hydration of air sensitive and pyrophoric materials; it is possible to handle materials, prepare reactions and store samples under an inert environment. The light metals, hydrides and halides used in this work were acutely air sensitive; the metals and hydrides were pyrophoric while many of the light metal halides were exceptionally hygroscopic. Therefore, for the majority of the work presented in this thesis, preparatory work was conducted in recirculating gloveboxes filled with inert gas, *i.e.*, dry $Ar_{(g)}$ or $N_{2(g)}$. Preparation tools were transferred in/out of the box using evacuable antechambers. To maintain low O_2 and H_2O levels in the box, the antechamber was evacuated and inert gas filled three times before opening the inner port door to the main chamber. The inert atmosphere of the gloveboxes was continuously filtered through a molecular sieve and a catalyst by a recirculation blower. (The recirculation blower was only switched off when sample weighing was conducted in order to maintain a steady environment for the balance and minimise errors in weighing reagents.)

The Saffron scientific gloveboxes shown in Figure 2-1 a) and b) were regenerated "off-box" meaning that the catalyst and molecular sieve chambers were removed for regeneration procedures.[2, 3] These were conducted under a flow of the appropriate regeneration gas (namely 5 % H_2 in Ar or 5 % H_2 in N_2, depending on the box environment) for a minimum of 12 hrs to remove water, oxygen and other contaminants.

The catalyst of the mBraun glovebox shown in Figure 2-1 c) was regenerated *in-situ* using a special gas blend of 5 % H_2 in Ar, where the box environment was $Ar_{(g)}$. Conducting these regeneration procedures on a regular basis (every two months) ensured that the glovebox environments were maintained at acceptable levels, *i.e.*, 0-5 ppm O_2 and 0-30 ppm H_2O. Analysers fitted to the gloveboxes indicated the respective levels in the box and upon any rise in the O_2 or H_2O levels operational checks were conducted. Regeneration activities were conducted more frequently depending on operations taking place in the box or after long periods of down-time.

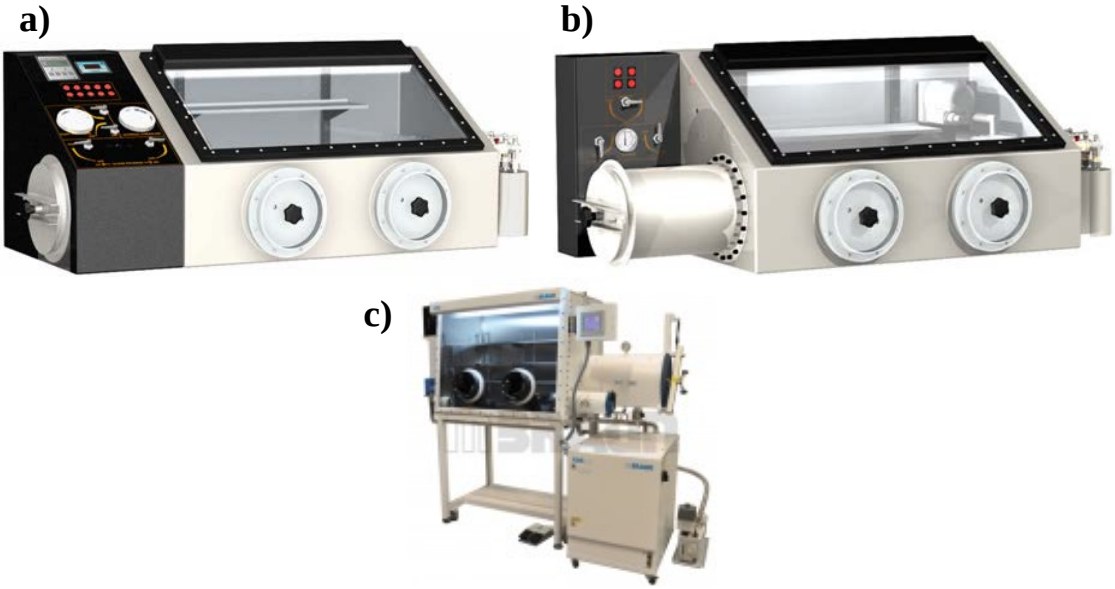

Figure 2-1 Images of the a) Alpha and b) Omega models of Saffron Scientific gloveboxes employed for sample preparation in this thesis, and c) UniLab mBraun glovebox employed as STA housing (see section 2.3.5.1).

2.2. Preparative Methods & Techniques

2.2.1. Mechanochemistry

2.2.1.1. Introduction to Mechanochemistry

Mechanochemistry, also known as tribochemistry, is deep rooted in the development of new, functional materials and has a rich history in progression of the chemical sciences.[4, 5, 6, 7] It may be defined as:

"*the branch of chemistry which is concerned with chemical and physico-chemical changes of substances of all states of aggregation due to the influence of mechanical energy.*" [8]

The recorded use of mechanical action in chemistry predates Christianity. The Greek philosopher and student of Aristotle, Theophrastus of Eresus (322 B.C.), described simple

hand grinding for extraction of mercury from its sulphide (HgS, cinnabar) in his early text on minerals, De Lapidibus.[8, 9] Scientists throughout history, including Faraday, have since used mechanochemical preparatory techniques to develop and understand chemical processes.[10] The American scientist M. C. Lea has been described as the father of modern day mechanochemistry.[11] His initial research on the effect of mechanical action on silver allowed him to then distinguish between the effects of mechanical and heat treatment in a variety of materials, proving by experiment that the processes were distinct. In the early 20th century, the relationship between chemical and mechanical energy formed part of the theories developed by Ostwald, who received a Nobel Prize in 1909 for his work on the "fundamental principles governing chemical equilibria and rates of reaction", where the term "mechanochemistry" was coined.[12]

Significant commercial interest in mechanochemistry has been growing since the 1980s to present day, over 100 years since the discoveries made by Lea. The shorter reaction times of this technique (relative to the thermochemical method) have been exploited to prepare materials in a solvent free environment using mechanical action alone.[13] These reaction time reductions are due primarily to the constant generation of fresh surfaces of the solids being milled and shorter diffusion path lengths as a result of the continued pulverisation of the particles throughout milling.[14] Mechanochemistry now plays a crucial role in the development of more environmentally responsible synthesis routes to functional solids (including materials for energy applications and pharmaceuticals), and plays an important role in developing solutions to environmental problems, such as the removal of persistent organic pollutants (POPs).[15, 16, 17] Mechanochemistry is currently one of the key preparatory methods for development of solid state hydrogen storage materials, including new hydrides, catalysed/doped hydrides, and composite hydrogen release systems. The hydrogen release properties of materials prepared by mechanochemistry have been demonstrated as competitive and even superior to those prepared by conventional thermochemical solid state methods as a result of the shorter hydrogen diffusion paths in the smaller particles.[14]

In principle, the technique seems relatively simple, but in reality it entails a number of simultaneously occurring complex processes (Figure 2-2).[18, 19]

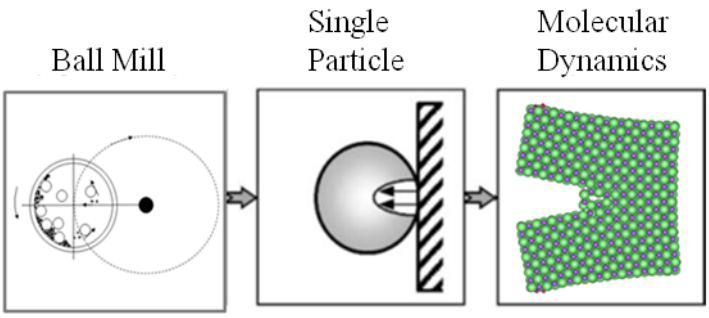

Figure 2-2 Illustration of the increasingly complex processes that occur across scales during milling. (Adapted from Reference 19.)

1. Milling reduces particle size (comminution) with the formation of new surfaces and thus an overall increase in surface area. The type of equipment used can greatly influence the degree to which this occurs owing to the way in which stress is applied to the materials. In modern milling instruments, there are a number of variables that can allow operators to define the relative stress applied to the material and these will be outlined later.
2. The mechanical properties of the material being milled also influences the way in which the milling processes take place, where hard materials will be affected by mechanical force in a significantly different way to brittle materials processed under the same conditions. Each particle will have contact with other particles, the milling media and the walls of the milling container and so the frequency of impacts will influence the impact of the milling process on a particular material.
3. Modification of the crystalline structure is an inherent effect of using this technique, where strain, structure defects and dislocations may be induced depending on the applied stress. Furthermore, crystalline polymorph transitions and chemical reactions (such as metathesis reactions, alloying, decomposition, redox reactions, *etc.*) are also possible.[20]

Understanding the mechanisms of mechanochemical processes is difficult, since many factors can affect the results obtained. However, emerging *in-situ* methods are allowing valuable information to be acquired regarding the reaction pathways followed in the mill.[21] Therefore there is much still to learn about the mechanisms taking place in mechanically driven reactions. Mechanochemistry will no doubt play a pivotal role in the development of solvent free, environmentally sustainable materials synthesis in a variety of research fields. With the growing interest in this technique, however, a wide variety of milling instrumentation and variables are now used by researchers, which can make interpretation and reproduction of results a complicated task.[22] Therefore, as much information as

possible should be provided about the experimental set-up and conditions used to produce the properties of the as-milled materials.

2.2.1.2. Milling Procedures

A planetary ball mill (Retsch PM100) was used to prepare samples in this work (Figure 2-3). Ball milling in planetary devices involves the rotation of a milling jar containing milling balls and reagents. The jar is fixed on a rotating plate known as a sun wheel which hosts a counterweight to minimise instrument vibration. Rotation of the sun wheel at a user defined rotation speed causes the milling jar platform to be rotated in the opposite direction to the sun wheel, where the jar and sun wheel rotate in a 2:1 ratio. This causes the milling balls to rotate and generate mechanical action on the materials in the jar. The forces involved in this milling process are known as Coriolis forces, where both impact and friction forces are at play. It is the combination of these forces that generate the high energy required to conduct milling operations in this method.[23]

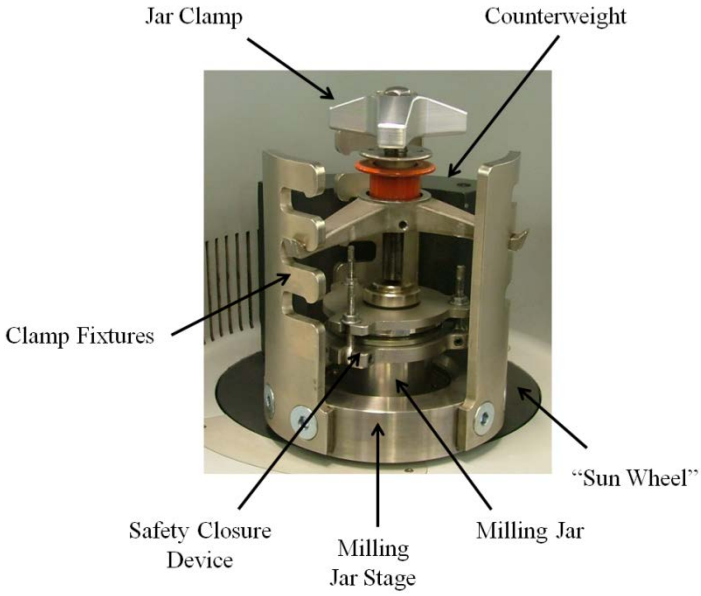

Figure 2-3 Configuration of the milling jar in the Retsch PM100 planetary ball mill.

The milling jar was loaded with the material(s) to be milled plus milling balls within an inert gas filled glovebox. The jar was then clamped shut under the inert gas using a safety closure device supplied by Retsch to completely avoid contact with air. The entire jar assembly was then clamped on to the rotating stage inside the milling chamber, and milling conditions programmed. The frequency of impacts and friction induced in milling is directly related to the milling variables defined by the user. Controllable variables for this set-up include:

- Milling speed (range: 100-600 rpm)
- Rotation direction (clockwise/anti-clockwise)
- Milling time (range: 1 s - 99 h), including break periods between rotation direction reversal
- Milling tools; stainless steel jar (50 ml) and stainless steel milling balls (10 mm diameter, 4 g/ball)
- Ball:powder mass ratio, *e.g.*, 40:1 ball:powder ratio achieved when 0.8 g material milled with 8x steel milling balls (32 g).

By changing these variables, the degree of energetic milling could be varied such that a more/less energetic milling scenario could be devised depending on the materials under consideration. In order to ensure milling was conducted as safely as possible, careful consideration was given to the counterbalance, which was set to the correct weight for each milling experiment to account for the total mass of the milling jar, milling balls, closure device, *etc*.

Milling operations covered in this study include comminution of hydrides, chemical reactions, polymorph transformation and alloying to form new crystalline ternary halide and ternary hydride phases. Further details regarding the specific synthesis conditions will be provided in the relevant results chapters.

2.2.2. Glassblowing & Furnaces

Glassblowing equipment was used to prepare bespoke glass tubes for experiments conducted in furnaces. The glassblowing torch is fed by two inlet gas lines; natural gas and $O_{2(g)}$. A low flow of natural gas must be applied before igniting the torch by a naked flame. The ratio of gas:oxygen was then varied to acquire the correct flame for use in silica tube splitting/vacuum sealing operations. Reactions to be conducted under vacuum were prepared in vacuum sealed tubes on the glassblowing line. Since the samples in this work were air sensitive, the sample tubes were prepared in a glovebox and sealed with a Suba-seal® septum and parafilm.

A bespoke bench-top furnace was employed in this research to conduct thermal desorption and conventional thermal preparatory work. Using programmable temperature controllers (Eurotherm), the heating ramp rate, dwell period and cooling rates could be specified allowing adequate control over the heating conditions employed. The typical set-up of the bespoke bench furnace used in this work is shown in Figure 2-4, which was used to synthesise materials under a flow of $Ar_{(g)}$, to heat samples for isolation of intermediate

species, and also to replicate STA (Simultaneous Thermal Analysis) conditions prior to STA experiments (see section 2.3.5). For gas flow conditions, the tube was sealed using a rubber septum (Suba-seal®) with an inlet flow and outlet vent created using syringes and tubing. The outlet gas flow was passed through a reversed empty Dreschel bottle then a suitable bubbler fluid, *i.e.*, water or paraffin oil, in a second Dreschel bottle (the empty Dreshel bottle prevents suck-back of the bubbler fluid in to the sample). After all furnace procedures, the sample vessels were removed once cooled to room temperature and the samples retrieved on the open bench or in a glovebox if the products were air sensitive.

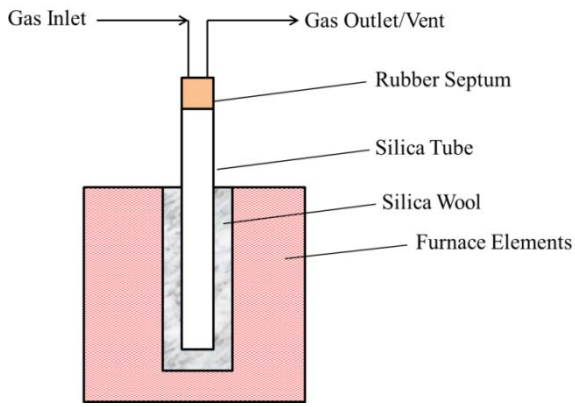

Figure 2-4 Bespoke bench-top furnace.

2.3. Characterisation Techniques

Before entering into any discussion about analytical techniques and tools used by chemists it is important to briefly introduce some aspects of atomic quantum theory, from which their capabilities are derived.[24] Physicists and chemists have developed a number of tools which rely on knowledge of the principles behind the nature of light. From elementary chemistry concepts, it is clear that light can be described as both a particle and as a wave, *i.e.*, the wave-particle duality, described elegantly by Einstein's solution to the photoelectric effect:

Equation 2-1

$$E = h\nu$$

E is the energy of the light particle (or photon), h is Planck's constant ($6.63 \times 10^{-34} J\ s$) and ν is the frequency of the light wave. The electromagnetic spectrum (Figure 2-5) describes the entire range of electromagnetic radiation, defined by the frequency (ν) and wavelength (λ) of the oscillating light waves ($c = 3.00\ \times 10^{8}$ m/s):

Equation 2-2

$$c = \nu\lambda$$

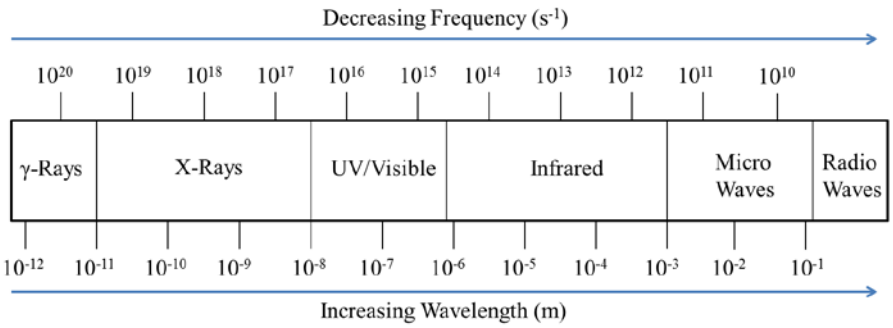

Figure 2-5 Simplified representation of the electromagnetic spectrum.

By understanding the duality of light concept, electromagnetic radiation can be used to conduct experiments that enable determination of the nature of matter. Using defined regions of the electromagnetic spectrum, scientists and engineers have designed instruments as analytical tools that can probe materials down to the sub-atomic level. A range of instruments and analytical techniques that exploit a wide range of the electromagnetic spectrum have been used herein in order to gather as much information as possible about the properties of the materials synthesised. These will now be described with some relevant theoretical discussion.

2.3.1. Crystallography and Diffraction

Crystallography is "*the study of crystal form and structure*".[25] Crystalline solids are comprised of planes of atoms arranged in a specific order and may be represented by the simplest repeating unit of the crystal structure, *i.e.*, the 3D unit cell. Figure 2-6 shows a simple unit cell, which can be described by three vectors; a, b, and c, and the angles between their axes; α, β and γ.

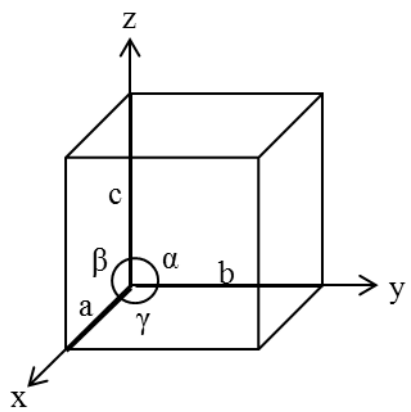

Figure 2-6 Basic cubic unit cell showing cell lengths and angles.

The unit cell of a crystal is defined by the minimum symmetry requirements of a particular crystalline structure. There are seven different crystal systems based on fundamental symmetry operations (Table 2-1), where more detailed information about the symmetry functions can be described using one of 32 point groups.[26] Moreover, a number of selection rules are used to describe the crystalline nature of solids and these will be highlighted in this section. First, basic diffraction theory with respect to crystallography will be introduced since this is fundamental to practical research in the field of solid state chemistry.

Diffraction occurs when a wave, *i.e.*, electromagnetic radiation, encounters matter (Figure 2-7). The waves may be aligned in phase or out of phase, which results in constructive or destructive interference, respectively. The vital information that may be used in crystallography studies is found from constructive interference. Diffraction can be mathematically explained using the Bragg law (Equation 2-3):

Equation 2-3

$$n\lambda = 2d\sin\theta$$

Where λ is the wavelength of the incident radiation, d is the spacing between crystal lattice planes, and θ is the Bragg angle at which the diffracted pattern for a particular plane is observed if the Bragg law is obeyed.[27] Usually, only first order diffraction is considered, and so the Bragg equation may be simplified further using n = 1, where n represents the order of the reflection, although n may be any positive integer.

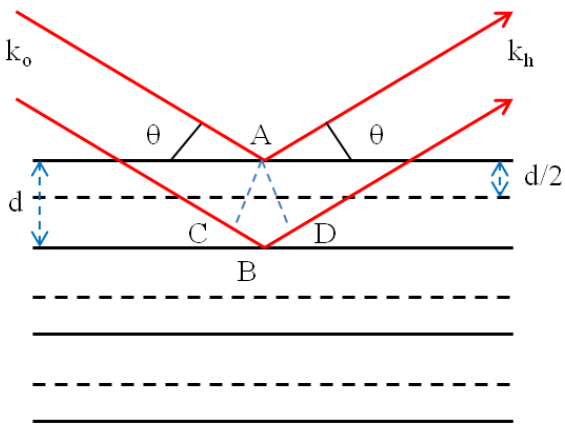

Figure 2-7 Representation of diffraction in a crystal where black solid lines indicate lattice planes, k_o and k_h are the incident and reflected wave vectors, d is the lattice spacing and θ is the angle between the lattice plane and k_o, where the incident and reflected angles are equivalent.

Crystal structure information is determined by collecting data over a range of θ, where the resultant diffraction of an incident beam of radiation, *e.g.*, X-rays or neutrons, is

represented in a diffraction pattern. The pattern shows diffraction maxima (peaks), which correspond to diffraction taking place at a particular Bragg angle, θ. The form, *i.e.*, shape, size and intensity, of each peak is important and will be discussed in more detail later. The crystal system of a crystalline solid is derived from the *d*-spacing information collected in the diffraction experiment and Miller indices, h, k and l, are used to describe the parallel planes of atoms that intersect the axes of the unit cell (a, b and c respectively). This yields the overall size of the unit cell. Further information may be provided about the unit cell by using Bravais lattice notation, which describes the 14 possible crystal configurations. This notation combines the seven crystal systems described in Table 2-1 and the possible types (or centerings) of the 3D lattice; primitive (P), body centred (I), face centred (F), base centred (centred on the (001) face) (C), or primitive rhombohedral (R).

Combining the above definitions, assignment of one of 230 space groups to a particular crystal can be made and these will be used throughout this work to indicate the crystallographic nature of the materials formed. Detailed information about the space groups may be found in the International Tables for X-Ray Crystallography.[28]

Table 2-1 Summary of crystallography notation and symmetry information for the seven crystal systems. [29]

Crystal System	Unit Cell Parameters	Min^{m} Symmetry Requirements	Bravais Lattices	Point Groups
Triclinic	$\alpha \neq \beta \neq \gamma \neq 90°$ $a \neq b \neq c$	None	P	1, $\bar{1}$ (C1, Ci)
Monoclinic	$\alpha = \gamma = 90°$ $\beta \neq 90°$ $a \neq b \neq c$	One twofold axis or one symmetry plane	P, C	2, *m*, 2/*m* (C_2, C_S, C_{2h})
Orthorhombic	$\alpha = \beta = \gamma = 90°$ $a \neq b \neq c$	Any combination of three mutually perpendicular twofold axes or planes of symmetry	P, C, I, F	222, *mm*2, *mmm* (D_2, C_{2v}, D_{2h})
Trigonal/ Rhombohedral	$\alpha = \beta = \gamma \neq 90°$ $a = b = c$	One threefold axis	R	3, $\bar{3}$, 32, 3*m*, $\bar{3}m$ (C_3, C_{3i}, D_3, C_{3v}, D_{3d})
Tetragonal	$\alpha = \beta = \gamma = 90°$ $a = b \neq c$	One fourfold axis or one improper axis	P, I	4, $\bar{4}$, 4/*m*,422, 4*mm*, $\bar{4}2m$, 4/*mmm* (C_4, S_4, C_{4h}, D_4, C_{4v}, D_{2d}, D_{4h})
Hexagonal	$\alpha = \beta = 90°$ $\gamma = 120°$ $a = b \neq c$	One sixfold axis or one sixfold improper axis	P	6, $\bar{6}$, 6/*m*, 622, 6*mm*, $\bar{6}m2$, 6/*mmm* (C_6, C_{3h}, C_{6h}, D_6, C_{6v}, D_{3h}, D_{6h})
Cubic	$\alpha = \beta = \gamma = 90°$ $a = b = c$	Four threefold axes at 109° 28’ to each other	P, I, F	23, *m*3, 432, $\bar{4}3m$, *m*3*m* (T, T_h, O,T_d, O_h)

2.3.1.1. Powder X-Ray Diffraction

X-rays lie at a lower wavelength than visible light in the electromagnetic spectrum, and their use in diffraction experiments originated from the work of Friedrich, Knipping and Laue in the early 20th century for single crystals.[30] W. H. Bragg and his son, L. Bragg, demonstrated the power of X-rays for chemical analysis by diffraction of X-rays by crystals.[31, 32, 33] This pioneering work promoted X-ray diffraction as an excellent analytical tool for crystal structure analysis.[34, 35] X-ray diffractometers are now commonplace in modern materials chemistry research facilities, and are considered one of the most powerful tools for analysis of crystalline materials across a range of research fields.

Powder X-ray diffraction (PXD) is used to establish structural information about bulk powdered materials by indicating the electron density and hence atomic configuration

within a crystalline substance containing many crystallites (as opposed to single crystal X-ray diffraction, which is beyond the scope of this study).[36, 37] X-rays produced by synchrotron light sources present an attractive alternative to lab X-rays, where the brightness and vertical collimation of the X-rays produced are significantly improved relative to the lab based sources, and this will be discussed.[38]

Three different lab-based diffractometers were employed to obtain diffraction data contributing to this work; a Bruker D8 Advance diffractometer, a Panalytical X'Pert Pro and a Siemens D500 diffractometer for hot stage experiments. Samples were analysed using Cu Kα1 radiation over the $5° \leq 2\theta \leq 85°$ (1 h, phase analysis) and $10° \leq 2\theta \leq 110°$ (10 h, structure refinement) ranges. The step size and scan speed used for phase analysis was 0.0167° at 1.57°/min, and for higher quality diffraction data for structure refinement the step size and scan speed were reduced to 0.008° and 0.165°/min respectively.

In addition, synchrotron X-ray diffraction (SXD) was conducted on some of the powdered samples. The NSRRC synchrotron facility in Taiwan was used for SXD experiments on the BL01C2 SWLS (Superconducting Wave Length Shifter) X-ray powder diffraction beamline.[39]

A diffractometer can be considered to comprise three separate sections; the radiation source, the sample stage and the detector.

The Radiation Source

The source of radiation used for diffraction experiments can greatly influence the quality of the data obtained and therefore the accuracy by which a structure may be known. In a conventional lab diffractometer, the fixed source produces X-rays by striking a metal (Cu for Bruker, Panalytical and D5000 instruments) with electrons such that high energy electrons in the metal fall to a lower energy orbital with the consequential release of a specific amount of energy (known as a photon). Lab X-ray diffractometers use a monochromator (*i.e.*, germanium crystal) designed specifically to select photons in the X-ray region of the electromagnetic spectrum, where the most intense $K_{\alpha 1}$ radiation ($\lambda = 1.54$ nm) for Cu was used in this work.

Synchrotron X-rays are produced in a remarkably distinct manner to lab X-rays, which results in their superior brilliance and diffraction capabilities. In a synchrotron particle accelerator, electrons are produced by applying an electrical and thermal current to an "electron gun". The electrons are then accelerated using a linear accelerator (linac) and a booster ring before entering the electron storage ring (Figure 2-8). Using a series of

magnets and insertion devices, *i.e.*, wigglers and undulators, it is possible to control the movement of the electrons around the electron storage ring, such that they follow a circular path. Synchrotron radiation is produced continuously in the electron storage ring using magnets that tangentially deflect the synchrotron radiation from the electron flux. The synchrotron radiation can then be directed on to a sample along a beamline. Beamlines comprise monochromators and mirrors to ensure the correct wavelength of radiation in the X-ray region of the electromagnetic spectrum is acquired for the desired analysis, *i.e.*, λ = 0.774908 nm for BL01C2.[39]

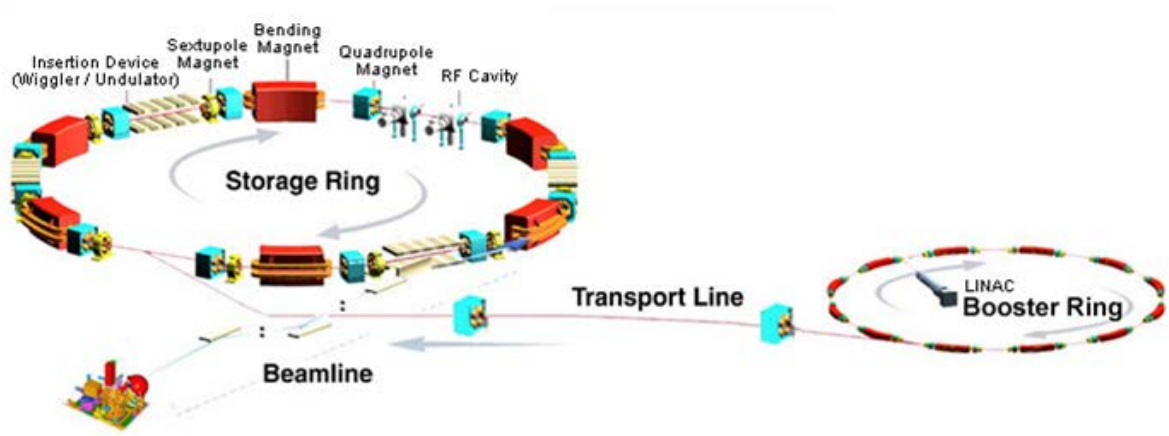

Figure 2-8 Configuration of the synchrotron source at NSRRC. [39]

More detailed information about radiation sources for materials science research may be found in Reference 40.

The Sample Stage and Geometry

The sample stages employed in this work, *e.g.*, capillary, bracket and hot stage were dependent on the nature and quantity of the sample. For air sensitive samples and limited sample quantities, glass capillaries (0.5 mm or 0.7 mm internal diameter) containing the powdered sample were used on both the D8 and X'Pert instruments. If necessary, samples were ground in an agate mortar and pestle prior to analysis in order to ensure a homogeneous powdered sample was used. The capillaries were aligned on the aluminium capillary holder by eye assisted by a microscope. The capillary mount was then fixed to the instrument goniometer, which was continuously rotated 360° throughout the analysis. A series of apertures (slits) and monochromators are used in series to influence the X-ray beam before and after interaction with the sample, and help to minimise beam divergence and background scattering. A pre-/post-sample slit size of 2.0 mm was used for capillary sample measurements in Debye-Scherrer transmission geometry (Figure 2-9). In this

configuration, the detector scans around a fixed sample, where the cross-section of the incident X-ray beam is sufficient to irradiate the whole sample.

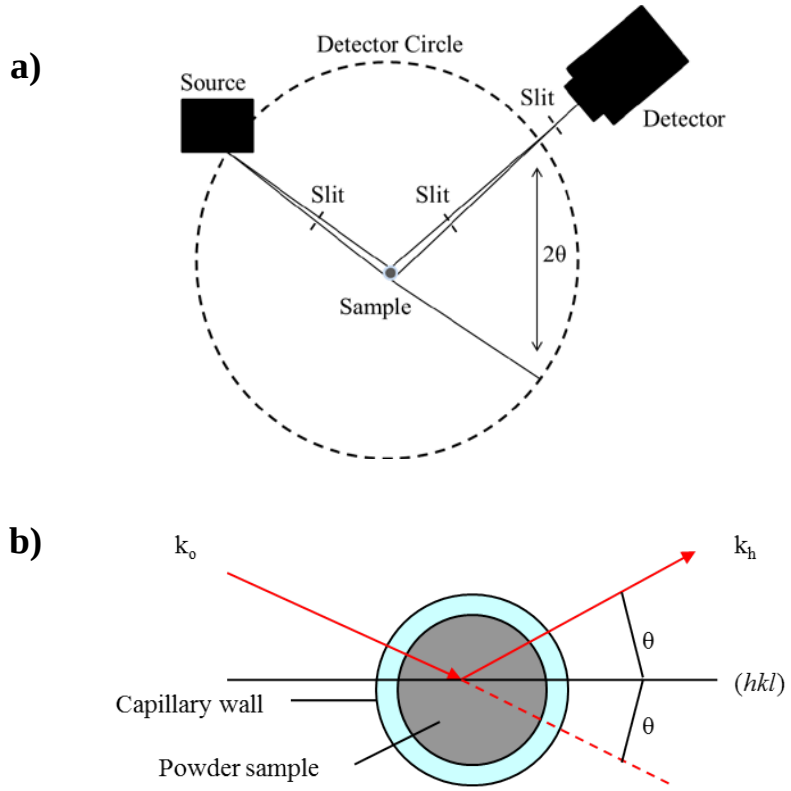

Figure 2-9 a) Configuration of capillary PXD analysis in Debye-Scherrer transmission geometry, and b) magnification of capillary orientation for both D8 and X'Pert diffractometer instruments.

Capillaries were also used for the SXD experiments. The samples were loaded and sealed in capillaries inside an inert gas filled glovebox, and then fitted to a bespoke sample stage for analysis. A Huber single-axis 410 goniometer was used for SXD capillary measurements, where a low temperature furnace was attached for non-ambient measurements (Figure 2-10).

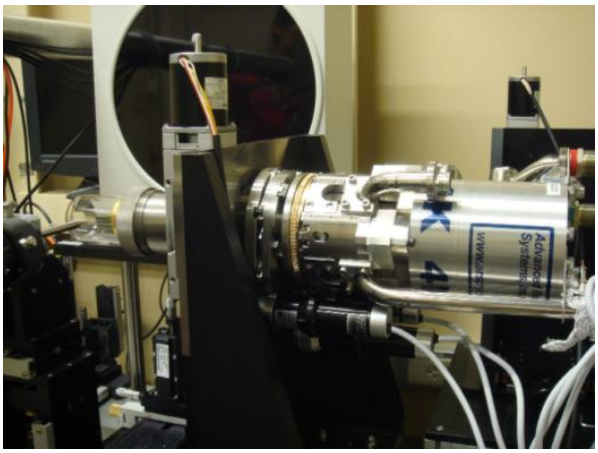

Figure 2-10 Low temperature furnace configuration on BL01C2.

For non-air sensitive samples, a 10 mm pre-sample slit was fitted in the X'Pert Pro instrument and the Bragg-Brantano reflection geometry employed. This configuration involves tilting the sample about an axis by an angle, θ, and the reflected radiation is collected by a detector which is rotated by 2θ. Samples were prepared on a quartz sample holder (bracket) that has a recess on the surface such that the maximum quantity of sample is used for analysis. Time-resolved PXD experiments were also conducted in this configuration, where a series of measurements (1 h) were conducted over a user-defined experiment duration (1-15 h). This was used to indicate changes in the diffraction characteristics of a sample with respect to the time exposed to air. Using the D5000 instrument, samples were prepared on an alumina sample holder which was then fitted inside the heating jacket fixed to the instrument. The D5000 was also operated in Bragg-Brentano geometry (Figure 2-11), where an $Ar_{(g)}$ flow was passed over the sample to avoid oxidation during heating (at a rate of 5 °C/min).

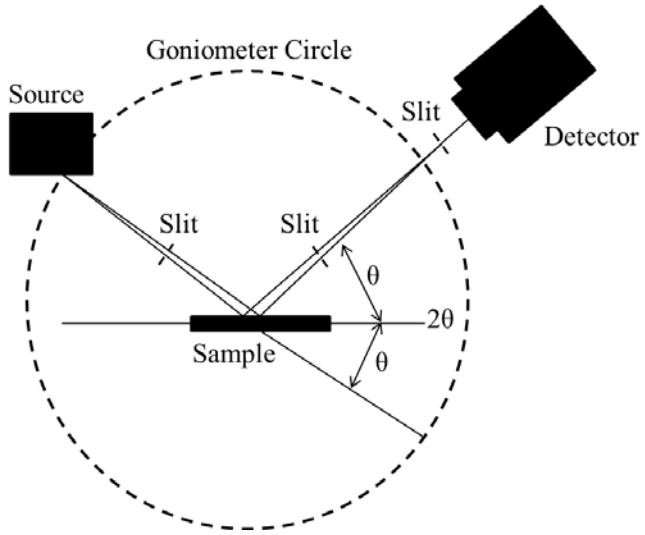

Figure 2-11 Bragg-Brentano reflection geometry used in X'Pert and D5000 measurements.

Detector

After the X-rays have interacted with the electrons of the atoms in the sample, the diffracted signals are collected by a detector. In PXD and SXD, diffraction signals are collected as a function of 2θ, as shown in the previous section. A NaI(Tl) scintillation detector was employed on BL01C2 to collect the diffracted radiation. The diffraction pattern of polycrystalline powder samples results from the cone diffraction of the crystallites through a user defined 2θ range, *e.g.*, $5° \leq 2\theta \leq 85°$. The cone diffraction may be reported as diffraction rings, where each ring represents a complete data set for diffracted radiation collected at a specific 2θ position. The resultant diffraction pattern in

graphical form shows what may be considered as a slice through the diffraction rings, with intensity on the y-axis and 2θ along the x-axis.

The peaks shown on the 1D patterns obtained by diffraction experiments may be compared with databases of known diffraction patterns or those calculated from known crystal structures. This helps to establish a correlation between diffraction data collected experimentally for a specific sample with known diffraction data for specific crystalline materials. This allows primary crystal structure identification and then allows the user to develop the structure analysis to obtain more detailed crystallographic information. Two different crystallographic databases were used in this study; the HiScore database collated by Panalytical and the ICSD (Inorganic Crystal Structure Database) now hosted by the Royal Society of Chemistry.[41, 42]

2.3.1.2. Impact of preparation method on diffraction characteristics

Typical diffraction patterns for mechanochemically produced and milled materials show broadening of the reflections, where small reflections may be obscured by a high background and those at high values of 2θ may be indistinguishable from the background. This introduces more complicated aspects to data interpretation for samples produced by this method. This cannot be avoided and is primarily the result of significant particle size reduction, although some contribution from amorphous components in the sample is also likely. For samples prepared in capillaries other factors can affect the quality of diffraction data, including diffraction from the glass capillary, misalignment of the capillary, and contribution from the wax capillary mount if the sample is incorrectly mounted.

2.3.2. The Scherrer Method

Beyond the crystallographic information derived from diffraction experiments, it is also possible to investigate and estimate the average size of the crystallites in a powder sample. To do this, both information obtained from the peak profiles and knowledge of the particle morpohology from, e.g., SEM (Scanning Electron Microscope) or TEM, are required. In this work, the crystallite size, D, could be determined from PXD patterns across well-defined reflections over a typical 2θ range of 30-50º (Equation 2-4).[43] A Scherrer constant (also known as the shape factor), K, was selected based on the morphology determined from SEM analysis conducted in this work.[44] To account for instrumental broadening a LaB_6 powder standard was used to correct the FWHM (Full Width Half Maximum; Equation 2-5), where B is the experimentally observed FWHM and b is the FWHM of the standard. All 2θ and FWHM values were converted from degrees to radians.

Equation 2-4

$$D = \frac{K\lambda}{\beta \cos\theta}$$

Equation 2-5

where, β = B-b

From this analysis, it was possible to estimate the average crystallite size in a sample from powder diffraction data collected in this work.

2.3.3. Structure Refinement & The Rietveld Method

Beyond basic pattern matching and peak assignment, structure refinement methods allow detailed structure information to be derived from diffraction data. Structure refinement uses a crystal structure model to which observed diffraction data may be fitted. Preliminary cell parameter indexing was conducted in the first instance, and was obtained using CELREF (CELREF: Graphical Unit Cell Refinement).[45, 46] CELREF is simple profile fitting software, which allows the user to match and compare an experimentally determined pattern with known crystallographic information. This enables identification of the crystal system and space group for the crystalline phase, and calculates the unit cell parameters. This gives a good primary indication of the fit of observed data to the selected structure model.

The Rietveld method is a full profile structure refinement method, where the GSAS-EXPGUI (General Structural Analysis System – EXP Graphical User Interface) software was employed in this work.[47, 48, 49] The principle of the Rietveld method is to obtain crystal structure information, rather than simple profile fitting.[50] This method requires selection of an adequate initial structure model, where model data files were acquired from the ICSD.[42] The operator may then begin refining parameters based on a number of different profile characteristics that are relevant to the nature of the crystalline material under investigation. The parameters used and the systematic method employed allows elucidation of the key structural information. The method involves best least-squares fitting of all observed diffraction data points (or steps, *i*) of specific intensity simultaneously, where the function S_y is minimised as follows:

Equation 2-6

$$S_y = \sum_i w_i \, (y_i - y_{ci})^2$$

Where y_i and y_{ci} are the observed and calculated intensities at the ith step respectively, and w_i is equal to $1/y_i$. The structure factor for the Kth Bragg reflection, F, is related to the contributions from the scattering amplitudes, f, and phases, δ, of each atom, j.

Equation 2-7

$$F_K = \sum_{j=1}^{N} f_j \, exp[i\delta]$$

Thus, the structure factor for the Kth Bragg reflection, F_K, may be given as:

Equation 2-8

$$F_K = \sum_{j} N_j f_j exp\left[2\pi\left(hx_j + ky_j + lz_j\right)\right] exp\left[-M_j\right]$$

and

Equation 2-9

$$M_j = 8\pi^2 \overline{u_s^2} sin^2\,\theta/\lambda^2$$

Where, h, k and l are the Miller indices, the position parameters for the jth atom are given by x_j, y_j, z_j and N_j is derived by dividing the site occupancy by the site multiplicity. The $\overline{u_s^2}$ term is related to the thermal displacement of the atom. $|F_K|^2$ is used to calculate y_{ci} which is derived from a summation of calculated contributions from relevant neighbouring Bragg reflections and background (y_{bi}) contributions, *i.e.*,

Equation 2-10

$$y_{ci} = s \sum_{K} L_K |F_K|^2 \emptyset(2\theta_i - 2\theta_K) P_K A + y_{bi}$$

Where s is the scale factor, K represents a specific Bragg reflection using hkl Miller indices, L_K combines Lorentz, polarization and multiplicity factors, $\emptyset$ is the reflection profile function, P_K is the preferred orientation function, and A is the absorption factor.

The iterative process by which Rietveld refinements are processed may be solved by an inverted normal matrix (Equation 2-11) involving adjustable parameters x_j, x_k:

Equation 2-11

$$M_{jk} = -\sum_{i} 2\,w_i \left[(y_i - y_{ci}) \frac{\partial^2 y_{ci}}{\partial x_j \partial x_k} - \left(\frac{\partial y_{ci}}{\partial x_j}\right)\left(\frac{\partial y_{ci}}{\partial x_k}\right)\right]$$

The solution of this matrix is based on the normal equations generated by the least squares refinement. Each step (or shift, Δx_k; Equation 2-12) in the iterative solution procedure is conducted using the user defined parameters that may be refined to improve the model. This process is repeated until the global minimum is reached.

Equation 2-12

$$\Delta x_k = \sum M_{jk}^{-1} \frac{\partial S_y}{\partial x_k}$$

Choosing an adequate starting model is therefore very important, since divergence from the global minimum or a false minimum will arise owing to the non-linear relationship

between the refinement parameters and the intensities used in the iterative process described.

Thus far, the mathematical principles and general concepts of the Rietveld method have been introduced. The refinable parameters and diffraction characteristics that allow such a method to be employed will now be discussed. Parameters to be simultaneously refined for any diffraction result may be placed into two categories; global parameters and phase parameters (Table 2-2).

Table 2-2 Primary Rietveld refinement parameters.

Global Parameters	Phase Parameters
2θ-Zero	x_j y_j z_j B_j N_j
Instrument profile	Scale factor
Profile Asymmetry	Specimen profile breadth
Background	Lattice parameters
Wavelength	Preferred crystallite orientation
Specimen displacement/transparency	Extinction
Absorption	

Note: j represents the jth atom in the unit cell, where x_j, y_j and z_j, are the position coordinates. B_j is an isotropic thermal parameter and N_j is the site-occupancy multiplier.

The peak shape describes important characteristics of crystal structures and the pseudo-Voigt (pV) profile function was determined to be the most appropriate peak shape refinement function for the data collected in this work. The pV function considers both Laurentzian (L) and Gaussian (G) contributions and may be expressed as:

Equation 2-13

$$pV = \eta L + (1 - \eta)G$$

The mixing factor, η, is given as a linear function of 2θ (Equation 2-14), where the NA and NB parameters may be refined.

Equation 2-14

$$\eta = NA + NB * (2\theta)$$

The FWHM (full-width-at-half-maximum) is used to measure breadth (H) of reflections, and dependence on H has been shown to vary with scattering angle, 2θ.[51] Both Gaussian and Lorentzian functions use H to establish the peak shape contribution from each in the pV function:

Equation 2-15

$$G = \frac{(4\ln 2)^{1/2}}{H_k\sqrt{\pi}} exp\left(\frac{-4\ln 2\,(2\theta_i - 2\theta_k)^2}{H_k^2}\right)$$

Equation 2-16

$$L = \frac{2}{\pi H_k} \Big/ \left[1 + 4\frac{(2\theta_i - 2\theta_k)^2}{H_k^2}\right]$$

H is derived using the following expression, where the *U*, *W* and *V* parameters may be refined:

Equation 2-17

$$H^2 = U\tan^2\theta + V\tan\theta + W$$

An alternative expression may be given, which minimises the opportunity for negative H^2 values to arise by incorporation of an additional parameter, θ_o, derived from a point near the middle of the data set:

Equation 2-18

$$H^2 = U'(\tan\theta - \tan\theta_o) + V'(\tan\theta - \tan\theta_o) + W'$$

R-values are the most commonly quoted refinement output values used to indicate the quality of fit for a Rietveld refinement and include: *R*-structure (R_F), *R*-Bragg (R_B), *R*-expected (R_e), *R*-profile (R_p) and *R*-weighted pattern (R_{wp}) factors. These help to indicate whether the starting model is adequate and that the end result is not in fact a false minimum.

Equation 2-19

$$R_F = \frac{\sum\left|\left(I_K('obs')\right)^{1/2} - \left(I_K(calc)^{1/2}\right)\right|}{\sum\left(I_K('obs')\right)^{1/2}}$$

Equation 2-20

$$R_B = \frac{\sum|I_K('obs') - y_i(calc)|}{\sum I_K('obs')}$$

Equation 2-21

$$R_e = \left\{(n-p)\Big/\sum_{i=1}^{n} w_i y_i^2\right\}^2$$

Equation 2-22

$$R_P = \frac{\sum|y_i(obs) - y_i(calc)|}{\sum y_i(obs)}$$

Equation 2-23

$$R_{wp} = \left\{\frac{\sum w_i\left(y_i(obs) - y_i(calc)\right)^2}{\sum w_i\left(y_i(obs)\right)^2}\right\}$$

R_{wp} is considered the most mathematically important index to indicate the quality of the refinement since the numerator of Equation 2-23 is the expression being minimised. The

‘goodness-of-fit” is usually represented by the χ factor (normally given as χ^2), which incorporates the weighted pattern (R_{wp}) and expected (R_e) *R*-indices in the ratio:

Equation 2-24

$$\chi^2 = \left[R_{wp}/R_e\right]^2$$

Stating χ^2 for a refinement gives an indication of whether the minimum reached is genuine: values significantly greater than 1.0 suggest the starting model is unsuitable and values less than 1.0 usually imply that the quality of the data may not be sufficient to be described by the parameters being used in the refinement. The χ^2 factor is, however, only a suggestion of the quality of the refinement and in fact the operator must make sensible judgements about the output from refinements to ensure the structure parameters are reasonable for the material being studied based on complementary analytical data.

2.3.4. Spectroscopy

Measurement of energy transitions in molecules allows important information to be collected about the bonding modes present in a chemical species. The total energy (E_{total}) associated with any molecule can be described in terms of the motion of its electrons (E_{el}), vibrations of the atoms (E_{vib}) and the rotations occurring within the molecule (E_{rot}), which may be represented as:[52]

Equation 2-25

$$E_{total} = E_{el} + E_{vib} + E_{rot}$$

When a molecule is subject to irradiation from a particular region of the electromagnetic spectrum, energy may be transferred to the molecule. The quantity of energy absorbed (ΔE) is defined as the difference in energy between two quantized states, and can be described in terms of the frequency (ν) of the incident light and Planck’s constant (*h*), Equation 2-26. An energy transition will only occur if Equation 2-27, *i.e.*, Bohr’s frequency condition, is fulfilled. The wavenumber ($\tilde{\nu}$) is more commonly used in this expression (Equation 2-28), and is derived from the wavelength (λ) of the incident light and the velocity of light (*c*) *via* the following equations.

Equation 2-26

$$\Delta E = h\nu$$

Equation 2-27

$$\Delta E = hc\tilde{\nu}$$

Equation 2-28

$$\tilde{\nu} = 1/\lambda = \nu/c$$

A simple description may be given for energy transitions in molecules (Figure 2-12). When absorption of a specific quantity of energy (+*ΔE*) occurs then the molecule is promoted to an excited state. An absorption spectrum is obtained by measuring the remaining frequencies of light after interaction with the molecule. Thus, the frequencies of light which are missing, *i.e.*, those having been absorbed, are those frequencies which are equal to the energetic transitions in the molecule. When the molecule returns to the ground state with the loss of a photon (-*ΔE*) the emission spectrum specific to that energetic transition may be determined.

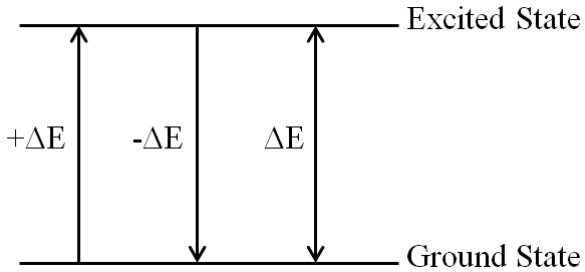

Figure 2-12 Simplified representation of an energy transition in a molecule.

The incident energy need not correspond to *ΔE* and when this occurs the photons may be scattered as a result of interaction with a molecule. The scattered light is collected at specific angles relative to the incident light and a spectrum is obtained, providing information about the different types of energetic transitions in the molecule.

The absorption, emission and scattering of electromagnetic radiation enable a spectroscopic fingerprint for molecules to be built. This fingerprint provides the information required to determine the bonding and symmetry within structures, which chemists describe using Group Theory.[53] Character tables are used in Group Theory to condense the vast amount of information about the symmetry operations of molecules. The information is categorised into classes that can be used to assign molecular vibrations. Each character in the tables is derived from matrices which take into account the symmetry operations which can be applied to a particular molecule.

Infrared and Raman spectroscopy are the two vibrational spectroscopy techniques used in this work and the theory and instrument information for these techniques will be outlined in the following sections.

2.3.4.1. Infrared Spectroscopy

Infrared (IR) spectroscopy involves subjecting a sample to a range of frequencies in the infrared region of the electromagnetic spectrum. The sample then absorbs specific frequencies of the IR radiation, *i.e.*, those which correspond to molecular vibrations of bonds or groups. The absorption of specific energy causes vibrational transitions from the ground state to vibrational excited states. A detector collects the radiation frequencies which have passed through the sample and an absorption spectrum is obtained. This spectrum allows identification of the various IR frequencies absorbed from a particular sample, and thus the fingerprint of the molecular vibrations in the molecule may be determined. Molecular vibrations may be termed IR active if a dipole in a bond or group arises from the absorption of energy.[53] The typical configuration of a Fourier Transform Infrared (FTIR) spectroscopy instrument is given in Figure 2-13, which shows the Michelson interferometer configuration of the instrument used in this work (Shimazdu FTIR8400s).[54]

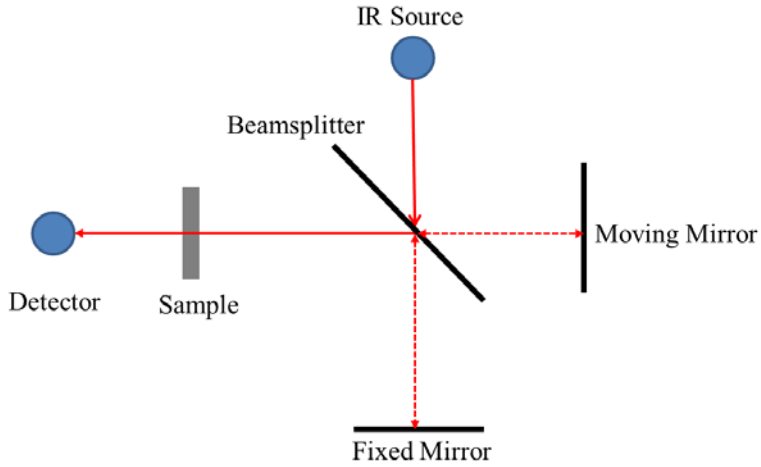

Figure 2-13 Optical schematic of a Michelson interferometer Fourier Transformer InfraRed spectrometer (reproduced from Reference 54).

Each measurement comprised 30 scans to obtain the best possible data, where a background was run before each new sample. Apodization is used in FTIR to improve the resolution and ripple size of a particular data set.[55] The Happ-Genzel apodization function (Equation 2-29) was applied in this work:

Equation 2-29

$$A(\delta) = 0.54 + 0.46\cos\pi\frac{\delta}{\Delta}$$

(where, $\delta = n\lambda$)

The apodized ac signal is represented by $A(\delta)$, δ is the optical retardation (or path difference) of the incident electromagnetic waves of wavelength (λ) multiplied by *n* (an integer) and Δ represents the integration range. Other apodization functions may be used depending on the analysis required, but the Happ-Genzel normally provides sufficient resolution. IR Solution software was used to monitor data accumulation and export the data for further analysis. Using data from literature and knowledge of the main absorption frequencies for particular molecular vibrations, it was possible to assign the peaks observed in this work.

2.3.4.2. Raman Spectroscopy

Raman spectroscopy involves the use of a laser beam of one specific wavelength, *i.e.*, monochromatic radiation, to cause electronic polarization within molecules. The interaction of the radiation with matter in this way results in the scattering of light of various wavelengths, from which a Raman spectrum may be derived.[36, 56] Figure 2-14 shows that radiation produced from a laser is focussed through a lens on to the sample. The scattered light is then focussed and deflected by a curved mirror and then directed towards the detector to produce a spectrum of the scattered light.

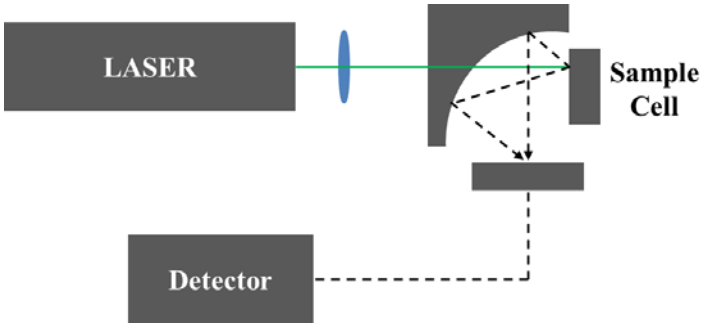

Figure 2-14 Typical Raman spectroscopy instrument optical configuration. (Reproduced from reference 36).

In Raman spectroscopy, three types of light scattering may be described (Figure 2-15):

- Stokes radiation is a result of the incident photons from the laser losing energy to the sample,
- Anti-Stokes radiation is a consequence of energy absorption by the incident photons from the sample, and
- Raleigh scattering results when the energy of the incident photon is conserved, and is also described as elastic scattering.

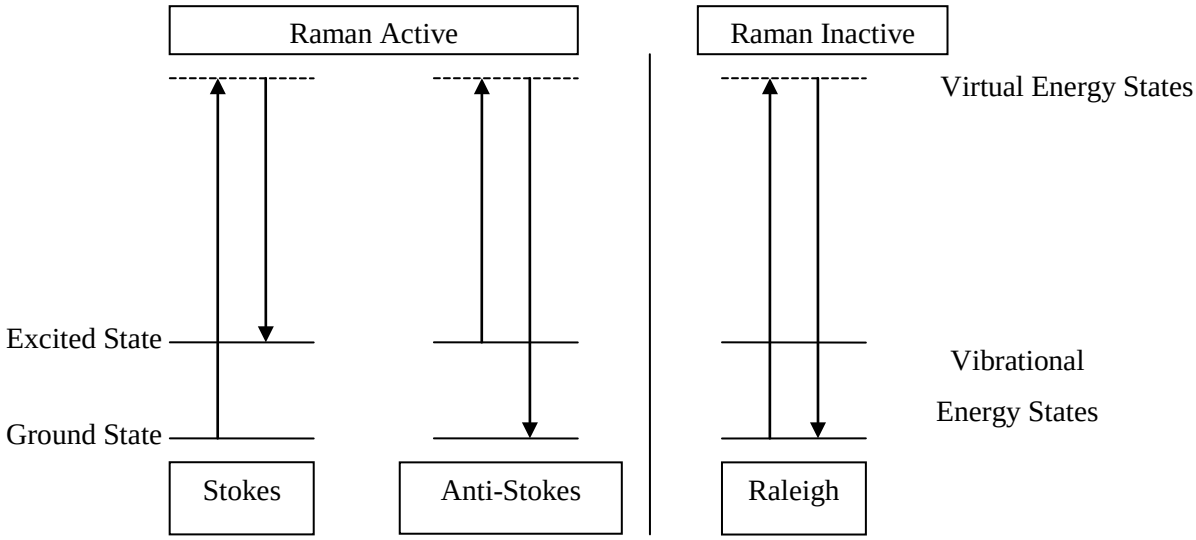

Figure 2-15 Schematic of energy changes associated with Raman scattering.

If an electric field, E, fluctuates at a frequency, ν, the incident light wave may be described as:

Equation 2-30

$$E = E_o cos\ 2\pi\nu t$$

Where the amplitude is given as E_o and t is time. The dipole moment (P) of a diatomic molecule irradiated by this light wave can therefore be described by the expression given in Equation 2-31, where α is the polarizability (a proportionality constant).

Equation 2-31

$$P = \alpha E = \alpha E_o\ cos\ 2\pi\nu t$$

The nuclear displacement, q, of a molecule vibrating at frequency, ν_i, and vibrational amplitude, q_o, can be described as:

Equation 2-32

$$q = q_o\ cos\ 2\pi\nu_I t$$

Therefore, the polarizability of a bond in a molecule is crucial in the application of Raman spectroscopy, where a molecular vibration is only Raman active if the polarizability is modified as a result of interaction with the incident light. With respect to symmetry operations, those molecular vibrations belonging to x_y, z_2, x_2-y_2, *etc*., will be Raman active, and Group Theory may again allow assignment of bonding modes by interpretation of data from Raman spectra.[53] Raman spectra show intense peaks at specific wavenumbers that correspond to the wavelength of light that has been scattered by the molecule. These are represented as shifts from the incident radiation giving the characteristic spectrum of a specific molecule. An Horiba Jobin Yvon LabRam instrument fitted with a confocal

microscope, 600/1200 grooves mm^{-1} grating, 100 µm aperture and a Synapse CCD (Charge-Coupled Device) detector was used for all analysis conducted in this work. Either a green (532 nm) or UV (Ultra Violet; 325 nm) laser was used.

2.3.4.3. Scanning Electron Microscopy-Energy Dispersive X-ray Spectroscopy (SEM-EDX)

Using advanced microscopy techniques, investigation of solid surfaces can provide significant insight in to the nature of the growth and structure of materials. Scanning electron microscopy (SEM) is a useful tool to evaluate the surface morphology of materials. Coupled to EDX (Energy Dispersive X-ray spectroscopy), the SEM-EDX technique can provide further information about the elemental composition of the sample relative to physical features observed. In SEM, primary electrons of a specific de Broglie wavelength are focussed directly on to a portion of the sample, where the wavelength used is controlled by modification of the voltage (*V*) applied. A range of different particles and waves are then scattered from the sample and collected by a detector (Figure 2-16).[57] The primary beam and detector scan the sample, where an image of the solid surface is built from the backscattered and secondary electron signals. Secondary electrons are relatively weak and arise from the interaction of the incident beam with the electrons of the atoms in the sample. These weaker electrons are primarily used to form the image since they are close to the sample surface. By comparison, the backscattered electrons result from the interaction of the incident electrons with the nuclei of the atoms in the sample. These backscattered electrons are much higher in energy than the secondary electrons and can provide more information about the sample, particularly differentiation between regions of different density. The quality of the image is relative to the wavelength of the primary electrons used and the focussing capability of the instrument. The X-ray/Auger electron emission from the sample provides information about the chemical composition at a specific site. This is based on knowledge of the X-ray emission spectra of specific elements. When an inner shell electron is ejected by the primary electron beam, the sample is said to exist in an excited state. Relaxation of the sample from this excited state to the ground state occurs when an outer shell electron falls down to the lower energy shell, which results in X-ray/Auger emission.

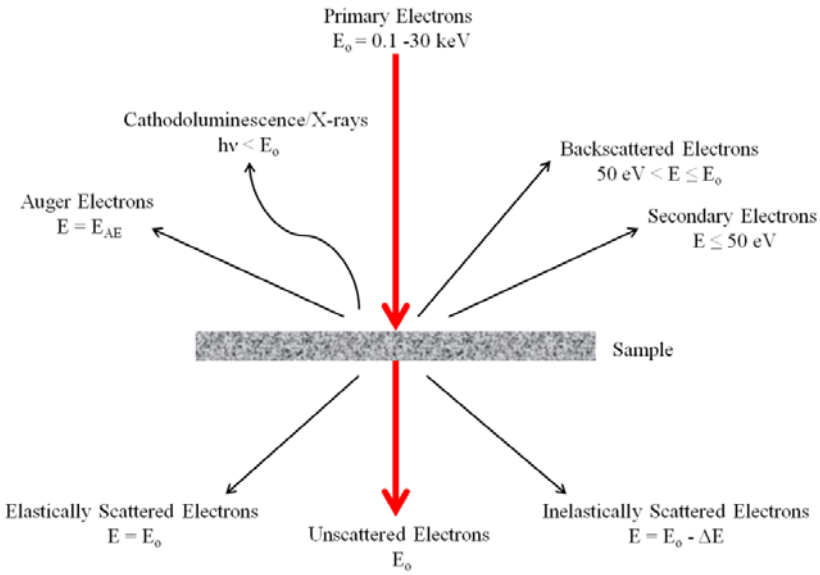

Figure 2-16 Signal scattering from a sample in SEM, where the energies of the scattered species are given relative to the primary beam. (Reproduced from reference 57.)

To obtain the SEM images reported herein, the material to be analysed was placed on a carbon tab that was fixed to a metal stub. A gold sputter coater was used to coat the samples prepared in this study, where the stubs holding the samples were sputter coated with a fine layer of a palladium-gold mixture in order to reduce the charging effects observed. The stub was then placed on the SEM sample stage inside the instrument chamber of either the Philips XL30 ESEM (Environmental Scanning Electron Microscope) or the Carl Zeiss Sigma Analytical SEM. The Philips XL30 ESEM was used to produce the majority of images in this work using a tungsten source (acceleration voltage = 25 kV) and a secondary electron detector. An Oxford Instruments X-act spectrometer comprising a silicon drift detector (SDD) was coupled to this microscope device for EDX analysis. By measuring the energy and quantity of the X-rays emitted from the sample, this technique allowed quantitative elemental analysis at specific points and over a user-defined region where elemental maps were generated to indicate element distribution throughout samples. The INCA® EDX analysis software was used to calibrate the instrument (Cu was used for all calibration measurements), designate analysis loci and define measurement conditions. For higher resolution images and backscattering analysis, the Carl Zeiss Sigma Analytical SEM was employed which uses a Schottky thermal field emitter source (acceleration voltage = 10 kV) and either the secondary or backscattered electron detectors. All SEM images were collected under a vacuum at a working distance of 8-10 mm. Owing to the procedure required for preparation of the samples, there was a small time window in which oxidation of air-sensitive materials may have occurred. Preparatory procedures were conducted as quickly as possible to keep air exposure to an absolute minimum.

2.3.5. Thermal Analysis

Thermal analysis is a powerful technique which has been adapted and developed over many decades to provide important information about the thermal processes which occur as a sample is heated. This analytical tool is essential for materials science research and an historical overview of the approaches used has been summarised by Ozawa.[58] Using Hess's law of summation it is possible to ascertain the enthalpy changes involved in a particular reaction. Followed by application of the Gibbs equation, the thermodynamic feasibility of the transformation from reactants to products can be established. Equation 2-33 shows the mathematical expression of Hess's law to determine the enthalpy change in a reaction, where *n* and *m* are the coefficients given in the balanced chemical equation and ΔH_f indicates that the enthalpy of formation for the components used in Equation 2-33. (By substituting *H* for *S* in this equation, it is also possible to establish the entropy change for a given reaction.)

Equation 2-33

$$\Delta H° = \sum n\,\Delta H_f^{\circ}(products) - \sum m\,\Delta H_f^{\circ}(reactants)$$

If enthalpy and entropy changes for a reaction are known, as suggested earlier, the Gibbs equation, shown below, can be used to establish the thermodynamics for that reaction:

Equation 2-34

$$\Delta G° = \Delta H° - T\Delta S°$$

If $\Delta G°$ is a large positive value then the reaction is denoted non-spontaneous under standard conditions approaching equilibrium. When $\Delta G°$ is a large negative value then the reaction will occur spontaneously under standard conditions and almost complete transformation to products is achieved at equilibrium. With $\Delta G°$ values close to zero, a mixture of products and reactants is obtained, *i.e.*, an equilibrium mixture. The thermodynamic parameters of some of the systems studied in this work were also predicted using the FACTWeb software.[59]

Preliminary experimental investigation of the thermal properties of samples was conducted using a bench furnace (see preparatory methods section) under a flow of $Ar_{(g)}$. This was required before using more sensitive analytical equipment in order to avoid the possibility of instrument damage. Particular vigilance in understanding the heating characteristics of the metathesis reaction systems was required as these are known to occur violently and spontaneously upon gentle mixing/heating.[60]

2.3.5.1. Simultaneous Thermal Analysis (STA)

STA comprises two analyses; differential thermal analysis-thermogravimetry (DTA-TG). Mass spectrometry (MS) can be coupled to this set-up in order to conduct evolved gas analysis (EGA) simultaneously. STA involves heating a fixed mass of sample to establish the enthalpy quantitatively (DTA) whilst simultaneously monitoring mass changes (TG). The mass changes observed may be correlated to data collected by the coupled MS device, which detects chemical species evolved from the sample throughout the heating programme. This technique may determine whether a chemical reaction or a phase change takes place or if intermediate phases are present upon heating of samples, which is important for establishing decomposition and reaction mechanisms. A Netzsch STA 409 coupled to a Hiden Analytical HPR20 mass spectrometer was employed in this work.

Differential thermal analysis involves heating two crucibles under the same conditions, where one of the crucibles contains the sample to be analysed (the sample crucible) and the other is empty (the reference crucible) and these are represented in Figure 2-17.

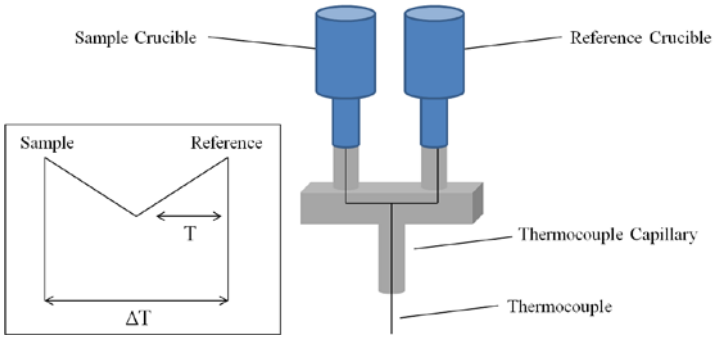

Figure 2-17 Diagram of Simultaneous Thermal Analysis crucible arrangement and principle behind the temperature difference being measured. (Modified from Netzsch STA 409 user information.[61])

The difference in temperature between the two crucibles is measured using sensitive thermocouples housed in an alumina capillary. The crucibles used in this work were also alumina, as these were suitable for the temperature ranges and materials being used. The alumina crucibles were re-used after cleaning; an initial *Aqua Regia* wash followed by calcination at 1200 °C for a minimum of 6 h ensured all residues from previous analyses had been removed.

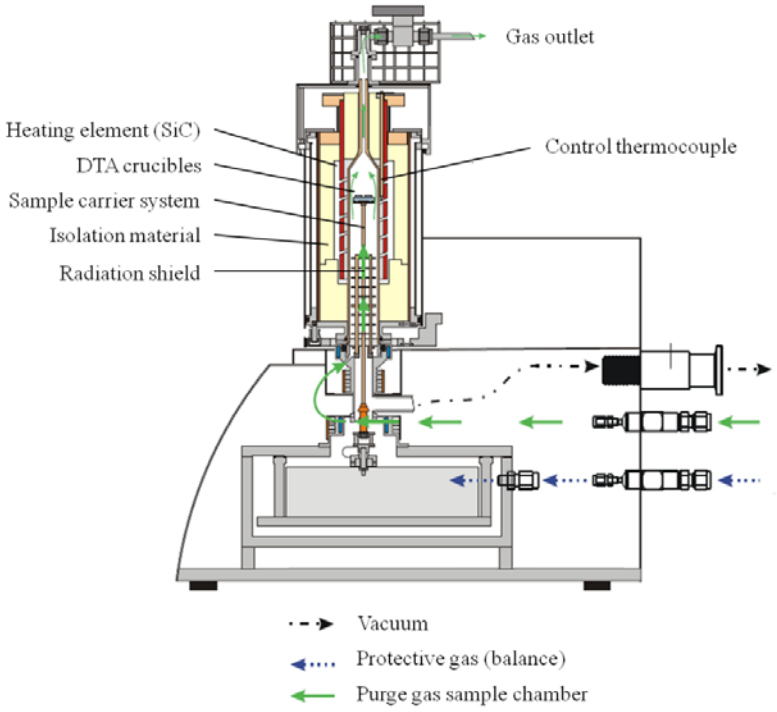

Figure 2-18 Schematic of the STA instrument employed in this work, indicating the main components of the analyser. (Modified from Netzsch STA 409 user information.)

The STA chamber configuration is given in Figure 2-18. All samples in this study were analysed under an anhydrous $Ar_{(g)}$ purge gas at a flow rate of 60 ml/min, however it should be noted that a real hydrogen fuel cell system operating environment will be $H_{2(g)}$. Many other hydrogen storage studies conduct thermal analyses under an anhydrous inert gas environment, *e.g.*, $Ar_{(g)}$ or $N_{2(g)}$, since these are inexpensive and typically employed in instruments configured for general use. The use of $H_{2(g)}$ as the purge gas would introduce a significant cost to the analysis since high purity anhydrous $H_{2(g)}$ would be required and this is significantly more expensive than the anhydrous inert gases. Furthermore, for MS coupled instruments such as that used in this work, the MS signals resulting from $H_{2(g)}$ release from the sample will be distinct from the inert purge gas and small $H_{2(g)}$ releases will not be masked by the purge gas, which could occur if a $H_{2(g)}$ purge gas was employed. The mass of sample used was dependent upon the total quantity of synthesised sample available but was usually between 30-40 mg. The majority of materials were analysed at a heating rate of 5 °C/min to obtain a simple thermal profile prior to more developed thermal analysis, where necessary. Thermal analysis data quoted in this work were derived from plots of the STA data using the Netszch Proteus® software. Quantitative data were determined from the analysis of samples prepared in this work, primarily to determine the enthalpy of decomposition (E_{dec}) for a particular thermal event. This required calibration of the STA instrument using recommended calibration standards which covered the total

temperature range over which the materials in this work were analysed; indium, bismuth, potassium perchlorate, zinc, potassium chromate and barium carbonate. Each standard (30 mg) was heated to above its melting point three times (with appropriate cooling between melting point measurements), and the peak temperature and peak area determined from the DTA trace for each melting point measurement. The peak temperature (T_m) for a specific event, *i.e.*, the absolute temperature at the maximum desorption rate for an endothermic/exothermic process was determined from the DTA plot using the peak evaluation function in the Proteus® software. Similarly, the onset temperatures (T_{onset}) and peak areas were determined using the onset and area functions in the software, respectively. The first derivative of the DTA trace was used to evaluate the rate of change for each event, and allowed accurate definition of the peak intervals, which was particularly important for evaluation of the peak areas. From this data, compilation of temperature and sensitivity calibration files was possible. A calcium oxalate standard was used to verify the calibration files, where the melting point, onset temperatures and mass losses associated with the three thermal events associated with its decomposition were verified with literature values. After verification, the calibration files were used in each measurement, and by measuring the peak area of a thermal event (given by the software in J/g) for a sample, the enthalpy associated with that event could be estimated quantitatively.

Beyond basic onset, peak and enthalpy evaluations of the thermal events occurring in a sample, advanced analysis allowed determination of the activation enthalpy of specific events. Data were collected using a range of heating rates (β); 2, 5, 10 and 20 °C/min, in order to compile Kissinger and Ozawa plots. These allowed the activation energy (E_a) for hydrogen desorption processes in specific samples to be determined.[62, 63] For Kissinger plots, the following mathematical expression was applied:

Equation 2-35

$$\ln(\beta/T_m^2) = -E_a/RT$$

Where, $R = 8.314\, J\, K^{-1} mol^{-1}$ and is commonly known as the gas constant. By plotting the left hand side of this equation on the y-axis against $1/T_m$ on the x-axis a straight line was obtained. The equation of the line (given by the line of best fit function in Excel, Equation 2-36) was used to derive a value for E_a from the gradient. In Equation 2-36, $\hat{y}$ represents the modelled linear plot, m is the gradient and c is the intercept:

Equation 2-36

$$\hat{y} = mx + c$$

Equation 2-37

$$m = -E_a/R$$

For comparison and verification purposes, the Ozawa method was also employed, where plots of log(β) *vs.* $1/T_m$ were compiled and the equation of the straight line for the data determined using the line of best fit function in Excel.[64, 65] The activation enthalpy, E_a, was determined from the gradient (m) and gas constant (R) using Equation 2-38.

Equation 2-38

$$E_a = \frac{mR}{-0.4567}$$

The TG plots revealed the change in mass observed over the duration of the heating program. The first derivative was employed to obtain the T_{onset} and comparisons were made with the MS data to verify the time-temperature relationship.

MS allowed determination of the species evolved during an STA experiment. In the MASsoft Pro control software, either a Faraday cup or a secondary electron multiplier detector was selected for use in this work.[66] These capture information for specific mass-to-charge (m/z) ratios, or scan for a range of m/z (instrumental range: 0-200 amu), respectively. Inside the Faraday cup detector, the ion beam from the sample strikes the walls of the metal "cup" (Figure 2-19 a).[67] The ions are neutralized by acquiring or donating electrons from the wall of the cup, which results in a current. The current is then amplified and detected to provide information regarding the abundance of specific ions.

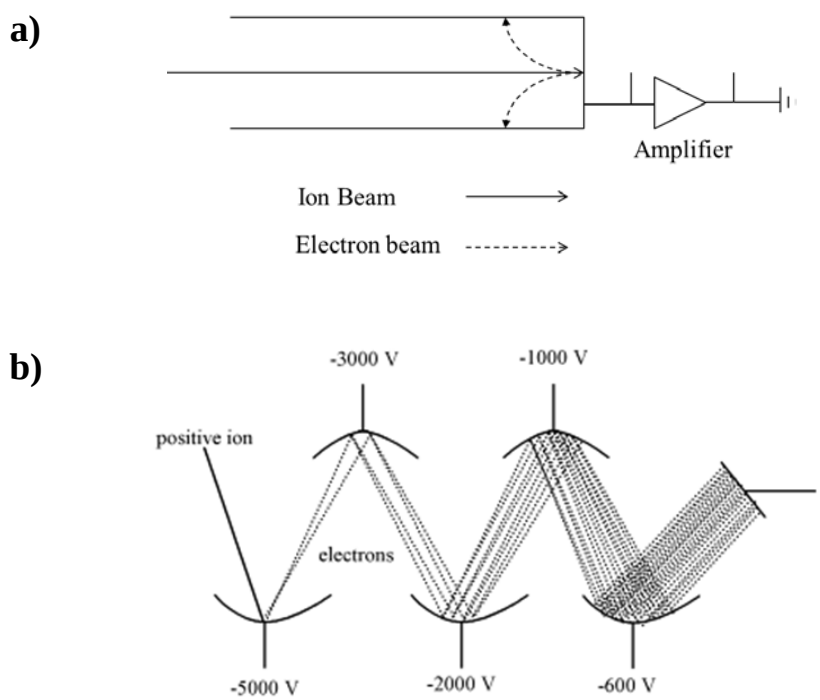

Figure 2-19 a) Faraday Cup detector and b) secondary electron multiplier (SEM) detector used in this work. (Reproduced from reference 67)

In the electron multiplier detector, a high voltage "conversion dynode" converts the incoming ion signal to secondary particles by application of a voltage to the accelerated ion beam (Figure 2-19 b). The secondary particles will be a mixture of electrons, positive/negative ions or neutral species. Another dynode then converts these secondary particles to electrons, which are amplified and a cascade of electrons are directed along the electron multiplier to form a current. This current is then detected and an appropriate *m/z* signal relative to the input ion beam can be produced.

From the MASsoft Pro software, MS data could be viewed and extracted in an XY format (X= time, Y = Torr) for re-plotting in Microsoft Excel 2007.

2.4. Errors & Statistical Analysis

For data in which linear trends were determined the linear trendline function of Excel was applied. This gave a linear trendline that was modelled against the input data and plotted on the graph. This function provided the equation of the line of best fit in the form of Equation 2-36.

The coefficient of determination for the linear model, R^2, which describes how well the linear model fits the data, can also be displayed using the linear trendline function. Further statistical analysis for the linear fit was determined using the LINEST function of Excel.[68] This function carries out a least squares calculation based on the input data for the linear trend to establish a number of statistical parameters for the linear regression.

The gradient (m) and its associated standard deviation (s_m) are provided for the linear model *via* Equation 2-39 and Equation 2-40, respectively. The x_i and $\bar{x}_i$ values are the x data and average x data respectively, and y_i represents the y data points.

Equation 2-39

$$m = \frac{n\sum_{i=1}^{n} x_i y_i - (\sum_{i=1}^{n} x_i)(\sum_{i=1}^{n} y_i)}{n\sum_{i=1}^{n} x_i^2 - \left(\sum_{i=1}^{n} x_i\right)^2}$$

Equation 2-40

$$s_m^2 = \frac{S_y^2}{\sum_{i=1}^{n}(x_i - \bar{x})^2}$$

The intercept (c) and its associated standard deviation (s_c) are given by Equation 2-41 and Equation 2-42, respectively.

Equation 2-41

$$c = \frac{(\sum_{i=1}^{n} x_i)^2(\sum_{i=1}^{n} y_i) - (\sum_{i=1}^{n} x_i\, y_i)(\sum_{i=1}^{n} x_i)}{n\sum_{i=1}^{n} x_i^2 - \left(\sum_{i=1}^{n} x_i\right)^2}$$

Equation 2-42

$$s_c^2 = \frac{S_y^2 \sum_{i=1}^{n} x_i^2}{n \sum_{i=1}^{n} (x_i - \bar{x})^2}$$

The S_y^2 value is the square root of the error on the *y* values and is determined in the LINEST function by Equation 2-43.

Equation 2-43

$$S_y^2 = \left(\frac{1}{n-2}\right) \sum_{i=1}^{n} (y_i - \hat{y})^2 = \frac{SS_E}{n-2}$$

The $\hat{y}_i$ value represents the linear model for the *y* data points. The S_y^2 value is used for the vertical error bars, assuming the *x* values are fixed. SS_E is another value which can be used to describe the goodness of fit, where a good fit is described by an SS_E value close to zero, and is determined from Equation 2-44.

Equation 2-44

$$SS_E = \sum_{i=1}^{n} (y_i - \hat{y}_i)^2$$

The SS_E value is incorporated in the determination of R^2, which is the statistical parameter quoted in this work to indicate the goodness of fit and is given by Equation 2-45. The R^2 value should be close to 1 to indicate a good fit.

Equation 2-45

$$R^2 = \frac{SS_T - SS_E}{SS_T}$$

The SS_T value in Equation 2.43 is determined from Equation 2-46, where $\bar{y}$ is the mean of the *y* data.

Equation 2-46

$$SS_T = \sum_{i=1}^{n} (y_i - \bar{y})^2$$

The error bar function of Excel was used to apply error bars to graphs given in this work. The error bars for a data set or for individual data points are given where appropriate.

2.5. Summary

This chapter has summarized the techniques and analytical methods employed throughout the research reported in this thesis. Relevant theoretical and technical information has been provided as appropriate, and reference to literature provided where further information may be found regarding the methods employed. Use of modern chemical apparatus has

enabled the progression of this work, and an in-depth practical understanding of the instruments used has been developed through this research.

---

[1] *Treatise on Solid State Chemistry: Volume 1 The Chemical Structure of Solids*, N. B. Hannay, Plenum Press, 1921
[2] *Saffron Scientific Equipment Ltd.*; http://www.saffron-uk.com
[3] *mBraun UK Ltd.*; http://www.mbraun.com; accessed 19/03/2014
[4] C. Suryanarayana, E. Ivanov and V. V. Bolyrev, *Materials Science and Engineering A-Structural Materials Properties*, 2001, **304-306**, 151
[5] Q. Zhang and F. Saito, *Advanced Powder Technology*, 2012, **23**, 523
[6] V. Šepelák and K.-D. Becker, *Journal of the Korean Ceramic Society*, 2012, **49**, 19
[7] C. Suryanarayana, *Progress in Materials Science*, 2001, **46**, 1
[8] "*Mechanochemistry in Nanoscience and Minerals Engineering*", P. Baláž, Springer-verlag, 2008
[9] "*Aristotelis Opera - Theophrasti De lapidibus*", 1495-1498
[10] W. B. Jensen, *Bulletin for the History of Chemistry*, 1991, **11**, 65
[11] L. Takacs, *Bulletin of the History of Chemistry*, 2003, **28**, 26
[12] "The Nobel Prize in Chemistry 1909". Nobelprize.org. Nobel Media AB 2013. Web. 11 Dec 2013. <http://www.nobelprize.org/nobel_prizes/chemistry/laureates/1909/>
[13] T. E. Fischer, *Annual Review of Material Science*, 1988, **18**, 303
[14] J. Huot, D. B. Ravinsbaek, J. Zhang, F. Cuevas, M. Latroche and T. R. Jensen, *Progress in Materials Science*, 2013, **58**, 30
[15] S. L. James, C. J. Adams, C. Bolm, D. Braga, P. Collier, T. Friscic, F. Gregioni, K. D. M. Harris, G. Hyett, W. Jones, A. Krebs, J. Mack, L. Maini, A. G. Orpen, I. P. Parkin, W. C. Shearouse, J. W. Steed and D. C. Wadell, *Chemical Society Reviews*, 2012, **41**, 413
[16] "*Environmental Chemistry: Green Chemistry and Pollutants in Ecosystems*", E. Lichtfouse, J. Schwarzbauer and D. Robert, Springer-verlag, 2005; M. Aresta, A. Dibenedetto, T. Pastore, Chapter 50, Part IV, pp 553-559
[17] I. Pri-Bar and B. R. James, *Journal of Molecular Catalysis A-Chemical*, 2007, **264**, 135
[18] J. F. Fernandez-Bertan, *Pure and Applied Chemistry*, 1999, **71**, 581
[19] W. Peukert, *International Journal of Mineral Processing*, 2004, **74S**, S3
[20] L. Tacaks, *Progress in Materials Science*, 2002, **47**, 355
[21] T. Friscic, H. Halasz, P. J. Beldon, A. M. Belenguer, F. Adams, S. A. J. Kimber, V. Honkimaki and R. E. Dinnebier, *Nature Chemistry*, 2013, **5**, 66
[22] A. Calka and A. P. Radlinski, *Materials Science and Engineering A-Structural Materials Properties*, 1991, **134**, 1350
[23] *Retsch*; http://www.retsch.com/products/milling/ball-mills/pm-100; accessed 19/03/2014
[24] "*General Chemistry*", D. D. Ebbing and S. D. Gammon, Houghton Mifflin Company, 2002
[25] "*Oxford Dictionary of Chemistry*", J. Daintith, Oxford University Press, 2008
[26] "*Crystal Structure Analysis; Principles and Practice*", Book Series 6, W. Clegg, A. J. Blake, R. O. Gould and P Main, Oxford University Press, 2006
[27] "*Solid State Chemistry; An introduction*", L. Smart and E. Moore,CRC Press Taylor & Francis Group LLC, 1995
[28] "*International Tables for X-Ray Crystallography*", N. F. M. Henry and K. Lonsdale, D. Reidel Pub. Co., 1976
[29] "*Crystal Structure Analysis for Chemists and Biologists*", J. P. Glusker, M. Lewis and M. Rossi, VCH Publishers Inc., 1994
[30] W. Paszkowicz, *Synchrotron Radiation in Natural Science*, 2006, **5**, 115
[31] W. H. Bragg, *Nature*, 1912, **90**, 219
[32] L. Bragg, *Nature*, 1912, **90**, 410
[33] W. H. Bragg, *Nature*, 1913, **91**, 477
[34] W. H. Bragg, *Nature*, 1914, **93**, 124
[35] L. Bragg, *Proceedings of the Royal Society A*, 1961, **262**, 145
[36] "*Atkins' Physical Chemistry*", P. Atkins and J. de Paula, Oxford University Press, 2002
[37] "*Structure Determination from Powder Diffraction Data*", IUCr Monographs on Crystallography, W. I. F. David, K. Shankland, L. B. McCusker and Ch. Berlocher, Oxford Science Publications, 2006
[38] "*Solid State Chemistry Techniques*", A. K. Cheetham and P. Day, Oxford Science Publications, 2001
[39] *National Synchrotron Radiation Research Centre*; http://www.nsrrc.org.tw/
[40] "*Neutrons and Synchrotron Radiation in Engineering Materials Science*", W. Reijmers, A. R. Pyzalla, A. Schreyer and H. Clemens, Wiley-VCH, 2008

[41] *HighScore Plus*; http://www.panalytical.com/Xray-diffraction-software/HighScore-Plus.htm; accessed 21/03/2014
[42] *Inorganic Crystal Structure Database (ICSD)*; http://icsd.cds.rsc.org/; accessed 21/03/2014
[43] "*X-ray diffraction procedures for polycrystalline and amorphous materials*", H. P. Klug and L.E. Alexander, J. Wiley & Sons, 1959 Edition
[44] J. I. Langford and A. J. C. Wilson, *Journal of Applied Crystallography*, 1978, **11**, 102
45 "*CELREF Unit-Cell Refinement Software on a Multiphase System*", J. Laugier and B. Bochu, Laboratoire des Materiaux et du Génie Physique de l'Ecole Supériore de Physique de Grenoble
46 *LMGP (Laboratoire des Materiaux et du Génie Physique de l'Ecole Supériore de Physique de Grenoble) program suite*; http://www.ccp14.ac.uk/ccp/web-mirrors/lmgp-laugier-bochu/
47 "*The Rietveld Method*", R. A. Young, IUCr Book Series 5, Oxford University Press, 1993
48 A. C. Larson and R. B. von Dreele, *The General Structure Analysis System*, Los Alamos National Laboratories, REPORT LAUR 086-748, LANL, Los Alamos, NM, 2000
49 B. H. Toby, *Journal of Applied Crystallography*, 2001, **34**, 210
[50] L. B. McCusker, R. B. Von Dreele, D. E. Cox, D. Louër and P. Scardi, *Journal of Applied Crystallography*, 1999, **32**, 36
51 G. Caglioti, A. Paoletti and F. P. Ricci, *Nuclear Instruments*, 1958, **3**, 223
52 "*Infrared and Raman Spectra of Inorganic and Coordination Compounds: Part A, Theory and Application in Inorganic Chemistry*", K. Nakamoto, J. Wiley & Sons, 2006
53 "*Molecular Symmetry and Group Theory*", A. Vincent, J. Wiley & Sons, 1983
54 "*Fundamentals of Fourier Transform Infrared Spectroscopy*", B. C. Smith, CRC Press LLC, 1996
55 "*Fourier Transform Infrared Spectrometry*", P. R. Griffiths and J. A. de Haseth, J. Wiley & Sons, 2007
56 "*Modern Raman Spectroscopy – A Practical Approach*", W. E. Smith and G. Dent, J. Wiley & Sons, 2005
57 "*Science of Microscopy*", P. W. Hawkes, J. C. H. Spence, Springer-verlag, 2007
58 T. Ozawa, *Thermochimica Acta*, 2000, **355**, 35
59 *Fact-Web suite of interactive programs*, C. W. Bale and E. Bélisle, www.factsage.com; accessed 14/05/2014
60 I. V. Parkin, *Chemical Society Reviews*, 1996, **25**, 199
61 Netzsch; http://www.netzsch-thermal-analysis.com/en/home.html; accessed 24/03/2014
62 H. E. Kissinger, *Journal of Research of the National Bureau of Standards*, 1956, **57**, 217
63 H. E. Kissinger, *Analytical Chemistry*, 1957, **29**, 1702
[64] T. Ozawa, *Bulletin of the Chemical Society of Japan*, 1965, **38**, 1881
[65] T. Ozawa, *Journal of Thermal Analysis and Calorimetry*, 1970, **2**, 301
[66] Hiden Analytical; http://www.hidenanalytical.com; accessed 02/07/2014
[67] "*Mass Spectrometry Principles and Applications*", E de Hoffman and V. Stroobant, J. Wiley & Sons, 2007
[68] "*Obtaining Uncertainty Measures on Slope and Intercept of a Least Squares Fit with Excel*", F. A. Morrison, CM3215 Fundamentals of Chemical Engineering Laboratory, Michigan Technological University, April 2014

3. Optimisation of MgH_2 Dehydrogenation properties by Milling with/without Non-Oxide Additives

3.1. Introduction

One of the main objectives for solid state hydrogen storage research is to produce systems which are compatible with fuel cell operating specifications. Magnesium hydride has been highlighted as a practical hydrogen storage material and is currently one of the most studied metal hydrides for this application (refer to Chapter 1). In this chapter the effect of milling conditions on the dehydrogenation properties of the as-received hydride will be studied. Then, non-oxide additives will be investigated to establish their impact on the hydrogen storage properties of MgH_2 in comparison to best performing composites in literature. First, the chemical and physical properties of the hydride will be described.

3.1.1. Structures of MgH_2 Polytypes

As a result of the drive for more commercially viable hydrogen storage systems, a more detailed chemical profile of the MgH_2 system has emerged beyond the practicalities of hydrogen storage. Many studies have been concerned with the structural modifications of MgH_2. From ambient conditions to the effects of high pressure and high temperature, this work has enabled a better understanding of the potential phase transitions involved in the synthesis and decomposition of this important hydride. A summary of known MgH_2 phases is given in Table 3-1. (It is important to note the discrepancies in the nomenclature of the MgH_2 hydride phases, and Table 3-1 describes the phases according to the prefixes used in the majority of MgH_2 literature. Furthermore, subtle variations are observed in the structural parameters between publications on MgH_2, which will be discussed in the following sections on each phase.) Using density functional modelling (total energy calculations), the phase transitions have been determined to occur in the order: $\alpha \rightarrow \gamma \rightarrow \beta \rightarrow \delta \rightarrow \varepsilon$, at 0.39 GPa, 3.84 GPa, 6.73 GPa and 10.26 GPa respectively.[1, 2] Later theoretical work using a variation of the density functional method (plane-wave pseudopotential method), determined the $\alpha \rightarrow \gamma \rightarrow \beta \rightarrow \varepsilon$ transitions to occur at higher pressures of 1.2 GPa, 9.7 GPa, 17.1 GPa respectively, with δ-MgH_2 being unstable at high pressure.[3] Experimental work using synchrotron XRD (X-ray Diffraction) showed that the following transformations took place: $\alpha \rightarrow \gamma \rightarrow \delta \rightarrow \varepsilon$, at 0.9 GPa, 9 GPa and 17 GPa, respectively, which corresponds relatively closely to the theoretical work of Cui *et al.* [4]

Table 3-1 Experimentally determined polymorphs of MgH_2; blue and red spheres represent Mg and H atoms, respectively.

Phase Prefix	Structure Type	Space Group	Unit Cell	Synthesis Conditions
Alpha (α)	Tetragonal, Rutile-type TiO_2	*P4/mnm*	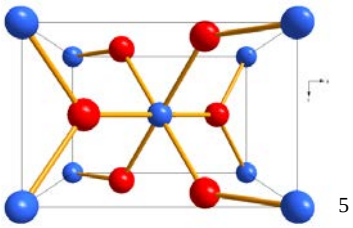 5	Mg under 20 MPa $H_{2(g)}$ at 730 K, 6 days.[4]
Beta (β)	Hexagonal (pseudocubic) modified CaF_2	$Pa\bar{3}$	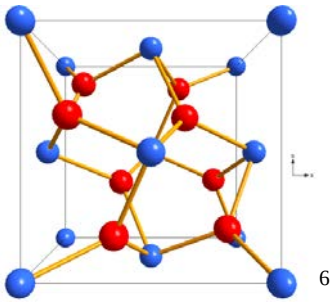 6	8 GPa, 800 °C for 1 h.[7]
Delta (δ)	Orthorhombic	Pbc_21	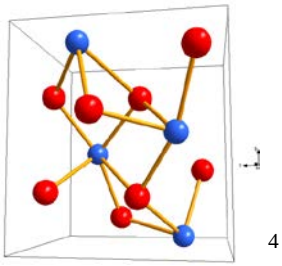 4	13.9 GPa, RT.
Gamma (γ) (mixture with α)	Orthorhombic α-PbO_2	*Pbcn*	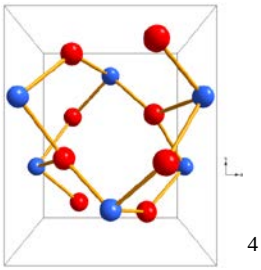 4	2.5 GPa, 250 °C.[7]
Epsilon (ε)	Orthorhombic Cotunnite/$AlAu_2$	*Pnma*	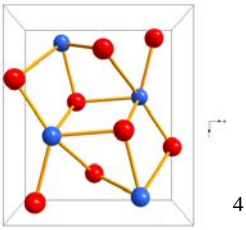 4	21.9 GPa, RT.

3.1.1.1. Alpha (α) Phase MgH_2

The rutile-type MgH_2 structure was first described by Ellinger and colleagues in the mid-1950s, and later confirmed by neutron diffraction (Table 3-2).[5, 8] Some literature now describes this as the alpha (α) phase [1, 3, 9], although other publications use the nomenclature from the Mg-H phase diagram given by San-Martin and Manchester.[10] For example,

publications describing the properties of β-MgH_2 exist where the hydride phase being described is that of tetragonal rutile-type MgH_2.[11, 12, 13] For purposes of clarity in this work, alpha (α) MgH_2 refers to the tetragonal rutile-type polymorph, which is stable at standard pressure and temperature conditions.

Table 3-2 Comparison of lattice parameters quoted for α-MgH_2.

Publication	Space Group	*a* / Å	*c* / Å
Ellinger *et al.*[5*]	*P*4/*mnm*	4.516(8)	3.020(5)
Bortz *et al.*[14*]		4.501(1)	3.0100(1)
Vajeeston *et al.*[1a]	*P*4$_2$/*mnm*	4.4853	2.9993
Vajeeston *et al.*[2*]		4.5176	3.0206
Morikawa *et al.*[4*]		4.5147(1)	3.0193(2)
Cui *et al.*[3a]		4.514	2.992
Er *et al.*[6a]		4.494	3.005

N.B. ESD (estimated standard deviation) values indicated in parenthesis where available. [a] Theoretical values. [*] Experimental values.

3.1.1.2. Beta (β) Phase MgH_2

The distorted CaF_2 structure of β-MgH_2 was proposed in 1980 by Bastide *et al.* who described this as a hexagonal (pseudocubic) phase with Mg having an eight coordination environment.[7] The β-MgH_2 was first observed at 4 GPa at 650 ^{o}C as a mixture with α-MgH_2, although Bastide found it as an isolated phase by applying harsher conditions; 800 °C, 8 GPa for 1 h. Later work by Vajeeston *et al.* indicated that the β-phase may be formed from the γ-phase at 3.84 GPa, and exists as a purely cubic phase.[2] A similar structure solution was also suggested in the theoretical work of Er *et al*. (Table 3-3).[6] Bastide *et al.* described the density of the fluorite-type β-phase to be 25 % greater than the α-phase. They also studied the thermal decomposition behaviour of the β-phase. This showed an endothermic decomposition profile comparable with the α-phase, although the decomposition onset temperature was 10-20 °C higher. An additional endothermic event occurring between 350 °C and 400 °C was observed, which suggests either the transition from β→α or β→γ according to Bastide and colleagues. They also recorded the thermal decomposition of the β-phase under vacuum (1 Pa), which again revealed a similar decomposition profile to α-MgH_2, where decomposition occurred at ~330 °C.

Table 3-3 Comparison of lattice parameters quoted for β-MgH_2.

Publication	Space Group	*a* / Å	*c* / Å
Bastide *et al.*[7*]	-	4.53	10.99
Vajeeston *et al.*[2*]	$Pa\bar{3}$	4.6655	-
Er *et al.*[6a]	$Pa\bar{3}$	4.796	-

[a] Theoretical values. [*] Experimental values.

3.1.1.3. Delta (δ) MgH_2

This is an unstable phase which has been experimentally determined by Moriwaki *et al.* and Vajeeston *et al.* by synchrotron XRD (Table 3-4).[2, 4] Phase transitions to the orthorhombic δ polytype have also been studied readily by theoretical chemistry methods.[1, 3] The transition from β→δ was proposed to occur at 6.73 GPa by Vajeeston *et al.*, with a decrease in unit cell volume of 1.1 $Å^3$/f.u relative to the β-phase. In both the works by Vajeeston *et al.* and Moriwaki *et al.*, two possible crystal structure solutions were compared for the high pressure phase; *Pbca* and Pbc_21. From the structure refinement work by Moriwaki, they concluded that the orthorhombic Pbc_21 space group, with a smaller cell (Z = 4), was most appropriate and was supported by the absence of superstructure reflections. However, Vajeeston *et al.* suggest that two distinct Pbc_21 and *Pbca* structures exist based on their experimental and theoretical work, which are denoted δ and δ', respectively. The latter is a metastable $AuSn_2$-type phase (Figure 3-1). The emergence of the δ' phase appears to be influenced by the pressure sequence used in the experimental method and the calculations by Vajeeston *et al.* suggest that these two polymorphs are energetically very similar.

Table 3-4 Comparison of lattice parameters quoted for δ-MgH_2 and δ'-MgH_2.

Phase	Publication	Space Group	*a* / Å	*b* / Å	*c* / Å
δ	Moriwaki *et al.*[4*]	Pbc_21	4.3966(11)	4.6965(7)	4.4118(13)
	Moriwaki *et al.*[4*]	*Pbca*	8.7739(19)	4.6927(7)	4.4097(10)
	Vajeeston *et al.*[1a]	Pbc_21	4.8604	4.6354	4.7511
	Vajeeston *et al.*[1a]	*Pbca*	9.3738	4.8259	4.7798
δ'	Vajeeston *et al.*[2*]	*Pbca*	8.8069	4.6838	4.3699
	Vajeeston *et al.*[2a]	*Pbca*	8.9476	4.6065	4.5625

[a] Theoretical values. [*] Experimental values.

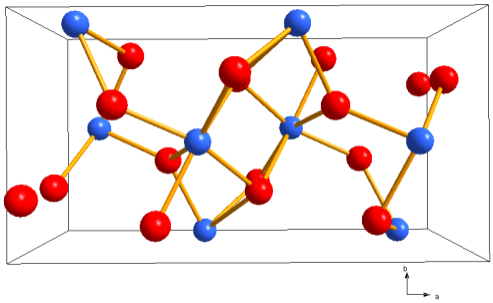

Figure 3-1 ***Pbca*** **structure of metastable δ'-MgH_2 phase observed above 10 GPa; blue and red spheres represent Mg and H, respectively.**[2]

3.1.1.4. Gamma (γ) Phase MgH_2

γ-MgH_2 is a high pressure MgH_2 phase which is obtained by conversion of α-MgH_2 at high pressure and temperature, although work has revealed that it may be obtained at high pressures alone. Once formed, it is stable at standard temperature and pressure conditions and has received significant interest after its initial identification by Bastide and colleagues (Table 3-5).[7, 14, 15] The γ-phase is orthorhombic with an α-PbO_2 structure (*Pbcn*) in which the Mg is in a six coordination environment. The lattice parameters have been determined in a number of different studies although no study has revealed a single phase sample for a more accurate determination of its structural parameters. More recent work has shown its synthesis by mechanochemical methods and by solution chemistry, but never as a solitary phase (Figure 3-2).[16, 17] Huot showed that after 20 h of milling, the resultant product comprised 18 % γ-MgH_2.

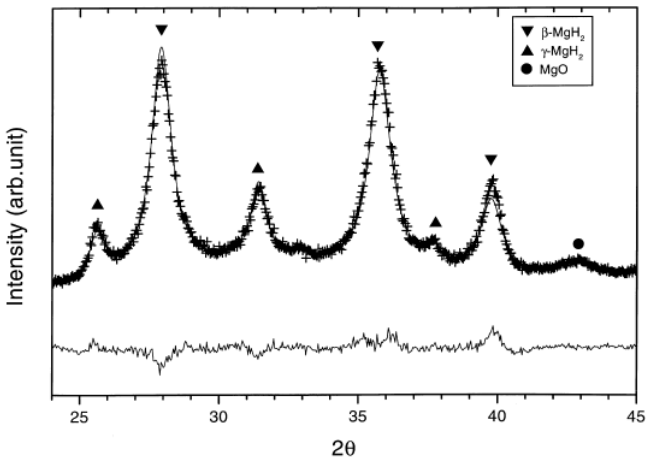

Figure 3-2 **α- and γ-MgH_2 synthesised by reactive milling of Mg under 2 bar H_2. (Note: β-MgH_2 in the figure refers to rutile-type MgH_2, denoted α-MgH_2 in this work.)**[16]

A study has also shown the γ-phase to arise from hydrogenation of Pd-capped Mg thin films at a relatively low temperature of 250 ^{o}C under 2 bar H_2 pressure for 12 h.[18]

Furthermore, Gutam *et al.* observed γ-MgH_2 by annealing α-MgH_2 at 250°C for 1 h under a mild vacuum. The γ-phase, however, has not yet been isolated from the α-phase.

Table 3-5 Comparison of lattice parameters quoted for γ-MgH_2.

Publication	Space Group	a / Å	b / Å	c / Å
Vajeeston *et al.*[1a]	*Pbcn*	4.5246	5.4442	4.9285
M. Bortz *et al.*[14*]		4.5213(3)	5.4382(3)	4.9337(3)
Moriwaki *et al.*[4*]		4.5139(5)	5.4391(6)	4.9406(5)
Shao *et al.*[17*]		4.5226(24)	5.4328(30)	4.9403(26)

[a] Theoretical values. [*] Experimental values.

3.1.1.5. Epsilon (ε) MgH_2

The Cotunnite-type ε-MgH_2 polymorph has been little studied by comparison to the other modifications (Table 3-6).[1, 3] Calculations be Vajeeston *et al.* suggest that it forms in a $AlAu_2$-type structure from the δ phase, stabilising at 10.26 GPa, with an equilibrium volume 19.5% smaller than that of the α-polymorph which is important for the volumetric considerations for use of MgH_2 in a hydrogen storage system. The transition pressure calculated in the work of Cui *et al.*, however, suggests a β→ε transition which occurs at a significantly greater pressure of 17.1 GPa, and the disparity between these results is likely to be a consequence of the different mathematical models chosen by the respective authors. Moriwaki *et al.* determined a Cotunnite CaH_2-type structure for ε-MgH_2 from SXD data collected at 21.9 GPa.[4]

Table 3-6 Comparison of lattice parameters quoted for ε-MgH_2.

Publication	Space Group	a / Å	b / Å	c / Å
Moriwaki *et al.*[4*]	*Pnma*	4.9536(11)	2.9453(5)	5.6677(11)
Vajeeston *et al.*[1a]		5.2804	3.0928	5.9903

[a] Theoretical values. [*] Experimental values.

3.1.2. Spectroscopic Properties of Commercial MgH_2

The bonding modes of rutile structures have been studied and provide a platform from which data for α-MgH_2 are derived.[19] Furthermore, modern theoretical modelling methods and experimental spectroscopic studies have provided bonding and vibrational information for MgH_2 polytypes to complement diffraction data.[20, 21, 22, 23] Recent Raman data given by Kuzovnikov *et al.* for the α- and γ-MgH_2 phases match well to the previously published data, and an additional mode for the α-phase (B_{2g} phonon mode) has been assigned.[15, 24, 25,

[26] Raman spectra of the high pressure MgH_2 phases are also described by Moriwaki *et al.* using an *in-situ* diamond anvil cell for Raman analysis at high pressure, but the vibrational bonding modes were not assigned for these samples.[4] Their work did, however, corroborate the structure assignment of the ε-MgH_2 phase, by comparing the Raman spectra of CaH_2 and the high pressure ε-MgH_2 phase since these were predicted as having the same Cotunnite-type structure. Two bands associated with hydrogen vibrations in ε-MgH_2 at 1130 cm^{-1} and 1450 cm^{-1} were shifted to higher wavenumbers relative to the CaH_2 bands (740 cm^{-1}, 1000 cm^{-1}). This was attributed to the smaller volume (57 % smaller) of ε-MgH_2 with respect to CaH_2.

Vibrational spectra collected using inelastic neutron scattering spectroscopy have provided information to suggest that the enhanced sorption properties of milled MgH_2 are primarily due to reduction in crystallite size through the milling treatment.[27] Comparing experimentally measured vibrational spectra and those obtained from density functional modelling, Schimmel *et al.* showed that the vibrational spectra of bulk un-milled MgH_2 and desorbed-rehydrided ball milled MgH_2 were nearly identical. The loss of the defects and stresses induced in the milling process, which are evident from significantly distorted vibrational spectra observed for ball milled MgH_2, were attributed to annealing of the samples during cycling. Since the same kinetic and thermodynamic behaviour of the milled samples was observed upon cycling, the lack of complementary milling effects (stresses/defects) on the rehydrided sample studied by Schimmel *et al.* indicated that the reduction in particle size (relative to the bulk powder) was the reason for the enhanced properties of the hydride rather than the complementary effects from milling. A more recent microstructure study by Paik *et al.* showed similar results for the reduction in stress upon milling using SEM and TEM. [28]

3.1.3. Thermal Behaviour of Commercial MgH_2

The thermal desorption properties and mechanisms of commercial MgH_2 have been studied extensively, using a variety of different models and analytical methods. The thermal stability of MgH_2, as mentioned earlier, is one of the main characteristics that researchers are striving to understand and modify.[29] Significantly reducing the enthalpy of decomposition of MgH_2 would improve the applicability of this hydride for implementation in mobile hydrogen storage systems. Thus, understanding the thermodynamic properties of MgH_2 is critical in establishing how the enthalpy of decomposition may be reduced. The hydride typically decomposes > 400 °C *via* a single endothermic event associated with the release of hydrogen. (Decomposition of the

commercial MgH_2 used in this work has been conducted using STA and will be described later in this chapter.) A summary of de-stabilisation methods used for improving the thermal behaviour of MgH_2 will now be described, including the effects of milling, nanoscaling and additives.

The decomposition of milled MgH_2 has been studied extensively, where the reduction in particle size and hence larger surface area of the particles has the effect of reducing hydrogen diffusion pathways. Huot *et al.* showed the development of two endothermic events in milled MgH_2 using DSC under 2 bar H_2. The emergence of two peaks in the DSC trace was attributed to the formation of the high pressure γ-phase during milling, and Huot *et al.* considered this to be a two-step decomposition process.[16, 30] The first desorption peak was proposed as the decomposition of the mixture of the high pressure (γ) and rutile (α) phases, while the second peak was attributed solely to the decomposition of the rutile phase:

Equation 3-1

$$\gamma\text{-}MgH_2 + \alpha\text{-}MgH_2 \rightarrow \alpha\text{-}MgH_2 \rightarrow Mg$$

The two-step decomposition was studied further using MgH_2 prepared by the reactive milling of Mg metal under 0.5 MPa H_2 to form a mixture of the γ- and α-phases as with milling under inert gas (Figure 3-3).[31] This work revealed that the γ-MgH_2 phase was no longer present after heating to 390 ^{o}C. It was then suggested that the γ-MgH_2 phase enhanced the decomposition of the α-MgH_2 phase by inducing stress on the latter as a result of volume contraction upon decomposition of the γ-phase. This concept was disputed after cycling experiments showed only rutile-type α-MgH_2 after re-hydrogenation, with the thermal decomposition profile of the re-hydrogenated material being consistent with that expected for α-MgH_2, *i.e.*, a single endothermic event at 414 °C.[32]

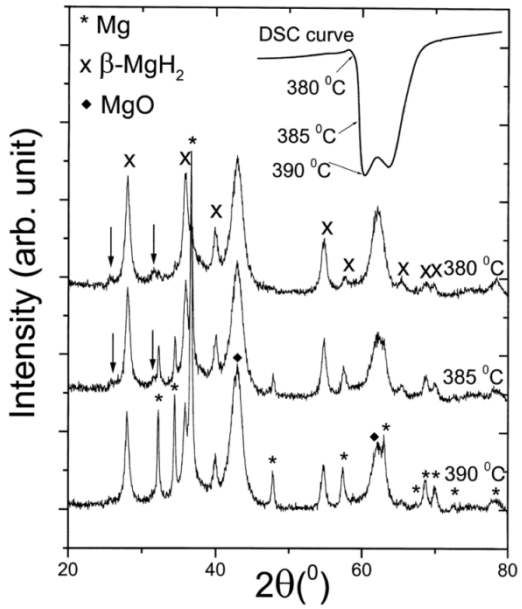

Figure 3-3 DSC profile of MgH_2 synthesised by reactive milling showing a two-step endothermic decomposition, and PXD of the decomposition products at 380 °C, 385 °C and 390 °C (γ-phase indicated by arrows). [31]

Another theory is evident from the literature which suggests that MgO may play a role in the decomposition pathway.[33] Varin and colleagues proposed that partial oxidation of the sample hindered the release of hydrogen from some of the material, *i.e.*, the smallest particles, and so hydrogen was released from non-oxidised product and then from the oxidised sample at a higher temperature. However, depending on the milling conditions applied, their work also supported the possibility of the two decomposition peaks being a result of the γ-MgH_2→α-MgH_2→Mg pathway. Further investigation by the same authors thwarted the hypothesis of MgO inhibition, where their DSC work was not consistent with the desorption behaviour expected if this were the case.[34] If the oxide inhibition on the smallest particles was the cause of the high temperature (HT) peak and cracking/permeation of the oxide layer was required before hydrogen release from these particles, then the HT peak would be expected to be at a reasonably low temperature since the hydride particles would be smaller than the coarse, bulk particles of commercial α-MgH_2. This was inconsistent with their observations from DSC, where the HT peak was at a temperature consistent with bulk hydride irrespective of milling conditions. Therefore, Varin *et al.* concluded that the oxide inhibition hypothesis was implausible. The possibility of particle size effects alone as the root cause of the two-step decomposition observed by DSC was also ruled out. Varin *et al.* proposed that a synergistic hydride phase-particle size effect may be occurring, and thus suggested that the smaller particles could be predominantly γ–MgH_2, which was previously proposed as having a lower decomposition

temperature than rutile α-MgH_2 by Gennari *et al.*[31] The DTA peaks were shown to be more disparate when samples were subject to cryomilling for 8 h then subsequent milling for 60 h under ambient conditions (Table 3-7).[35]

Table 3-7 Summary of milled Mg-MgH_2 studies showing DSC/DTA doublet.

Source	Milling Conditions	LT peak / °C	HT peak / °C
Huot[30]	Milled MgH_2, ≥20 h, 10:1 b:p	365.9	383.2
Gennari[31]	MgH_2 prepared by reactive milling of Mg under H_2 ≥100 h, 44:1 b:p	(Peak temperatures not provided)	
Huang[32]	Milled MgH_2; 48 h under H_2 (b:p omitted)	364	405
Varin[33]	MgH_2 prepared by reactive milling of Mg under H_2[36, 37, 38]	354	382
Zhuo[39]	MgH_2 prepared by reactive milling of 70:30 wt% Mg:$C_{graphite}$ (under 1 MPa H_2); 30:1 b:p		
	a) 3 h	344.2	-
	b) 5 h	301.3	340.3
	c) 20 h	286.2	340.3
Aguey-Zinsou	a) Milled MgH_2, 100 h, 10:1 b:p[40]	336	352
	b) Commercial MgH_2 milled 200 h, 10:1 b:p[41]	323	354
Tian	a) 8 h cryomilled MgH_2, 10:1 b:p[35]	365	~400
	b) 8 h cryomilled MgH_2, 10:1 b:p followed by 60 h milling in $Ar_{(g)}$[42]	365	~410-420

Cabo *et al.* observed the α- and γ-MgH_2 polymorphs after milling the hydride with Ni and Co oxide catalysts. A two-step decomposition process was determined from the DTA traces collected for the as-prepared oxide catalysed MgH_2. They described the low temperature (LT) and HT decomposition events to be the result of the α- and γ-MgH_2 phases, respectively. Cabo *et al.* explained that the modification of the two-step decomposition of the hydride was the result of the α-MgH_2 phase being influenced by the catalyst.[43] Relative to the as-milled sample (Figure 3-4), the second, HT peak in the DTA

profiles of the doped samples becomes more prominent, and the difference in the T_{peak} of the DTA curves becomes less disparate, with almost complete merging of the peaks for the NiO doped sample and the lowest T_{peak} for desorption.

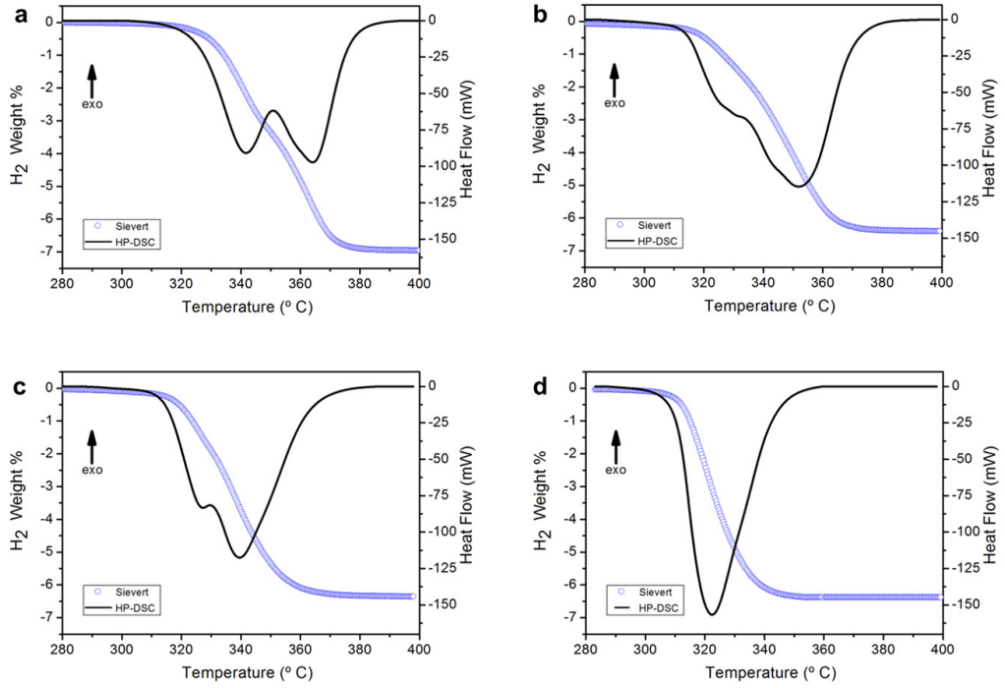

Figure 3-4 DTA of a) milled MgH_2, b) Co_3O_4-doped, c) $NiCo_2O_4$-doped and d) NiO-doped MgH_2 samples.[43]

Non-saturated magnesium hydride, *i.e.*, $MgH_{2-\delta}$, has been studied. The $MgH_{2-\delta}$ phase ($MgH_{1.2}$) was first proposed as a new phase by Schimmel and colleagues using *in-situ* neutron diffraction for Nb catalysed MgH_2.[44] They described the sub-stoichiometric phase as a facilitator for hydrogen sorption due to vacancies in the structure. Later, a study by Borgschulte *et al.* investigated the impact of catalytic quantities of Nb_2O_5 on the emergence of the destabilised, sub-stoichiometric hydride (Figure 3-5).[45] Their work alluded to a special interaction of the sub-stoichiometric $MgH_{2-\delta}$ phase with the oxide catalyst, leading to faster sorption kinetics. Figure 3-5, reproduced from reference 45, describes the effects observed upon cycling of the ball milled oxide catalysed MgH_2;

i) Ball milling of MgH_2 and oxide catalyst where the initial particle size of the hydride and catalyst are large, with the catalyst being relative non-disperse.

ii) Small particles of MgH_2 are produced by milling, where the hydride has a higher surface area and a high dispersion of catalyst throughout the hydride

iii) Cycling of the catalysed hydride causes annealing of the particles which results in increased particle sizes. During cycling, the destabilised $MgH_{1.2}$ phase may

be described as a "shell" layer surrounding the bulk hydride, and forms as a result of interactions at the bulk hydride-catalyst interface.

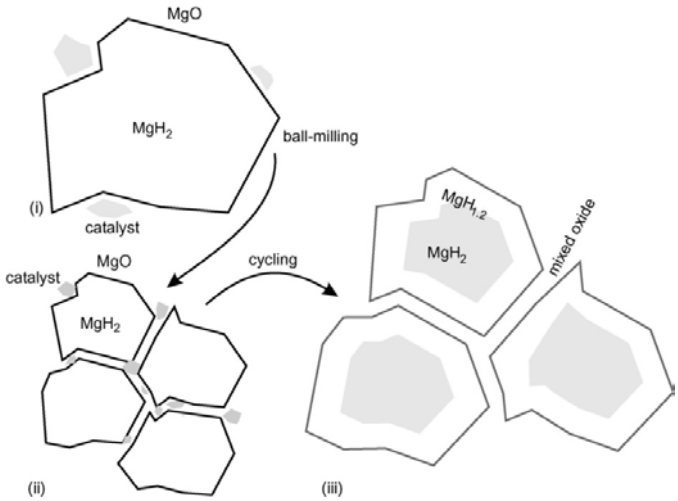

Figure 3-5 Suggested non-stoichiometric phases of MgH_2 and interactions with MgO as one possible solution to the two-step decomposition phenomenon.[45]

The scope of additives being investigated to enhance the Mg-H system has been rapidly expanding over decades, as highlighted in Chapter 1. This next section introduces some of the most prominent research in non-oxide additives for MgH_2 that are relevant to this work.

3.1.3.1. Carbon & Carbides

Carbon based additives have been studied extensively with MgH_2. The carbon structure and carbon pre-treatment methods used have a significant impact on the resultant hydrogen storage properties of the hydride.[46, 47] From activated carbon[48] to carbon nanotubes (CNTs)[49, 50] many novel concepts for enhancing the hydrogen storage properties of MgH_2 by incorporation of carbon materials have been described.[51] The work of Imamura *et al.* on MgH_2-graphite composites in the 1990s and into the 21st century led the way for the inclusion of catalytic amounts of graphite in the Mg-H system.[52, 53, 54, 55, 56, 57, 58] Most of these early studies involved milling magnesium metal and graphite with/without organic solvents, *e.g.*, THF, benzene, cyclohexane. Thereafter, graphitic carbon has received significant attention in this area of research, and is reflected in the breadth of literature available on the properties of MgH_2-graphite systems prepared by mechanical grinding and/or inclusion in pellet composites. [59, 60, 61, 62] The results of Sheng and Guo suggested that the dispersion of graphite influenced the dissociation of hydrogen at the Mg-MgH_2 surfaces. Additionally, they suggested that graphite on the surface of the material may inhibit the growth of MgO at the Mg/MgH_2 surfaces, which was reaffirmed in more recent

work using high pressure DSC.[63] Huang *et al.* studied MgH_2-5 wt% graphite composites prepared by milling and suggested that the presence of the γ-MgH_2 phase did not enhance the hydrogen desorption properties of the α-MgH_2 phase, based on their cycling studies.[64] Graphite is already used in stationary solid state hydrogen storage composites, including that of the solid state hydrogen storage commercial forerunner, McPhy Energy. [65, 66]

Multi component systems comprising carbon and one or more other additives have been used to tackle the thermodynamic and kinetic issues of MgH_2, where the benefits of incorporation of graphite and other carbons was studied by Bouaricha *et al*. [67, 68] A more recent example shows that milling a mixture of Nb_2O_5-graphite with Mg was shown to promote excellent thermodynamic properties for hydrogen cycling relative to un-doped and un-milled MgH_2.[69] Furthermore, relative to earlier work using mixtures prepared by 20 h milling of 0.5 mol% Nb_2O_5-MgH_2, only 1 h of milling enabled the best cycling properties of the composites incorporating graphite, which is a significant improvement with respect to processing costs.[70]

Mg-Co-MWCNT (multi-walled carbon nanotubes) composites were shown to impact the position of the DTA peaks, where tuning the milling times was vital to achieve improved hydrogen desorption properties.[71] Milling 5 wt% of MWCNTs in MgH_2 (400 rpm, 4:1 b:p ratio) caused the peak temperature of the hydrogen desorption to drop with the emergence of two DTA peaks after only 10 h milling (*i.e.*, T_{LT}: 350 °C, T_{HT}: 358 °C). Cobalt metal performed significantly better at reducing the T_{peak} after only 5 h of milling but only one peak was evident from the DTA profile (T_{peak}: 331 °C). After 50 h of milling with 5 wt% Co, the two-step decomposition in the DTA trace becomes evident, and the LT peak is more prominent than the high temperature peak (T_{LT}: 325 °C, T_{HT}: 345 °C). When MWCNTs were combined with 50 h milled MgH_2+Co, a single desorption step was observed where the T_{peak} was relatively low at short milling times (*i.e.*, 332 °C and 323 °C for 1 h and 5 h milling respectively), but at longer milling times (10 h) the T_{peak} of the DTA profile increased to 337 °C. Recent theoretical and experimental studies on hydride-graphite composites for hydrogen storage systems indicate that the high thermal conductivity of such composites improves sorption kinetics. [65, 72, 73] From this work, tuning of the H_2 sorption times was possible by modification of the graphite loading, where higher loadings of graphite translated to higher thermal conductivity and thus faster sorption kinetics.

One of the mechanisms by which carbon materials are proposed to assist in hydrogen storage systems is by hydrogen spillover.[74] On the basis of carbon support materials

containing metal catalyst particles, this involves initial absorption of hydrogen on to the metal catalyst then spillover of hydrogen on to the support material. This is commonly discussed in relation to nanoconfinement of hydrogen storage materials.[75] Recent work suggests that hydrogen spillover may also be relevant when carbon is used as the additive in metal hydride storage systems.[76] Zhou *et al.* suggest that hydrogen spillover may contribute towards the enhanced hydrogen sorption characteristics observed in their milled magnesium-coal composites, where the MgH_2-carbon interface facilitates desorption of hydrogen from the system as a result of C-H bond formation. Furthermore, inclusion of the coal prevents particle aggregation during cycling.

Refractory carbide additives have received surprisingly little interest in MgH_2 research, by comparison to oxides. Their hardness makes them appealing for use as a milling aid for MgH_2 in order to decrease particle size and thus increase surface area (Table 3-8). Furthermore, their high thermal conductivity would be advantageous for improving the hydrogen sorption kinetics based on previous work.[65, 72] Crucially, they do not contain oxygen and so Mg-containing oxide formation resulting from the additive upon milling and cycling is eliminated as may be the case when using some oxide additives.

Table 3-8 Important properties of carbon and refractory carbide materials used as additives for the Mg-H system. [77]

Carbon/Carbide	Thermal Conductivity @ 293 K / W/m.K	Vickers Hardness / GPa
Graphite	130	7-11 kg/mm^2
SiC	120	24.5
TiC	21	28-35
Mo_2C	21.5	15.5-24.5
WC	63	22

The most studied carbide additive is SiC, which is relatively inexpensive, stable and may be easily and rapidly prepared from abundant materials.[78] Use of SiC as a hydrogen release promoter in the Mg-H system has been reported under various conditions, including by use of microwave irradiation.[79] Milling of MgH_2 and SiC has been conducted in cyclohexane under inert conditions, which was shown to decrease the hydrogen desorption temperature of MgH_2 by more than 24 ^oC.[80] The proportion of SiC used had a significant impact on the resultant hydrogen release properties, where a greater mol% SiC improved H_2 desorption onset temperatures. However, at these high loadings it was found that a significant amount

of the hydrogen was lost in the mill and lower milling times proved to be more useful for retaining the hydrogen within the hydride prior to thermal desorption. Reversibility studies by Ranjbar using MgH_2-SiC composites milled in an H_2 environment showed that high SiC loading has a negative effect on the diffusion of hydrogen from the samples, leading to high hysteresis in cycling and slow H_2 sorption.[81]

Titanium carbide, TiC, has been the most studied of the TMCs (transition metal carbides) and the size of the additive has been shown to have a pronounced effect on the desorption properties of the hydride.[82] Particles in the 50 nm range were shown to allow 90 % absorption in 5 min and desorption of > 6 wt% H_2 within 20 min, a capacity that was maintained even after 5 cycles.[83] Recent work showed that 2 mol% Mo_2C has the effect of increasing the proportion of the second, high temperature peak after 8 h cryomilling.[35]

It is clear from the above brief review of MgH_2 literature that a dearth of research has been conducted towards the reduction of the temperature at which MgH_2 releases hydrogen. Based on the need for simple and industrial scale synthesis of MgH_2 for the target application, ball milling was deemed the best way forward for this research. This is based on the current success of this technique for preparation of MgH_2 for stationary hydrogen storage, and the ease with which it may be easily scaled-up for synthesis at an industrial level. Owing to recent success in the use of carbide materials as effective additives for MgH_2, this work comprises a comparative study using graphite and SiC with commercial MgH_2, both as individual additives and as a 1:1 molar SiC:graphite additive composite. SiC was chosen based on its high thermal conductivity; comparable with graphite and much higher than other transition metal carbides, and the high hardness of SiC. The aim of which is to provide both enhanced milling effects, such as particle size reduction and high thermal conductivity to aid hydrogen desorption kinetics, which will be studied in this work.

3.2. Aims of the work described in this Chapter

1. To evaluate the effect of milling parameters on the thermal decomposition of commercial MgH_2 using STA.
   a. Indicate which milling conditions provide a route to the greatest drop in desorption temperature, without significant loss of hydrogen, and thus create a “baseline” to which MgH_2-additive composites may be compared.
   b. Show the impact of milling conditions on the two-step decomposition observed by DTA for MgH_2, indicating what parameter(s) influence this phenomenon.

2. To determine suitable additives for commercial MgH_2 to reduce hydrogen desorption temperature without overly compromising the hydrogen capacity.
   a. Evaluate the influence of silicon carbide on the thermal decomposition of MgH_2; in relation to both reducing the desorption temperature and on the two-step decomposition process.
   b. Determine whether partial substitution of graphite for the transition metal carbide has a significant impact on hydrogen desorption from doped MgH_2.

3.3. Results & Discussion

3.3.1. Commercial MgH_2

The morphology and diffraction pattern of commercial MgH_2 used in this work are provided in Figure 3-6, which reveals that the powder contains trace amounts of Mg as well as α-MgH_2, which is likely to be the result of incomplete hydrogenation in the manufacturing process. Using CELREF and the parameters given by Ellinger *et al.* as a model, the unit cell parameters of the commercial material were determined; a = 4.5180(9) Å, c = 3.0220(2) Å.[5]

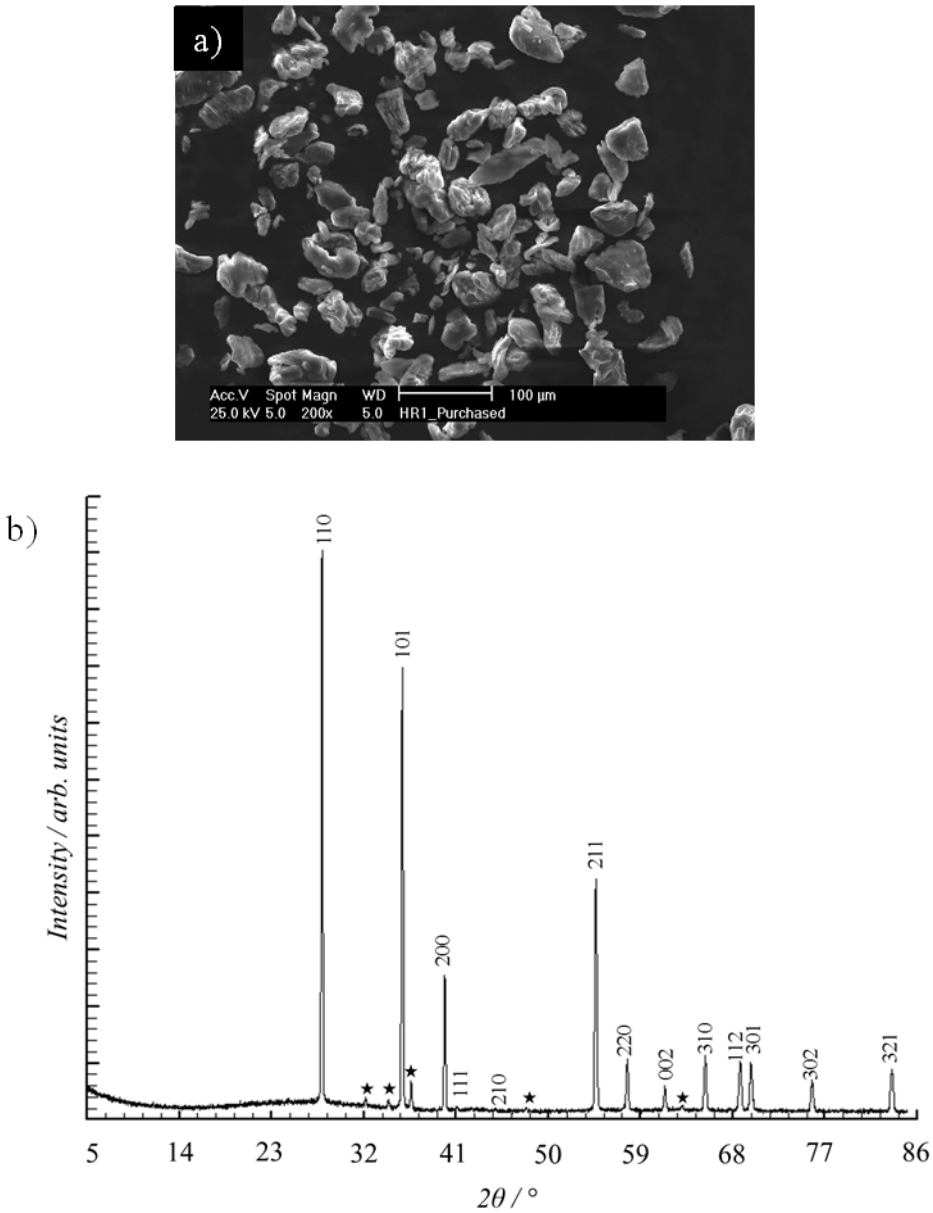

Figure 3-6 a) SEM image of commercial MgH_2 as-purchased, and b) PXD of commercial MgH_2 as-received (*hkl* values given for each α-MgH_2 reflection, and ★ indicates Mg reflections).

Rietveld refinement of the as-received hydride allowed quantification of the Mg present (Figure 3-7, Table 3-9). It also confirmed the close approximation of the cell parameters of the hydride previously described using CELREF (ICSD-26624).

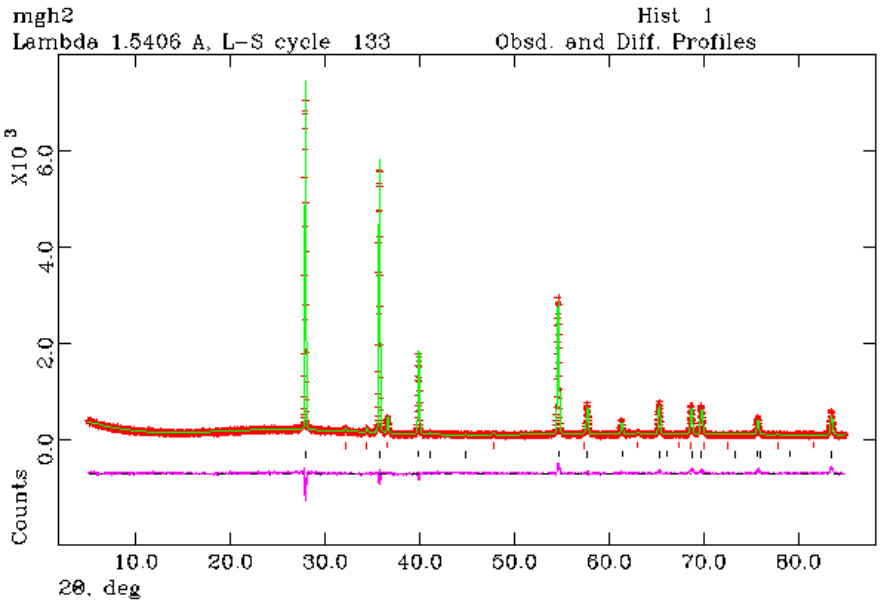

Figure 3-7 Rietveld plot for commercial MgH_2; observed and calculated data are shown by red crosses and the green continuous plot, respectively. Black and red tick marks indicate MgH_2 and Mg phases, respectively. The lower continuous pink line is the difference plot.

Table 3-9 Refinement data for commercial MgH_2.

Chemical Formula	*MgH_2*	*Mg*
Crystal System	Tetragonal	Hexagonal
Space Group	*P4/mnm*	*$P6_3/mmc$*
Z	2	2
***a* / Å**	4.51489(9)	3.2099(3)
***c* / Å**	3.01963(6)	5.2107(9)
***V* / Å^3**	61.551(3)	46.497(8)
Formula Weight / g	52.642	48.610
Calculated Density, ρ_x / g cm^{-3}	1.420	1.736
Phase Fraction / %	96.48(1)	3.52(9)
Refinement Parameters	24	
Data Points	4847	
R_{wp}	9.26 %	
R_p	7.37 %	
χ^2	1.741	

The FTIR spectrum shown in Figure 3-8, is characteristic of MgH_2, with a broad band in the 900-1600 cm^{-1} region due to Mg-H stretching.[84, 85] The absence of an -OH stretch expected at ~3800 cm^{-1} characteristic of $Mg(OH)_2$ indicates that the hydride used in this

study does not contain any of the hydroxide phase (or water), even on exposure to air over the time period of a spectroscopy measurement.[86]

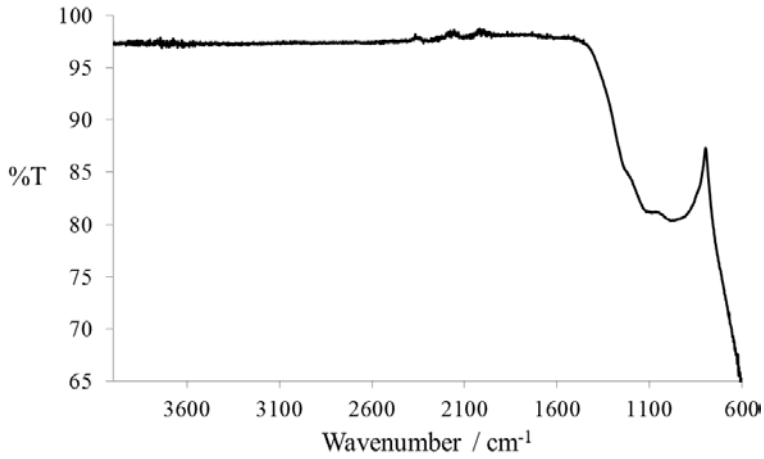

Figure 3-8 FTIR spectrum of commercial MgH_2.

The Raman spectrum collected for the commercial α-MgH_2 used in this work is shown in Figure 3-9, with a comparison of the known bonding mode assignments in Table 3-10. The profile of the spectrum and values assigned for the B_{1g}, E_g and A_{1g} optical phonon modes are in good agreement with literature data.[25] The B_{2g} mode described by Kuzovnikov *et al.* was also observed in the expected range quoted in their recent work (1470-1790 cm^{-1}). The assignment of B_{2g} in this work, 1497.8 cm^{-1}, is reasonably close to the values calculated by Lasave *et al*. Their work involved using both a shell model and the linear augmented-plane wave (LAPW) calculation method, where comparison of the results from these methods showed consistent values for the optical Brillouin zone centre modes.[15, 23] Furthermore, the phonon dispersion curves obtained by Lasave *et al.* are consistent with those obtained in the first-principles study by Ohba *et al.*, indicating good agreement across a variety of theoretical models using the high symmetry lines in the Brillouin zone of MgH_2.[22]

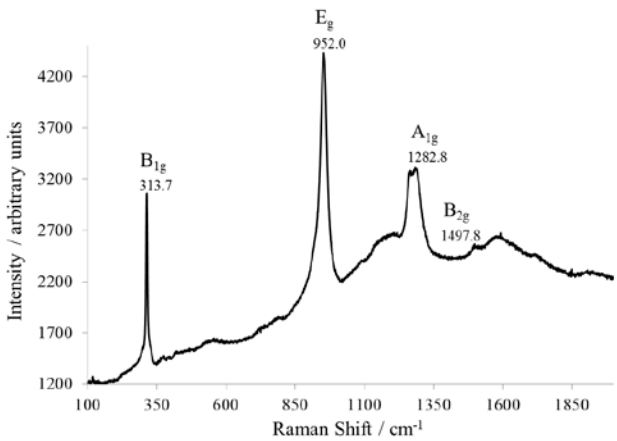

Figure 3-9 Experimental Raman spectrum for commercial MgH_2.

Table 3-10 Comparison of Raman shift information for MgH_2.

	Phonon Mode			
Source	B_{1g}	E_g	A_{1g}	B_{2g}
This Work	313.7	952.0	1282.8	1497.8
Lasave[23] (LAPW)	289	963	1277	1461
Lasave[23] (Shell model)	312	940	1274	1463
Santisteban[24]	300	950	1276	-
Reed & Book[26]	315.3	947.9	1276.6	-

The decomposition properties of the commercial, unmodified magnesium hydride used in this work are shown in Figure 3-10. The total enthalpy of decomposition for the hydrogen desorption event E_{dec} was estimated from the DTA measurement collected at 5 ^{o}C/min (72.43 kJ/mol) using the integral of the endothermic decomposition event (see Section 2.3.5.1) and is consistent with values given previously in literature. The DTA profile shows a single peak using 5, 10, and 20 ^{o}C/min heating rates (Figure 3-10a, Appendix A, A.1). A two-step DTA trace is revealed using a 2 ^{o}C/min heating rate; the primary lower temperature peak occurs at 403.2 ^{o}C and the secondary step emerges at 412.0 ^{o}C. The heating rate has a significant effect on the kinetic profiles for any material, and the E_a deduced from the Kissinger plot (Figure 3-10b) for decomposition of the MgH_2 used in this project is 144±5 kJ/mol, which is lower than the value quoted by Campostrini *et al.* (175±9 kJ/mol) in their recent work on the decomposition of commercial MgH_2 using the Kissinger method.[29] A number of variables may result in the observed differences, *e.g.*, the different heating rates (2, 5, 10, 20 °C/min *vs.* 10, 13, 16, 19, 22 °C/min) and number of data points (4 *vs.* 5) used in this work relative to that used by Campostrini *et al*. Differences in the instrumental set-up including calibration, flow rate, sample pan, *etc.*, will also result in variation between studies. The Ozawa method was employed to verify the E_a result obtained using the Kissinger method (Appendix A, A.2). This gave an E_a of 148±4 kJ/mol, which is slightly higher than the value determined by the Kissinger method. The higher E_a determine using the Ozawa method relative to the Kissinger method is in agreement with the results obtain by Campostrini *et al*.[29]

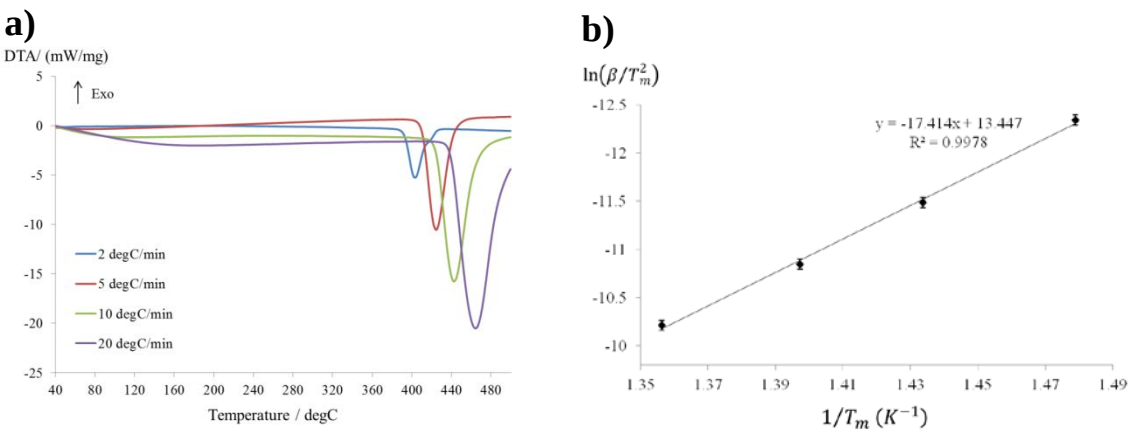

Figure 3-10 a) DTA traces and b) Kissinger plot of commercial MgH_2 used in this work, where each point is the T_{peak} for decomposition taken from the DTA plots.

Simultaneous accumulation of TG and MS data allowed the hydrogen desorption profiles for the commercial product to be derived (Figure 3-11). MS confirmed that hydrogen was the only species detected during these experiments, and therefore the mass loss could be attributed to hydrogen only. The mass loss was ~7 wt% H, which is slightly less than the theoretical capacity of 7.6 wt% H. The MS traces show asymmetric peaks where hydrogen is released, indicating that hydrogen is given off at different rates from the sample as it is heated. The peak shape of the sample heated at 2 ^{o}C/min differs from the 5, 10 and 20 ^{o}C/min samples and agrees with observations in the DTA data.

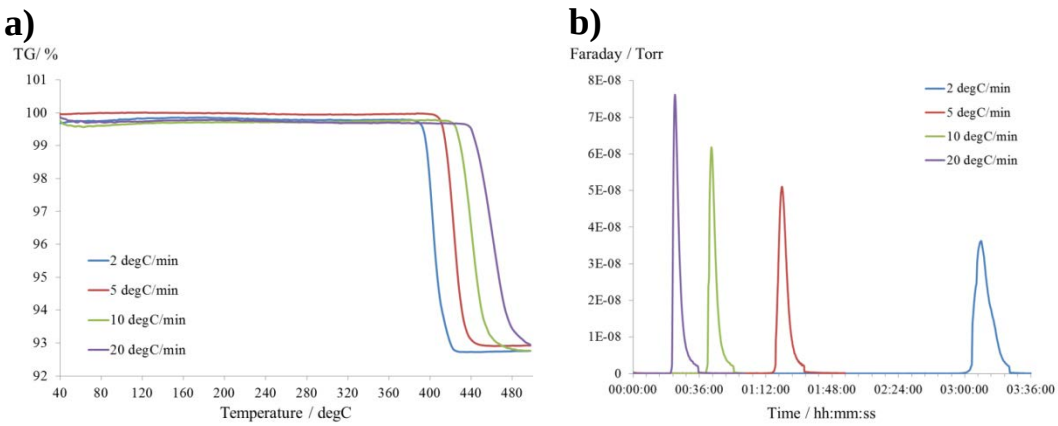

Figure 3-11 a) TG and b) MS (*m/z* = 2) data collected for commercial MgH_2 at the four heating rates employed.

3.3.2. Milling MgH_2

It is well known that milling of commercial MgH_2 causes significant changes to the thermal behaviour of the hydride, which may be tuned to a degree by controlling the milling conditions. It is also possible for high pressure γ-MgH_2 to form by mechanical action alone. To begin this investigation, it was important to evaluate the effect of the milling conditions applied to the hydride itself before including any additive materials,

thus creating a baseline of milled-MgH_2 properties against which the additive samples could be compared. Samples of commercial MgH_2 (without additives) were prepared by ball milling under the conditions given in Table 3-11. In order for consistent results to be obtained, separate milling procedures were used to obtain each product rather than taking samples intermittently throughout a single milling experiment. The reason for doing so is that opening the jar mid-experiment causes a change in the milling environment, and therefore the milling conditions are not consistent throughout the remainder of the milling procedure.

Table 3-11 Samples of milled commercial MgH_2 investigated in this work, all milling conducted at 450 rpm.

Sample ID	B:P ratio	Milling Duration / h	No. Milling Balls
1	40:1	0.5	2
2	40:1	2	2
3	40:1	5	2
4	40:1	10	2
5	40:1	20	2
6	40:1	40	2
7	40:1	0.5	8
8	40:1	2	8
9	40:1	5	8
10	80:1	0.5	8
11	80:1	2	8
12	80:1	5	8

Using relatively mild conditions (Samples **1-6**, 40:1 b:p, 2 milling balls), the effect of milling time was studied using a variety of techniques. Compared with the smooth, rounded particles of the commercial product, the samples milled under mild conditions comprise flattened particles which can be >100 μm in diameter across and ~10 μm in width. These larger particles are shown to have smaller particles on the surface, which decrease in size as milling time is increased (Figure 3-12).

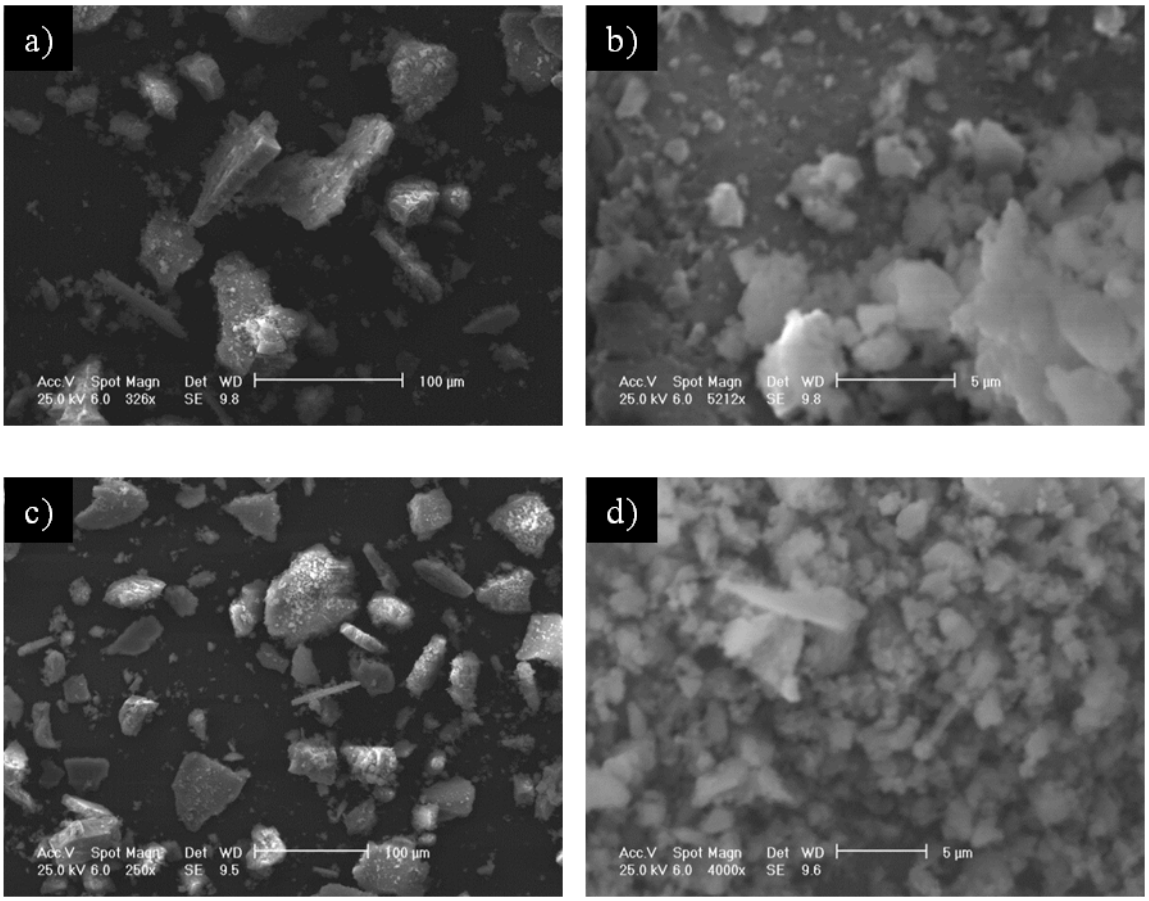

Figure 3-12 Low (a) and high (b) magnification images showing flattened particles of Sample 3 milled for 5 h. Low (c) and high (d) magnification images showing plate-type large particles remain after 20 h milling (Sample 5).

SEM images of Sample **11** and **12** reveal roughly spherical particles that are polydisperse; from micron sized aggregates to nano-scale particles (Figure 3-13). Milling for 5 h (Sample **12**) at the higher b:p ratio shows significantly smaller particles relative to the 2 h milled sample (Sample **11**). From PXD, the Scherrer equation was used to estimate the average particle size of Sample **11** and **12** using the highest intensity (*110*) reflection for α-MgH_2: 1.4 µm, and 678 nm, respectively. This confirms that the particle size has decreased as a result of milling the sample longer and is consistent with the observations made by SEM.

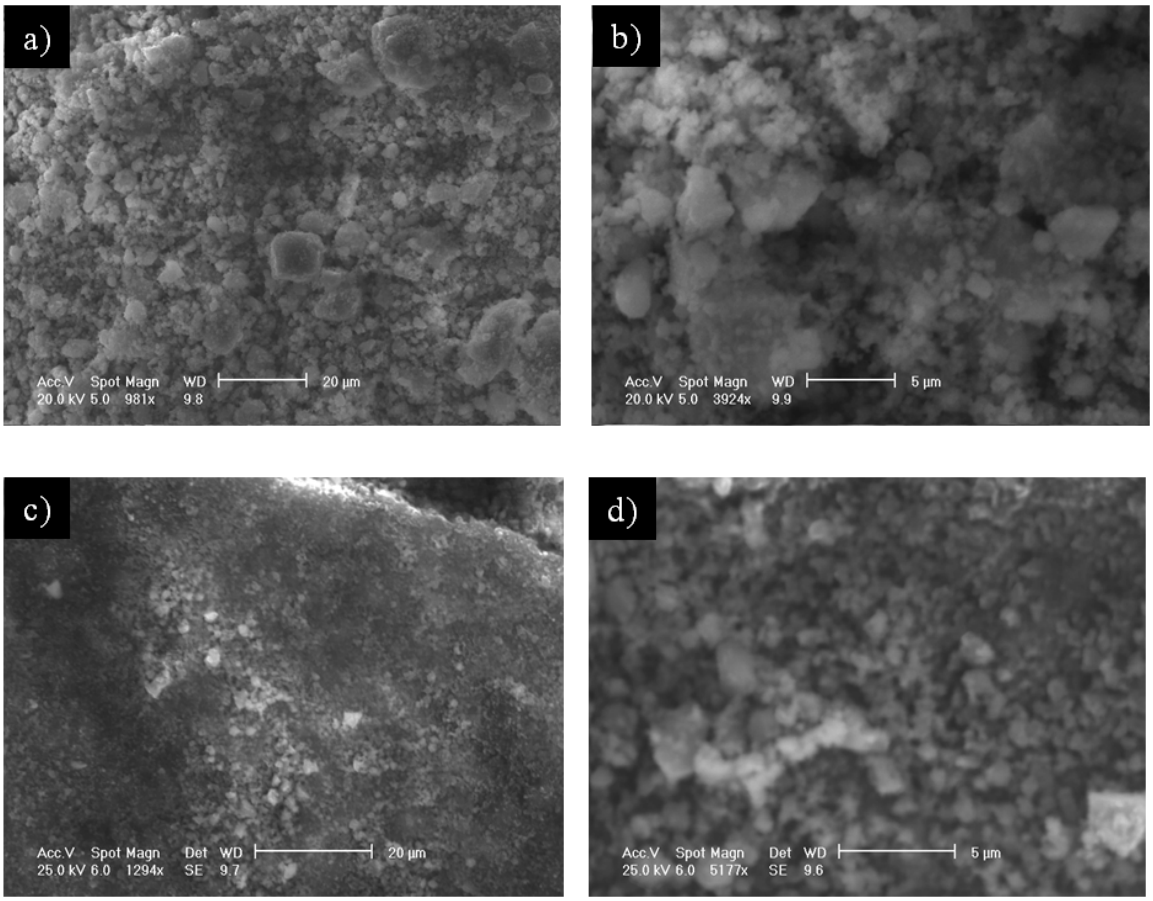

Figure 3-13 SEM images of milled-MgH_2; Sample 11 at a) 20 µm and b) 5 µm scale, and Sample 12 at c) 20 µm and d) 5 µm scale.

The phase fraction of Mg relative to MgH_2 is observed to increase from Rietveld refinement of the XRD pattern for Sample **1** milled under the mildest conditions (Figure 3-14). This suggests that even mild milling causes partial decomposition of the hydride with subsequent loss of the hydrogen in the mill. The cell parameters for Sample **1** as determined from CELREF were a = 4.5187(5) Å, c = 3.0217(1) Å, which are in close approximation to those of the un-milled, commercial MgH_2 (Table 3-12). No evidence was found to suggest that a sub-stoichiometric, $MgH_{2-\delta}$-type phase had formed.

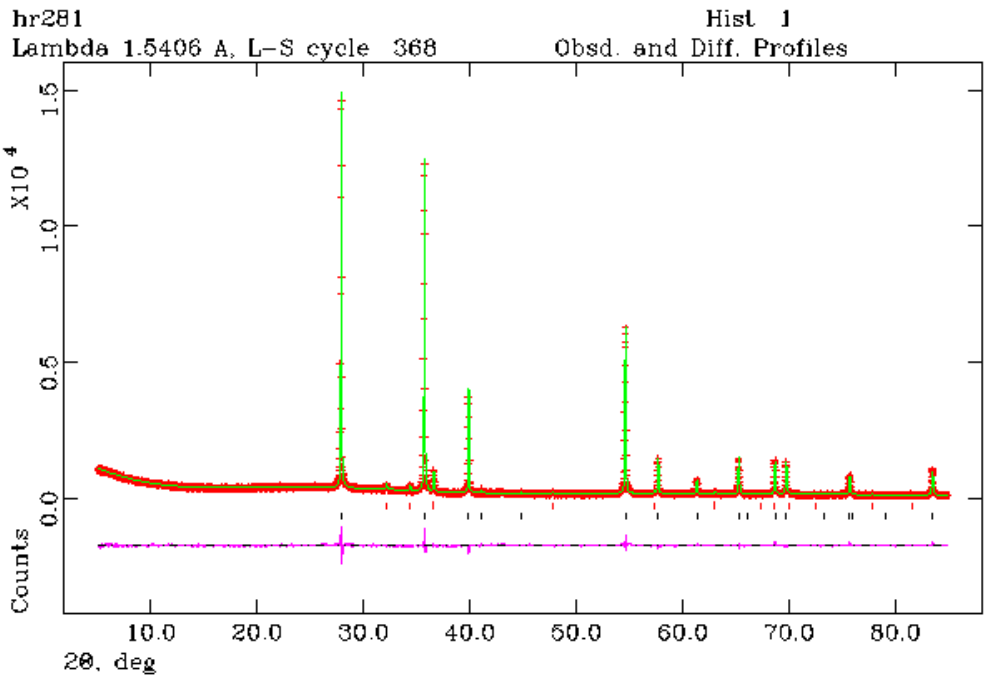

Figure 3-14 **Rietveld plot for Sample 1; measured and calculated data given by red crosses and the green continuous plot, respectively. Red and black tick marks indicate reflections from Mg and α-MgH_2, respectively. The difference plot is given by the continuous pink plot.**

Table 3-12 **Rietveld refinement data for Sample 1.**

Chemical Formula	***MgH_2***	***Mg***
Crystal System	Tetragonal	Hexagonal
Space Group	*P4/mnm*	*$P6_3/mmc$*
Z	2	2
***a* / Å**	4.51553(4)	3.2096(2)
***c* / Å**	3.01999(3)	5.2107(5)
***V* / Å^3**	61.551(3)	46.497(8)
Formula Weight / g	52.642	48.610
Calculated Density, ρ_x / g cm^{-3}	1.420	1.736
Phase Fraction / %	96.04(1)	3.96(8)
Refinement Parameters	26	
Data Points	4846	
R_{wp}	6.68 %	
R_p	5.10 %	
χ^2	1.657	

After 2 h of milling (Sample **2**), the emergence of the gamma phase is evident from the presence of the weak, broad reflection at ~26° (Figure 3-15).

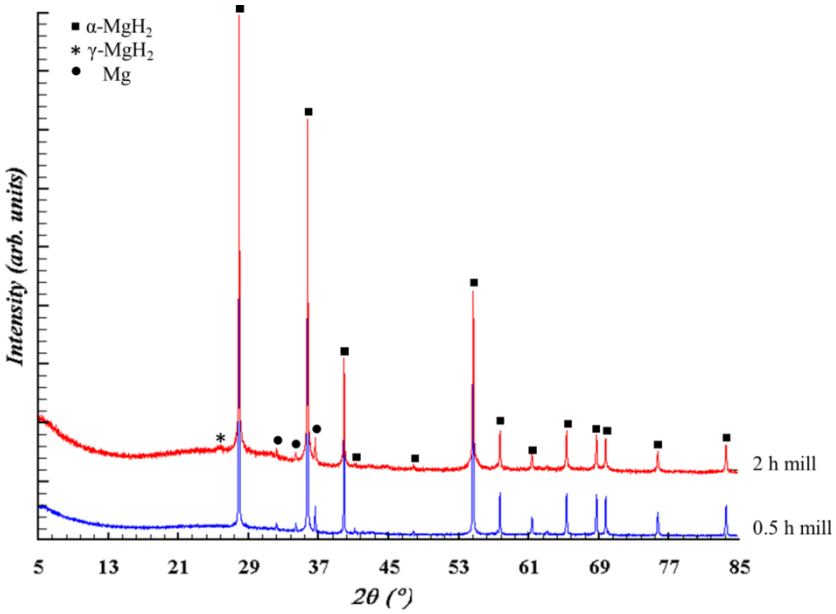

Figure 3-15 PXD showing the emergence of γ-MgH_2 after only 2 h of milling (red pattern) compared with 0.5 h milled sample (blue).

The frequency of collisions was also studied by increasing the number of milling balls used from 2 to 8, where the b:p ratio, 40:1, was kept constant by adjusting the mass of MgH_2 used. Samples were prepared at 0.5 h, 2 h and 5 h in order to form a comparison between both the milling time and frequency of collisions. From PXD data alone, it is evident that the particle size of the hydride is significantly affected by the number of collisions, since the diffraction peaks are broadened and the reflections from γ-MgH_2 phase are more prominent in the samples prepared using 8 balls (Figure 3-16). Further, as milling time increases, the samples become less crystalline as indicated by the amorphous band in the samples milled for 5 h. Using the Scherrer method (assuming roughly spherical particles; K = 0.9), the particle size was shown to drop significantly even after only 0.5 h milling, *e.g.*, the average particle size for Samples **1** and **7** were 1.9 μm and 1.6 μm, respectively. For Sample **9**, the average particle size dropped to 978 nm, which is a marked improvement relative to Sample **3** (1.96 μm). Therefore, increasing the relative number of impacts has a significant influence on the particle size of the resultant milled sample. Using CELREF, the cell parameters for each sample were determined and no significant trend could be ascertained with respect to the milling conditions used, where the cell parameters of the samples studied remained in close proximity to the un-milled MgH_2, even in the presence of the γ-phase.

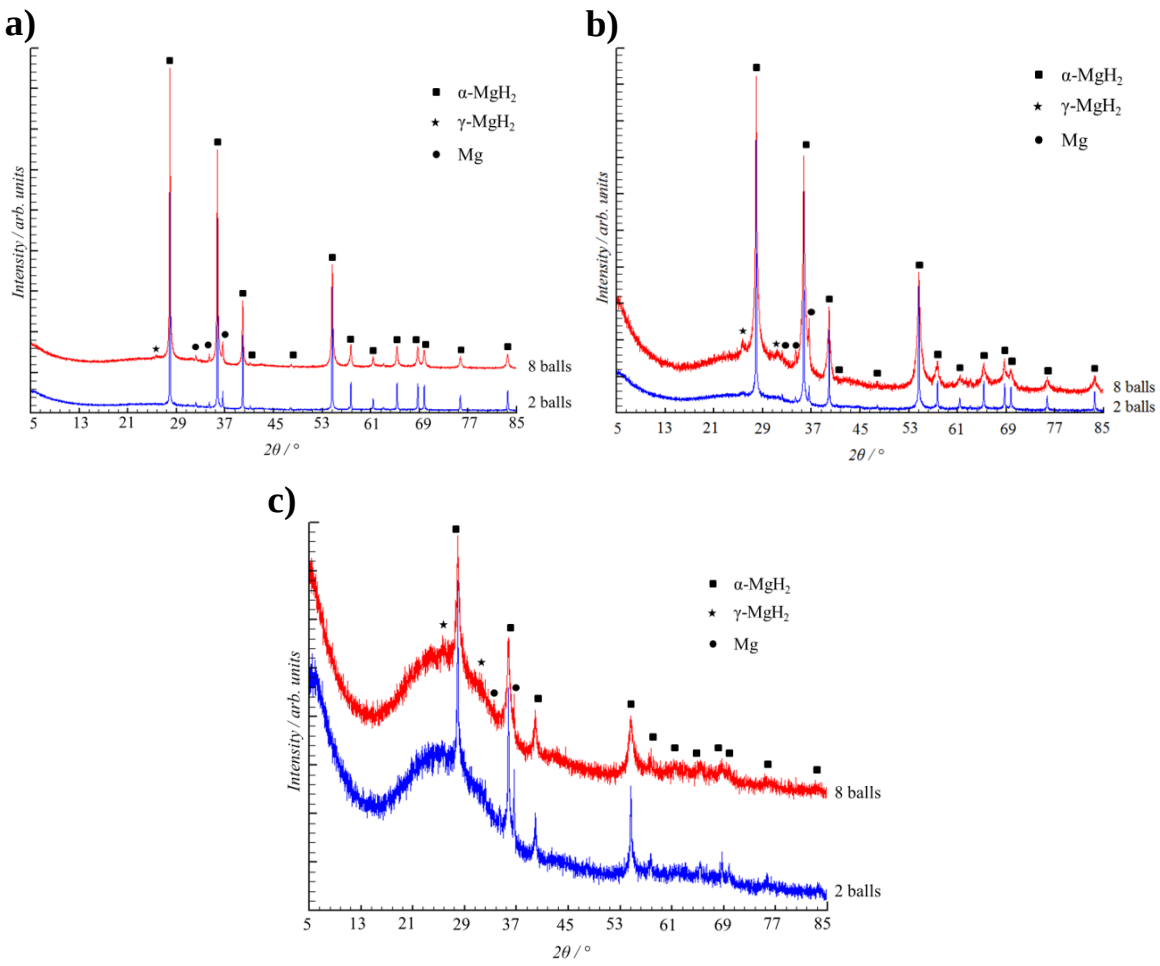

Figure 3-16 PXD of commercial MgH_2 milled for a) 0.5 h (Samples 1 **and** 7**), b) 2 h (Samples** 2 **and** 8**) and c) 5 h (Samples** 3 **and** 9**).**

Under the harshest conditions applied the particle size was only slightly reduced by increasing the milling time, where the average particle size for Sample **10** and Sample **12** were very similar, *i.e.*, 699 nm and 678 nm, respectively.

The dehydrogenation behaviour was shown to be influenced significantly by the milling conditions applied (Table 3-13). The first derivative of the measured data was used to determine the rate of change in the gradient of the relevant signals. This allowed the T_{onset} and T_{peak} values to be determined. The total enthalpy of decomposition was estimated from DTA data for samples heated at 5 °C/min by measuring the total area under the decomposition endotherm, including both decomposition steps where applicable.

Table 3-13 DTA-TG data collected for un-doped, milled MgH_2 (Samples 1-12).

Sample	DTA		TG		$^{\dagger}E_{dec}$ (kJ/mol)
	T_{onset} /°C	T_{peak} /°C	Mass Loss T_{onset} /°C	Mass Change / %	
1	**LT:** 346.2 **HT:** 380.9	**LT:** 355.3 **HT:** 400.7 ***ΔT*** = 44.7	382.2	6.92	66.12
2	**LT:** 337.6 *368.2	**LT:** 362.7 **HT:** 391.9 ***ΔT***=29.2	**LT:** 352.9 **HT:** 387.3	**LT:** 4.33 **HT:** 2.42	60.01
3	**LT:** 334.0 **HT:** 384.1	**LT:** 357.4 **HT:** 391.7 ***ΔT*** = 34.3	**LT:** 339.2 **HT:** 366.4	**LT:** 4.10 **HT:** 2.91	58.61
4	319.8	347.8	324.1	6.79	55.30
5	334.7	357.6 ***386.3 ***ΔT*** = 28.7	340.1	**LT:** 5.70 **HT:** 1.08	54.75
6	329.0	354.8	335.8	7.02	57.93
7	338.9	367.7	348.4	6.84	61.19
8	325.0	349.4	331.5	6.95	60.14
9	320.7	345.8	326.6	6.90	58.35
10	328.2	353.2	334.5	6.87	57.11
11	318.3	343.3	325.4	6.96	59.33
12	329.0	350.6	335.1	6.69	61.43

(* indicates an inflection in the gradient of the curve at a given temperature, and the $\Delta T = T_{HT} - T_{LT}$ is given for the endothermic maxima where a two-step decomposition is observed. $^{\dagger}E_{dec}$ determined from data collected at 5 °C/min.)

The DTA trace after only a short period of milling under the mild conditions is shown to be significantly different in comparison to the un-milled material. After only 0.5 h, a shoulder is evident on the DTA trace at a lower temperature to the primary decomposition peak (Figure 3-17a). As milling time is increased, this shoulder becomes more resolved and a LT and HT peak may be distinguished (Figure 3-17b).

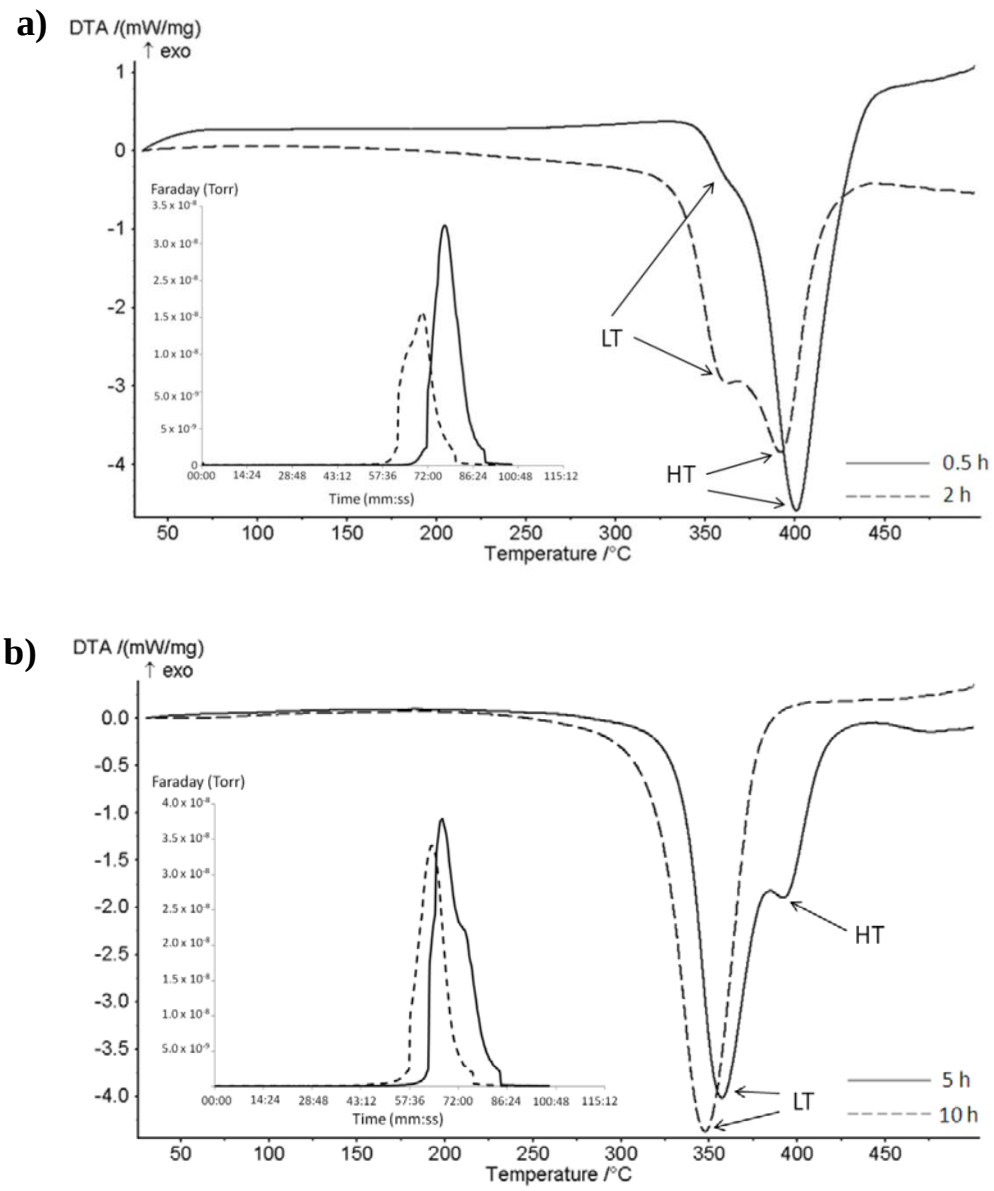

Figure 3-17 DTA-MS data collected at 5°C/min for MgH_2 for a) Samples 1 and 2 and b) Samples 3 and 4.

The sample milled for 5 h, shows the low temperature peak has become enhanced relative to the high temperature peak, and this is of significant importance for understanding how the enthalpy of decomposition may be lowered. Milling for longer times, 20 h and 40 h (Samples **5** and **6**), caused an increase in the T_{peak} for MgH_2 relative to Sample **4**. The estimated total enthalpy of decomposition was found to decrease significantly upon increased milling time up to 20 h (Figure 3-18), where it was reduced by 24.4% with respect to un-milled MgH_2. The estimated total enthalpy of decomposition was observed to increase after milling for a total of 40 h. This effect is likely to be the result of agglomeration of the particles at longer milling times.

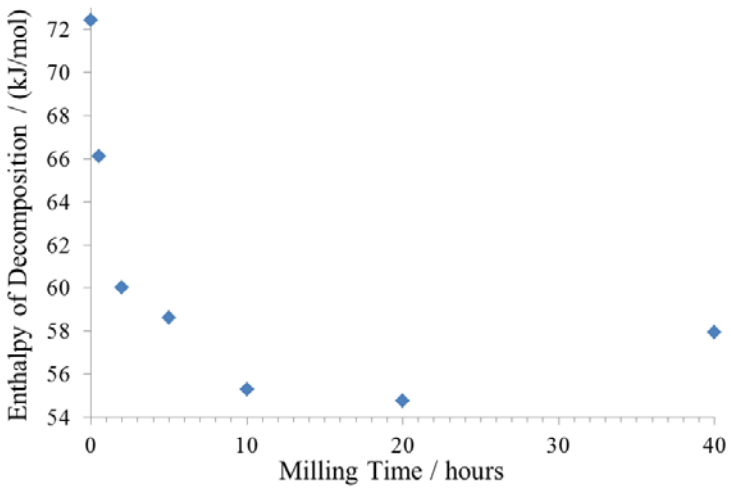

Figure 3-18 Trend in estimated total enthalpy of decomposition data collected for commercial, un-milled MgH_2 and MgH_2 milled for different durations (Samples 1-6).

Sample **3** is the first in this series to show the intensity of the LT peak to be dominant and so further thermal analysis was conducted (Figure 3-19). The activation energy for the two-steps was determined using the Kissinger and Ozawa methods. The linear plots show a good fit to both models based on R^2 values (also known as the coefficient of determination) for the simple linear regression trendlines applied to the dataset. Activation energy values for the LT (Kissinger: E_a = 113±7 kJ/mol, Ozawa: E_a= 118±7 kJ/mol) and HT (Kissinger: E_a = 140±6 kJ/mol, Ozawa: E_a = 144±6 kJ/mol) peaks indicate that the two events are distinct, and both are lower in energy with respect to the unmilled hydride (E_a = 144±5 kJ/mol). The E_a of the LT peak in Sample **3** is lower in energy with respect to that determined for Sample **2** (Kissinger: E_a = 127±12 kJ/mol, Ozawa: E_a = 131±11 kJ/mol), while the HT peak is actually higher than that of Sample **2** (E_a = 138±7 kJ/mol, Ozawa: E_a = 142±6 kJ/mol). (Kissinger plots for Sample **2** are given in Appendix A; A.3 & A.4, respectively.) The distinct nature of the two decomposition steps suggests that two modes of hydrogen transport through the material takes place as the temperature increases and that milling conditions have a significant effect on the proportion of the material which releases at low and high temperature. This may be explained by consideration of previous kinetics investigations, where it has been suggested that the decomposition of MgH_2 may actually be segregated in to three distinct processes.[87, 88] The formation of α-Mg metal at the particle surfaces is described as the initiation step in the decomposition process of MgH_2, and then nuclei of Mg are formed. Finally, Mg particles arise upon complete desorption of the hydrogen with contraction of the particles facilitating complete hydrogen loss. From the results given here, only two distinct peaks are obvious from DTA traces. It may be reasoned, however, that the 1st LT peak corresponds to the formation of Mg nuclei

with initial loss of hydrogen, and the second HT step is from the contraction of the particles allowing complete diffusion of hydrogen from the material and thus decomposition of the material is complete. Therefore, the two-step decomposition observed for samples prepared under mild milling conditions is indicative of enhanced Mg nuclei formation upon an increase in milling time, where the growth of the Mg phase occurs thereafter.[89] This is likely to be the result of the decrease in particle size (corresponding to an increase in the particle surface area).

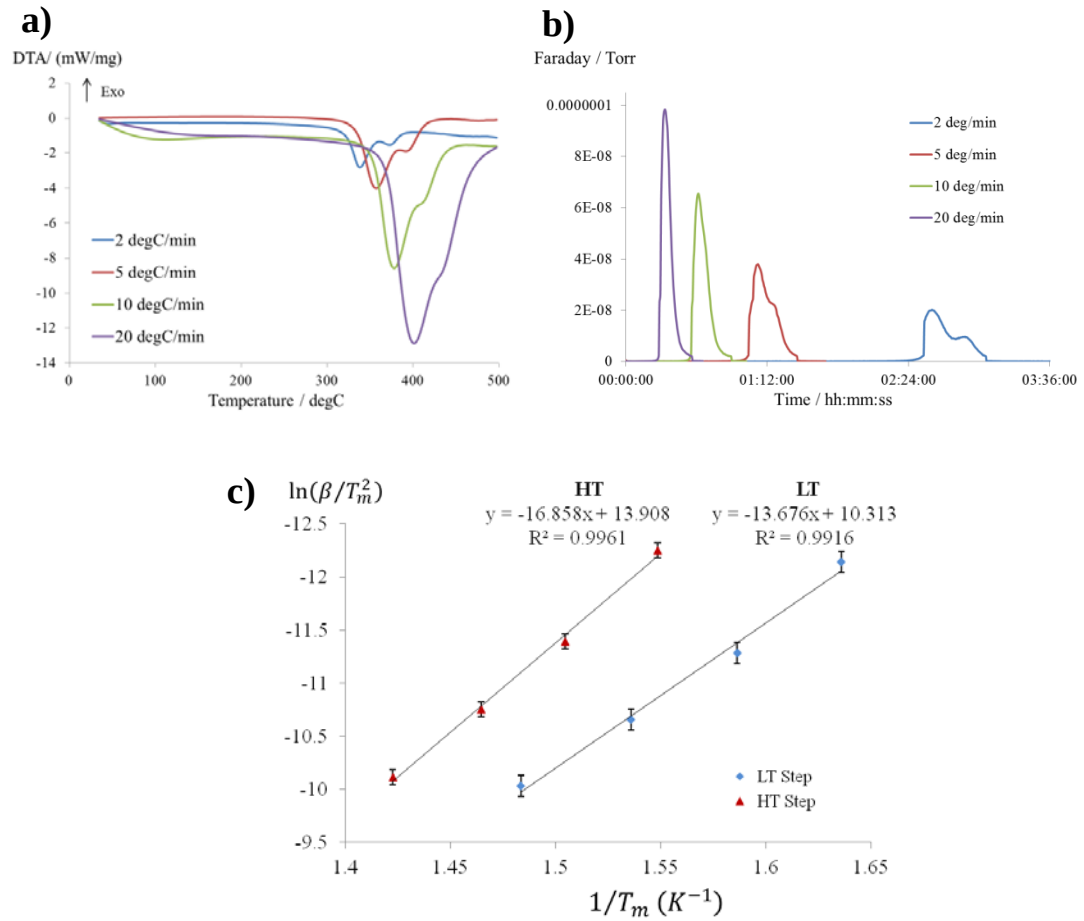

Figure 3-19 a) DTA profiles, b) MS data (*m/z* = 2) and c) Kissinger plots for Sample 3 collected by STA at 2, 5, 10 and 20 °C/min. (Ozawa plots given in Appendix A; A.5.)

XRD analyses of the post STA samples collected for Sample **3** show that hydrogen desorption is complete since Mg is the main decomposition product with a small contribution from MgO. (Figure 3-20)

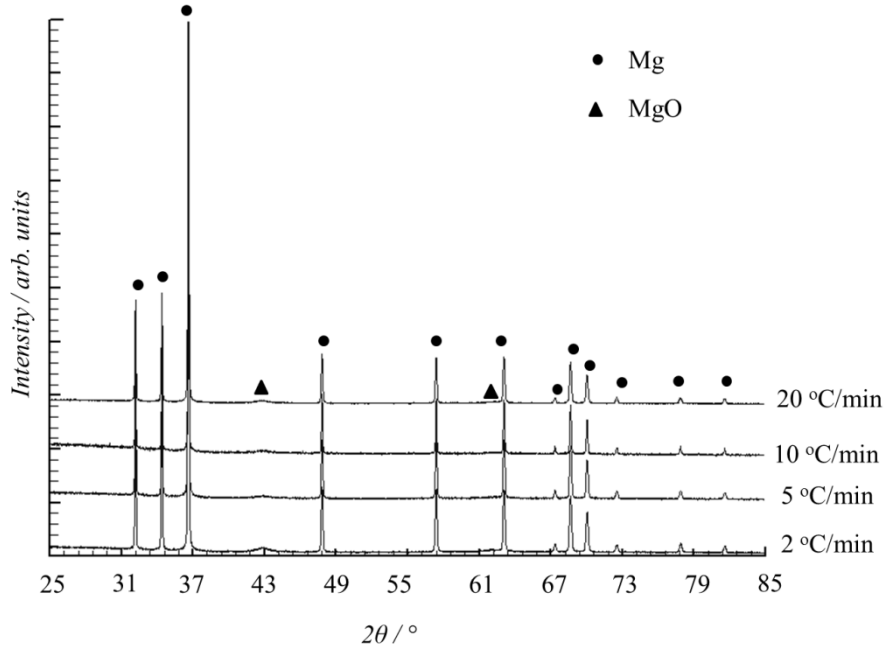

Figure 3-20 X-ray diffraction patterns of post STA products collected for Sample 3 after heating at each ramp rate used.

The two-step decomposition is no longer evident when the number of collisions is increased (Figure 3-21). This suggests that only one type of hydrogen diffusion from these samples takes place. Based on the previous hypothesis regarding the two-step decompositon, this could imply that the hydrogen desorption appears to occur in one step as a result of a greater potential for Mg nuclei formation in the samples milled with a greater number of impacts and thus the total desorption occurs at a lower temperature.

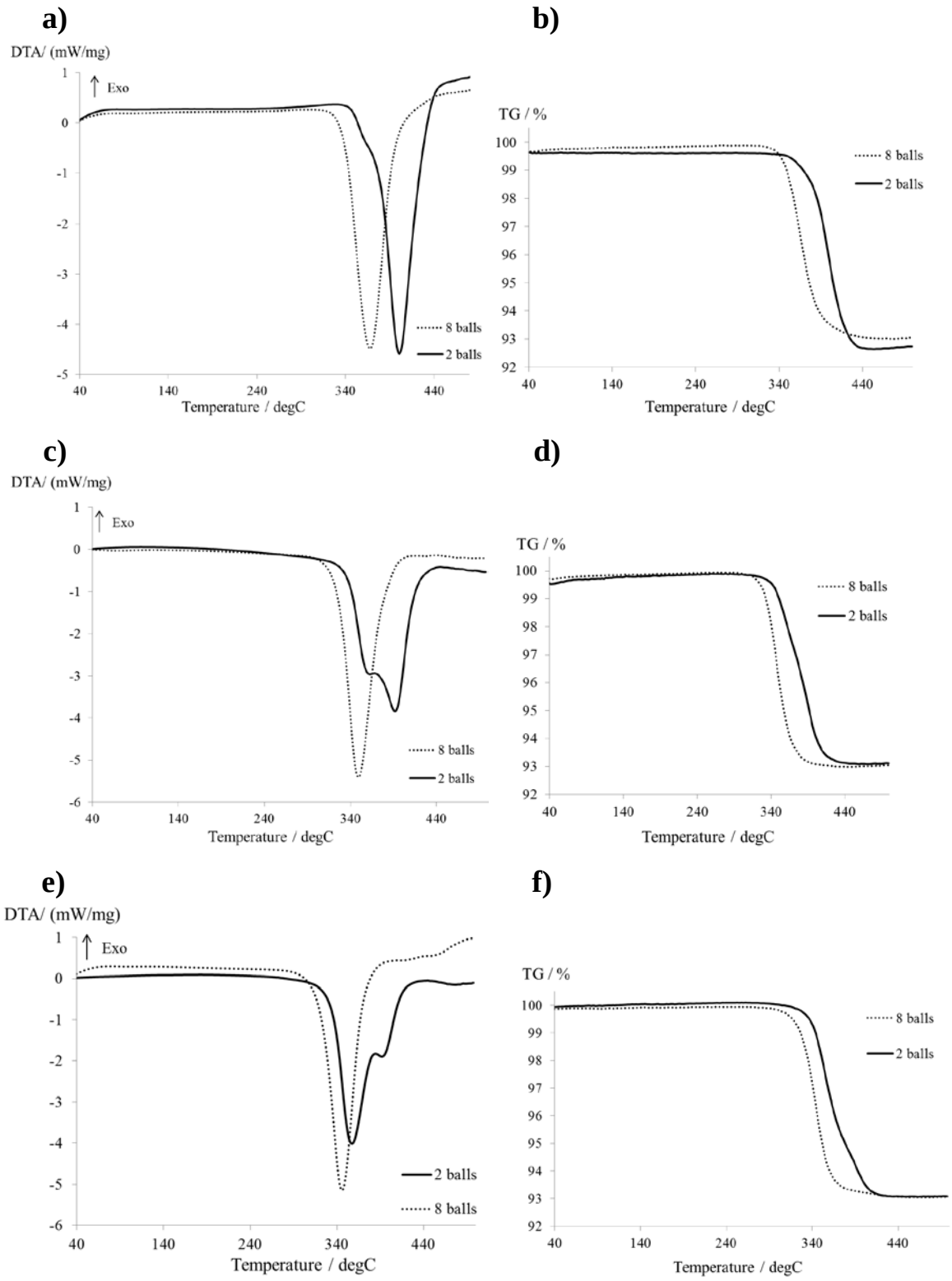

Figure 3-21 Comparison of DTA and TG traces for samples milled using 2 balls (solid line) or 8 balls (dashed line) as indicated for a) & b) Samples 1 and 7, c) & d) Samples 2 and 8, and e) & f) Samples 3 and 9.

In order to obtain a significant reduction in the hydrogen desorption temperature harsher milling conditions were necessary; b:p ratio increased, from 40:1 to 80:1. Time-resolved PXD was conducted on the Panalytical X'Pert Pro diffractometer in Bragg Brentano geometry under ambient conditions to determine the air sensitivity of Sample **11** (Figure 3-

22). A series of 1 h measurements were taken over a 15 h period and these demonstrate that the hydride does not react with air based on the absence of any emerging MgO, or $Mg(OH)_2$ reflections.

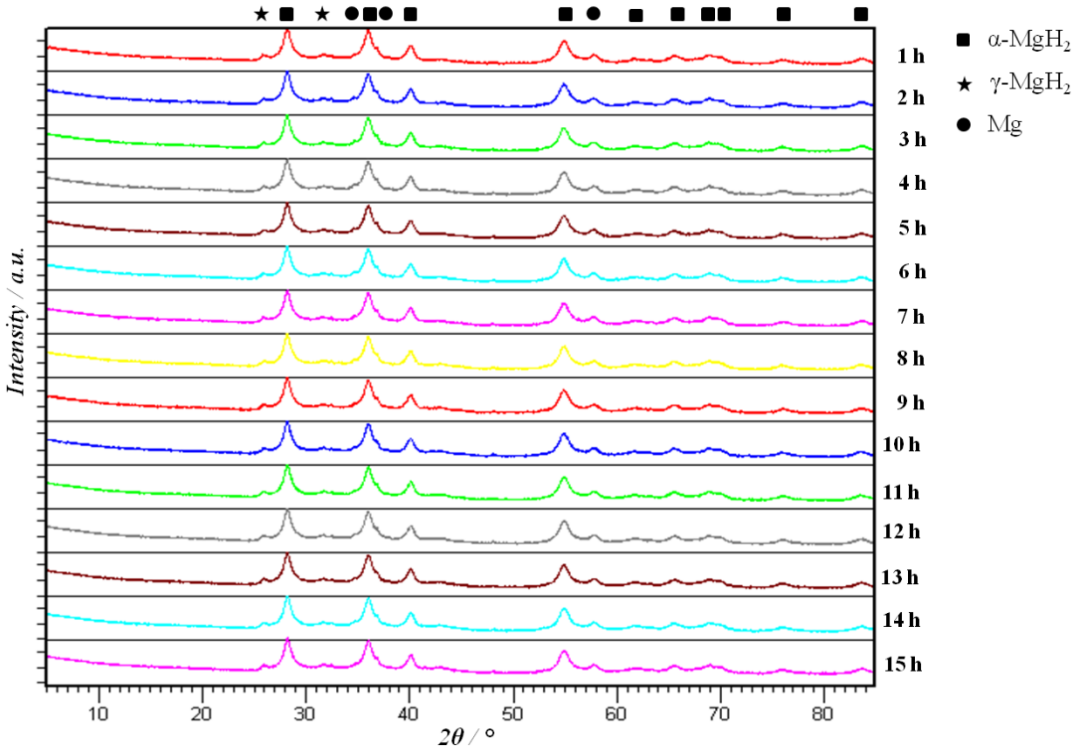

Figure 3-22 Time resolved PXD for sample milled Sample 11.

Previous work by Friedrichs *et al.* showed that a 3-4 nm MgO layer forms on milled MgH_2, even if handled under inert gas.[90] This nano-oxide layer was found to prevent further oxidation of the hydride. Furthermore, an amorphous hydroxide-type layer was also found to form on the outermost surface of milled hydride particles. In fact, MgO has also been evaluated as a milling aid in the Mg-H system.[40] Neither MgO or $Mg(OH)_2$ reflections were evident from the XRD analysis of hydrides synthesised in this work. EDX analysis of Sample **11** did not show any indication of contamination from the milling tools since no Fe or Cr are indicated in this analysis; these are typical components that would be expected upon contamination from the stainless steel milling jar. The $K\alpha_1$ lines for magnesium (86.83 wt%) and oxygen (13.17 wt%) are evident (Figure 3-23). The sample exposure to air for preparation and loading into the SEM chamber may have caused the oxidation of the sample, but from the work by Friedrichs it is expected that the oxygen in the sample will have been present before air exposure. No distinct oxide peaks from the time resolved XRD analysis can be seen, therefore, it may be that the oxide layer is only on the surface as in the work of Friedrichs *et al*. (The carbon is from the adhesive carbon tabs used for sample mounting.)

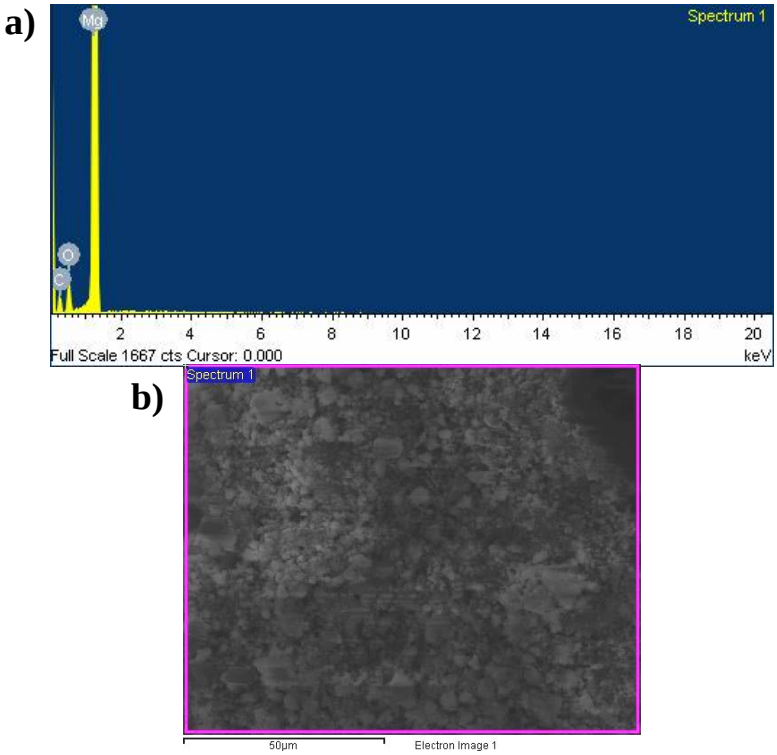

Figure 3-23 a) EDX spectrum of Sample 11 and b) SEM image of area from which the spectrum was collected (50 µm scale).

From FTIR spectra, the characteristic broad band of MgH_2 between 900-1600 cm^{-1} is shown to be modified after milling. Spectra collected for Samples **11** and **12** reveals three pronounced peaks in the MgH_2 band, which are more prominent in Sample **12** milled for 5 h (Figure 3-24). This indicates that the Mg-H stretching modes, and thus the MgH_2 lattice, may have been modified by milling where the sample milled at longer milling times was more significantly affected. This may be the result of the additional phase present in the hydride sample, where the Mg-H vibrational bonding modes in MgH_2 are likely to be different in the α and γ phases. However, it may simply be a matter of better resolution of the bands in Sample **12** with respect to Sample **11**. Again, despite analysis being prepared and conducted in air, there does not appear to be any sign of a significant –OH stretch from formation of a hydroxide layer.

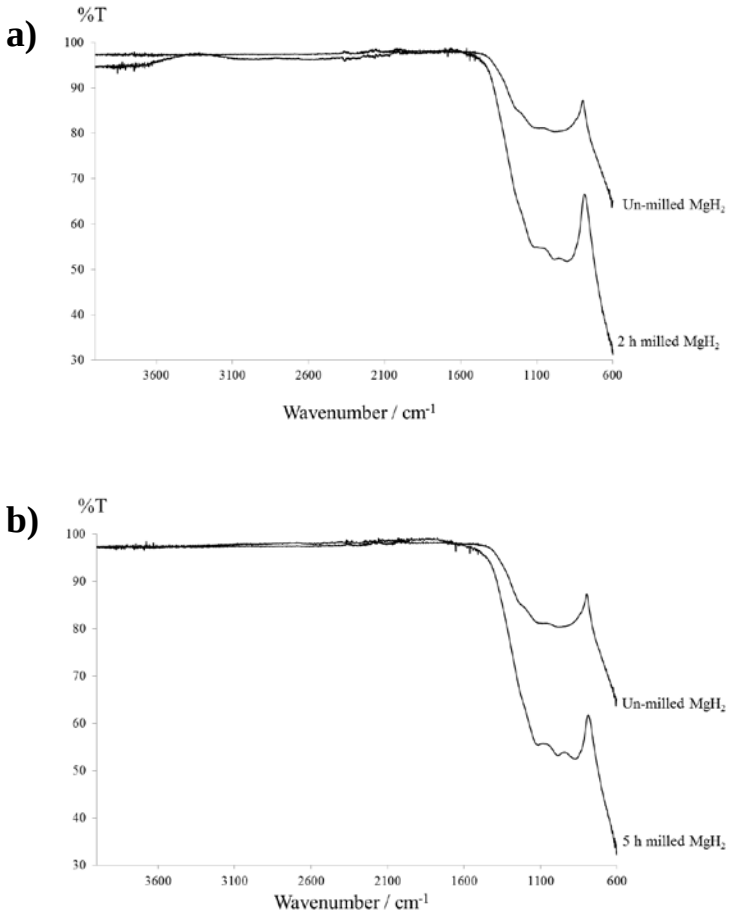

Figure 3-24 Comparison of FTIR spectra collected for commercial, un-milled MgH_2 and Samples a) 11 and b) 12.

Kissinger plots for Samples **11** and **12** reveal that the E_a for hydrogen decomposition from these samples is very similar; E_a = 110±7 kJ/mol (E_a = 114±7 kJ/mol) and E_a = 110±13 kJ/mol (E_a = 115±12 kJ/mol), respectively, where values in parentheses are derived from Ozawa plots (Figure 3-25; See Appendix A for Ozawa plots). Therefore, the milling duration under these conditions has a relatively small impact on the thermal decomposition for these samples.

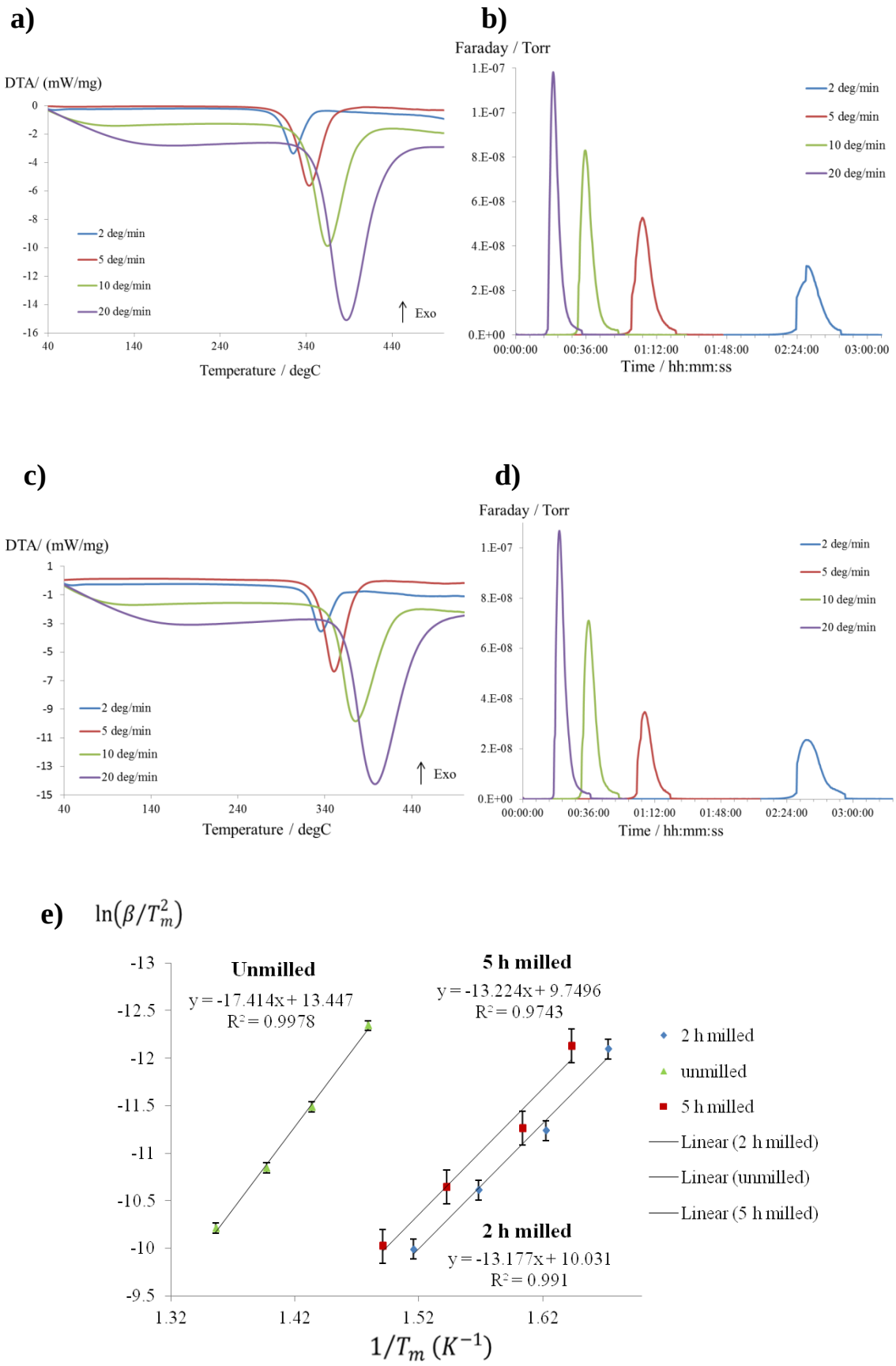

Figure 3-25 DTA and MS (*m/z* = 2) traces obtained used to obtain Kissinger plots for Sample 11 milled for 2 h (a & b) and Sample 12 milled for 5 h (c & d). e) Overlay of Kissinger plots for one step decomposition observed in Samples 11 and 12 compared with commercial, un-milled MgH_2 (Ozawa plot overlay given in Appendix A).

3.3.2.1. Summary of Findings from Milling MgH_2

The XRD patterns of all milled-MgH_2 show characteristic broadening of the reflections relative to the commercial material, where this becomes more pronounced as the milling time and number of milling balls (relative frequency of impacts) is increased. The cell parameters of the α-MgH_2 are unchanged after milling, but the crystallite size is reduced based on a crude evaluation by the Scherrer method. In comparison to the thermal data for samples milled under mild conditions, the DTA trace shows only one decomposition event for MgH_2 milled under harsher conditions, and that the T_{peak} may be decreased significantly at relatively short milling times. (The two-step decomposition was not observed until >35 h milling under the conditions used by Gennari and colleagues.[31]) Therefore, the milling variables used are important for tailoring the hydrogen desorption behaviour, and milling time should not be studied in isolation to understand thermal desorption behaviour of the hydride.

3.4. Additive Study

Non-oxide additives have been investigated in this research project including graphite and SiC. SiC:graphite mixtures in a 1:1 molar ratio were also studied. Using the results from the preliminary work on milling MgH_2 alone, comparisons could be made using a number of milling conditions.

1. 1-20 wt% additive; 40:1, 2 balls, 5 h milling
2. 5 wt% additive; 80:1, 8 balls, 5 h milling
3. 5 wt% additive; 80:1, 8 balls, 2 h milling

The first allows insight into the effect that the catalyst has on the temperature of the two decomposition events observed in the DTA curve, while the second employs significantly harsher conditions to establish improved thermal behaviour which is important for commercial applications. The third comparison indicates whether similar thermal decomposition profiles may be obtained for samples milled for less time by reducing the milling time from 5 h to 2 h.

As shown above, milling of MgH_2 under relatively mild conditions results in a two-step decomposition based on observations from DTA data. The effect of a number of specific catalysts has been covered in the literature, and this chapter will cover both the effect that the additives employed in this study have on the two-step DTA phenomenon and also the

most suitable conditions for improving commercial applicability by reducing dehydrogenation temperature.

3.4.1. MgH_2-*x* wt% Graphite (*x* = 1-20 wt%)

MgH_2-x wt% graphite composites were prepared by adding the appropriate wt% of graphite to un-milled MgH_2 into the stainless steel grinding jar in an inert gas-filled glovebox. Milling was then conducted using the various conditions indicated in Table 3-14, where the total experiment time is twice the milling duration due to the inclusion of 5 min rest periods between 5 min mill periods. The rotation direction was reversed after each milling period.

Table 3-14 MgH_2-x wt% graphite samples (x = 1-20).

Sample	wt% additive	B:P ratio	No. Milling Balls	Milling Duration / h
13	1	40:1	2	5
14	5	40:1	2	5
15	10	40:1	2	5
16	20	40:1	2	5
17	5	80:1	8	2
18	5	80:1	8	5

SEM analysis shows that all the MgH_2- x wt% graphite composites milled under mild conditions (Samples **13-16**) have smaller particles on the surface of relatively un-changed MgH_2 particles (Figure 3-26). It is evident that the smaller particles formed are in the micron scale. For Sample **17**, milled under harsher conditions (80:1 b:p, 8 milling balls), the hydride forms large plate-type particles which are >10 μm in width. At higher magnification, the small particles on the surface of the "host" hydride particles show a polydisperse size distribution. After 5 h milling under the harsher conditions (Sample **18**), the larger hydride particles have been significantly reduced in size, but again the particle size distribution in the sample is polydisperse, with roughly spherical samples being shown to range from sub-micron to >10 μm in diameter.

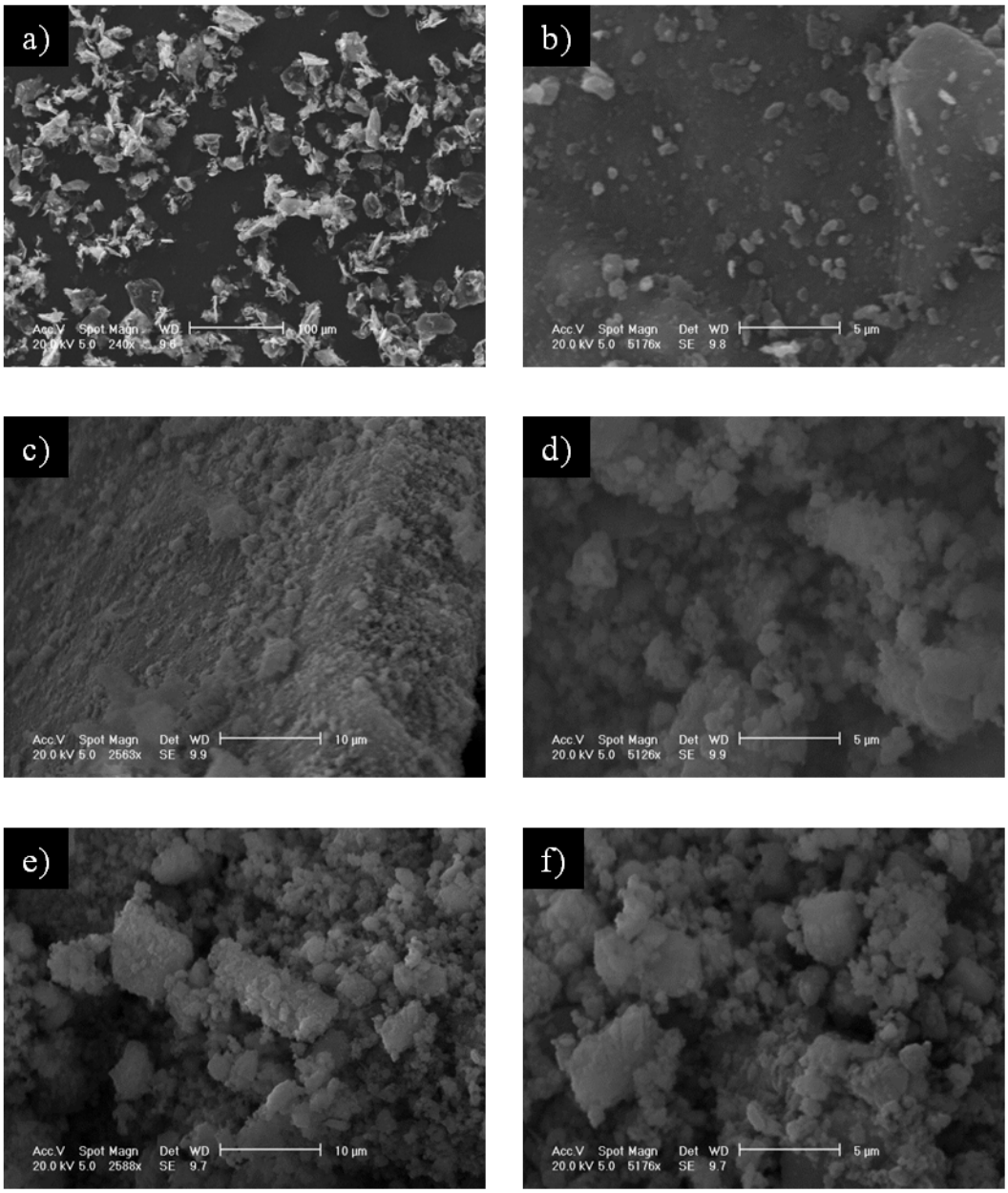

Figure 3-26 SEM image of a) as-received graphite (100 µm scale), b) Sample 15, c & d) Sample 17, and e & f) Sample 18.

For Samples **13-16**, the α-MgH_2 reflections appear relatively unchanged after milling with no evidence to suggest magnesium carbide formation, and this is consistent with the negligible solubility of C in Mg.[91] As expected, the (002) reflection for graphite at $2\theta \approx 26.5^{o}$ becomes more prominent as the additive loading is increased (Figure 3-27). From this, an estimate of the graphite crystallite size parallel to the *c*-direction was determined using the Scherrer method, applying a Scherrer constant of K = 0.91.[92] This indicated that the particles sizes for graphite in the MgH_2 samples with 1 and 5 wt% graphite were approximately 813 nm and 1.6 µm, respectively, while the graphite in both the 10 and 20 wt% samples was 1.9 µm.

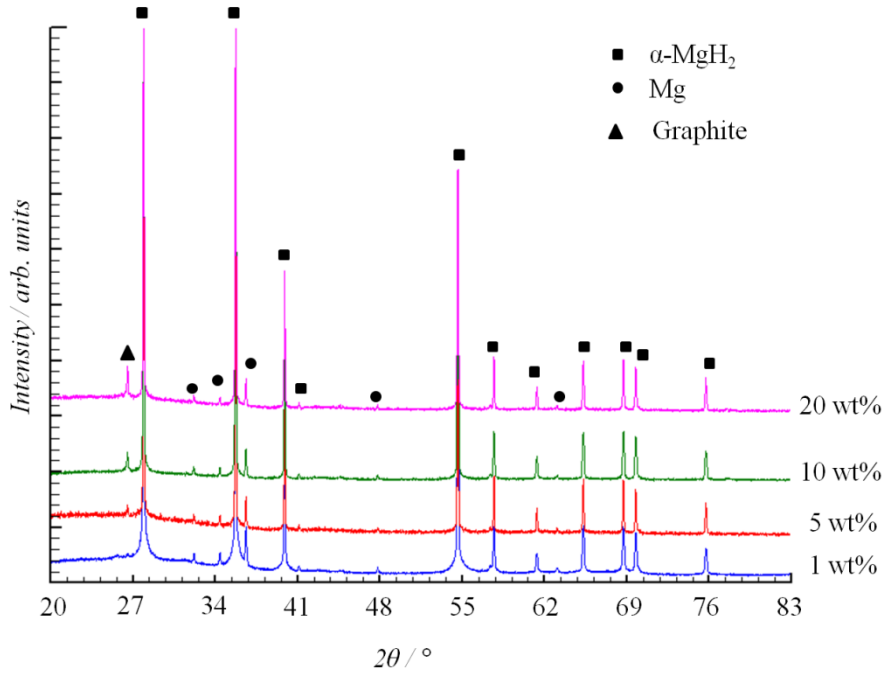

Figure 3-27 PXD of MgH_2 Samples 13-16.

Slight broadening of the hydride reflections is evident but no peak shifts are observed. There does not appear to be any contribution from Fe as a contaminant from the milling tools, nor is there any evidence for MgO reflections resulting from significant oxidation.

Diffraction data for samples milled under harsh conditions for different durations are distinct where the diffraction pattern shown here for the 5 h milled sample is symptomatic of MgH_2 milled for longer durations (Figure 3-28). The average particle size of α-MgH_2 in the 2 h and 5 h samples was approximated using the Scherrer method and found to be 1.9 µm and 1.4 µm, respectively. This suggests that the particles sizes are reasonably similar, but does not account for a highly polydisperse particle size distribution which is likely to be the case for samples milled for longer.

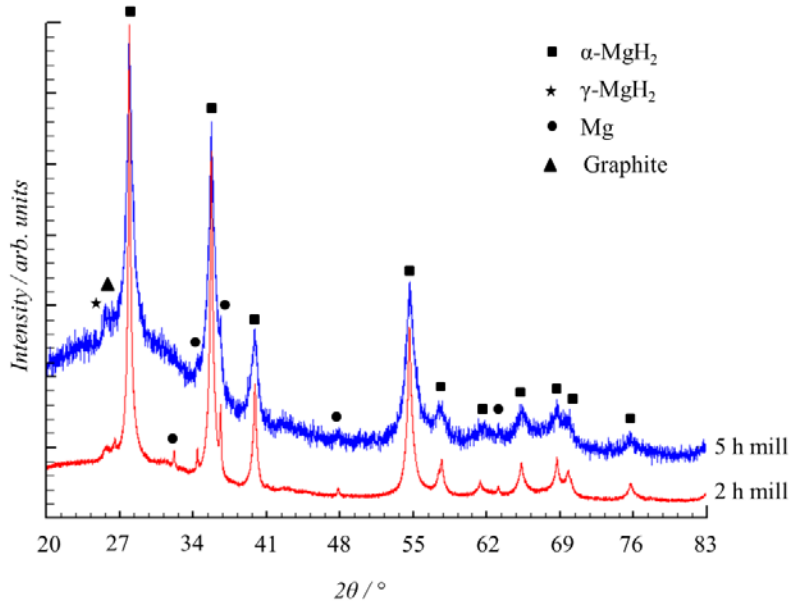

Figure 3-28 PXD of MgH_2 samples 17 (red) and 18 (blue).

Under the milder conditions employed (Samples **13-16**), increased proportions of graphite had a negative effect on the thermal decomposition of the hydride in comparison to the milled hydride itself, where the hydrogen desorption temperature of the composites actually increased with increasing graphite proportions (Figure 3-29a & b). The study of MgH_2-graphite composites by Shang and Guo also indicated that the hydrogen desorption properties of MgH_2 were not enhanced at relatively mild milling conditions upon inclusion of higher graphite proportions.[93] Mass loss associated with hydrogen release began earliest in the MgH_2-5 wt% graphite sample (Sample **14**), but in fact the 1 wt% sample (Sample **13**) performed best with respect to reducing the initial T_{peak}. Furthermore, the markedly sharper gradient of the TG data indicates that the initial hydrogen desorption kinetics of the 1 wt% sample is improved relative to the other samples. Evidence of a two-step process in the DSC curve was observed in the work of Zhou *et al.* who milled MgH_2 with coal derived carbon.[39] The effect of milling time was shown to have a significant impact on the position of the two DSC peaks of MgH_2, where longer milling times enhanced the first DSC peak, while the second event stayed relatively constant and the authors implied that this was a result of a greater proportion of γ-MgH_2 in the samples. The same conclusion regarding the increased proportions of the γ-MgH_2 cannot be drawn here, as the presence of γ-MgH_2 was not observed by PXD. Upon further inspection of the DTA profiles, the estimated total enthalpy of decomposition (Table 3-15) is seen to drop as the loading levels are increased, and all are well below that of the commercial, un-milled hydride but comparable to milled MgH_2 without graphite (see section 3.3). Thermal decomposition begins at the lowest temperature with the 5 wt% doped sample milled under mild

conditions. Figure 3-29c & d give the DTA and TG data for Samples **17** and **18**, where, the T_{onset} and T_{peak} for Sample **18** are slightly higher than those recorded for Sample **17**.

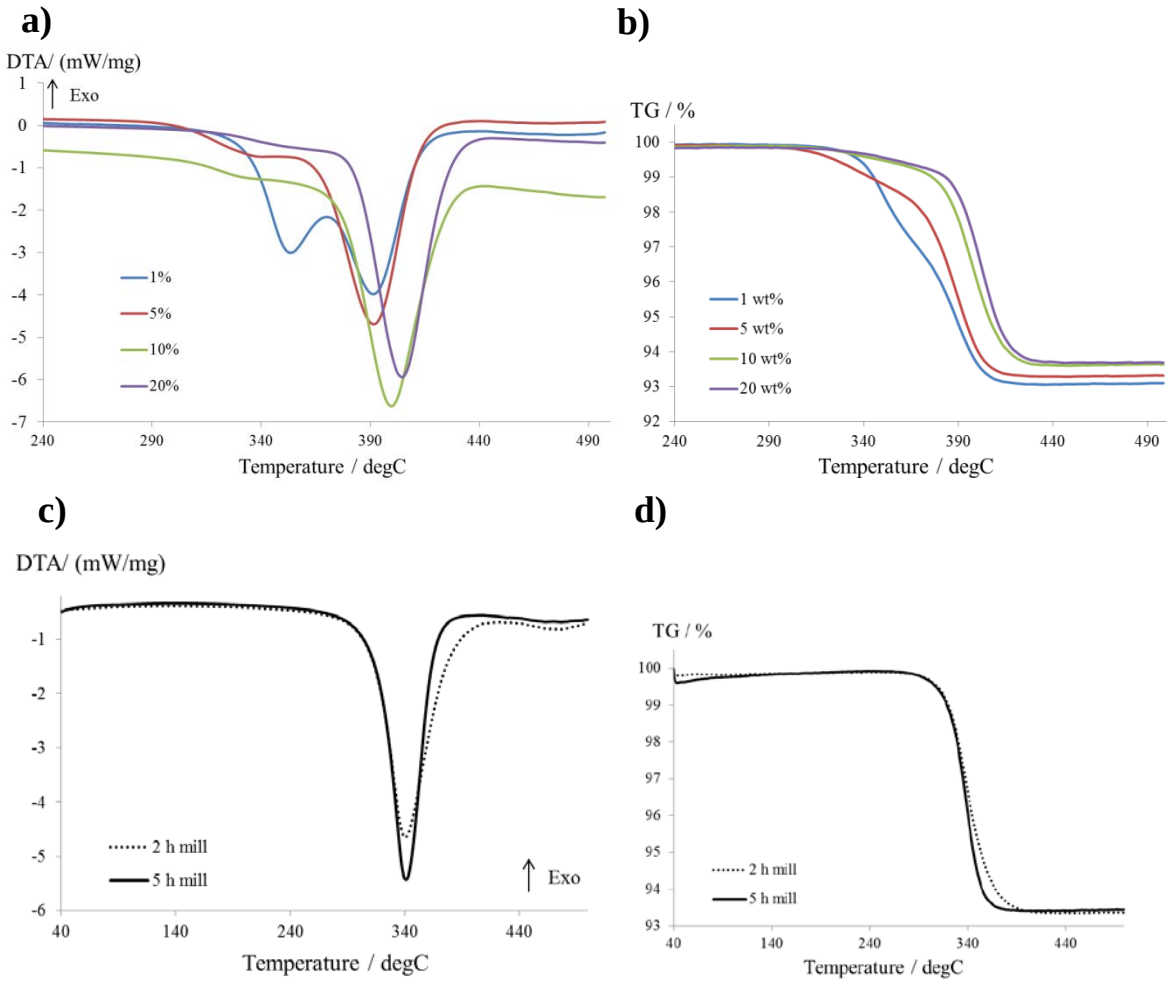

Figure 3-29 a & b) DTA and TG data respectively for Samples 13-16. c & d) DTA and TG data respectively for Samples 17 (dashed line) and 18 (solid line).

PXD analysis of the samples retrieved after STA once again allowed analysis of the graphite (002) reflection by the Scherrer method. This revealed that the particle size for the 5 wt% (as-milled: 1.6 µm → post-STA: 1.4 µm) and 20 wt% (as-milled: 1.9 µm → post-STA: 1.6 µm) samples milled at mild conditions were slightly smaller after thermal analysis than in the as-milled sample.

Table 3-15 Thermal analysis data for MgH_2-x wt% graphite (Samples 13-18).

Sample ID	wt% additive	DTA		TG		†E_{dec} / kJ/mol
		T_{onset} / °C	T_{peak} / °C	T_{onset} / °C	Mass Loss / %	
13	1	LT: 334.4 HT: 375.5	LT: 353.6 HT: 391.5 ΔT = 37.9	LT: 336.8 *364.2	LT: 2.97 HT: 3.90 ∑ = **6.87**	64.38
14	5	LT: 300.9 *341.8	HT: 391.4	LT: 262.5 *341.6	LT: 0.89 HT: 5.75 ∑ = **6.64**	60.27
15	10	LT:305.1 *342.0	HT: 399.6	LT: 287.1 *342.0	LT: 0.34 HT: 5.94 ∑ = **6.28**	57.00
16	20	LT: 320.6 *355.6	HT:404.4	LT: 306.2 *355.6	LT: 0.33 HT: 5.81 ∑ = **6.14**	54.75
17	5	312.1	340.4	321.6	6.50	57.27
18	5	315.5	341.1	321.8	6.50	53.83

(* indicates an inflection in the gradient of the curve at a given temperature, and the ΔT= T_{HT}-T_{LT} is given for the endothermic maxima where a two-step decomposition is observed. † E_{dec} determined from data collected at 5 °C/min.)

Raman spectroscopy helped to indicate whether the graphite was affected in the milling process and also after hydrogen desorption (Figure 3-30). The relative intensity ratio for the two characteristic first order Raman stretches of graphite is a reasonable indicator for structure characteristics of carbon materials.[94, 95] The first order D and G bands are found at ~1350 cm^{-1} and ~1580 cm^{-1}, respectively, and the I_D/I_G relative intensity ratio has been determined for these samples by reading the maximum intensity value from the spectra for the observed bands. These Raman active modes are related to the D_{6h} symmetry function of the of $P6_3/mmc$ space group to which the layered graphitic carbon structure may be assigned. The D band has been described as indicative of smaller graphite crystallite sizes, while the G band provides information about C-C E_{2g} stretching.[96] Raman spectra for all of the graphite doped samples show that the I_D/I_G ratio increases after milling (Table 3-16). This is consistent with findings from literature, where the I_D/I_G ratio was observed to increase from 0.8 to 3.49 after milling MgH_2 with 5 wt% graphite in the work of Huang *et al.*, indicating a higher proportion of disordered graphite in the milled samples.[97] After heating, the relative intensity ratio, I_D/I_G, was again found to increase, which indicates that

the carbon structure may be further modified upon heating to decompose the hydride. The presence of a weak band at ~2700 cm^{-1} confirms that the graphite particles are small but a degree of crystallinity remains. Huang *et al.* suggest that the I_D/I_G ratio was relatively unchanged upon rehydrogenation of the milled Mg-graphite composite.[64] Raman spectra of the dehydrogenated products in their study were not shown and so it is not possible to say to what degree the structural modifications occur in the graphite upon rehydrogenation in their earlier work relative to the findings here. However, it may be postulated that the structure of the graphitic carbon may have an important role in the hydrogen release process from MgH_2, where the particle size of polycrystalline graphite may be crucial for enhanced activity in this system.

Table 3-16 Relative Raman intensity ratios, I_D/I_G, for Samples 13-16.

	I_D/I_G	
Sample	**Post Mill**	**Post STA**
13	1.04	1.26
14	1.29	1.30
15	1.10	1.28
16	1.20	1.21

(I_D/I_G = 0.35 for un-milled, commercial graphite used in this work).

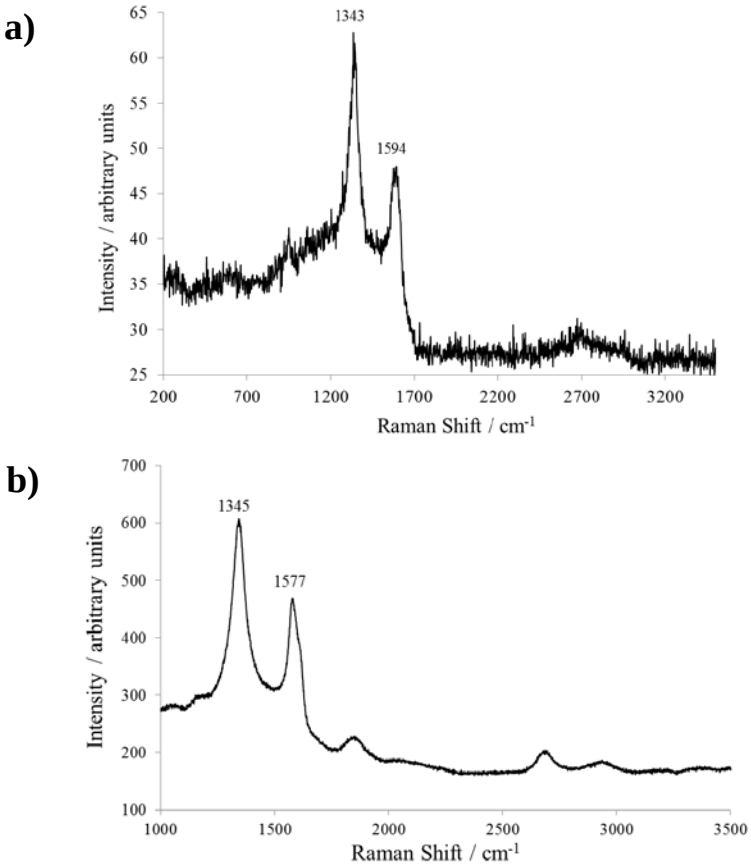

Figure 3-30 Raman spectra of Sample 14 a) as-milled and b) post STA product.

3.4.1.1. Summary of Graphite Additive Effects

The effect of graphite on the Mg-H system has been explored under the mild and harsh milling conditions selected for this work. At mild milling conditions, the thermal analysis results show that the HT decomposition is stabilised by addition of the graphite, resulting in a poorer performance of the hydride relative to the material milled under the same conditions without additive. At harsher conditions, a similar effect from the graphite is not apparent, and in fact the total enthalpy of decomposition for the one step decomposition is decreased relative to the un-doped sample. The T_{peak}, however, is not significantly decreased. Raman analysis has given significant insight into the properties of graphite after milling with MgH_2 and after the 1st desorption, and indicates that a high dispersion of small crystalline particles of graphite may be involved in the improvements observed in the enthalpy of desorption. Based on XPS (X-ray Photoelectron Spectroscopy) data, Bouachira *et al.* suggest that improvements in Mg milled with graphite are due to the inhibition of oxide layer formation, where this was accredited to the adsorption of a graphene layer over the surfaces of the particles.[67, 68] Furthermore, they proposed that highly reactive C species (derived from radicals formed by the rupture of C-C graphene bonds during milling of graphite) may react with oxide species or diffuse on to the Mg surfaces, and thus prevent

oxide re-formation. This has recently been corroborated in the work of Lototskyy *et al.* using a variety of carbon based additives.[51] A study using XPS recently demonstrated that carbon nanorods decorated with Ni are shown to prevent particle agglomeration as a result of the dispersion of carbon over the hydride surfaces, resulting in improved cyclic stability.[98]

Literature on use of graphene with MgH_2 is emerging. In recent work by Liu *et al.*, they demonstrate that the performance of graphene as an additive for MgH_2 may be enhanced by inclusion of nanomaterials on the graphene layers.[99] This was demonstrated by embedding amorpous TiB_2 nanoparticles on graphene nanosheets (GNS), then milling of 5 wt% of the TiB_2-GNS composite with MgH_2. A synergistic effect was observed for the TiB_2-GNS in comparison to the 5 wt% TiB_2-MgH_2 and 5 wt% GNS-MgH_2 samples. The novel composite revealed a decomposition temperature 44 °C lower than the as-milled, undoped MgH_2 to give a decomposition T_{peak} of 319 °C. Furthermore, a significant improvement in the desorption kinetics was observed, where they obtained >6 wt% H_2 from the 5 wt% TiB_2-GNS doped MgH_2 in <10 min using 5 kPa at 300 °C. Liu *et al.* suggest that the observed improvements for H_2 release from MgH_2 in the 5 wt% TiB_2-GNS doped samples is the result of enhanced hydride-dopant interfaces, with a high number of catalytic sites and H "diffusion channels".

3.4.2. MgH_2-*x* wt% Silicon Carbide (*x* = 1-20 wt%)

Silicon carbide has already been shown to improve the properties of MgH_2 and, for comparative purposes using the conditions employed previously for graphite in this study, MgH_2-x wt% SiC composites were prepared and investigated further (Table 3-17). Confirmation by PXD analysis of the commercial as-received product showed that the carbide used was the most common 6H-SiC polymorph.[100]

Table 3-17 MgH_2-x wt% SiC samples (x = 1-20 wt%).

Sample	*x* wt% additive	B:P ratio	No. Milling Balls	Milling Duration / h
19	1	40:1	2	5
20	5	40:1	2	5
21	10	40:1	2	5
22	20	40:1	2	5
23	5	80:1	8	2
24	5	80:1	8	5

SEM images for Sample **21** show that the particle size has been modified, although the MgH_2 particles exist in large flat plates which are ~16 μm in width (Figure 3-31a). At higher magnification, it is possible to see that the particles size is polydisperse, with the majority of particles at the micron scale although some sub-micron particles were observed (Figure 3-31b). Milling for 2 h (Sample **23**, Figure 3-31c & d) and 5 h (Sample **24**, Figure 3-31e & f) at harsher conditions shows a significant difference in the particle size relative to the mild conditions used where images of these samples reveal sub-micron sized particles, although some larger particles, ~5 μm, remain.

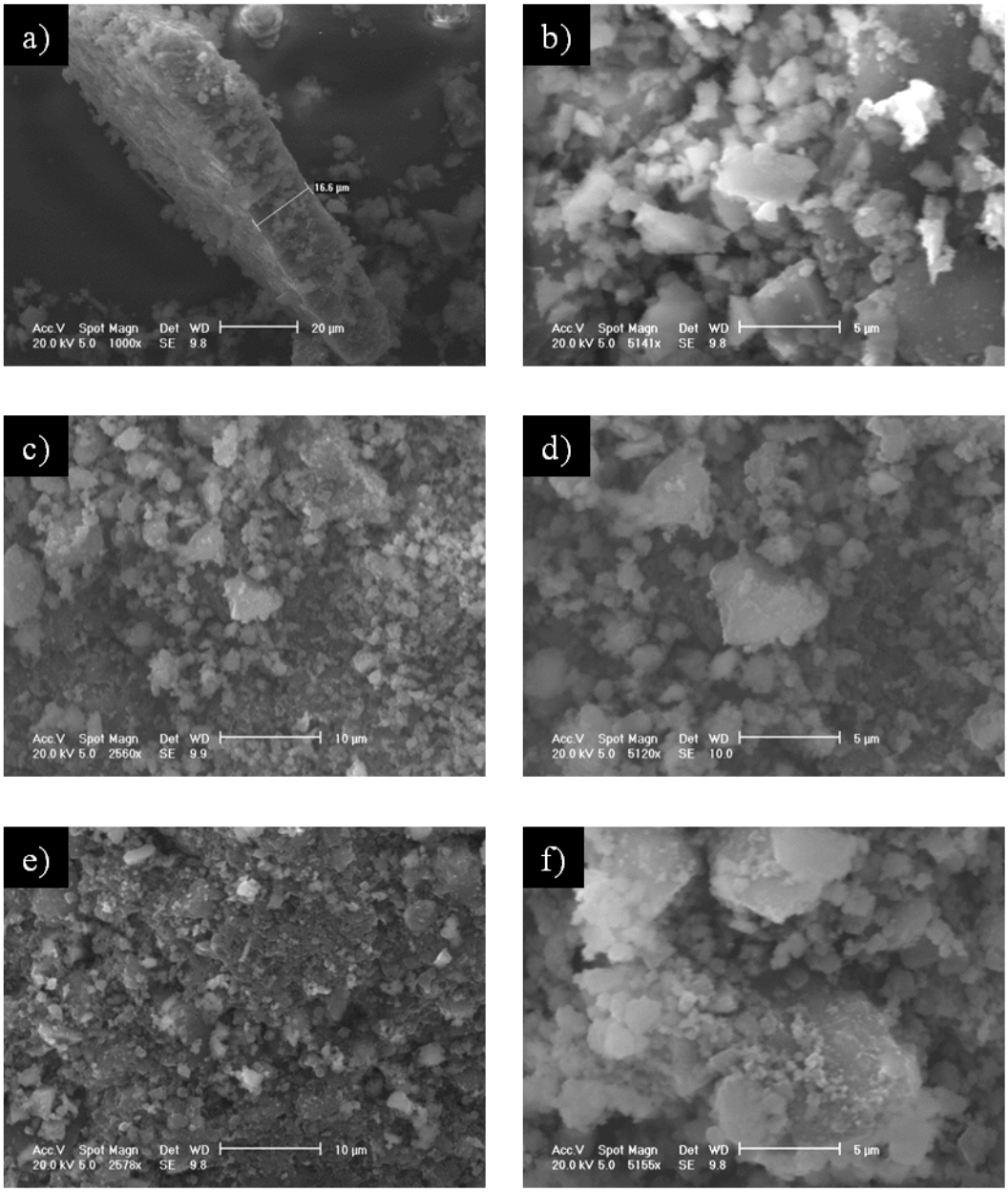

Figure 3-31 SEM micrographs of (a & b) Sample 21, (c and d) Sample 23 and (e & f) Sample 24 using low and high magnification.

Samples milled under mild conditions show slight broadening of the reflections and the emergence of Fe upon 10 wt% SiC inclusion (Figure 3-32).

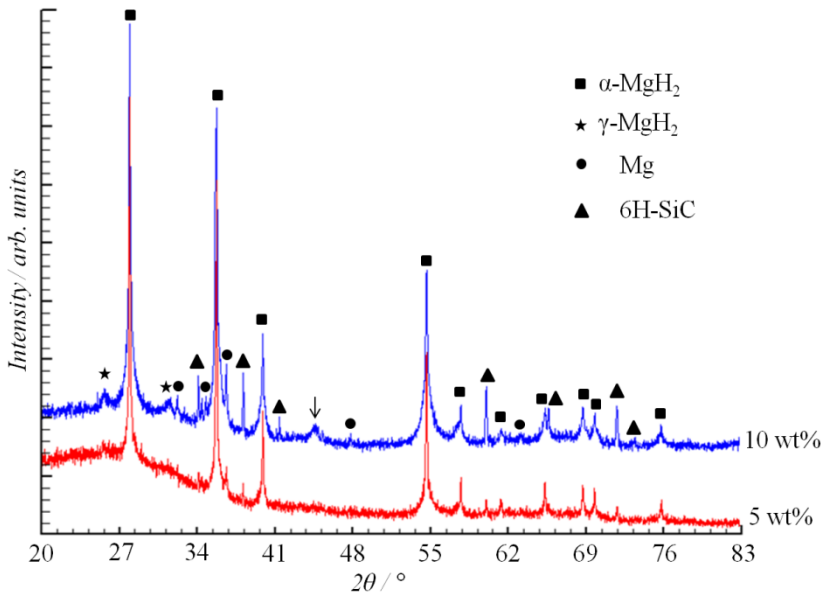

Figure 3-32 Exemplar PXD patterns of MgH_2 milled Samples 20 and 21. (Downward arrow indicates Fe reflection from stainless steel milling tools.)

The diffraction patterns of the samples milled under harsh conditions (Samples **23** and **24**) show significantly broadened reflections for α-MgH_2 with respect to the samples milled under milder conditions, indicating a decrease in particle size (Figure 3-33). Contamination from the steel milling tools is evident in these samples, where an approximate threefold increase in the relative intensity of the (110) reflection for Fe ($2\theta = 44.60^{\circ}$) was determined for Sample **23** relative to Sample **24**. From PXD, the same degree of contamination was not evident for the samples milled under mild conditions. A similar contamination effect, however, has been observed in literature when milling SiC only in stainless steel media for particle size reduction.[101] In previous work on MgH_2-x wt% SiC composites, also conducted in a steel milling vessel, a reflection in this region was assigned to MgO by Ranjbar.[102] In the work of Kurko *et al.*, an unassigned reflection which would match that of Fe is also apparent but unexplained.[103]

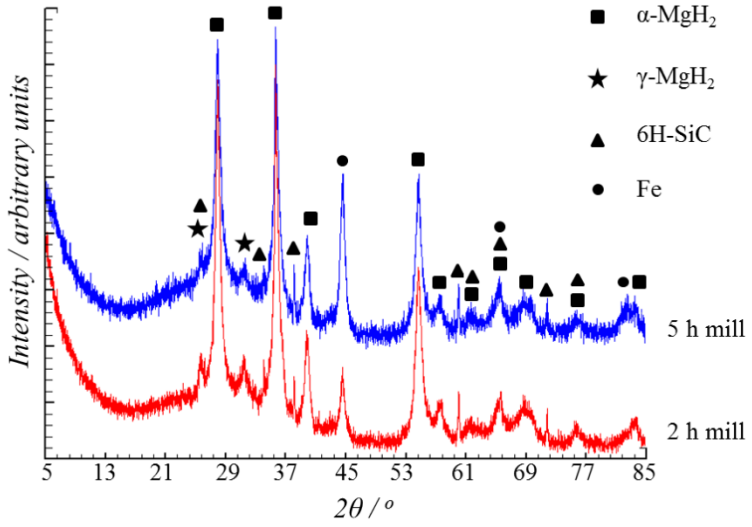

Figure 3-33 PXD of Sample 23 and Sample 24.

The crystallite size was found to be markedly improved, *i.e.*, reduced, by use of harsher milling conditions using 5 wt% SiC. The average crystallite size (approximated using the Scherrer method) for Sample **20** and was determined to be > 2 μm in size, while the average crystallite size of those milled under harsh conditions were significantly diminished. The 5 h milled sample (Sample **24**) was actually found to be larger than that of the 2 h sample (Sample **23**), 489 nm and 407 nm respectively, and this may be the result of agglomeration in the former.

Raman analysis of the SiC samples did not show significantly resolved peaks at loadings beyond 1 wt% of SiC, where broadening of the noisy signals shown in Figure 3-34 worsen at higher carbide loading and using harsh milling conditions. There is evidence, however, to suggest weak bands at ~765 cm^{-1} and 930-940 cm^{-1} for SiC in the subsequent samples milled under mild conditions. For Samples **20 – 24** milled under harsh conditions, these bands lie at a slightly lower Raman shift than expected for SiC; ~780 cm^{-1} and ~960 cm^{-1} for the TO (Transverse Optical phonon mode) and LO (Longitudinal Optical phonon mode) bands, respectively. This shift is likely to be the result of amorphization of the carbide.[104]

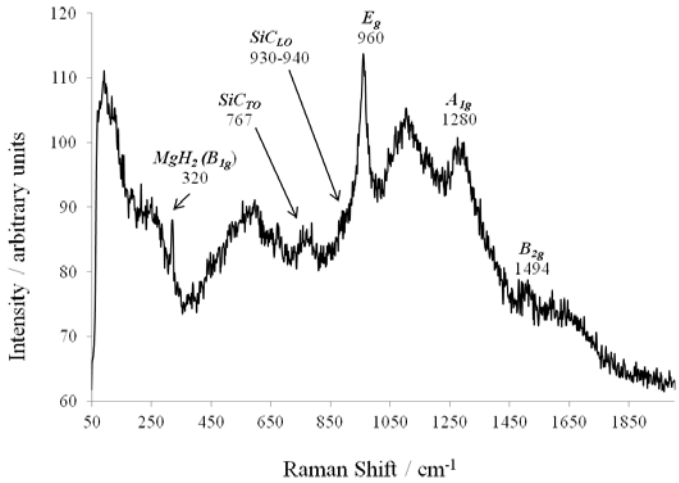

Figure 3-34 Raman spectrum collected for Sample 19.

Comparison of thermal analysis data for the samples milled under mild conditions (Samples **19-22**) indicates that the LT peak becomes enhanced upon an increase in additive loading up to 10 wt%, at which point the DTA trace indicates only one peak (Figure 3-35a & b, Table 3-18). Using 20 wt% (Sample **22**), the thermal properties appear significantly different. A two-step decomposition re-emerges, and this is similar to that observed by Ranjbar *et al.*, who suggest that elevated SiC doping levels affect the hydrogen desorption pathways, leading to diminished hydrogen storage properties, for instance, lower hydrogen capacity, high hysteresis upon cycling, poor sorption kinetics.[81] These effects were attributed to the dopant blocking the hydrogen diffusion pathways at elevated loading levels. Their work suggested an optimised doping level of the SiC to be 5 wt%. At harsh milling conditions using 5 wt% SiC in this work (Samples **23** and **24**, the T_{peak} of the hydride is shown to be remarkably improved both in relation to the un-doped samples and also relative to the results of Ranjbar and colleagues (Figure 3-35c & d). The distinction between the desorption properties observed in this work and that seen previously is likely to be a direct result of the milling conditions employed, where reactive milling under H_2 was employed to produce the composites described by Ranjbar *et al*.

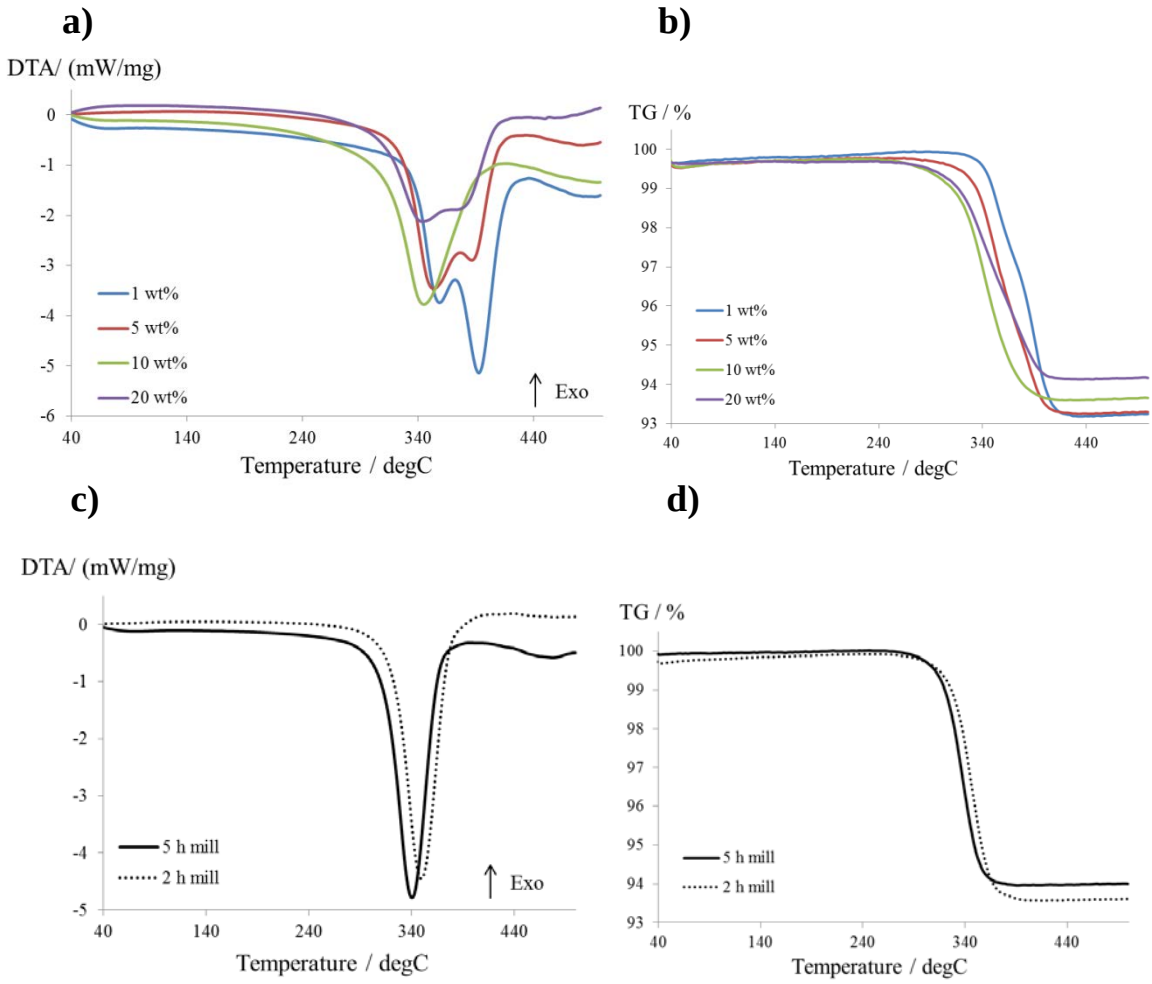

Figure 3-35 a & b) DTA and TG traces respectively for Samples 19-22, c & d) Comparison of DTA-TG traces for Sample 23 (dashed line) and Sample 24 (solid line).

Table 3-18 Thermal analysis data for Samples 19-24.

Sample	*x* wt% additive	DTA T_{onset} / °C	DTA T_{peak} / °C	TG Mass Loss T_{onset} / °C	TG Mass Change / %	†E_{dec} / kJ/mol
19	1	**LT:** 335.6 **HT:** 377.6	**LT:** 358.3 **HT:** 392.3 ***ΔT*** = 34.0	**LT**: 341.1 *372.5	**LT:** 2.88 **HT:** 3.84 **∑= 6.72**	63.06
20	5	**LT:** 327.0 **HT:** 378.6	**LT**: 353.3 **HT**: 386.4 ***ΔT*** = 33.1	LT: 337.1 *365.7	**LT:** 3.67 **HT:** 2.80 **∑ = 6.47**	60.01
21	10	‡313.7	344.7	316.8	**6.15**	52.48
22	20	**LT**:310.9	**LT:** 344.3 *369.2	**LT**:317.6 *357.6	**LT:** 3.16 **HT:** 2.36 **∑ = 5.52**	50.56
23	5	322.0	349.2	325.5	**6.35**	54.09
24	5	312.3	340.1	319.7	**6.03**	51.30

(* indicates an inflection in the gradient of the curve at a given temperature, and the ***ΔT*** = T_{HT}-T_{LT} is given for the endothermic maxima where a two-step decomposition is observed. † E_{dec} determined from data collected at 5 °C/min. ‡Asymmetric peak.)

Destabilisation of the MgH_2 system using Si has been studied previously, where the formation of magnesium silicide during the decomposition process was determined as the mechanism by which a reduction in the decomposition temperature of MgH_2 was achieved (Equation 3-2).[105] The drawback of this reaction is the irreversible nature of the Mg_2Si formation. Mg does not readily form a hydride, and therefore if added as a relatively small wt% dopant reduces the total Mg available for reversible hydrogen storage in systems of this kind.

Equation 3-2

$$MgH_2 + Si \rightarrow Mg_2Si + H_2$$

The PXD results for the post-STA samples do not show the presence of magnesium silicide (or Si) in analogy to the work of Olsen and Vajo (Figure 3-36), which is expected based on the high thermal stability of SiC (~2700 °C).[106] This suggests that the reversibility of the samples prepared here are not likely to suffer from diminished cyclability properties as a result of side reactions involving Si within the temperature range used for hydride decomposition and rehydrogenation.

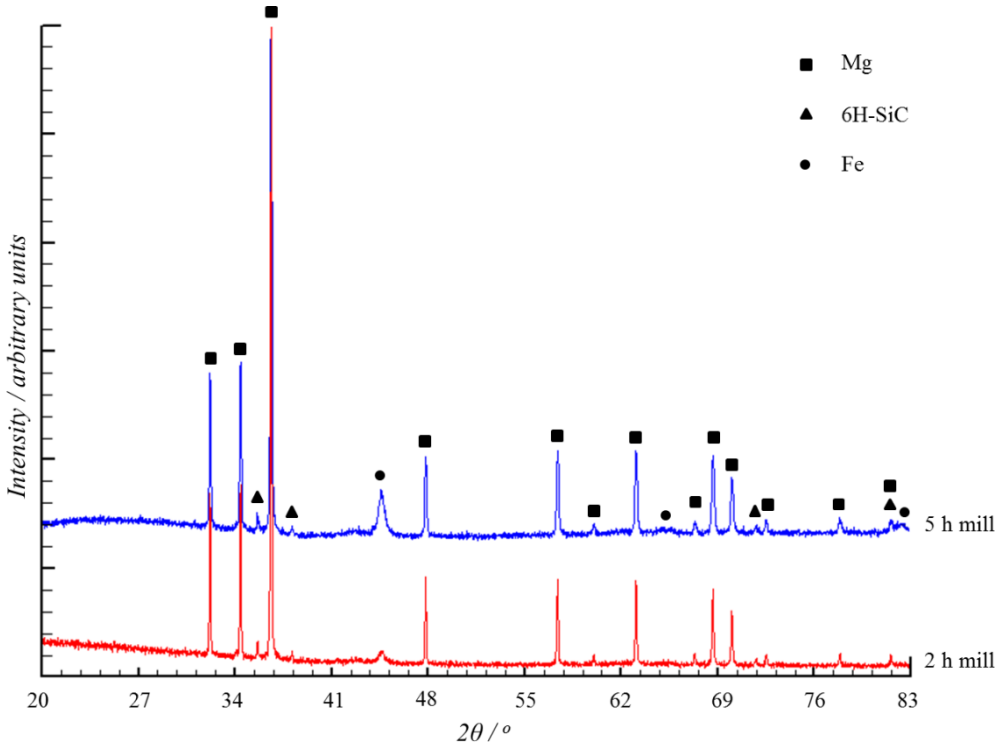

Figure 3-36 Post STA PXD analysis of samples milled for 2 h (Sample 23, red) and 5 h (Sample 24, blue).

Imamura reported significant improvement for MgH_2-22 mol% SiC nanocomposites milled in cyclohexane, although they reported a loss of 5.3 wt% hydrogen during milling.- From the data provided in Table 3-18, the MgH_2-*x* wt% SiC composites prepared in this work (with the exception of Sample **22**) show hydrogen release exceeding 6 wt%, and therefore any apparent hydrogen loss in the mill is comparatively small.

3.4.2.1. Summary of SiC Additive Effects

It is clear from this work that SiC generates severe attrition conditions in which comminution of MgH_2 particles occurs. The presence of Fe suggested from the diffraction patterns indicates contamination from the stainless steel milling media, which highlights the intensity of the milling procedure in the MgH_2-*x*SiC samples relative to the milled, un-doped MgH_2 and MgH_2-*x*Graphite samples, in which no evidence of Fe contamination was found. The thermal desorption properties of the SiC doped samples are not significantly improved relative to the Graphite doped samples, where the T_{peak} values at the same milling conditions with the same dopant loadings were not dramatically reduced. In fact, the T_{peak} values for samples milled for 2 h and 5 h at the harsher conditions were nominally the same as those for the analogous Graphite doped samples. The E_{dec} values were only marginally reduced. It is expected that the harsh conditions which arise as a result of the inclusion of the hard carbide actually contribute to a degree of particle agglomeration that

hinders the hydride by increasing the path length of hydride diffusion. Therefore, it seemed prudent to combine the harsh milling properties of the SiC dopant with the potentially catalytic properties of graphite that may also act as a milling lubricant and in turn could reduce the severity of the milling action to prevent contamination from the milling tools.

3.4.3. MgH_2-*x* wt% Silicon Carbide:Graphite (*x* = 1-20 wt%)

A 1:1 molar mixture of SiC and graphite was mixed thoroughly using an agate mortar and pestle on the open bench. The additive was then added in 1 - 20 wt% proportions to MgH_2 and milling conducted under a number of different conditions to establish optimum conditions and additive proportion for this system (Table 3-19).

Table 3-19 Sample data for MgH_2-x wt% SiC-graphite.

Sample ID	*x* wt% additive	B:P ratio	No. Milling Balls	Milling Duration /h
25	1	40:1	2	5
26	5	40:1	2	5
27	10	40:1	2	5
28	20	40:1	2	5
29	1	80:1	8	2
30	5	80:1	8	2
31	10	80:1	8	2
32	20	80:1	8	2

SEM images show that particle size is influenced by the additive even under mild milling conditions. Under mild conditions (Samples **25-28**), smaller particles exist on the surface of larger “host” particles rather than an overall reduction in size of the material (Figure 3-37a) & b)). At higher magnification, the smallest particles were found to be nano-sized (Figure 3-37c)). Backscattered electron imaging (Figure 3-37d)), shows that there is a degree of contamination from the stainless steel milling jar, where the brighter regions indicate heavier elements, *i.e.*, Fe from the stainless steel. Samples **29-32** appear to be comprised of smaller particles overall, relative to the highly polydisperse samples prepared under milder conditions. The “host” particles appear to have been broken down, which will increase the overall surface area of the sample.

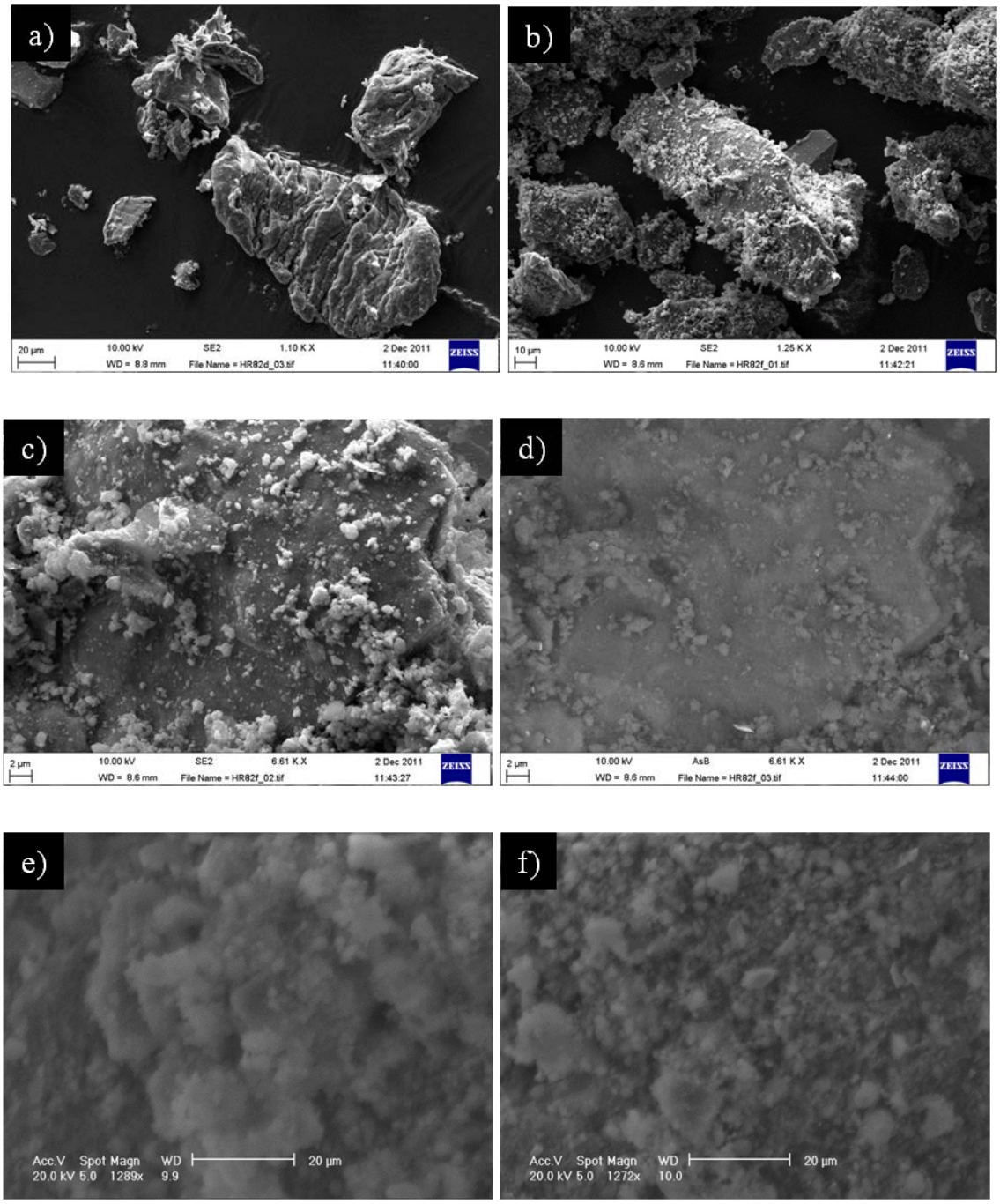

Figure 3-37 SEM images comparing commercial MgH_2 milled under mild conditions a) without additive (20 µm) and b) Sample 28 (10 µm). Images of Sample 28 at higher magnification using c) secondary electron and d) back scattering electron imaging. SEM images for e) Sample 29 and f) Sample 32 (20 µm).

PXD analysis of the as-milled samples revealed crystalline MgH_2, Mg and the SiC additive, however, no reflections were evident for graphite or γ-MgH_2 (Figure 3-38).

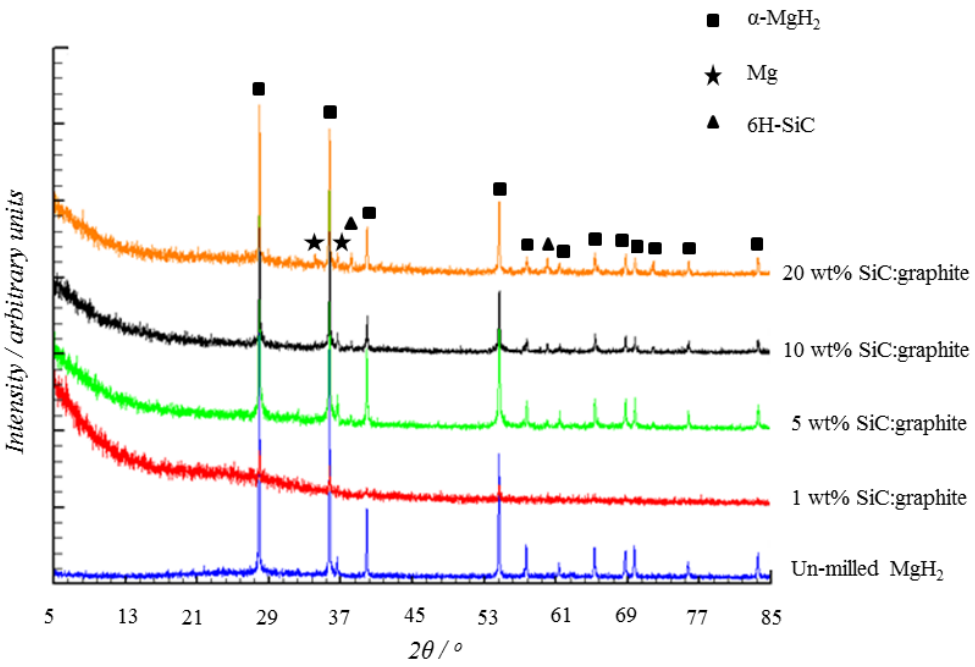

Figure 3-38 PXD data for Samples 25-28.

EDX data for Sample **30** shows that the Si and C are well-dispersed in the MgH_2 sample although some clustering of carbon is evident (Figure 3-39). The presence of Fe shows evidence of contamination from the milling tools used, and oxygen appears as with the commercial, milled MgH_2.

a)

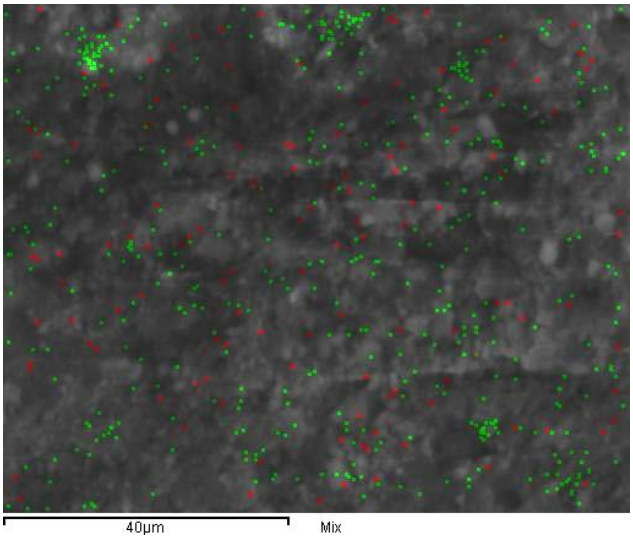

b)

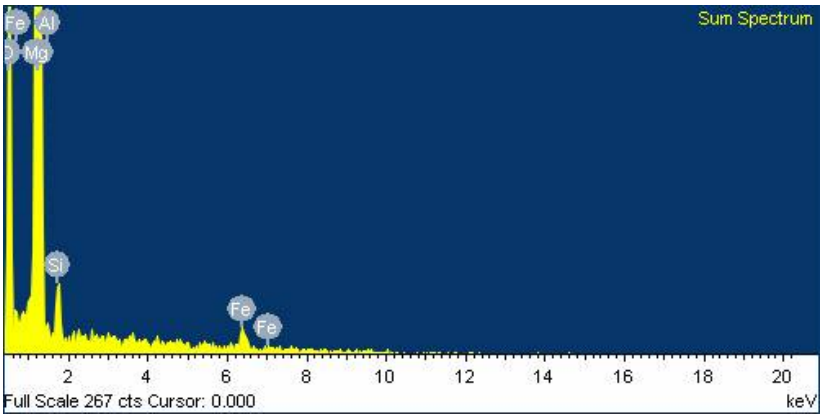

Figure 3-39 a) Map of elemental Si (red) and C (green) dispersion (40 µm) and b) EDX spectrum for Sample 30.

The effect of using both SiC and graphite shows a distinct change in the two-step decomposition observed in the DTA trace (Figure 3-40, Table 3-20). Comparing DTA traces for Samples **25-28**, it is evident that the LT peak is enhanced upon increasing additive loading as observed with the SiC-only samples under the same conditions. The greatest difference in T_{peak} between the LT and HT events was determined for Sample **27**.

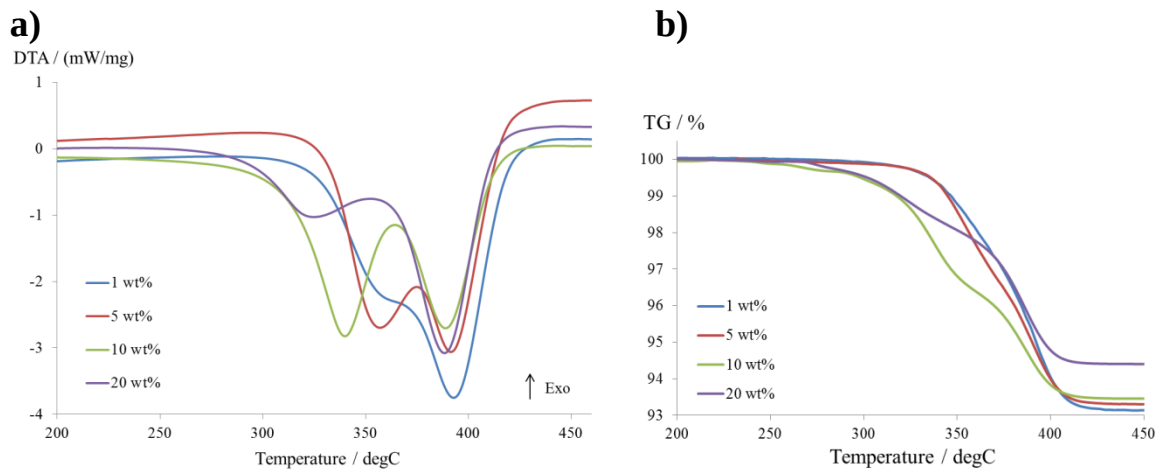

Figure 3-40 **DTA & TG data collected using 5 °/min heating rate for Samples 25-28.**

Table 3-20 **DTA-TG data for Samples 25-28.**

Sample	wt% additive	DTA T_{onset} / °C	DTA T_{peak} / °C	TG Mass Loss T_{onset} / °C	TG Mass Change / %	†E_{dec} / kJ/mol
25	1	LT:327.3 *363.8	 HT: 393.2	LT: 357.4 *389.6	LT: 4.71 HT: 2.14 ∑ = 6.85	65.62
26	5	LT: 331.5 HT: 378.6	LT: 357.0 HT: 391.4 ***ΔT*** = 34.4	LT: 337.0 HT:373.9	LT: 3.38 HT: 3.25 ∑ = 6.63	60.19
27	10	LT:314.4 HT:369.9	LT:339.9 HT: 388.8 ***ΔT*** = 48.9	LT:317.6 *360.5	LT: 3.51 HT: 2.92 ∑ = 6.43	55.46
28	20	LT: 293.1 HT: 367.7	LT: 324.7 HT: 388.3 ***ΔT*** = 63.6	LT: 306.1 *347.5	LT: 1.78 HT: 3.74 ∑ = 5.52	68.98

(* indicates an inflection in the gradient of the curve at a given temperature, and the $\Delta T = T_{HT} - T_{LT}$ is given for the endothermic maxima where a two-step decomposition is observed. †E_{dec} determined from data collected at 5 °C/min.)

Both EDX and PXD analysis indicate the presence of Fe to indicate contamination from milling tools using harsh conditions, which indicates significantly harsh attrition conditions whereby erosion of the stainless steel occurred (Figure 3-39 and Figure 3-41). This effect was not observed in the samples milled at mild conditions where reflections for $Fe_{(110)}$ were not obvious from PXD analysis. Upon comparison of relative intensities for $Fe_{(110)}$ in the PXD patterns of Samples **23** and **30**, a 1.4 fold increase is observed, and so the Fe "pick-up" is more pronounced in the SiC:graphite sample. (The intensity of $Fe_{(110)}$

reflection was measured relative to the MgH_2 phase in each case.) This suggests that the attrition procedure is intensified by inclusion of the SiC:graphite mixture relative to SiC alone. A 15 fold increase in relative intensity for the $Fe_{(110)}$ reflection was determined from the diffraction patterns of Samples **29** and **32**, indicating that the Fe "pick-up" increases dramatically with increasing additive proportions in the sample.

PXD does not indicate reflections which would indicate the presence of an Mg-Si phase, *e.g.*, Mg_2Si. As with the milled MgH_2 sample presented earlier, PXD analysis of Samples **29** and **30** under ambient conditions in Bragg-Brentano geometry indicates no signs of oxidation over a 15 h analysis period (Figure 3-41, Appendix A; A.7). This is a significant finding, since recent work indicates that magnesium hydroxide forms during milling of MgH_2-TiB_2-SiC composites milled under Ar, and thus has a significant impact on the thermal behaviour and cyclability of the composite.[107]

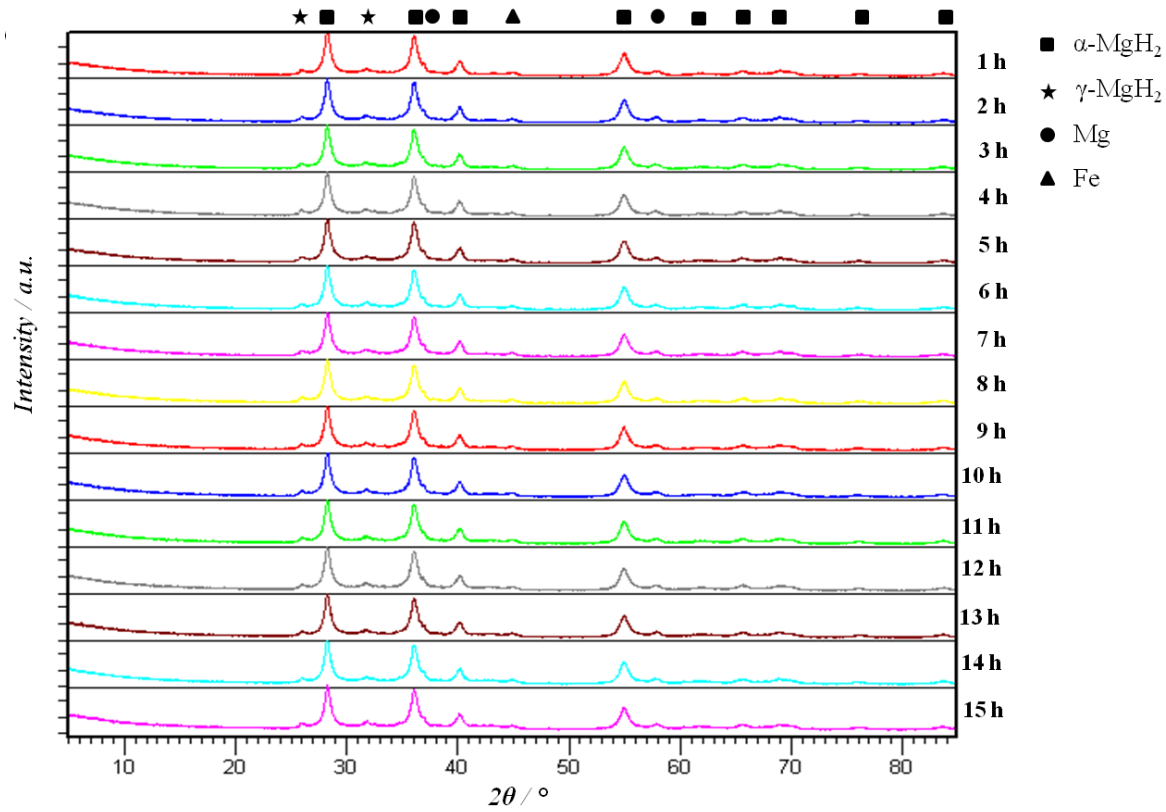

Figure 3-41 Time resolved PXD of Sample 29.

The average particle size approximated by the Scherrer method was shown to decrease upon increased additive proportion by almost a half; Sample **29** was found to be 945 nm and decreased to 489 nm in Sample **32**. In addition, PXD analyses of the samples were collected 2 months apart and the diffraction patterns are unchanged. This indicates that the

hydride may be stored for relatively long durations without a change in the crystallinity or significant oxidation.

FTIR shows a broad band in the 900-1600 cm^{-1} region characteristic of Mg-H stretching in all the composite samples (Appendix A, A.8), with the three more pronounced bands which were observed to emerge in the un-doped, milled MgH_2 shown earlier (Figure 3-24). Zhou *et al.* suggest that the three bands emerging from the broad Mg-H stretch are characteristic of aromatic C-H bonds, which are observed in the FTIR spectra of their milled anthracite coal-doped MgH_2 samples at 890, 1005 and 1143 cm^{-1}.[76] (They do not show the spectra of un-doped, milled MgH_2 for comparison in their paper.) Their study uses these FTIR C-H assignments to justify C-H bond formation *via* chemisorption of hydrogen by unsaturated carbon bonds that are produced in the coal during milling of the coal-hydride composite. Zhou *et al*. state that the hydrogen desorbs faster from the hydrogen in the carbon (*i.e.*, the C-H component) relative to the MgH_2, to explain the faster kinetics of their product. This requires further clarification and more developed analysis to confirm whether the C-H phenomenon occurs during the milling procedure.

Raman analysis of the as-milled and post STA samples revealed again that the effect on the I_D/I_G ratio of graphite was significant (Figure 3-42). The ratio also increased as the proportion of additive increased, *e.g.*, I_D/I_G for Sample **29** was 1.193, and significantly higher (1.40) for Sample **32**. This implies that the graphite in the sample is becoming more amorphous after milling, and the crystallinity of the graphite continues to degrade after decomposition of the composite to 500 ^{o}C.

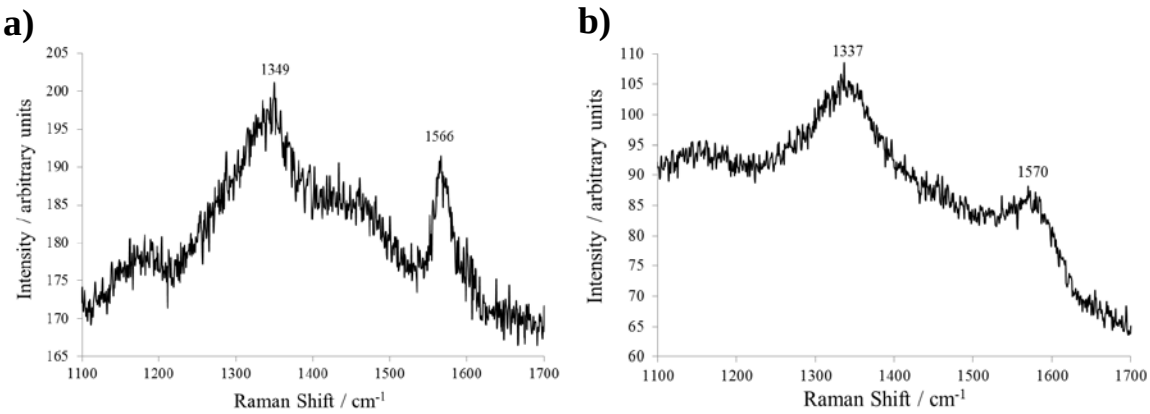

Figure 3-42 Exemplar Raman spectra for SiC-graphite doped MgH_2 milled under harsh conditions; Sample 31 a) as-milled and b) post STA.

The T_{peak} of Samples **29-32** improved with increasing proportions of the additive composite, with the expected consequential decrease in the hydrogen capacity (Figure 3-

43, Table 3-21). Comparing STA data collected at 5 ^{o}C/min, the corresponding MS traces show that the hydrogen release onset occurs much earlier in the doped samples with respect to un-doped MgH_2, even at the lowest composite loading.

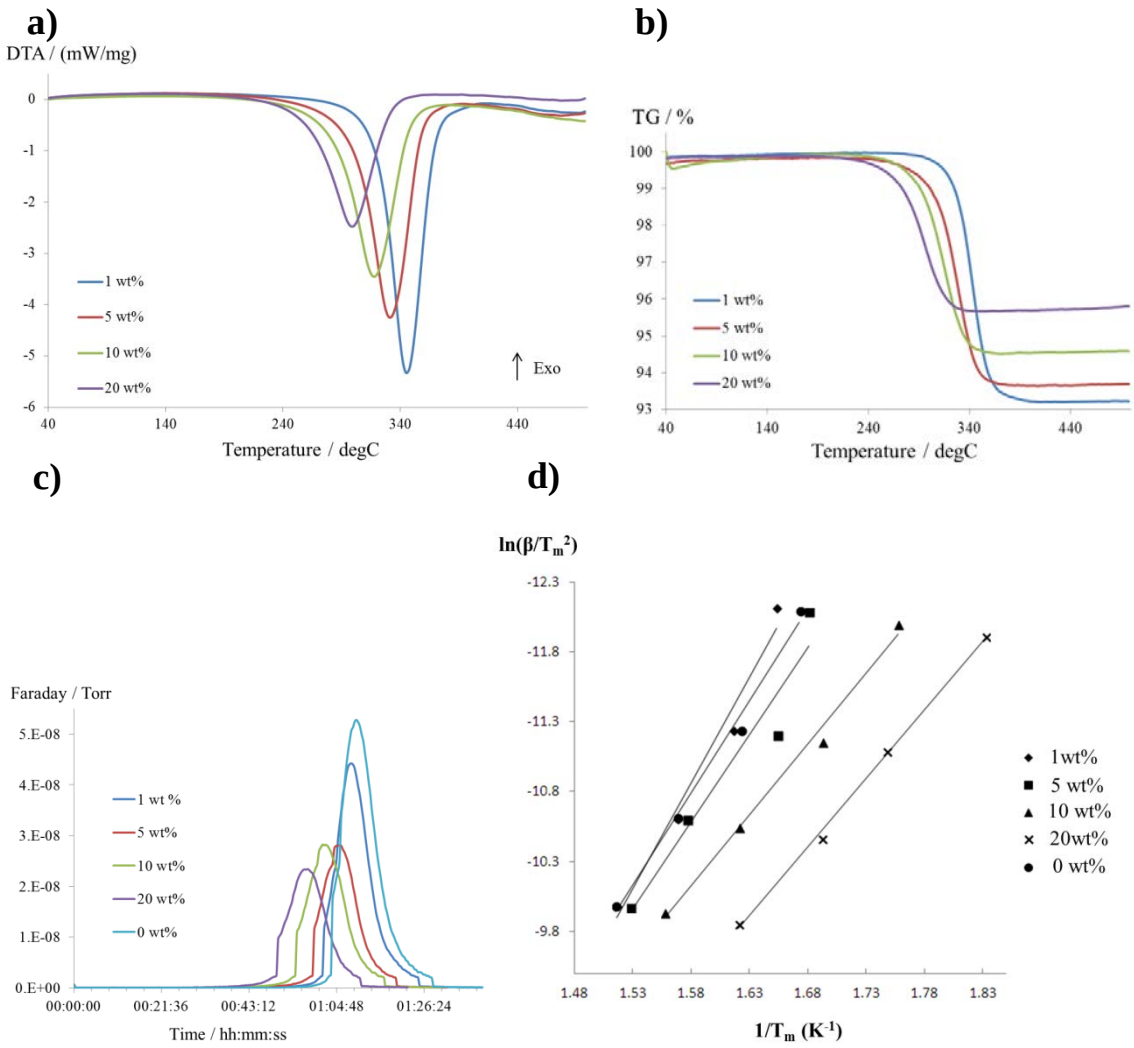

Figure 3-43 Thermal analysis data for Samples 29-32. a) DTA, b) TG and c) MS (*m/z* = 2) plots (including comparison with milled un-doped MgH_2) collected at 5 ^{o}/min. d) Kissinger plots obtained by heating at 2, 5, 10 and 20 °C including comparison with milled un-doped MgH_2. (Error bars omitted for clarity; see Appendix A, A.9 for individual Kissinger plots of Samples 29-32 including error bars.)

Table 3-21 DTA-TG data for Samples 29-32.

Sample	wt% additive	DTA		TG		Kissinger E_a / kJ/mol	Ozawa* E_a / kJ/mol	†E_{dec} / kJ/mol
		T_{onset} / °C	T_{peak} / °C	Mass Loss T_{onset} / °C	Mass Change / wt%			
29	1	320.3	345.7	324.8	6.76	126±14	130±14	59.12
30	5	300.3	331.4	307.2	6.18	103±19	108±18	56.32
31	10	282.4	317.9	292.0	5.37	84±5	90±5	49.22
32	20	261.4	299.0	268.1	4.17	82±3	87±3	40.64

†E_{dec} determined from data collected at 5 °C/min. *Ozawa plots in Appendix A, A.10.

Increasing the additive loading beyond 10 wt% was not found to decrease the E_a significantly more, although the 20 wt% loading did release hydrogen at the lowest temperature in the series of MgH_2 samples studied. Each of the MgH_2-1, 5, 10 wt% SiC:graphite composites release >5 wt% H, which is desirable for practical solid state storage.

Investigation of the post-STA PXD patterns revealed that graphite peak expected at 26.5^o is absent in all of the samples after heating to 500 ^{o}C, suggesting complete degradation of the crystalline graphitic structure (Figure 3-44). This confirmed the observations derived from the I_D/I_G relative intensities in Raman spectra. Furthermore, no unexpected mass loss in the TG data or release of CO, CO_2 species were observed in the MS to suggest other side reactions which would involve the release of C from the system.

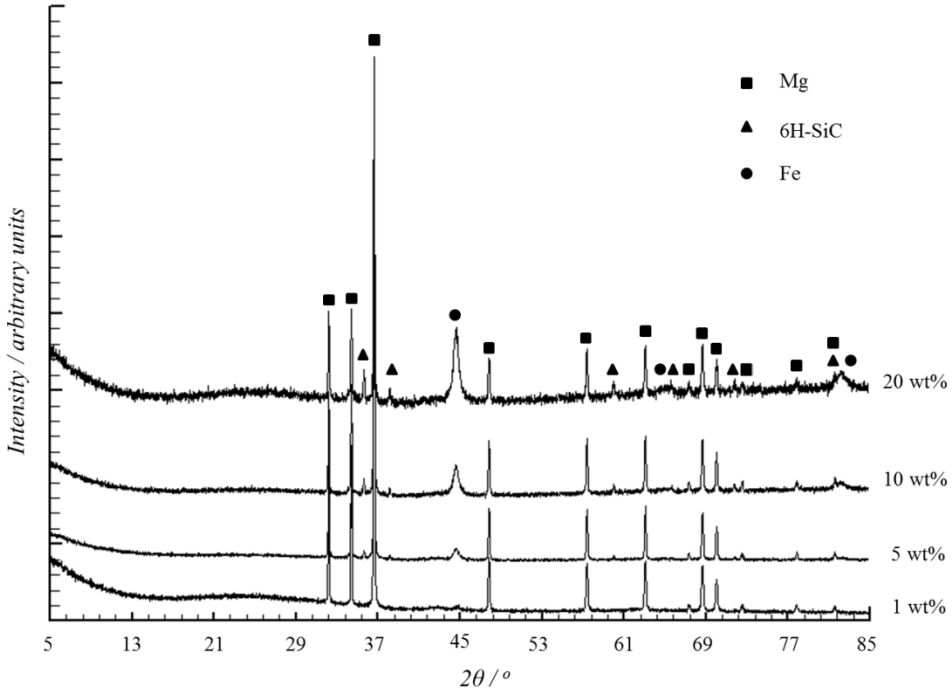

Figure 3-44 X-ray diffraction patterns for MgH_2-x wt% SiC:graphite (x = 1, 5, 10, 20) samples collected post STA.

As seen in the post-milled samples, the intensity of the $Fe_{(110)}$ reflection is observed to intensify with increasing SiC:graphite content. The effect of adding Fe to the MgH_2 system has been studied.[108] After 24 h of milling under 12 atm. H_2, desorption of hydrogen from MgH_2-5 wt% Fe system occurs between 310-350 °C, which is an improvement relative to the milled MgH_2 (370-390 °C). EDX of the as-milled, un-doped MgH_2 sample prepared in the recent work of Shahi *et al*. does not suggest that Fe contamination has occurred. Upon inclusion of 5 wt% of Fe as a catalyst, Shahi *et al.* assign two peaks in their diffraction pattern at ~36.5° and ~62° to be the ternary hydride Mg_2FeH_6. This assignment seems dubious, since these reflections also appear to be present in the un-milled and as-milled (un-doped) samples.

Another important criteria for the use of MgH_2 in commercial systems, is the integrity of the material upon decomposition. Pressing ball milled powder into pellets can have significant benefits for commercialisation as a result of compaction of the storage matrix, *i.e.*, volume reduction, in to a shape which is appropriate for a particular tank design. A preliminary study on the pelletisation of MgH_2-*x* wt% SiC:graphite composites is presented here.[65] The sample must be able to withstand desorption conditions without deforming significantly, *i.e.*, becoming embrittled, within the system. Many studies use hydride composites in the form of a pellet, and the final part of this study looks at how the integrity of a MgH_2-5 wt% SiC:graphite system is affected after the first dehydrogenation.

Using a pellet (5 mm in diameter, 0.0958 g powder) of Sample **30** formed in a hand press under N_2 in a glovebox, the sample integrity after the first desorption was tested. The shiny pellet was inserted into a silica tube and sealed using a rubber Suba-seal® septum and parafilm (Figure 3-45 a), then heated using the same temperature programme as employed in the STA experiments run at 5 ^{o}C/min. The sample was then retrieved in a glovebox after cooling to room temperature (Figure 3-45 b).

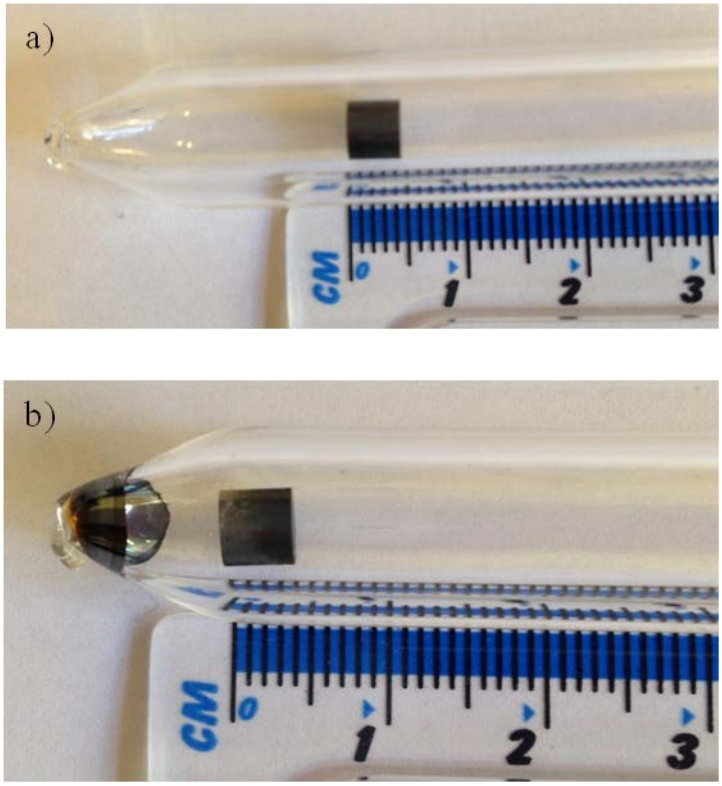

Figure 3-45 Images of Sample 30 prepared as a 5 mm (diameter) pellet shown a) before and b) after heating to 500 ^{o}C under $Ar_{(g)}$.

The pellet remained intact, with only slight discoloration from shiny black to grey at the end of the pellet that was in contact with the silica tube. A metallic film was observed on the bottom of the silica tube. Once cooled, the pellet was re-weighed, then ground to a powder in an agate mortar and pestle under $N_{2(g)}$ then PXD analysis conducted. The sample was found to lose less weight than expected, ~3 wt%. Neither pattern obtained after heating (in the milled powder using STA or the pellet heated in the bench furnace) showed residual MgH_2, indicating full decomposition of the hydride to Mg metal. The same preparation was employed for the 10 wt% sample, and similar results were obtained.

3.4.3.1. Summary SiC:graphite Additive Effects

The lowest T_{peak} in this series of samples was recorded for the MgH_2-20 wt% SiC:graphite composite (Sample **31**), which gives a significant improvement relative to the un-milled sample. One suggestion as to why the SiC:graphite composite performance is improved relative to the SiC and graphite doped samples alone is that a synergistic catalytic effect is introduced, which was also demonstrated by Milanese *et al.*[69] The SiC aids in the comminution of the MgH_2 (and graphite) particles, as suggested by Ranjbar previously. Meanwhile, the highly dispersed small particles of graphite act as a means by which the hydrogen may diffuse out of the system more easily. Early work by Immamura *et al.* suggested that the close contact between the aromatic graphite rings and Mg was responsible for improved performance in their Mg-Pd-graphite composites, where a charge transfer effect was observed by XPS.[52, 53, 55, 57] Thus, the latent structure of graphite in the samples prepared in this work is likely to play a considerable role in the diffusion pathway of hydrogen in and out of the Mg-H system as observed in previous studies involving interaction of hydrogen with graphitic carbon, graphene sheets, and intercalation compounds comprising alkali metals.[109, 110, 111, 112] Bouaricha *et al.* proposed that graphene layers form on the surface of Mg particles during milling, which was confirmed by XANES (X-ray Absorption Near Edge Structure) analysis.[68] Their work suggested that a reduction in the surface tension of the powder is induced by formation of graphene layers on fresh surfaces formed during milling. Two hypotheses were described for the inhibition of oxide formation in the hydride;

1. the protective graphene layer prevents further oxidation, and/or
2. preferential reaction of highly reactive C-species with oxides on the particle surfaces.

Therefore, for samples prepared using the milder milling conditions in this work, oxide inhibition could be the cause of the enhanced hydrogen desorption characteristics observed. This was manifested as an increase in the ΔT between the LT and HT peaks of the DTA trace. Further, it may explain the increase in ΔT for the LT and HT peaks also observed by Zhou *et al.*, who attributed the two-step process to the formation of smaller particles and defects in the MgH_2, with the lowering of the LT being caused by an increased conversion from α-MgH_2 to γ-MgH_2, despite a lack of quantification for this hypothesis.[39] A more likely cause of the two-step DTA events observed in this work and by Zhou and colleagues is the influence of cleaved graphite on the Mg samples, where the effect of milling for longer creates more Mg-graphite particle interfaces, resulting in the T_{peak} for the LT DTA peak. Therefore the two-step DTA effect is influenced in part by a

particle size effect, and cannot simply be attributed to the presence of the γ-MgH_2 phase. In this work, the increasing proportion of graphite in the composite has effectively given the same result. The impact of graphite has also ensured the oxide layer which may normally inhibit the diffusion of hydrogen from the particles is replaced by the graphite layer proposed by Bouaricha and colleagues. Therefore incorporation of both SiC and graphite can significantly reduce particle size and allow a high dispersion of cleaved graphite on the surface of the hydride, which may account for the LT event. However, the diffusion of hydrogen through the Mg metal is relatively unchanged, which is evidenced by the HT event.

There are a number of advantages of the SiC:graphite system over transition metal based catalysts. Both SiC and graphite are non-toxic, inexpensive and may be synthesised from waste products, thus providing significant environmental justification for the use of such materials in the Mg-H system over expensive transition metals.

3.4.4. Conclusions

Ball milling of MgH_2 is a facile method of tuning the hydrogen storage properties of this important hydride for optimising performance. The process of milling itself enables the reduction of decomposition enthalpy and activation energy relative to the commercial, un-milled hydride as a result of particle size reduction. The use of SiC and graphite in the MgH_2 has been explored further through the use of SEM, PXD, STA-MS and Raman spectroscopy to determine the influence of the graphitic structure on the desorption properties of the MgH_2- *x* wt% graphite/-SiC/-SiC:graphite composites. The effect of SiC is pronounced, and evidence was provided in this work to show that the carbide significantly reduced the particle size of MgH_2 upon milling using SEM imaging. Further evidence given by EDX and PXD indicates that the energy of the attrition procedure with SiC included is such that the erosion of Fe from the stainless steel milling tools is evident. This is significantly higher than that seen in un-doped milled MgH_2 and that milled with graphite. The new MgH_2-x wt% SiC-graphite composites have shown significant improvements in decomposition performance relative to either additive individually. Comparing T_{peak} for milled (2 h, 80:1 b:p, 8 balls) MgH_2 without additive (343.4 °C) and with 5 wt% of the additives employed, it can be shown that T_{peak} is improved slightly using graphite (340.4 °C), and SiC is observed to increase the T_{peak} (349.2 °C) relative to the milled sample. The sample doped with 5 wt% SiC:graphite, however, shows a drop of >10 °C (331.4 °C) relative to un-doped, milled MgH_2 with only a minor decrease in the overall wt% H_2 desorbed (6.96 wt% H_2 *vs.* 6.18 wt% H_2, respectively). In addition, this work has

shed light on the reasons for the two-step decomposition observed by DTA, and the synergistic effect that mechanically cleaved graphite has on the decomposition of the hydride at the surfaces of small particles, which are produced as a result of intense milling with SiC. Pellets of the composites showed that the doped hydride in pellet form remained intact after the first desorption, which is a promising sign that neither appreciable volume changes nor loss of structural integrity would occur in a storage tank after the first use, although this requires experimental verification.

---

[1] P. Vajeeston, P. Ravindran, A. Kjekshus and H. Fjellvåg, *Physical Review Letters*, 2002, **89**, 175506
[2] P. Vajeeston, P. Ravindran, B. C. Hauback, H. Fjellvåg, A. Kjekshus, S. Furuseth and M. Hanfland, *Physical Review B*, 2006, **73**, 224102
[3] S. Cui, W. Feng, H. Hu, Z. Feng and Y. Wang, *Solid State Communications*, 2008, **148**, 403
[4] T. Moriwaki, Y. Akahama, H. Kawamura, S. Nakano and K. Takemura, *Journal of the Physical Society of Japan*, 2006, **75**, 074603
[5] F. H. Ellinger, C. E. Holley Jr., B. B. McInteer, D. Pavone, R. M. Potter, E. Staritzky and W. H. Zachariasen, *Journal of the American Chemical Society*, 1955, 77, 2647
[6] S. Er, M. J. van Setten, G. A de Wijs and G. Brocks, *Journal of Physics-Condensed Matter*, 2010, **22**, 074208
[7] J.-P. Bastide, B. Bennetot, J.-M. Letoffe and P. Claudy, *Materials Research Bulletin*, 1980, **15**, 1215
[8] W. H. Zachariasen, C. E. Holley Jr. and J. F. Stamper Jr., *Acta Crystallographica*, 1963, **16**, 352
[9] D. Moser, G. Baldissin, D. J. Bull, D. J. Riley, I. Morrison, D. K. Ross, W. A. Oates and D. Noreus, *Journal of Physics-Condensed Matter*, 2011, **23**, 305403
[10] A. San-Martin and F. D. Manchester, *Bulletin of Alloy Phase Diagrams*, 1987, **8**, 431
[11] K. Zeng, T. Klasses, W. Oelerich and R. Bormann, *International Journal of Hydrogen Energy*, 1999, **24**, 989
[12] M. Tanniru and F. Ebrahimi, *International Journal of Hydrogen Energy*, 2009, **34**, 7714
[13] M. Tanniru, H.-Y. Tien and F. Ebrahimi, *Scripta Materialia*, 2010, **63**, 58
[14] M. Bortz, B. Bertheville, G. Bottger and K. Yvon, *Journal of Alloys and Compounds*, 1999, **287**, L4-L6
[15] M. A. Kuzovnikov, V. S. Efimchenko, E. V. Filatov, A. A. Maksimov, I. I. Tartakovkii and A. J. Ramirez-Cuesta, *Solid State Communications*, 2013, **154**, 77
[16] J. Huot, G. Liang, S. Boily, A. V. Neste and R. Schulz, *Journal of Alloys and Compounds*, 1999, **293-295**, 495
[17] H. Shao, M. Felderhoff, F. Schüth and C. Weidenthaler, *Nanotechnology*, 2011, **22**, 235401
[18] Y. K. Gautam, A. K. Chawla, R. Walia, R. D. Agrawal and R. Chandra, *Applied Surface Science*, 2011, **257**, 6291
[19] R. S. Katiyar, *Journal of Physical Chemistry C*, 1970, **3**, 1087
[20] H. Smithson, C. A. Marianetti, D. Morgan, A. Van der Ben, A. Predith and G. Ceder, *Physical Review B*, 2002, **66**, 144107
[21] T. Noritake, S. Towata, M. Aoki, Y. Seno, Y. Hirose, E. Nichibori, M. Takata and M. Sakata, *Journal of Alloys and Compounds*, 2003, **356-357**, 84
[22] N. Ohba, K. Miwa, T. Noritake and A. Fukumoto, *Physical Review B*, 2004, **70**, 035102
[23] J. Lasave, F. Dominguez, S. Koval, M. G. Stachiotti R. L. Migoni, *Journal of Physics-Condensed Matter*, 2005, **17**, 7133
[24] J. R. Santisteban, G. J. Cuello, J. Dawidowski, A. Fainstein, H. A. Peretti, A. Ivanov and F. J. Bermejo, *Physical Review B*, 2000, **62**, 37
[25] H. G. Schimmel, M. R. Johnson, G. J. Kearley, A. J. Ramirez-Cuesta, J. Huot and F. M. Mulder, *Materials Science and Engineering B*, 2004, **108**, 38
[26] D. Reed and D. Book, *Current Opinion in Solid State and Materials Science*, 2011, **15**, 62
[27] H. G. Schimmel, M. R. Johnson, G. J. Kearley, A. J. Ramirez-Cuesta, J. Huot and F. M. Mulder, *Journal of Alloys and Compounds*, 2005, **393**, 1
[28] B. Paik, I. P. Jones, A. Walton, V. Mann, D. Book and I. R. Harris, *Journal of Alloys and Compounds*, 2010, **492**, 515
[29] R. Campostrini, M. Abdellatief, M. Leoni and P. Scardi, *Journal of Thermal Analysis and Calorimetry*, 2014, **116**, 865
[30] R. Schulz, J. Huot, G. Liang, S. Boily, G. Lalande, M. C. Denis and J. P. Dodelet, *Materials Science and Engineering A*, 1999, **267**, 240

[31] F. C. Gennari, F. J. Castro and G. Urretavizcaya, *Journal of Alloys and Compounds*, 2001, **321**, 46
[32] Z. G. Huang, Z. P. Guo, A. Calka, D. Wexler, J. Wu, P. H. L. Notten and H. K. Liu, *Materials Science and Engineering A*, 2007, **447**, 180
[33] R. A. Varin, S. Li, Ch. Chiu, L. Guo, O. Morozova, T. Khomenko and Z. Wronski, *Journal of Alloys and Compounds*, 2005, **404-406**, 494
[34] R. A. Varin, T. Czujko, Ch. Chiu and Z. Wronski, *Journal of Alloys and Compounds*, 2006, **424**, 356
[35] M. Tian and C. Shang, *Journal of Chemical Science and Technology*, 2012, **1**, 54
[36] R. A. Varin, T. Czujko and J. Mizera, *Journal of Alloys and Compounds*, 2003, **354**, 281
[37] R. A. Varin, T. Czujko and J. Mizera, *Journal of Alloys and Compounds*, 2003, **350**, 332
[38] R. A. Varin, S. Li, A. Calka and D. Wexler, *Journal of Alloys and Compounds*, 2004, 373, 270
[39] S. Zhou, H. Chen, C. Ding, H. Niu, T. Zhang, N. Wang, Q. Zhang, D. Liu, S. Han and H. Yu, *Fuel*, 2013, **109**, 68
[40] K.-F. Aguey-Zinsou, J. R. Ares Fernandez, T. Klassen and R. Bormann, *Materials Research Bulletin*, 2006, **41**, 1118
[41] K.-F. Aguey-Zinsou, J. R. Ares Fernandez, T. Klassen and R. Bormann, *International Journal of Hydrogen Energy*, 2007, **32**, 2400
[42] "*Modification of Magnesium Hydride by Transition Metal Carbides for Hydrogen Storage*", M. Tian, Masters Thesis, University of East Anglia, 2010
[43] M. Cabo, S. Garroni, E. Pellicer, C. Milanese, A. Girella, A. Marini, E. Rossinyol, S. Surinach and M. D. Baro, *International Journal of Hydrogen Energy*, 2011, **36**, 5400.
[44] H. Gijs Schimmel, J. Huot, L. C. Chapon, F. D. Tichelaar and F. M. Mulder, *Journal of the American Chemical Society*, 2005, **127**, 14348
[45] A. Borgschulte, U. Bosenberg, G. Barkhordarian, M. Dornheim and R. Bormann, *Catalysis Today*, 2007, **120**, 262
[46] M. A. Lillo-Rdena, Z. X. Guo, K. F. Aguey-Zinsou, D. Cazorla-Amors and A. Linares-Solano, Carbon, 2008, **46**, 126
[47] T. Spassov, Z. Zlatanova, M. Spassova, and S. Todorova, *International Journal of Hydrogen Energy*, 2010, **35**, 10396
[48] Y. Jia, Y. Guo, J. Zou and X. Yao, *International Journal of Hydrogen Energy*, 2012, **37**, 7579
[49] C. Z. Wi, P. Wang, X. Yao, C. Liu, D. M. Chen, G. Q. Lu and H. M. Cheng, *Journal of Alloys and Compounds*, 2006, **420**, 278
[50] A. Ranjbar, M. Ismail, Z. P. Guo, X. B. Yu and H. K. Liu, *International Journal of Hydrogen Energy*, 2010, **35**, 7821
[51] M. Lototskyy, J. M. Sibanyoni, R. V. Denys, M. Williams, B.G. Pollet and V. A. Yartys, 2013, **57**, 146
[52] H. Imamura and N. Sakasai, *Journal of Alloys and Compounds*, 1995, **231**, 810
[53] H. Imamura, N. Sakasai and Y. Kajii, *Journal of Alloys and Compounds*, 1996, **232**, 218
[54] H. Imamura, N. Sakasai and T. Fujinaga, *Journal of Alloys and Compounds*, 1997, **253-254**, 34
[55] H. Imamura, Y. Takesue, T. Akimoto and S. Tabata, *Journal of Alloys and Compounds*, 1999, **293-295**, 564
[56] H. Imamura, Y. Takesue, S. Tabata, N. Shigetomi, Y. Sakata and Susumu, Tsuchiya, *Chemical Communications*, 1999, **22**, 2277
[57] H. Imamura, S. Tabata, N. Shigetomi, Y. Takesue and Y. Sakata, *Journal of Alloys and Compounds*, 2002, **330-332**, 579
[58] H. Imamura, M. Kusuhara, S. Minami, M. Matsumoto, K. Masanari, Y. Sakata, K. Itoh and T. Fukunaga, *Acta Materialia*, 2003, **51**, 6407
[59] V. Fuster, F. J. Castro, H. Troiani, G. Urretavizcaya, *International Journal of Hydrogen Energy*, 2011, **36**, 9051
[60] A. Kubota, H. Miyaoka, M. Tsubota, K. Shimoda, T. Ichikawa and Y. Kojima, *Carbon*, 2013, **56**, 50
[61] C. Polmann, L. Röntzsch, T. Weiβgärber and B. Kieback, *International Journal of Hydrogen Energy*, 2013, **38**, 1685
[62] D. M. Gattia, A. Montone, L. Pasquini, *International Journal of Hydrogen Energy*, 2013, **38**, 1918
[63] G. Urretavizcaya, V. Fuster and F. J. Castro, *International Journal of Hydrogen Energy*, 2011, **36**, 5411
[64] Z. G. Huang, Z. P. Guo, A. Calka, D. Wexler, J. Wu, P. H. L. Noten and H. K. Liu, Materials Science and Engineering A, 2007, **447**, 180
[65] A. Chaise, P. de Rango, Ph. Marty, D. Fruchart, S. Miraglia, R. Olivès and S. Garrier, *International Journal of Hydrogen Energy*, 2009, **34**, 8589
[66] *McPhy* ; http://www.mcphy.com/en/; accessed 05/02/2014
[67] S. Bouaricha, J. P. Dodelet, D. Guay, J. Huot and R. Schulz, *Journal of Alloys and Compounds*, 2001, **325**, 245
[68] S. Bouaricha, J.-P. Dodelet, D. Guay, J. Huot and R. Schulz, *Journal of Materials Research*, 2001, **16**, 2893

[69] C. Milanese, A. Gierlla, S. Garroni, G. Bruni, V. Berbenni, P. Matteazzi and A. Marini, *International Journal of Hydrogen Energy*, 2010, **35**, 9027
[70] G. Barkhordarian, T. Klasses, R. Bormann, *Journal of Alloys and Compounds*, 2004, **364**, 242
[71] M. G. Veron, H. Troiani and F. C. Gennari, *Carbon*, 2011, **49**, 2413
[72] C. Pohlmann, L. Röntszch, S. Kalinichenka, T. Hutsch and B. Kieback, *International Journal of Hydrogen Energy*, 2010, **35**, 12829
[73] K. Herbrig, L. Röntzsch, C. Pohlmann, T. Weißgärber and B. Kieback, *International Journal of Hydrogen Energy*, 2013, 38, 7026
[74] A. D. Lueking and R. T. Yang, *Applied Catalysis A: General*, 2004, **265**, 259
[75] C. Zlotea and M. Latroche, *Colloids and Surfaces A*, 2013, **439**, 117
[76] S. Zhou, H. Chen, W. Ran, N. Wang, Z. Han, Q. Zhang, X. Zhang, H. Niu, H. Yu and D. Liu, *Journal of Alloys and Compounds*, 2014, **592**, 231
[77] "*Handbook of Refractory Carbides and Nitrides*", H. O. Pierson, Noyes Publications, 1996.
[78] L. Carassiti, A. Jones, P. Harrison, P. S. Dobson, S. Kingman, I. MacLaren and D. H. Gregory, *Energy and Environmental Science*, 2011, **4**, 1503
[79] H. Zhang, H. Geerlings, J. Lin and W. S. Chin, *International Journal of Hydrogen Energy*, 2011, **36**, 7580
[80] H. Immamura, S. Nakatomi, Y. Hashimoto, Y. Sakata, H. Mae and M. Fujimoto, *Journal of Alloys and Compounds*, 2009, **488**, 265
[81] A. Ranjbar, Z. P. Guo, X. B. Yu, D. Wexler, A. Calka, C. J. Kim and H. K. Liu, *Materials Chemistry and Physics*, 2009, **114**, 168
[82] M.-Q. Fan, S.S. Liu, Y. Zhang, J. Zhang, L.X. Sun and F. Xu, *Energy*, 2010, **35**, 3417
[83] J. H. Shin, G.-J. Lee, Y. W. Cho and K. S. Lee, *Catalysis Today*, 2009, **146**, 209
[84] V. I. Mikheevaz and N. N. Mat'tseva, *Zhurnal Strukturnoi Khimii*,1963, **4**, 698
[85] X. Wang and L. Andrews, *Journal of Physical Chemistry A*, 2004, **108**, 11511.
[86] L . Andrews and X. Wang, *Inorganic Chemistry*, 2005, **44**, 11.
[87] P. Selvam, B. Viswanathan, C. S. Swamy and V. Srinivasan, *International Journal of Hydrogen Energy*, 1986, **11**, 169
[88] K. Bohmhammel, B. Christ and G. Wolf, *Thermochimica Acta*, 1998, **310**, 167
[89] C. M. Stander, *Journal of Inorganic Nuclear Chemistry*, 1977, **39**, 221
[90] O. Friedrichs, J. C. Sanchez-Lopez, C. Lopez-Cartes, M. Dornheim, T. Klassen, R. Bormann and A. Fernandez, *Applied Surface Science*, 2006, **252**, 2334
[91] A. A. Nayeb-Hashemi and J. B. Clark, *Phase Diagrams of Binary Alloys*, 1988
[92] M. S. Seehra and A. S. Pavlovic, *Carbon*, 1993, **31**, 557
[93] C. X. Shang, Z. X. Guo, *Journal of Power Sources*, 2004, **129**, 73
[94] G. Katagiri, H. Isheda and A. Ishitani, *Carbon*, 1988, **26**, 565
[95] D. S. Knight and W. B. White, *Journal of Materials Research*, 1989, **4**, 385
[96] F. Tuinstra and J. L Koenig, *Journal of Chemical Physics*, 1970, **53**, 1126
[97] Z. G. Huang, Z. P. Guo, A. Calka, D. Wexler and H. K. Liu, *Journal of Alloys and Compounds*, 2007, **427**, 94
[98] C. An, G. Liu, L. Li, Y. Wang, C. Chen, Y. Wang, L. Jiao and H. Yuan, *Nanoscale*, 2014, **6**, 3223
[99] G. Liu, Y. Wang, L. Jiao, H. Yuan, *International Journal of Hydrogen Energy*, 2014, **39**, 3822
[100] G. C. Capitani, S. Di Pierro, G. Tempesta, *American Mineralogist*, 2007, **92**, 403
[101] A. Kumar, V. Agarwala, and D. Sing, *Ceramics International*, 2014, **40**, 1797
[102] "*Effect of catalysts on hydrogen storage properties of MgH2*", A. Ranjbar, PhD Thesis, University of Woollongong
[103] S. Kurko, Z. Raskovic, N. Novakovic, B. P. Mamula, Z. Jovanovic, Z. Bascarevic, J. B. Novakovic and L. Matovic, *International Journal of Hydrogen Energy*, 2011, **36**, 549
[104] H. Harima, Microelectronics Engineering, 2006, **83**, 126
[105] G. L. Olsen, J. J. Vajo, DOE Hydrogen Program, FY2006 Annual Progress Report, IV.A. 4d, p 310
[106] "*Handbook of Chemistry and Physics*", 61st Edition, R. C. Weast and M. J. Astle, CRC Press Inc., B-143
[107] I. Milanovic, S. Milosevic, Z. Raskovic-Lovre, N. Novakovic, R. Vujasin, L. Matovic, J. F. Fernandez, C. Sanchez and J. G. Novakovic, *Ceramics International*, 2013, **39**, 4399
[108] R. R. Shahi, A. P. Tiwari, M. A. Shaz and O. N. Srivistava, *International Journal of Hydrogen Energy*, 2013, **38**, 2778
[109] A. Chalmers, C. Park, R. Terry, K. Baker and N. M. Rodriguez, *Journal of Physical Chemistry B*, 1998, **102**, 4253
[110] C. P. Herrero and R. Ramirez, *Journal of Physics D-Applied Physics*, 2010, **43**, 255402
[111] A. Du, Z. Zhu and S. C. Smith, *Journal of the American Chemical Society*, 2010, **132**, 2876
[112] M. Pumera, *Energy and Environmental Science*, 2011, **4**, 668

4. Facile Synthesis of Ternary Metal Hydrides *via* Mechanochemistry

Part of this work is based on the publication "Facile Synthesis of Nanosized Sodium Magnesium Hydride, $NaMgH_3$", which was an invited paper for a special edition of Progress in Natural Science.[1] My thanks are extended to Miss Natalia Mazur, an excellent IAESTE project student from the Norwegian University of Science and Technology (NTNU) who contributed to this work. In addition, I would like to thank Prof. Ru-Shi Liu and Dr. Chun Che Lin for arranging and conducting the SXD experiments at NSRRC.

4.1. Introduction

Ternary hydrides are of significant importance in the development of candidate hydrogen storage systems. The hydrides of magnesium compounds are of particular interest given the potential for high capacity, low cost materials.[2] Extensive reviews by Yvon *et al.* describe an array of ternary and quaternary hydride compounds containing combinations of alkali, alkaline earth and transition metals.[3] Synthesis of such compounds typically requires the high pressure sintering of respective metals/metal hydrides or alloys.[4, 5] Mechanical modification of metals and their hydrides has been shown to improve hydrogen sorption characteristics *via* enhanced surface characteristics (*e.g.*, surface defects, increased surface area, increased surface: volume ratios). Significant reduction of particle size to the nanoscale can improve not only the kinetics but also the thermodynamics of hydrogen uptake and release, although this is the subject of much debate.[6, 7, 8]

Among possible ternary hydrides, ABH_3 perovskites (where A is usually an alkali or alkaline earth metal and B is a transition metal) are considered strong competitors to nanoscale binary hydrides, *e.g.*, MgH_2.[9, 10] Replacement of transition metals (B) with early alkali/alkaline earth metals in ABH_3 compounds maximises potential gravimetric capacity and computational studies have shown that such high capacity hydrides may exist ($LiMgH_3$ and Li_2MgH_4 contain 8.84 and 9.57 wt% H_2, respectively).[11, 12] These compounds, however, have yet to be realised experimentally. $KMgH_3$ has been extensively studied, both experimentally and computationally.[11, 13, 14, 15, 16, 17, 18, 19, 20] Both conventional solid state and mechanochemistry techniques have been employed to prepare $KMgH_3$ and desorption of hydrogen from the hydride occurs in one step. $NaMgH_3$ may be synthesised *via* reactive mechanochemical means. Use of 1 MPa (10 bar) H_2 during milling of a 1:1 $NaH:MgH_2$ mixture formed the hydride, which displayed an experimental capacity of 5.8

wt% H (*cf.* a theoretical capacity of 6.0 wt%).[15, 21] Prior to this work, the synthesis of $NaMgH_3$ involved reaction of the hydrides at 753 K under 10 bar of hydrogen.[22, 23] Cryo-milling of the binary hydrides with subsequent high pressure H_2 sintering treatments has also been employed.[24, 25, 26] Indeed, mechanochemical approaches provide not only less energy-intensive routes to the hydrides, but also ensure particles sizes are minimised, improving the dehydrogenation kinetics of the ternary hydrides compared to those prepared at high temperature.[27, 28] There is a growing interest in $NaMgH_3$ and related hydrides and a drive to understand the sorption mechanisms in these systems in more detail by both experimental and computational methods.[29, 30, 31, 32, 33, 34, 35]

Synthesis and properties of ternary hydrides formed from AB_5 and AB_2 Laves-type transition metal alloys have been well studied for hydrogen storage applications.[36] The overall gravimetric/volumetric capacity of these systems is problematic for hydrogen storage applications, however, and modification of their properties, *e.g.*, by particle size adjustment, have been attempted.[37] Incorporation or even complete substitution of transition metals by lighter metallic components to form ternary/quaternary hydrides are also of significant interest. Starting with the very lightest metals, formation of alloys comprising alkaline and alkaline earth metals is possible, typically *via* induction melting.[38] The equilibrium phase diagrams of the lightest metals, *e.g.*, Li-Mg, Li-Ca, Na-Mg, Na-Ca and Ca-Mg indicate that intermetallic alloys may be produced and these have been studied extensively for hydrogen storage purposes.[39, 40, 41, 42, 43]

Laves-type Mg and Ca alloys have been studied experimentally, where research on the Mg-TM (transition metal) phases is prevalent.[44] Ternary Ca hydride systems comprising Group I hydrides, (*e.g.* $KCaH_3$ $LiCaH_3$ and $NaCaH_3$) have been investigated.[45, 46, 47] Recent work has shown that hydrogenation of the $CaLi_2$ alloy results in the formation of the binary hydrides, CaH_2 and LiH, with no evidence of a ternary Ca-Li hydride phase.[48] Liu *et al.* suggest that the advantage of starting from the alloy is that the diffusion of Li in the system results in faster hydrogenation to form the binary hydrides. The first work on ternary Ca-Mg hydrides dates back to the late 1970s when binary alloys were used to synthesise hydrides using high pressure sintering methods under H_2.[49] More recently, the structures of various alkali metal $MCaH_x$-type hydrides have been predicted, where M = Li, Na, K, Rb, Cs.[50, 51]

Synthesis of ternary hydrides, $Ca_4Mg_3H(D)_{14}$ and $Ca_{19}Mg_8H(D)_{54}$, has been studied by direct high pressure-high temperature synthesis from the $CaMg_2$ alloy, or in the latter case from reaction of the binary hydrides at similarly harsh conditions in a sealed autoclave

(Figure 4-1, Table 4-1).[52, 53] Gingl *et al.* described the first purely alkaline earth metal ternary structure, $Ca_4Mg_3H(D)_{14}$, where synthesis of the ternary hydride phase took 6 days in a high temperature (683(10) K), high pressure (53(3) bar) autoclave. Harsher conditions were required for the deuteride; seven days at 738(5) K, 95(5) bar. The product was found in a mixture of CaH_2, MgH_2 and Mg impurity phases.[52] Bertheville and Yvon later described the structure of another Ca-Mg hydride, $Ca_{19}Mg_8H(D)_{54}$, which was found to be iso-structural to $Yb_{19}Mg_8D_{54}$.[53] The synthesis route involved preparation of pellets comprising a mixture of CaH_2:MgH_2 in a ratio of 2:1. The ternary phase was then formed in a multi-anvil pressure cell over a period of 3 h. This technique is typical for synthesis of ternary and quaternary hydride compounds.[4, 5] This resulted in a multi-phase product comprising the cubic ternary phase, CaH_2, the α– and γ–MgH_2 phases and MgO.

Ball milling was used by Sartori *et al.* in their study of mixed hydride systems, and the $Ca_4Mg_3H_{14}$ and $Ca_{19}Mg_8H_{54}$ ternary hydrides arose in their work on the Mg-Al-Ca-H system, although never as a single phase.[54] Quaternary and multinary Ca-Mg hydrides containing transition metals, *e.g.*, La, Ti, Fe, Co, and Ni, are commonly encountered in the literature, but transition metal compounds are beyond the scope of this work.[4, 55, 56]

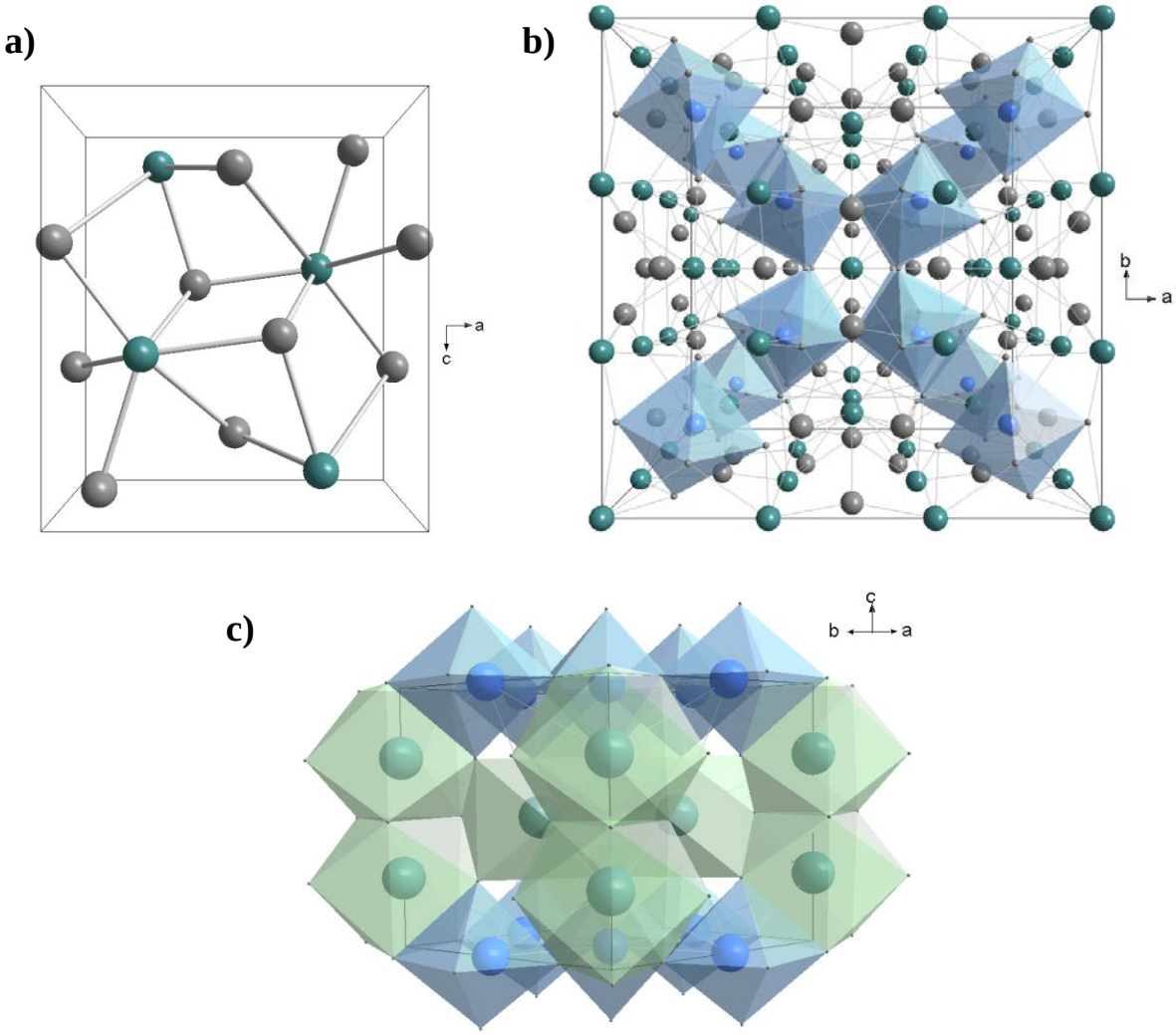

Figure 4-1 **a) Unit cell of CaH_2 and the ternary phases b) $Ca_{19}Mg_8D_{54}$ and c) $Ca_4Mg_3D_{14}$. (Grey, blue and green spheres represent H, Mg and Ca, respectively.)**

Table 4-1 Crystallographic properties of CaH_2 and known ternary Ca-Mg hydrides at room temperature.

	CaH_2[57]	$Ca_4Mg_3D(H)_{14}$[52]	$Ca_{19}Mg_8D(H)_{54}$[53]
Crystal System	Orthorhombic	Hexagonal	Cubic
Space Group	$Pnma$ (62)	$P\bar{6}2m$ (189)	$Im\bar{3}$ (204)
Z	4	1	2
***a* / Å**	5.948	6.2902(2) (6.3056(2))	12.0642(8) (12.1457(6))
***b* / Å**	3.607	*a*	*a*
***c* / Å**	6.852	6.8540(3) (6.8820(2))	*a*
***V* / Å^3**	147.01	234.86	1755.88
Formula Weight / g	42.10	247.39	1010.54
Calculated Density, ρ_x / g cm^{-3}	Not given.	Not given.	2.01
T_{dec} / K	~873	~ 750	~ 650-700
Gravimetric capacity / wt% H	4.80	5.72	5.40

N.B. Unit cell parameters quoted in parentheses indicate values obtained for hydrides for comparison with the deuteride.

Perhaps surprisingly, however, the dehydrogenation of these ternary Ca-Mg hydrides has only been suggested by Yvon *et al.* and no data have been fully reported in the literature to suggest detailed decomposition mechanisms of the ternary hydride in isolation. In addition, mechanochemical methods have not yet been explored for their synthesis, which offers a simple, scalable method by comparison with the high pressure-high temperature methods.

Relative to the wealth of literature available for Mg hydrides, information about hydrogen storage in Ca hydrides is comparatively sparse, which is surprising based on the high abundance of this light weight alkaline earth metal. The thermodynamic stability of CaH_2, and higher mass of Ca (*vs.* Mg) is probably the greatest barrier for developing it as a competitive solid state hydrogen storage component. Much of the recent work on CaH_2 focusses on theoretical speculation about the promise of this hydride.[58, 59] Novel solid state routes to CaH_2 for hydrogen storage have been demonstrated by experiment in the communication published by Ney and colleagues, where a 1:2 molar mixture of Ca metal and phenylphosphonic acid was used to generate CaH_2 (and the corresponding Ca acid; $Ca(O_3PC_6H_5)$) by mechanochemistry.[60]

Hydrolytic decomposition of CaH_2 for hydrogen production has been studied as an alternative to direct thermal desorption, where its promise was highlighted by use of water vapour (rather than liquid water) in the work of Kong and colleagues.[61]

Equation 4-1

$$CaH_2 + 2\,H_2O \rightarrow Ca(OH)_2 + 2\,H_2$$

Furthermore, the hydrolytic properties of an MgH_2-5 atomic % Ca composite prepared by milling were shown to be improved relative to MgH_2 alone, where increasing Ca content up to 20 at% enabled faster reaction kinetics.[62] Ball milling of MgH_2-20.3 mol% Ca composites by Tessier *et al.* did not reveal an additional ternary phase, but indicated the transfer of hydrogen from the Mg to Ca to produce a composite comprising three phases Mg-MgH_2-CaH_2, from which >80 % H_2 yields were realised.[63] Recent use of CaH_2 milled with a magnesium alloy, $Mg_{17}Al_{12}$, as a composite for hydrolytic hydrogen production showed high hydrogen yields (94.8 % conversion for the alloy doped with 10 wt% CaH_2), but the exothermic nature of hydrolysis reactions remains a challenge for practical application.[64] Zhu *et al.* confirmed that CaH_2 was one of the most promising hydrides for application in micro-PEMFCs. First, using a simple millimetre scale lab set-up, the yields of H_2 from CaH_2 exceeded 99 %.[65] Subsequent work by the same authors made use of a hybrid silicon fuel cell charged with CaH_2, which showed that operation of the system was reasonably consistent over more than 6 h, whereupon the reaction ceased. It is clear from this brief catalogue of research that the product of the hydrolysis reaction plays a significant role in the success of hydrogen production from CaH_2, where the permeability of the insoluble $Ca(OH)_2$ product from CaH_2 hydrolysis assists in the complete release of hydrogen from the system based on the above mentioned work. Beyond hydrolysis, thermal decomposition of composite systems including CaH_2 and complex hydrides such as ammonia borane and borohydrides, have also been covered in the literature.[66, 67, 68] As expected, the gravimetric hydrogen capacities are lower when these complex hydrides are combined with CaH_2 relative to the respective MgH_2 systems.

Over two results chapters this work describes the facile mechanochemical synthesis of nanoscale ternary hydrides comprising alkali metal and alkaline earth metals without a requirement for hydrogen during milling. The influence of milling conditions is investigated using a combination of characterisation techniques, to indicate the impact on both on the progress of the mechanochemical reaction and on the identity and properties of the ternary hydride products. Furthermore, the effect of varying the initial reagent stoichiometry on the products is also studied.

4.2. Experimental

All manipulations were performed in an $Ar_{(g)}$-filled recirculating glovebox (Saffron Scientific, 1 ppm H_2O, 1 ppm O_2). Mixtures of anhydrous binary hydrides of NaH (Sigma Aldrich, 95 %) and MgH_2 (Alfa Aesar, 98 %), and MgH_2 and CaH_2 (Sigma Aldrich, 95 %) were milled using stainless steel milling media (50 ml jar, 10x 10 mm milling balls) under a nitrogen atmosphere at ambient conditions using a Retsch PM100 planetary ball mill. For the $NaMgH_3$ samples, various ball:powder (b:p) mass ratios were studied using a total mill time of 5 hours. Samples were milled at 450 rpm for 5 minute periods with 5 minute rest intervals between each mill. The synthesis of the ternary hydride was studied using 1 h, 2h and 5 h of milling to establish how the ternary phase developed over milling time (Table 4-2).

Table 4-2 List of samples prepared in the NaH-MgH_2 study.

Sample ID	Milling Time	b:p
33	1	70:1
34	2	70:1
35	5	47:1
36	5	70:1
37	5	85:1
38	5	100:1

For the CaH_2-MgH_2 samples, milling was conducted under the same conditions for each hydride stoichiometry studied (Table 4-3), where the b:p of 76:1 and 450 rpm rotation speed was used for each 10 h milling experiment; 5 min rest periods between each 5 min milling interval using rotation direction reversal between each milling period. This gave a total milling time of 5 h.

Table 4-3 List of samples used in the MgH_2-CaH_2 study.

Sample ID	CaH_2:MgH_2 ratio
39	2.375:1
40	2:1
41	1:0.75
42	1:1
43	1:2

The ternary hydride samples used for SXD experiments were prepared from the appropriate stoichiometries of the binary hydrides in the same way as for the lab PXD analysis, applying identical milling conditions. PXD was conducted before sending the samples to the NSRRC in order to verify that the samples were consistent with those previously prepared. At NSRRC, the samples were prepared in glass capillaries for SXD analysis in a glovebox, and sealed using epoxy resin. SXD data were then collected for each sample over the $5 \leq 2\theta / ^{o} \leq 45$ range for 3 minutes using a high intensity X-ray beam (λ = 0.774908 nm) on the powder diffraction beamline at NSRRC (BL01C2) employing a 2D detector. After room temperature analysis, two of the samples; **39** and **42**, were analysed between 373-673 K, at 50 K intervals. A controllable heat gun was used to heat the sample, and a heating rate of 10 K/min used. The high temperature analysis was conducted using the sealed capillaries, with no gas vent or flow to remove any evolved gaseous products.

TPD experiments were performed for all samples *via* thermogravimetric-differential thermal analysis-mass spectrometry (TGA-DTA-MS; Netzsch STA 409 coupled to a Hiden HPR20 mass spectrometer). All thermal analysis experiments were conducted within an $Ar_{(g)}$-filled recirculating glovebox (MBraun UniLab; 0.1 ppm H_2O, 0.1 ppm O_2) using alumina sample pans under a constant flow of Ar at a 5 K min^{-1} heating rate. Kissinger plots for each sample were obtained by heating at 2, 5, 10 and 20 K min^{-1} to determine the activation enthalpy.

Post-milled and post-thermal analysis samples were investigated by PXD using a Bruker D8 powder diffractometer in transmission geometry with spinning sealed capillaries. Data were collected between $5 \leq 2\theta / ^{o} \leq 85$ for 1 h for initial characterisation and over $10 \leq 2\theta / ^{o} \leq 110$ for between 10-14 h to obtain higher resolution, higher intensity data (for structure refinement). Samples were also exposed to air and analysed *in-situ* using a PANalytical XPERT Pro MPD (Multi Purpose Diffractometer) in Bragg-Brentano reflection geometry (Cu Kα1 radiation). Data were collected for 1 hour in the $5 \leq 2\theta / ^{o} \leq 85$ range for phase determination in the air exposed samples. For time resolved analysis under ambient conditions, a total analysis time of 15 h was used for collection of 15x 1 h samples in order to determine how quickly the sample degraded in air.

All collected diffraction patterns were compared to reference data in the ICDD (International Centre for Diffraction Data) database using the PANalytical High Score Plus Software package. Rietveld refinement for the $NaMgH_3$ Sample **36** was performed using GSAS/EXPGUI[69, 70] with reference data obtained from the Inorganic Crystal Structure

Database (ICSD)[71] and the previously published structure for $NaMgH_3$ (ICSD-91795) as a starting model.[22] For the $NaMgH_3$ study, background was modelled using Function 1 within GSAS; a shifted Chebyschev function. Peak shapes were modelled using the Thompson-Cox-Hastings pV function (Function 2) with asymmetry also being taken in to consideration. The unit cell parameters were varied, followed by the atomic and temperature parameters. Major peaks from $Mg(OH)_2$ and MgO impurity phases in the $NaMgH_3$ samples were broad and could not be adequately fitted and so these 2θ ranges were excluded from the refinement. Rietveld refinements were also conducted for the $(Ca_{1-x}Mg_xH_2)_n$ samples (Samples **39-43**) using the data obtained by both PXD and SXD analysis. The background was refined using the reciprocal interpolation function (Function 8) to obtain a good fit to the data and zero corrections were also included. Again, peak shapes were modelled using the Thompson-Cox-Hastings pV function (Function 2) with asymmetry being considered. Phase fractions were obtained by refining the scale factors. The atomic positions and temperature factors were refined where possible, and constrained to the values given in literature where significant divergence occurred.

SEM-EDX experiments were performed at 20 keV under a nitrogen atmosphere using a Philips XL30 ESEM instrument equipped with an Oxford Instruments X-act spectrometer to determine particle morphology and atomic proportions, respectively. Samples were prepared on carbon tabs under an inert environment. Initially, the samples were loaded in a sputter coater and coated with gold at 25 keV. However, this caused significant oxidation of the samples, and so most samples were loaded directly from a sealed vial to the SEM sample chamber. Although exposure of the samples to air was unavoidable during this analysis procedure, it was minimised as much as possible to obtain representative results of the as-prepared samples.

Raman spectroscopy was conducted at room temperature (Horiba LabRam HR confocal microscope; 325 nm UV laser, 100 μm aperture, 600 grooves/mm grating, Synapse CCD). Spectroscopic data for ternary magnesium hydrides are limited and herein experimental spectra for $NaMgH_3$ is compared to previously calculated vibrational data and tentatively assign vibrational bonding modes. Sealed glass capillaries were used to contain the sample and thereby prevent air/moisture exposure during spectroscopic analysis.

4.3. Results & Discussion

4.3.1. Synthesis and Characterisation of Nanosized Sodium Magnesium Hydride, $NaMgH_3$

Using a stoichiometric initial hydride ratio (1:1, $NaH:MgH_2$) the PXD of Sample **33** showed that $NaMgH_3$ forms after only 1 h of milling, and after 5 h (Sample **36**) the reaction to the ternary hydride was complete. Increased PXD peak widths for the ternary phase after a 5 h milling time indicated a significantly reduced average particle size. For Sample **35**, the particle sizes were inferred to be similar to those of Sample **36**, but conversion was not complete and significant binary hydride phases were observed *via* PXD. When the b:p ratio reached 100:1, PXD patterns revealed that products were largely amorphous. The identity of the ternary hydride was confirmed from PXD data by reference to the known structure given in the ICSD (ICSD-91795).[23] The as-synthesised $NaMgH_3$ sample was extremely air-sensitive, changing colour immediately from brown to grey/white. It was evident from PXD experiments that samples were indeed acutely sensitive to air. Despite best efforts to minimise air-exposure, poorly crystalline $Mg(OH)_2$ and MgO phases were frequently formed (Figure 4-2). No crystalline sodium-containing impurity phases were observed. Longer term exposure to moist air revealed that after a few minutes of air exposure, powder samples would ignite rapidly upon agitation. PXD analysis showed MgO, NaOH, Mg and $Mg(OH)_2$ to be present in the air-exposed products.

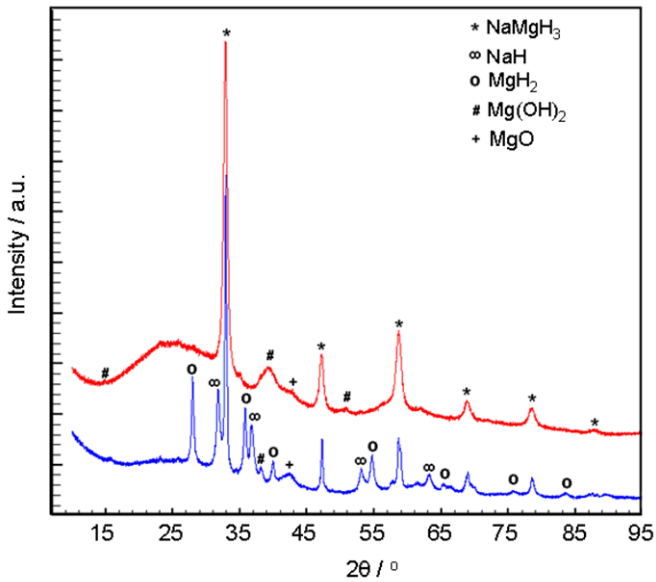

Figure 4-2 X-ray diffraction patterns of 1:1 molar mixtures of NaH and MgH_2 milled for 1 h (Sample 33, blue) and 5 h (Sample 36, red).

The Scherrer method (Equation 2-4) was applied to determine the approximate crystallite size, D. A Scherrer constant of 0.9 was used for K since the particle morphology appeared approximately isotropic from SEM imaging (Figure 4-3).[72] The average crystallite size (more precisely, the average size of the crystalline domain) was estimated to be 430 nm for Sample **36**. Figure 4-3 shows SEM micrographs for this sample. Low magnification images (*e.g.* Figure 4-3a) show that the milled particles have a narrow size distribution but that agglomeration occurs during milling (as is often characteristic for the method). Higher magnification images (Figure 4-3b) demonstrated that samples ranged from ~100 nm across up to 1 μm in size (the latter for particle agglomerations). The directly imaged particles show dimensions comparable with that estimated by Scherrer analysis of PXD data. The results of elemental mapping by EDX are shown in Figure 4-3(c) and Figure 4-3(d) and show good dispersion of Na and Mg throughout the sample. EDX point scans yielded approximate 1:1 elemental ratios of Na:Mg. Both findings are thus consistent with the formation of $NaMgH_3$ and these results were obtained routinely for a number of samples prepared under the same conditions.

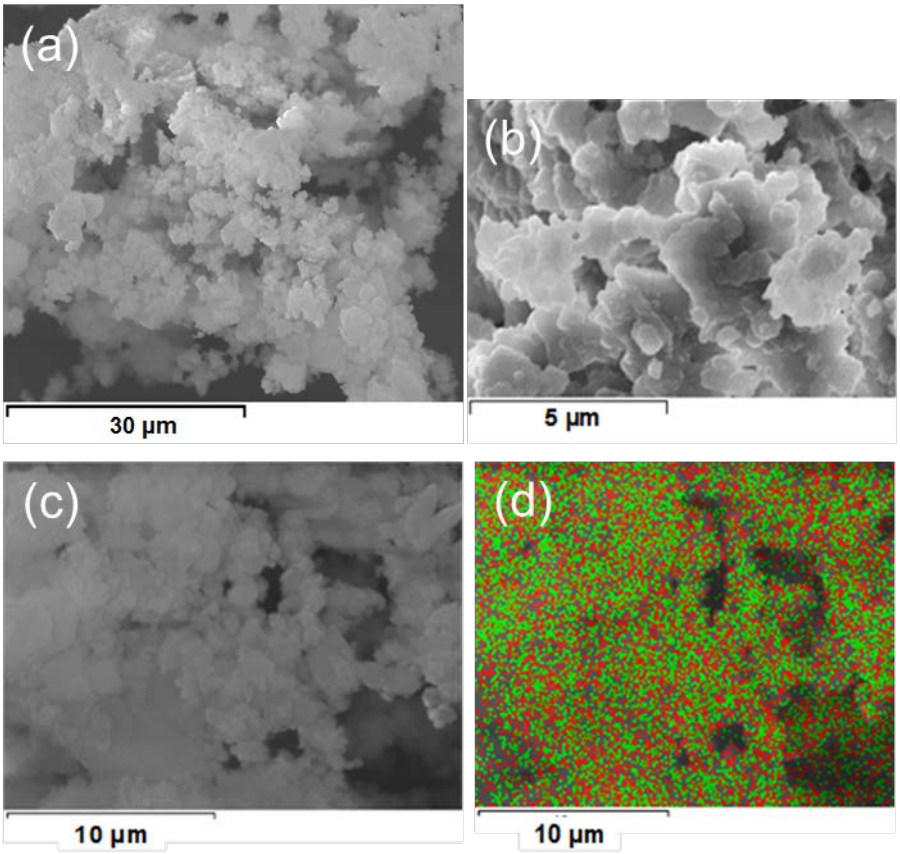

Figure 4-3 SEM image of as-synthesised $NaMgH_3$ (Sample 36) at (a) low magnification and (b) high magnification, and (c & d) morphology and elemental mapping of Na (red) and Mg (green) in Sample 37.

Rietveld refinement against PXD data was performed with an $NaMgH_3$ structural model based on that of Bouamrane *et al*.[22] The refinement converged swiftly and smoothly to the previously reported orthorhombic perovskite structure (Table 4-4 and Table 4-5). The Rietveld profile plot is shown in Figure 4-4(a) and shows a good fit to the experimental data; major peaks from $Mg(OH)_2$ and MgO were excluded from the refinement. Given the inability of PXD to locate light atoms accurately, the hydride positions were fixed as those from the starting model.[22] Considering the broad, undulating background in the PXD profile, it is quite possible that amorphous phases are also present in the milled material. From the data collected by Ikeda *et al*, it is also not possible to determine whether starting reagents or other impurities were contained in hydride products in their milling study, although the experimental weight loss they obtained on dehydrogenation (5.8 wt% vs. 6.0 wt% theoretically) would suggest that any such phases were not substantial.[21] The lattice parameters for the sample in this study are in reasonable agreement with those previously reported (a = 5.463 Å, b = 7.703 Å, c = 5.411 Å)[22], although, notably, despite a cell volume within 3σ of the previous value, the a-parameter and c-parameter are smaller and larger respectively in this work. It is also worth noting that the cell volume is significantly larger than that of the corresponding deuteride.[24] Figure 4-4(b) and Figure 4-4(c) show representations of the $GdFeO_3$ Perovskite-type structure of the ternary hydride. The $GdFeO_3$ structure is well-known and the details of the structure of $NaMgH_3$ are discussed in detail in previous publications.[22, 23, 24] As in previous literature models, the Na^+ cations are surrounded by 12 H^- anions and Mg^{2+} cations are coordinated octahedrally to 6 H-anions, where Figure 4-4(c) indicates the Mg centred octahedra in red.

Table 4-4 Diffraction data for Sample 36.

Sample	36
Chemical Formula	$NaMgH_3$
Crystal System	Orthorhombic
Space Group	*Pnma* (N°. 62)
Z	4
***a* / Å**	5.437(2)
***b*/ Å**	7.705(5)
***c* / Å**	5.477(2)
***V* / Å^3**	229.49(9)
Formula Weight / g	201.276
Calculated Density, ρ_x / g cm^{-3}	1.456
Refinement Parameters	40
Data Points	5086
R_{wp}	2.21 %,
R_p	1.68 %
χ^2	2.110

Table 4-5 Atomic parameters for Sample 36.

Atom	Site	x	y	z	$U_{iso} \times 100$ / Å^2
Mg	4*b* (0,0,½)	0	0	½	5.9(4)
Na	4*c* (x,¼,z)	0.004(1)	¼	0.013(1)	0.3(4)
H_1	4*c* (x,¼,z)	0.503[a]	¼	0.093[a]	2.5[a]
H_2	8*d* (x,y,z)	0.304[a]	0.065[a]	0.761[a]	2.5[a]

[a] Parameters fixed in the refinement process.

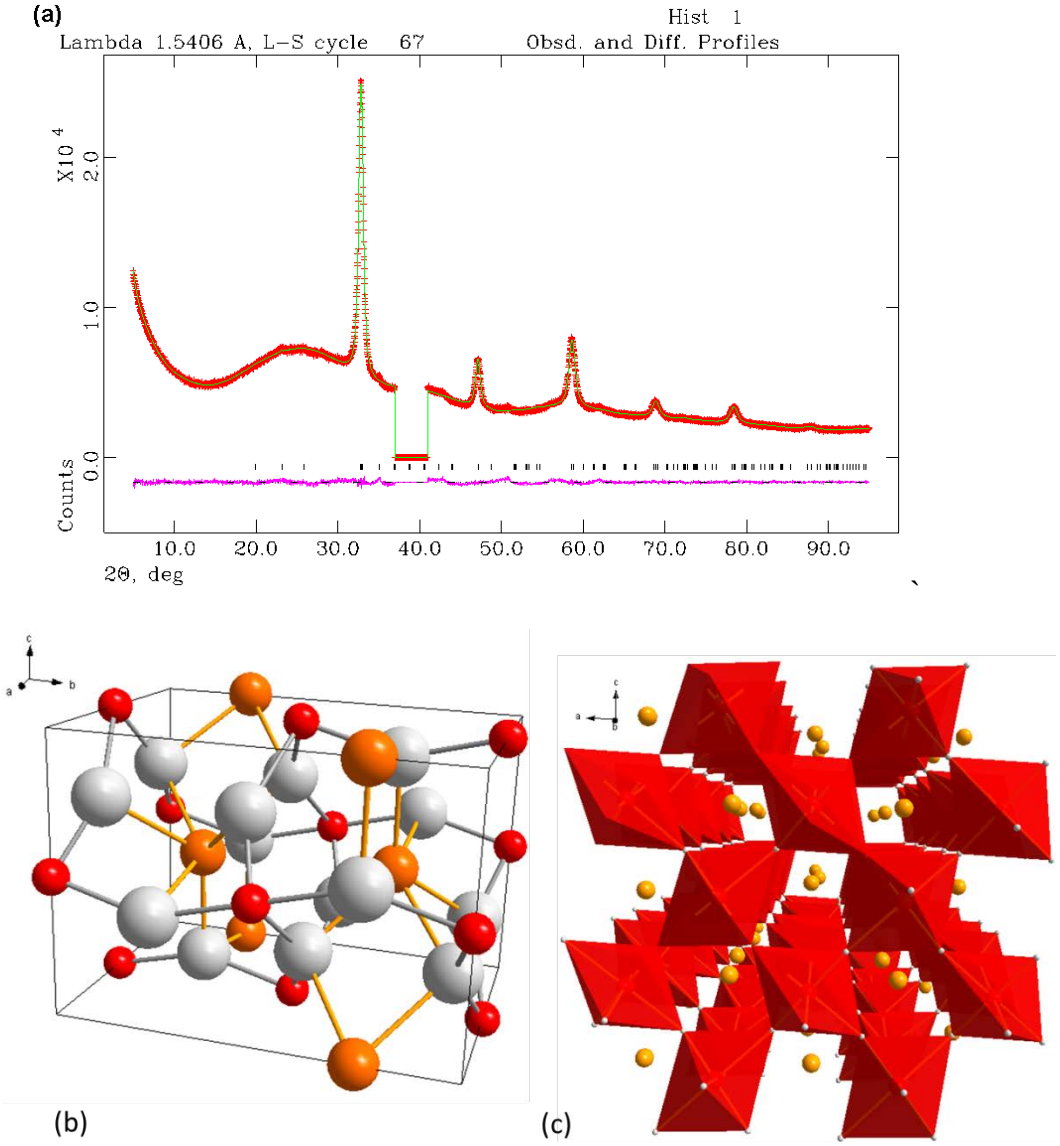

Figure 4-4 (a) Rietveld refinement profile for Sample 36. (Observed data are shown by red crosses, the calculated plot is shown as a green continuous line, the tick marks indicate the reflection positions for orthorhombic $NaMgH_3$ and the difference plot is shown below in pink); (b) Unit cell of $NaMgH_3$, where gold, red and light grey spheres represent Na, Mg and H, respectively; (c) Extended structure of $NaMgH_3$ as a polyhedral representation viewed along the [010] direction.

The $NaMgH_3$ sample was observed to be acutely sensitive to the 532 nm (visible) laser when collecting Raman spectroscopy data and fluorescence effects were evident in spectra. Raman analysis was therefore conducted using (UV) laser irradiation at 352 nm (Figure 4-5). To the best of the author's knowledge, there are no previous experimental Raman spectra for $NaMgH_3$ in the literature. IR (Infra Red) and Raman bonding mode symmetries and frequencies have been calculated computationally in two separate studies previously.[26, 34] The experimental data is in broad agreement with these studies allowing the tentative assignment of the experimental spectrum (Table 4-6). Shifts at low wavenumber (380 cm^{-1}) indicate tilting/rotation of the MgH_6 octahedra, whereas the bands at 581 cm^{-1}, 791 cm^{-1}

and 992 cm^{-1} suggest H-Mg-H angle distortions. In fact, the broad band at 992 cm^{-1} might represent a merging of two A_g bands calculated by Bouhadda *et al*. at 906.8 cm^{-1} and 1071.4 cm^{-1}.[34] The band at 1101 cm^{-1} is in the Mg-H bond mode region and has been assigned to the symmetric Mg-H stretch. This assignment is again consistent with the bands calculated by Bouhadda *et al*. Data collected for samples milled for shorter durations (Samples **33** and **34**) did not show developed bands at higher Raman shift values, *i.e.*, 700-1300 cm^{-1}, although the broad overlapping band between 200-700 cm^{-1} is evident. Spectra for Samples **36** and **37** are very similar in most respects, although the bands between 700-1300 cm^{-1} diminish again at the higher 100:1 ball:powder ratio (Sample **38**), which may be the result of increased amorphisation and hence disorder within the sample milled at higher energy.

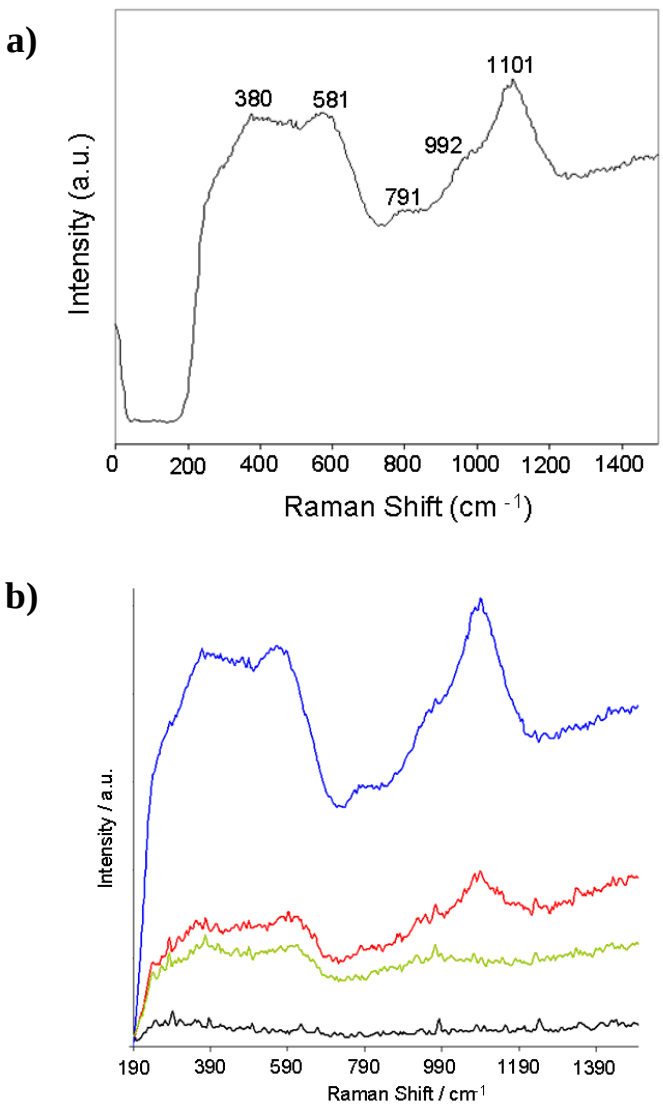

Figure 4-5 a) Raman spectrum of Sample 36 collected using the UV laser (325.1 nm). b) Comparison of Raman spectra for Samples 34 and 36 given by black and blue lines respectively, and the red and green lines show the spectra of Samples 37 and 38.

Table 4-6 Assignment of the Raman spectrum for Sample 36.

Raman shift / cm^{-1}	Expected Symmetry	Tentative assignment
380	B_{1g}	MgH_6 octahedral tilt
581	B_{3g}	δ, H-Mg-H
791	B_{3g}	δ, H-Mg-H
992	A_g	δ, H-Mg-H
1101	B_{1g}	ν_s Mg-H symmetric stretch

Comparison of the DTA-TG data for samples prepared using different b:p ratios are given in Appendix B, B.1 a) and b). This demonstrates that the lowest T_{peak} value for the ternary phase is given for Sample **36** and the most distinctive two-step profile is evident for this sample.

The TPD data determined for Sample **36** are given in Figure 4-6 and Table 4-7. Analysis of the DTA profile showed concurrent thermal events over the weight loss period corresponding to a two-step decomposition of the ternary hydride with concomitant hydrogen evolution as confirmed by MS. The onset temperatures of the two reaction steps (Equation 4-2 and Equation 4-3; Table 4-7) could be determined from both the DTA and d(TG)/dT profiles, where the latter are omitted for clarity. Very similar thermal profiles were found for $NaMgH_3$ samples prepared at lower b:p ratios, although given some starting reagents were evident from the PXD data for these samples, the second endothermic decomposition step was observed as broader and more pronounced. The desorption mechanism described by Ikeda *et al.* is given in Equation 4-2 and Equation 4-3, where two losses of hydrogen are ascribed to the decomposition of $NaMgH_3$ and NaH respectively (Table 4-7).[21, 27, 28]

Equation 4-2

$$NaMgH_3 \rightarrow NaH + Mg + H_2$$

Equation 4-3

$$NaH + Mg + H_2 \rightarrow Na + Mg + 3/2\ H_2$$

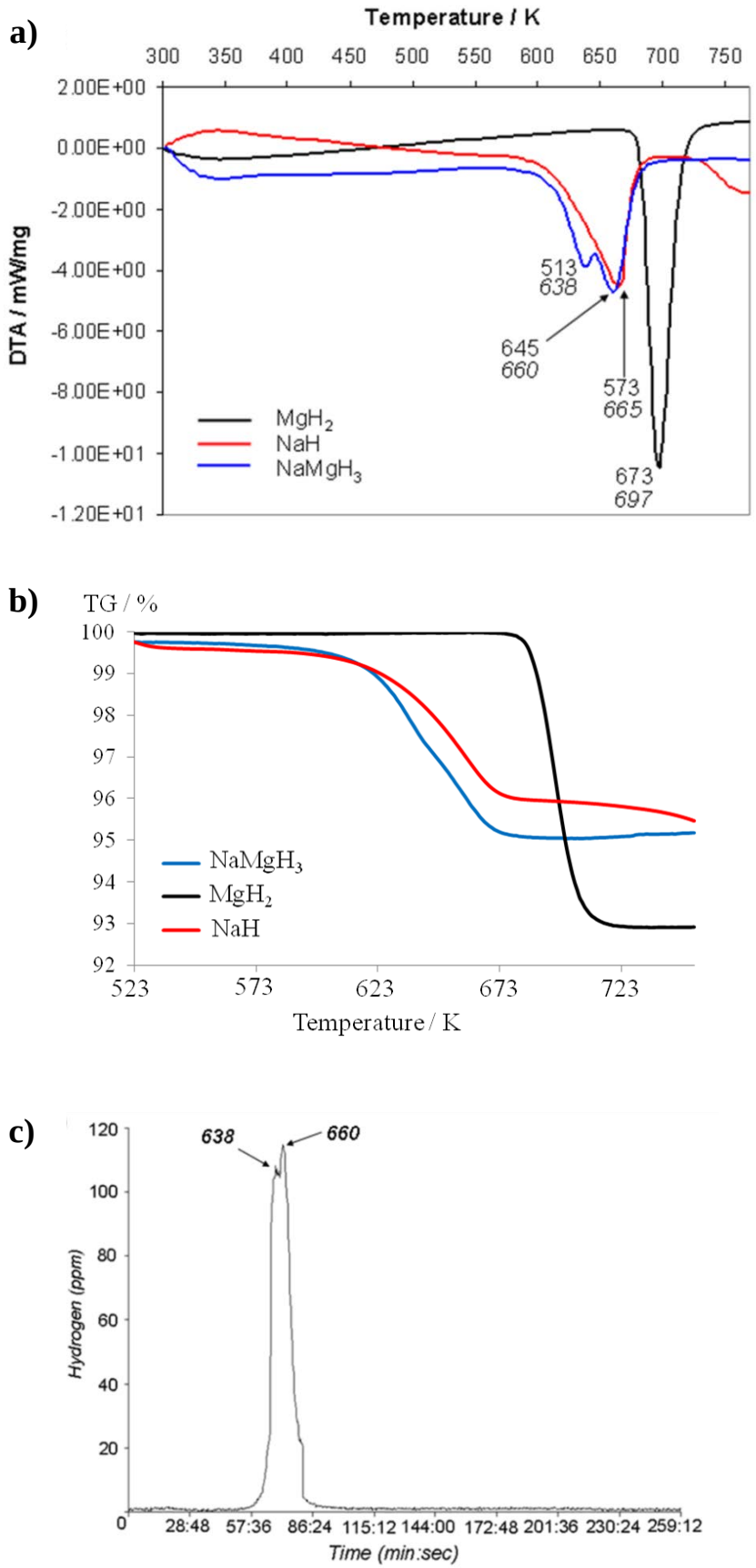

Figure 4-6 **a) DTA and b) TG data comparison for un-milled binary hydrides NaH and MgH_2 and ternary hydride, Sample 36. Values shown on DTA profiles indicate onset and peak H_2 desorption temperatures, T_{onset} and T_{peak} (italics), respectively. c) MS data for Sample 36 where the corresponding T_{peak} values are indicated on the plot.**

Table 4-7 TGA-DTA-MS results for Sample 36 compared with literature data.

Event	Theoretical	This Work		Ikeda *et al.*[21]		Pottmaier *et al.* [26b]	
	wt% H_2	T_{onset}[a] / K	wt% H_2	T_{onset} / K	wt% H_2	T_{onset} / K	wt% H_2
Step 1	4.0	513	2.67	-	-	664	-
Step 2	2.0	645	2.04	-	-	709	-
∑	6.0	-	(4.71)	-	(5.8)	-	-

[a] Temperature of wt loss onset; [b] H_2 desorption onset temperatures determined by HP-DSC (High Pressure – Differential Scanning Calorimetry) at 0.1 MPa H_2.

The mass loss in the first step of the process (and therefore the total mass loss) associated with hydrogen release is significantly diminished with respect to that determined by Ikeda *et al*. and that expected theoretically. The data indicate that hydrogen may be lost during the milling process, either pre-or post-reaction to form the ternary hydride (*i.e.*, either *via* likely decomposition of the MgH_2 starting material or *via* the first step of the dehydrogenation of the ternary hydride itself (Equation 4-2). Further evidence for this premise exists in the PXD patterns, where evidently Mg and/or MgH_2 in the milled products reacts rapidly with air during handling to form the respective binary hydroxide ($Mg(OH)_2$) and oxide (MgO). Milling under elevated hydrogen pressure, therefore, may be one way in which this initial hydrogen loss may be prevented (although in subsequent rehydrogenation-dehydrogenation cycles the initial loss is not likely to be important unless phases react with air). PXD analysis of post-TPD samples revealed Na and Mg metal accompanied by MgO and NaOH (likely to be a result of the acute air-sensitivity of the samples despite best efforts to minimise exposure during analysis). Crucially, no hydride phases were identified therefore suggesting complete dehydrogenation of $NaMgH_3$ occurs by 723 K.

From Figure 4-6 and Table 4-7, the onset temperature of the first dehydrogenation step is significantly lower than the equivalent temperatures for both the component binary hydrides. By comparison of the DTA profile of $NaMgH_3$ with those of the respective component binary hydrides, it is evident that the second hydrogen loss is associated with NaH decomposition. The onset temperature for hydrogen loss as determined by dTG/dT and corresponding mass spectrometry data is lower than that previously recorded for $NaMgH_3$ by Pottmaier *et al*. This depression in temperature can be regarded in terms of particle size reduction (as a result of milling) and as a function of hydrogen partial pressure

(Pottmaier *et al.* observed from DSC measurements that the onset temperatures decreased as the hydrogen pressure was reduced).[26]

Comparing Kissinger plots for the 1st and 2nd decomposition steps it is apparent that the two decomposition events are distinct. (These plots were prepared from data collected by heating Sample **36** to 500 °C at 2, 5, 10 and 20 °C/min heating rates.) The activation enthalpies for both of the decomposition steps of $NaMgH_3$ have thus been determined (Figure 4-7, Table 4-8). The E_a of the 1st step, associated with decomposition of the ternary phase to NaH and Mg with the release of hydrogen, is slightly higher than that of commercial MgH_2 (144±5 kJ/mol, Chapter 3). The activation enthalpy of H diffusion in $NaMgH_3$ is discussed by Shane *et al.* in their NMR (Nuclear Magnetic Resonance) study, where they determined the E_a for H diffusion as 95 kJ/mol for $NaMgH_3$.[73] Their work employed a sample which had been prepared from the binary hydrides also by the mechanochemical method and was annealed at 673 K. (It is prudent to note that at 673 K the sample would be expected to decompose, based on the STA conducted herein, although Shane *et al.* do not provide thermal analysis data for their as-prepared $NaMgH_3$ material.) An alternative computational method (first principles plane wave density functional theory method) describes a higher E_a of 118 kJ/mol for H diffusion in $NaMgH_3$.[31] In the MgH_2-$NaAlH_4$ composites prepared by Ismail *et al.*, the decomposition enthalpy of $NaMgH_3$ (an intermediate in the decomposition process of this system) was determined to be 142 kJ/mol using the Kissinger method.[74] This is in close approximation to the E_a value determined for the first step of $NaMgH_3$ decomposition found by the same Kissinger method applied in this work. The E_a determined by Ismail *et al.*, however, was likely to be influenced by other decomposition processes and components in the system. Similarly, the E_a determined here may have been affected by the presence of impurities in the product. The E_a of the 2nd step, associated with NaH decomposition, is slightly higher than that determined for NaH decomposition in the work of Šburt and Tobola (115 kJ/mol).[75]

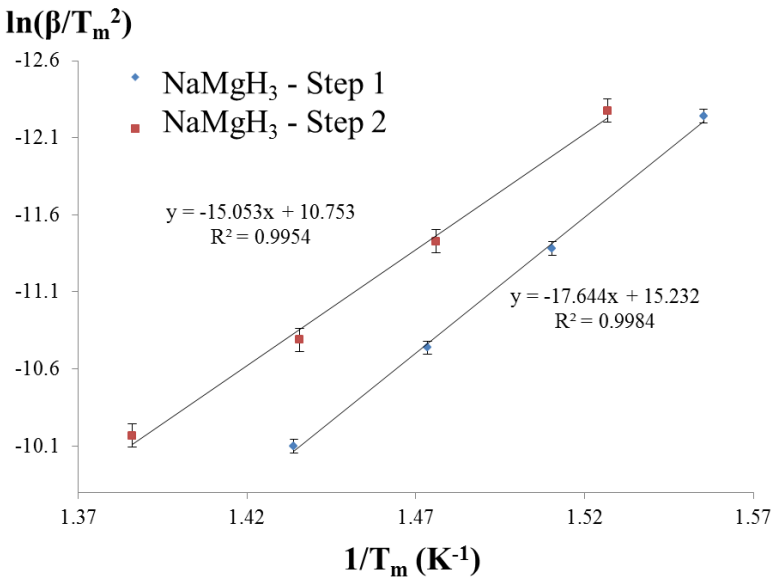

Figure 4-7 Comparison of the Kissinger plots for the two endothermic decomposition processes observed for Sample 36.

Table 4-8 Kissinger plot linear trendline data and statistics for Sample 36.

Sample	Trendline Equation	R^2	E_a / kJ/mol
$NaMgH_3$ - Step 1	$y = -17.644x + 15.232$	0.9984	147±4
$NaMgH_3$ - Step 2	$y = -15.053x + 10.753$	0.9954	125±6

The decomposition enthalpies of the materials produced in this work could not be determined directly from the DTA traces, since the two decomposition events overlap. The dehydrogenation enthalpies and entropies of $NaMgH_3$ have, however, been studied elsewhere in literature by both computational and experimental means (Table 4-9).

Table 4-9 Experimentally determined enthalpy and entropy for dehydrogenation of $NaMgH_3$. (Modified from supplementary material in Reference 25.)

Process	ΔH / kJ mol^{-1} H_2	ΔS / J K^{-1} mol^{-1} H_2	Reference
Step 1 $NaMgH_3 \rightarrow NaH + Mg + H_2$	+88	-	21, 28
	+93.9	+116.2	27
	+94	+140	16
	+86.6	+132.2	25
	+92	+123	26
Step 2 $NaH + Mg + H_2 \rightarrow Na + Mg + 3/2\ H_2$	+114.1	-	21
	+102.2	+125.9	27
	+116	+165	16

4.3.1.1. Conclusions

$NaMgH_3$ has been synthesised *via* mechanochemical methods under an inert atmosphere. The milled materials are nanocrystalline and the crystal structure of the ternary hydride is consistent with previous crystallographic data. Avoiding the use of high pressure sintering techniques is of significant importance for the facile preparation of hydrogen storage materials. Furthermore, synthesis in this way minimises the particle sizes, which has been shown to improve not only hydrogen desorption kinetics but also thermodynamics (*e.g.* in MgH_2). Relatively high ball:powder ratios are essential to ensure complete reaction to the ternary hydride (without milling under hydrogen). However, if this ratio is taken above a critical value, the ternary product loses crystallinity over similar milling times. The onset of weight loss and hydrogen evolution in mechanochemically synthesised $NaMgH_3$ occurred at lower temperatures than previously reported, although otherwise the two-step dehydrogenation proceeds as has been observed previously. The Kissinger plots for both decomposition steps of $NaMgH_3$ have been determined and the activation energies for these processes were found to be 147±4 kJ/mol and 125±6 kJ/mol, respectively. The TPD data in this work confirms that desorption proceeds *via* two endothermic steps, even when the ternary hydride is prepared in an inert environment. The ability to simplify the synthesis and processing of $NaMgH_3$ plus the prospect of tuning the kinetics and thermodynamics of hydrogen uptake and release, offers the potential both to develop $NaMgH_3$ as a storage system in its own right and to implement the ternary hydride as part of a "composite" approach (as demonstrated with NH_3BH_3, for example).[76]

4.3.2. New Ternary Alkaline Earth Metal Hydrides $(Ca_{1-x}Mg_xH_2)_n$; synthesis, structure and thermal properties

This second section investigates whether a similar mechanochemical approach could be used to incorporate other small lightweight elements into the Mg-H system. As noted in the introduction of this Chapter CaH_2 forms a ternary hydride when combined with MgH_2 but synthesis to date has involved high temperature-high pressure methods. Thus for the first time $(Ca_{1-x}Mg_xH_2)_n$ type alloys will be investigated by mechanochemistry.

SEM images of the as-synthesised hydrides revealed powder products which were comprised of small particles clumped together (Figure 4-8). The particles are polydisperse in size and range from the micron to the nano-scale, which is typical of milled samples. The samples exposed to air for a number of hours may be described as fluffy white powders, where the particles are more discrete than in the as-synthesised hydride.

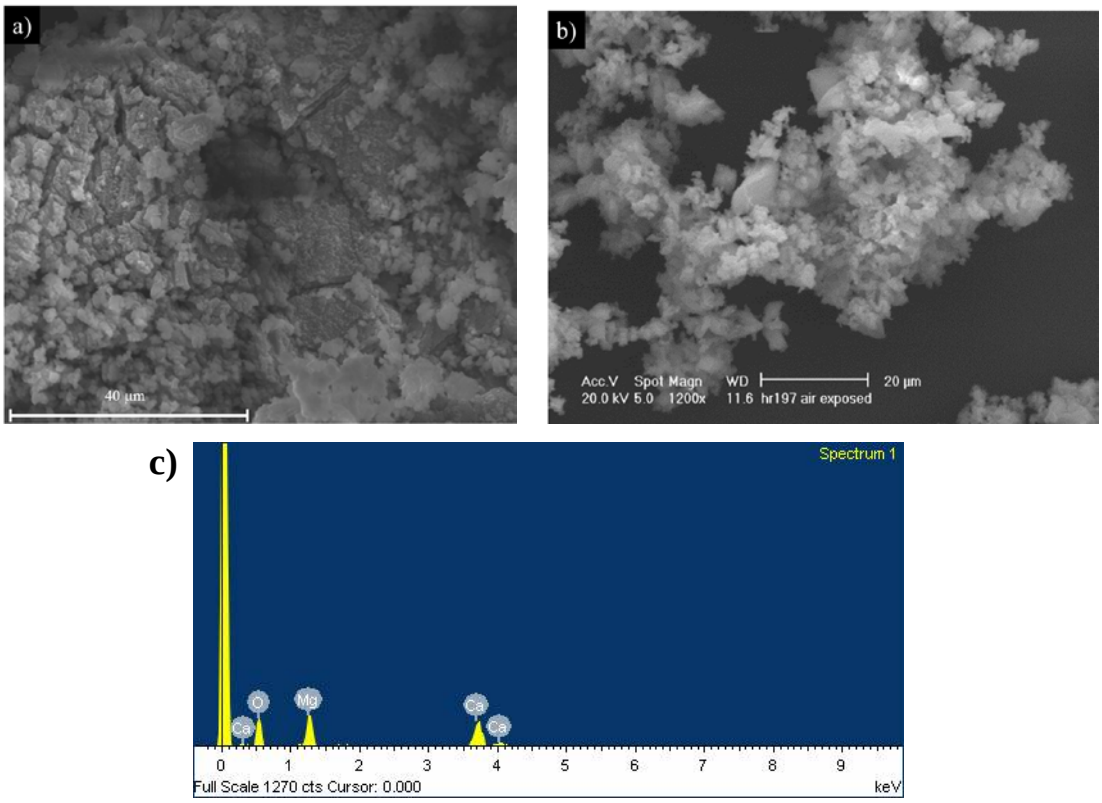

Figure 4-8 Typical morphologies of a) as-synthesised Ca-Mg-H Sample 39 (40 µm) and b) air exposed Ca-Mg-H Sample 39 (20 µm). EDX analysis shown in c) for as-prepared Ca-Mg-H Sample 42.

EDX analysis revealed that a significant amount of oxygen (~63 wt%) was present in the samples analysed by SEM, which is expected as a result of the rapid hydrolysis of the sample in air. This was observed by a change in colour of the powder from brown to grey/brown-white and was unavoidable as a result of the method of sample preparation for

SEM. To minimise this extent to which the materials were affected samples were not gold coated, as this would increase the exposure time, and transferred as quickly as possible into the SEM chamber from vials sealed in under inert atmosphere.

PXD patterns of the materials were collected in Bragg-Brentano geometry after a few hours of exposure to air, and the diffraction patterns revealed very broad reflections which could be assigned to $Ca(OH)_2$. In addition, time resolved PXD analysis was conducted for Sample **39**, where the as-prepared sample was loaded on to a dimpled glass bracket and transferred to the instrument goniometer as quickly as possible (Figure 4-9). The first measurement commenced immediately and a total of 15 measurements were collected using a 1 h measurement period. This analysis revealed that the sample hydrolyses rapidly since the 1st measurement indicates that none of the ternary phase remains and the broad reflections of $Ca(OH)_2$ are evident. This phase persists throughout the remainder of the analysis.

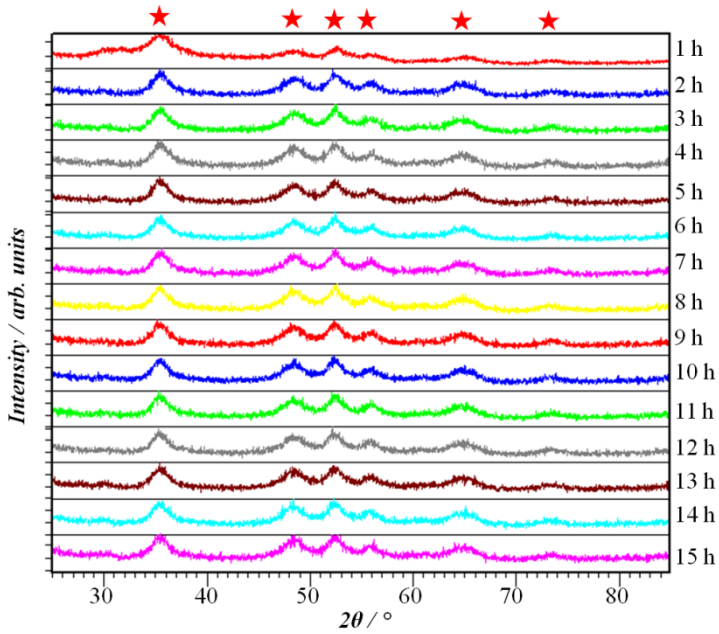

Figure 4-9 Time resolved PXD analysis of Sample 39 under ambient conditions (red stars indicate the broad reflections for $Ca(OH)_2$).

STA was conducted for Samples **39** and **43** exposed to air in order to determine the decomposition properties at the highest Ca and Mg loadings used after air exposure (Appendix B, B.3). A major endothermic event is evident between 350-480 °C in both cases, with the DTA and TG profiles being very similar for both samples. The T_{peak} determined for the Sample **43** is slightly lower than that of the Sample **39**: 717.0 K *vs.* 723.7 K. From the MS data, the mass loss observed in the TG trace is associated with loss

of water from the samples. Water evolution begins at 373 K, although the most intense signal for water evolution is observed during the endothermic event. The same mass of sample was analysed in each case, and the mass loss associated with water evolution is slightly greater in Sample **43** (30.45 wt%) compared with Sample **39** (28.14 wt%).

4.3.2.1. Structure determination of $(Ca_{1-x}Mg_xH_2)_n$ phases by room temperature PXD and SXD

PXD analysis of the as-synthesised samples, which were kept under inert atmosphere and prepared in capillaries, was performed using the D8 diffractometer in Debye-Scherrer geometry. A cubic ternary phase was evident in each sample which could be closely related to the $Ca_{19}Mg_8H_{54}$ phase described by Bertheville and Yvon.[53] Using CELREF, the unit cell parameter, *a*, of the cubic phase in each sample could be determined (Table 4-10).

Table 4-10 CELREF estimation of ternary phase unit cell parameters and volumes compared with known ternary hydride, $Ca_{19}Mg_8H_{54}$.

Sample / CaH_2:MgH_2	a / Å	Volume / Å^3
Bertheville *et al.*[53]	12.1457(6)	1791.71
39 / *2.375:1*	12.220(7)	1824(1)
40 / *2:1*	12.223(7)	1826(1)
41 / *1:0.75*	12.16(1)	1799(2)
42 / *1:1*	12.109(7)	1776(1)
43 / *1:2*	12.103(5)	1773.0(7)

From this preliminary interpretation, it is clear that the unit cell of the ternary phase of these samples is affected by the initial starting ratio of the binary hydrides. The *a* unit cell parameter of Sample **41** has the closest value to that of the original cell parameter for the ternary hydride described by Bertheville. The samples with a higher ratio of CaH_2, *i.e.*, Samples **39** and **40**, have a larger unit cell and excess CaH_2 is evident from the diffraction patterns. For samples with a higher proportion of MgH_2, *i.e.*, Samples **42** and **43**, there is a smaller unit cell relative to Sample **41**. Investigation of the pattern for Sample **42** reveals an additional phase that can be approximated to the second known ternary phase, $Ca_4Mg_3H_{14}$. The diffraction pattern for Sample **43** indicates that an excess of MgH_2 is present. The Rietveld method was used to determine the structure characteristics of the samples more adequately from data collected by the Bruker D8 diffractometer. Refinement data for the ternary phases obtained are given in Table 4-11, and the refined plots are given in Appendix B; B.4 to B.8. Using the $Ca_{19}Mg_8H_{54}$ phase as a starting model, the

refinements quickly converged to give a satisfactory fit to the ternary phase. The ternary phase was refined first and then second phases (CaH_2, α-MgH_2 and $Ca_4Mg_3H_{14}$) were introduced as appropriate (refinement data for the second phases are given in Appendix B, B.9). Hydrogen positions were fixed to literature values for all phases introduced. Temperature factors for the metal sites were refined where possible.

Table 4-11 Rietveld refinement data for the cubic ternary phase in Samples 39-43.

Sample / ***CaH_2:MgH_2***	**39** / ***2.375:1***	**40** / ***2:1***	**41** / ***1:0.75***	**42** / ***1:1***	**43** / ***1:2***
Chemical Formula			$Ca_{19}Mg_8H_{54}$		
Crystal System			Cubic		
/ Space Group			/ $Im\bar{3}$ (204)		
Z			2		
a / Å	12.210(4)	12.214(1)	12.256(2)	12.103(1)	12.097(1)
V / Å^3	1820.4(7)	1822.2(7)	1796.1(7)	1772.7(5)	1770.4(5)
Formula Weight / g			2020.784		
Calculated Density, ρ_x / g cm^{-3}	1.843	1.841	1.868	1.893	1.895
Phase Fraction / %	47.2(4)	59.3(8)	100	82.8(8)	69.7(6)
Refinement Parameters	40	47	30	52	51
Data Points	12117	5452	11829	5323	12117
R_{wp} / %	4.88	3.46	5.43	3.12	3.61
R_p / %	3.78	2.71	3.91	2.42	2.76
χ^2	1.638	1.400	1.256	1.579	1.597

The unit cell parameters and cell volumes derived from CELREF and from the Rietveld method are in close approximation to one another, showing the same trend in the unit cell parameter and unit cell volume as the CaH_2:MgH_2 stoichiometry is varied. As the proportion of Ca increases, both the cell parameter and cell volume increase in near linear fashion (Figure 4-10). It was suggested, therefore, that changing the initial binary hydride ratio allowed formation of a range of non-stoichiometric ternary hydrides of the $(Ca_{1-x}Mg_xH_2)_n$ general formula.

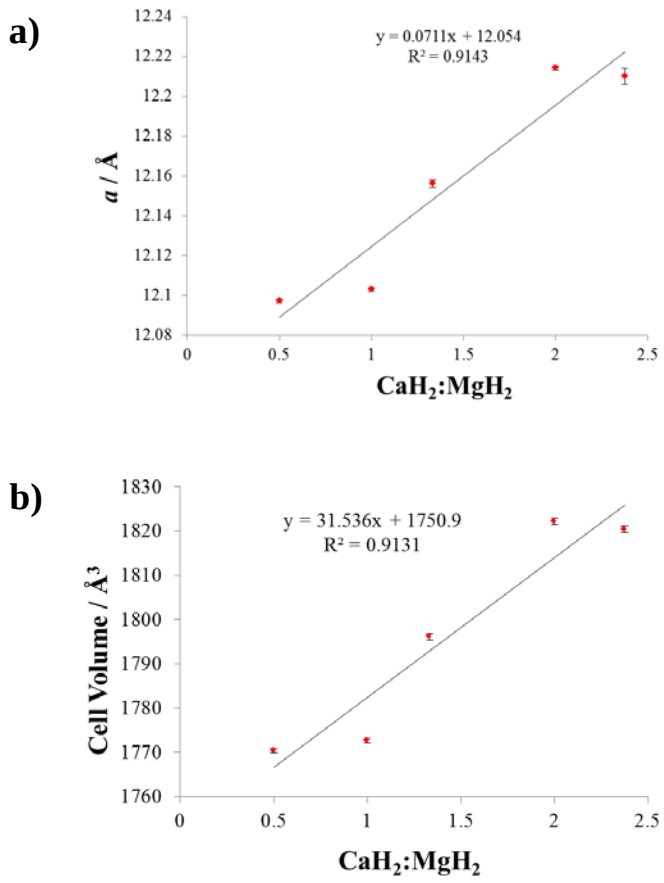

Figure 4-10 Ternary phase unit cell a) *a* parameter, and b) cell volume derived from Rietveld refinement of lab PXD data plotted relative to initial CaH_2:MgH_2 ratio employed (Samples 39-43).

SXD was conducted to elucidate further structural information about the non-stoichiometric ternary phases proposed for these samples. As before, Rietveld refinements were conducted and a reasonable fit was obtained with respect to the initial ternary phase model, $Ca_{19}Mg_8H_{54}$.[53] The profile parameters were then considered to obtain a good model of the peak shapes obtained. Then atomic parameters were included. Temperature factors for the H atoms were fixed to the values given by Bertheville as before, and those of the metal atoms were refined isotropically where possible or fixed if they caused significant instability of the refinement. Attempts were made to refine these anisotropically but the refinements rapidly became unstable. In order to evaluate the changes in the Ca:Mg stoichiometric ratio in the ternary phase, an additional Mg atom was added in the "Mg rich" samples in the Ca *24g* position. For the "Ca rich" samples, an additional Ca atom was placed on the Mg *16f* position. In each case, the Site Occupancy Factor (SOF) was allowed to vary using appropriate constraints for the metals on these positions and the refinement conducted until convergence was achieved. The resultant ternary phases and the crystallographic data obtained by Rietveld refinements for each sample analysed by SXD at room temperature are given in Table 4-12.

Table 4-12 Crystal structure data for samples analysed by SXD.

Sample / CaH_2:MgH_2 ratio	**39 / 2.375:1**	**40 / 2:1**	**41 / 1:0.75**	**42 / 1:1**	**43 / 1:2**
Chemical Formula	$Ca_{21.4(3)}Mg_{5.6(3)}H_{54}$	$Ca_{21.6(1)}Mg_{5.1(1)}H_{54}$	$Ca_{15.6(3)}Mg_{11.4(3)}H_{54}$	$Ca_{15.2(2)}Mg_{11.8(2)}H_{54}$	$Ca_{13.3(8)}Mg_{13.8(8)}H_{54}$
Crystal System / Space Group			Cubic / $Im\bar{3}$ (204)		
Z			2		
a / Å	12.2035(6)	12.2074(7)	12.1420(5)	12.0927(9)	12.081(1)
V / $Å^3$	1817.4(3)	1819.1(3)	1790.1(2)	1768.3(4)	1763.2(5)
Formula Weight / g	2096.721	2210.314	1915.602	2007.999	1949.594
Calculated Density, ρ_x / g cm^{-3}	1.916	2.018	1.777	1.886	1.836
Phase Fraction / %	53.1(2)	79.0(1)	-	82.3(2)	83.0(5)
Refinement Parameters	42	45	41	60	64
Data Points	3999	3999	3999	3999	3999
R_{wp} / %	3.35	3.27	4.14	4.26	3.91
R_p / %	2.47	2.48	3.01	3.15	2.85
χ^2	0.9547	0.6089	0.7977	1.285	1.053

The refinement plot (Figure 4-11), interatomic distances (Table 4-13) and atomic parameters (Table 4-14) are given in for the 1:0.75 sample, where full data for the remaining samples are given in Appendix B, B.10 through to B.19, inclusive. Supplementary information regarding the additional phases is also given in Appendix B, B.20. The high quality SXD data confirmed the assignment of the second phases for each sample as appropriate (see Appendix B for refinement data of the additional phases), and verified the absence of any residual CaH_2 or MgH_2 in the 1:0.75 sample.

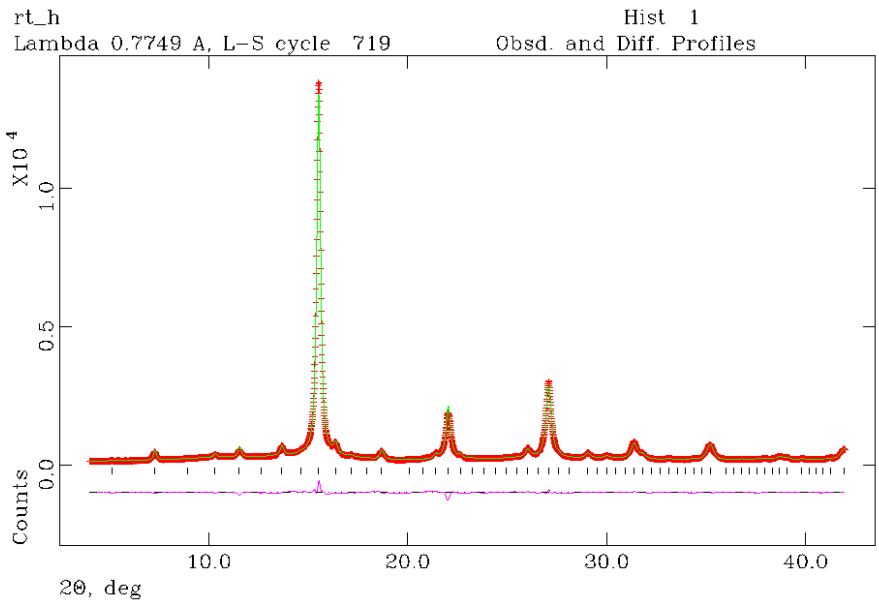

Figure 4-11 Rietveld plot for Sample 41 analysed by SXD showing a highly resolved diffraction profile for the ternary phase only (black tick marks). Red crosses indicate observed data, the green line shows the calculated pattern and the magenta line indicates the difference plot.

Table 4-13 Interatomic distances for $Ca_{15.6(3)}Mg_{11.4(3)}H_{54}$ (Sample 41).

Interatomic Distance	Literature Values[53] /Å	Length / Å
Ca(1)/Mg*-H(1) ×2	2.21(2)	2.1740(18)
Ca(1)/Mg*-H(1) ×2	2.47(1)	2.4949(7)
Ca(1)/Mg*-H(2) ×2	2.23(2)	2.2640(23)
Ca(1)/Mg*-H(2) ×1	2.20(1)	2.2126(22)
Ca(1)/Mg*-H(4) ×1	2.27(2)	2.3452(22)
Ca(2)-H(1) ×4	2.51(1)	2.51898(35)
Ca(2)-H(2) ×2	2.36(2)	2.3737(11)
Ca(2)-H(3) ×2	2.34(3)	2.3521(27)
Ca(2)-H(4) ×2	2.46(3)	2.4882(27)
Ca(3)-H(3) ×12	2.48(2)	2.48923(7)
Mg(1)-H(1) ×3	1.92(1)	1.9364(17)
Mg(1)-H(3) ×3	2.032(9)	2.0380(28)

N.B. Mg* represents the additional Mg on the Ca site.

Table 4-14 Atomic parameters for $Ca_{15.6(3)}Mg_{11.4(3)}H_{54}$ (Sample 41)

Atom	Site	*x*	*y*	*Z*	$100xU_{iso}$ / Å^2	SOF
Ca1	24*g*	0	0.3107(2)	0.3437(2)	3.9(1)	0.72(1)
Ca2	12*d*	0.3325(3)	0	0	3.4(1)	1
Ca3	2*a*	0	0	0	4.0(5)	1
Mg1	16*f*	0.1598(2)	0.1598(2)	0.1598(2)	1.6(2)	1
Mg*	24*g*	0	0.3107(2)	0.3437(2)	3.9(1)	0.28(1)
H1	48*h*	0.3109	0.1109	0.174	2.926	1
H2	24*g*	0	0.3985	0.184	2.926	1
H3	12*g*	0	0.173	0.11	2.926	1
H4	24*e*	0.118	0.5	0	2.926	1

N.B. Atomic parameters for H1-4 were fixed to literature positions. Mg* represents the additional Mg on the Ca site.

Upon comparison of the *a* unit cell parameter for each sample given by the lab PXD and SXD, it is evident that the values obtained by SXD (Table 4-12, Figure 4-12) are all slightly smaller than the values obtained by lab PXD (Table 4-11, Appendix B; B.4 to B.8). It is clear, however, that the general trends in cell volume and *a* cell parameter with respect to the initial CaH_2:MgH_2 ratio determined by CELREF, lab PXD and SXD are comparable.

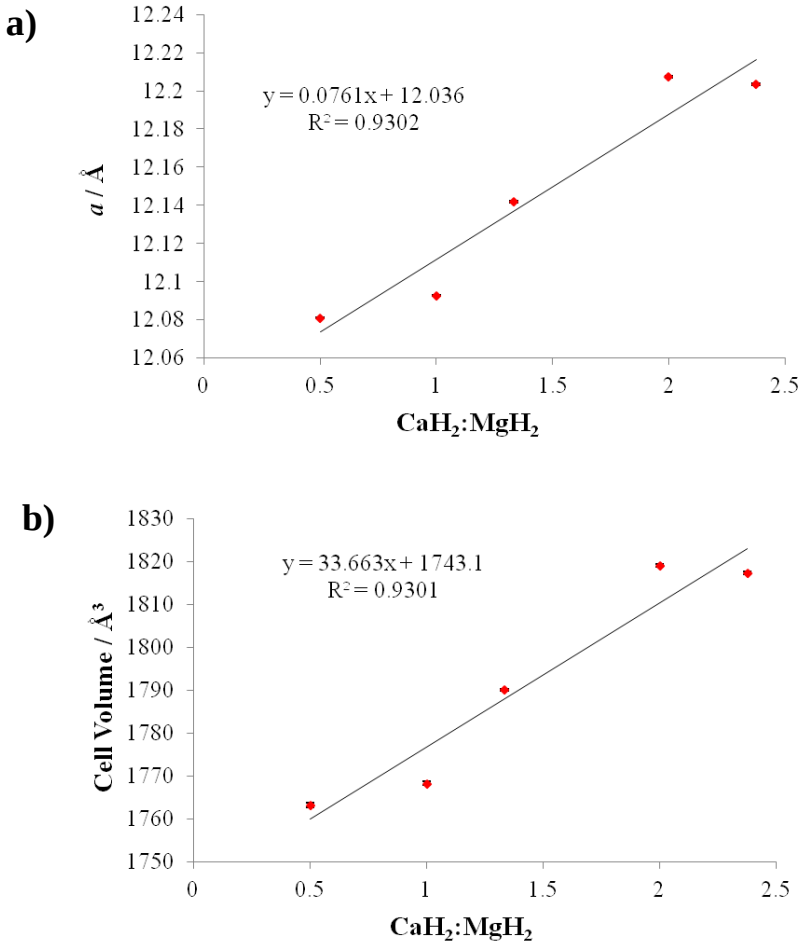

Figure 4-12 Ternary phase unit cell a) *a* parameter, and b) cell volume derived from Rietveld refinement of SXD data plotted relative to initial CaH_2:MgH_2 ratio employed.

In each sample, the atomic parameters of the samples were shifted with respect to the values given by Bertheville, suggesting modifications to the crystal lattice as a result of the incorporation of excess Ca or Mg on specific sites. To determine the excess Ca/Mg in each phase, additional atoms were introduced on to specific sites and the site occupancy factors (SOFs) were varied. Excess Ca was introduced on to the 16*f* position of Mg for Samples **39** and **40**; this being the only site that Bertheville *et al.* had determined to be fully occupied by Mg. The unit cell representation and coordination of the 16*f* site for the excess Ca sample, Sample **39**, with a chemical formula determined as $Ca_{21.4(3)}Mg_{5.6(3)}H_{54}$, are given in Figure 4-13. The bipyramidal polyhedra highlighted in blue and indigo represent the octahedrally coordinated Ca/Mg-H configuration of the 16*f* site for $Ca_{21.4(3)}Mg_{5.6(3)}H_{54}$ and $Ca_{21.6(1)}Mg_{5.1(1)}H_{54}$, respectively. Surprisingly, the Sample **40** has a slightly larger unit cell than Sample **39**, and this result is consistent across all analysis methods used herein.

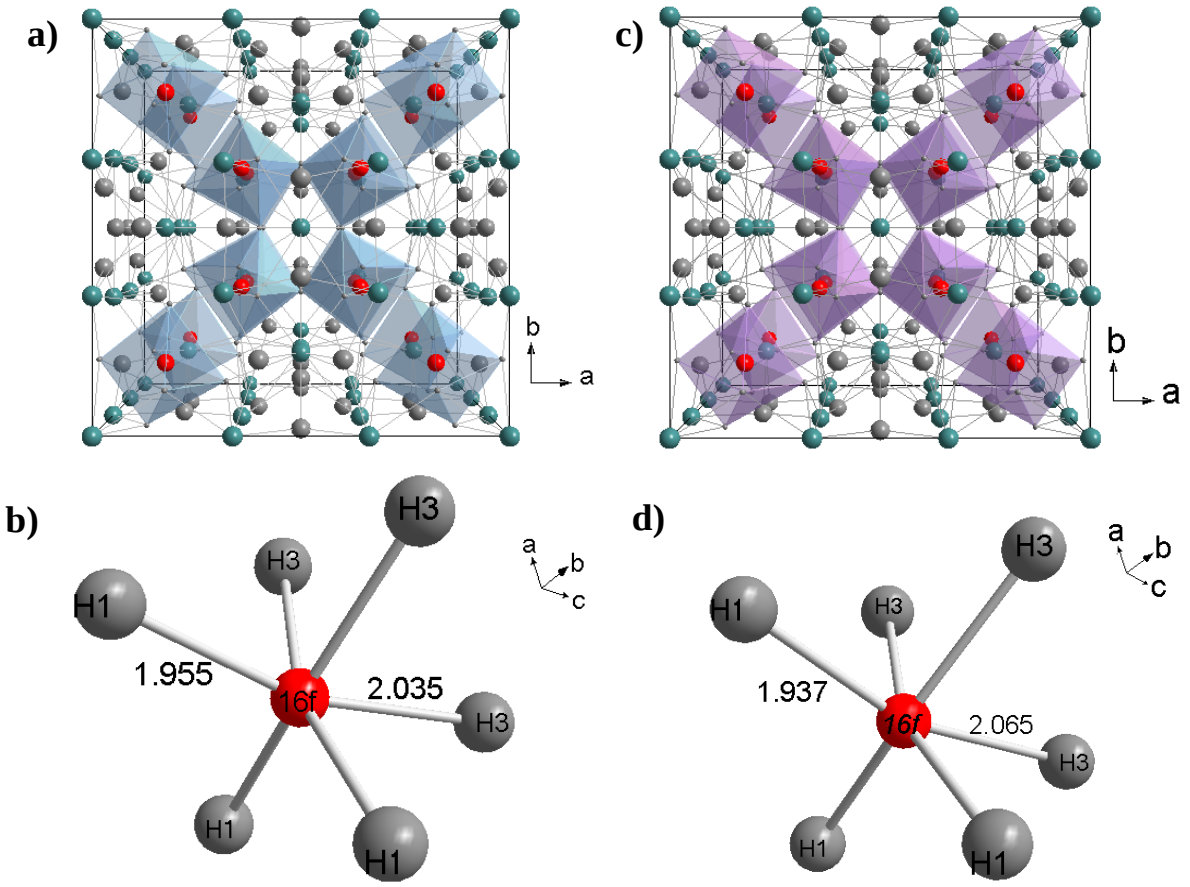

Figure 4-13 a) Unit cell representation of Sample 39; $Ca_{21.4(3)}Mg_{5.6(3)}H_{54}$, and b) coordination of its Ca/Mg-centred 16*f* site. c) Unit cell representation of Sample 40; $Ca_{21.6(1)}Mg_{5.1(1)}H_{54}$, and d) coordination of its Ca/Mg-centred 16*f* site. (Ca = green, Mg = blue, Ca/Mg = red, H = grey.)

Excess Mg was introduced on to the 24*g* (Ca1) position since this has the shortest Ca-H length (2.20(1) Å)[53] and therefore was proposed as the most likely position on which Mg could be incorporated. The unit cell of the single phase sample (Sample **41**) determined as $Ca_{15.6(3)}Mg_{11.4(3)3}H_{54}$ is depicted in Figure 4-14(a). The metal-hydrogen coordination of the 16*f* and 24*g* positions are represented by blue and pink polyhedra, respectively. The former being the Mg-only positions which exist in an octahedral, six coordinate configuration, and the latter indicating where excess Mg has been introduced on the eight coordinate icosahedral Ca1 24*g* site.

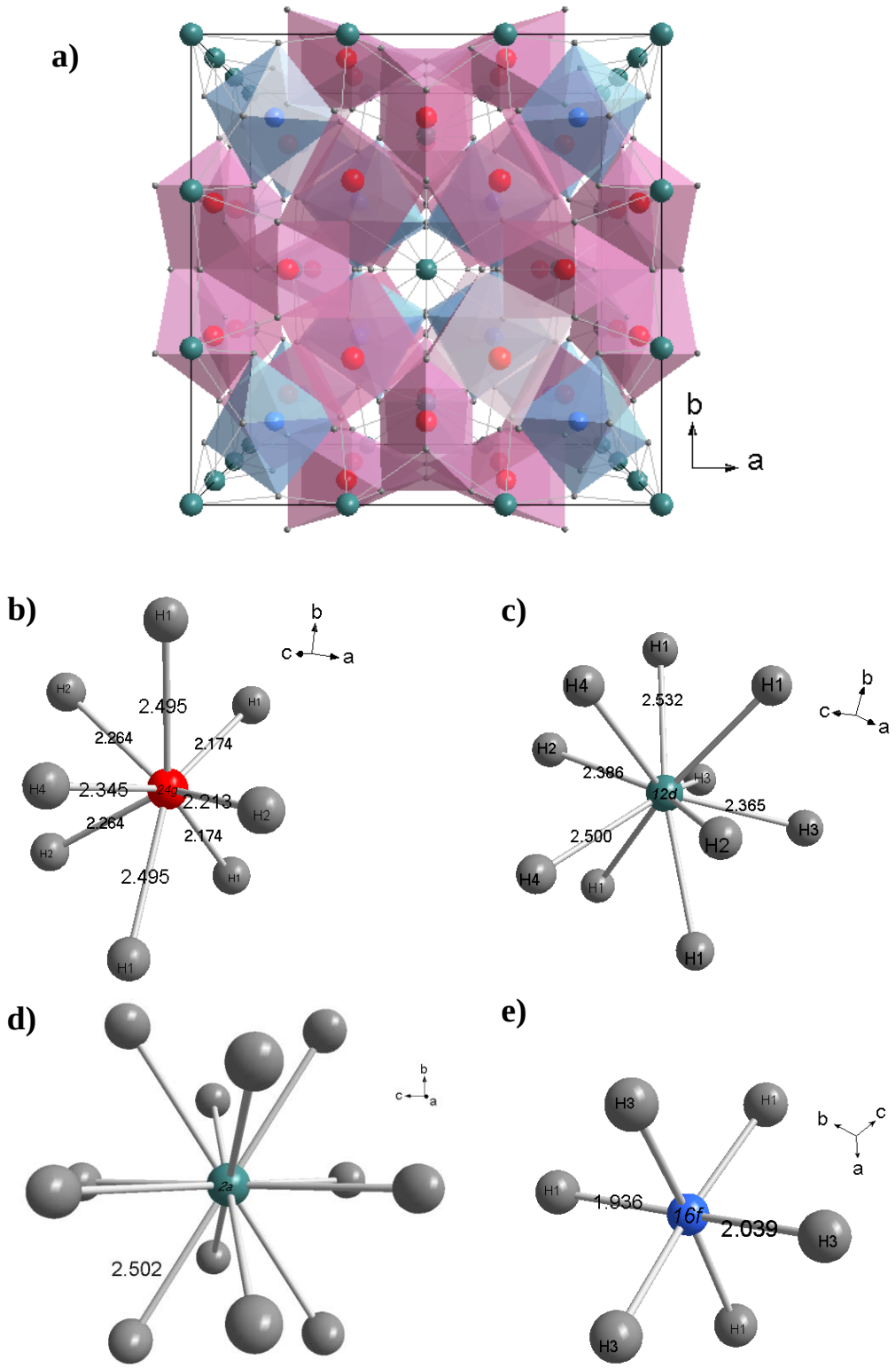

Figure 4-14 Unit cell representation of a) Sample 41; $Ca_{15.6(3)}Mg_{11.4(3)}H_{54}$, and b-e) the coordination orientations of the 24*g*, 12*d*, 2*a* and 16*f* metal sites, respectively. (Ca = green, Mg = blue, Ca-Mg = red, H = grey.)

For Samples **42** and **43**, the unit cell is contracted further and these are represented in Figure 4-15 a) and Figure 4-15 b), respectively, with the fawn and grey polyhedra of the shared Ca/Mg 24*g* site highlighted and their coordination orientations revealed (Figure 4-

15 c) and Figure 4-15d)). As before, the blue polyhedra indicate the six coordinate Mg-only 16*f* site.

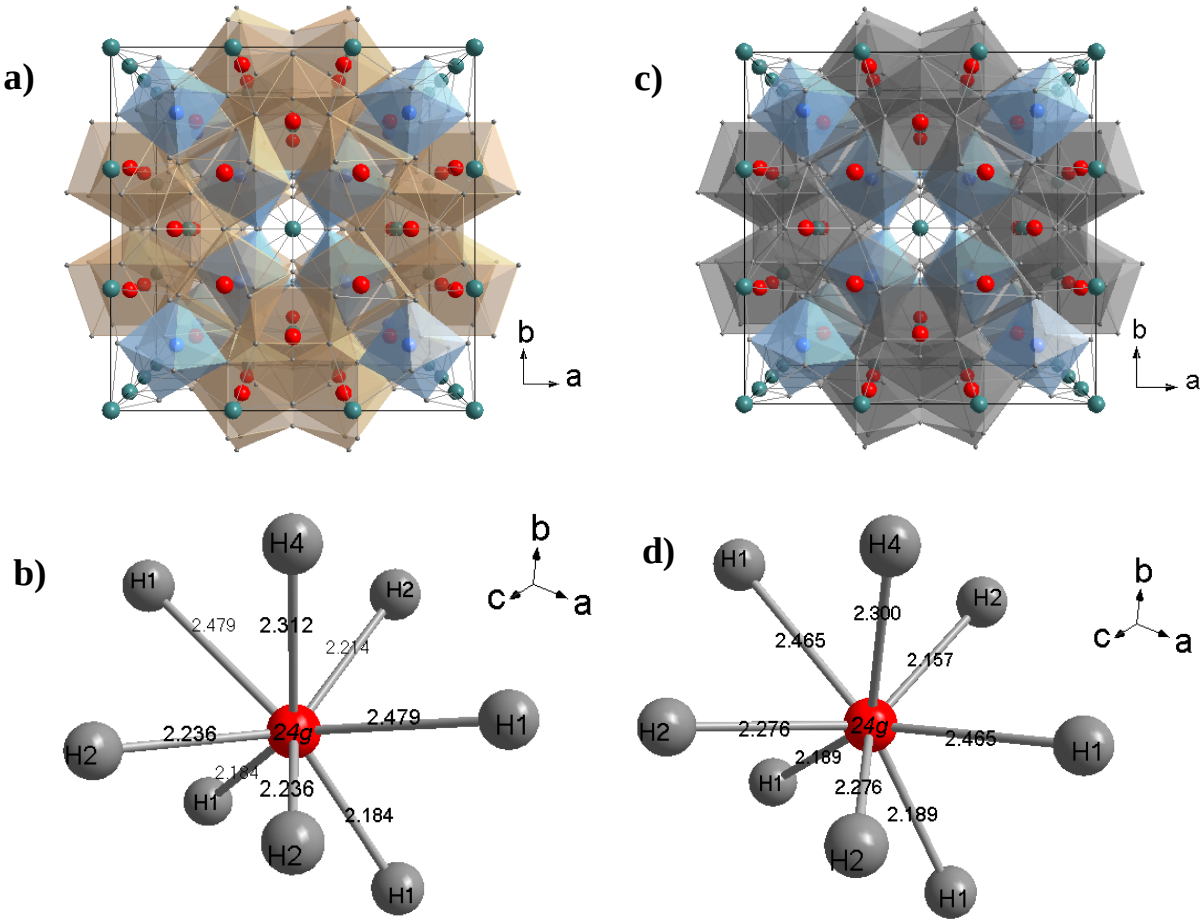

Figure 4-15 a) Unit cell representation of Sample 42; $Ca_{15.2(2)}Mg_{11.8(2)}H_{54}$, and b) coordination of its 24*g* site. c) Unit cell representation of Sample 43; $Ca_{13.3(8)}Mg_{13.8(8)}H_{54}$, and d) coordination of its 24*g* site. (Ca = green, Mg = blue, Ca-Mg = red, H = grey.)

4.3.2.2. Thermal decomposition of the $(Ca_{1-x}Mg_xH_2)_n$ phases

Thermal analysis of the samples was conducted to evaluate the hydrogen release properties of the hydrides. The thermal and mass loss profiles indicate a single endothermic peak for each sample associated with the loss of hydrogen occurring between 350-450 ^{o}C. Subsequent hydrogen loss occurs above 600 ^{o}C with the TG profiles indicating a melting process to be associated with this second hydrogen release (Figure 4-16). The MS data reveals that the onset temperature of the hydrogen release events in each sample was influenced by the initial CaH_2:MgH_2 ratio used, *i.e.*, hydrogen is released earlier from those containing a higher proportion of Mg and *vice versa*. Interesting information at high temperatures may be extracted to show that the decomposition at this point may occur *via* a multi-step process.

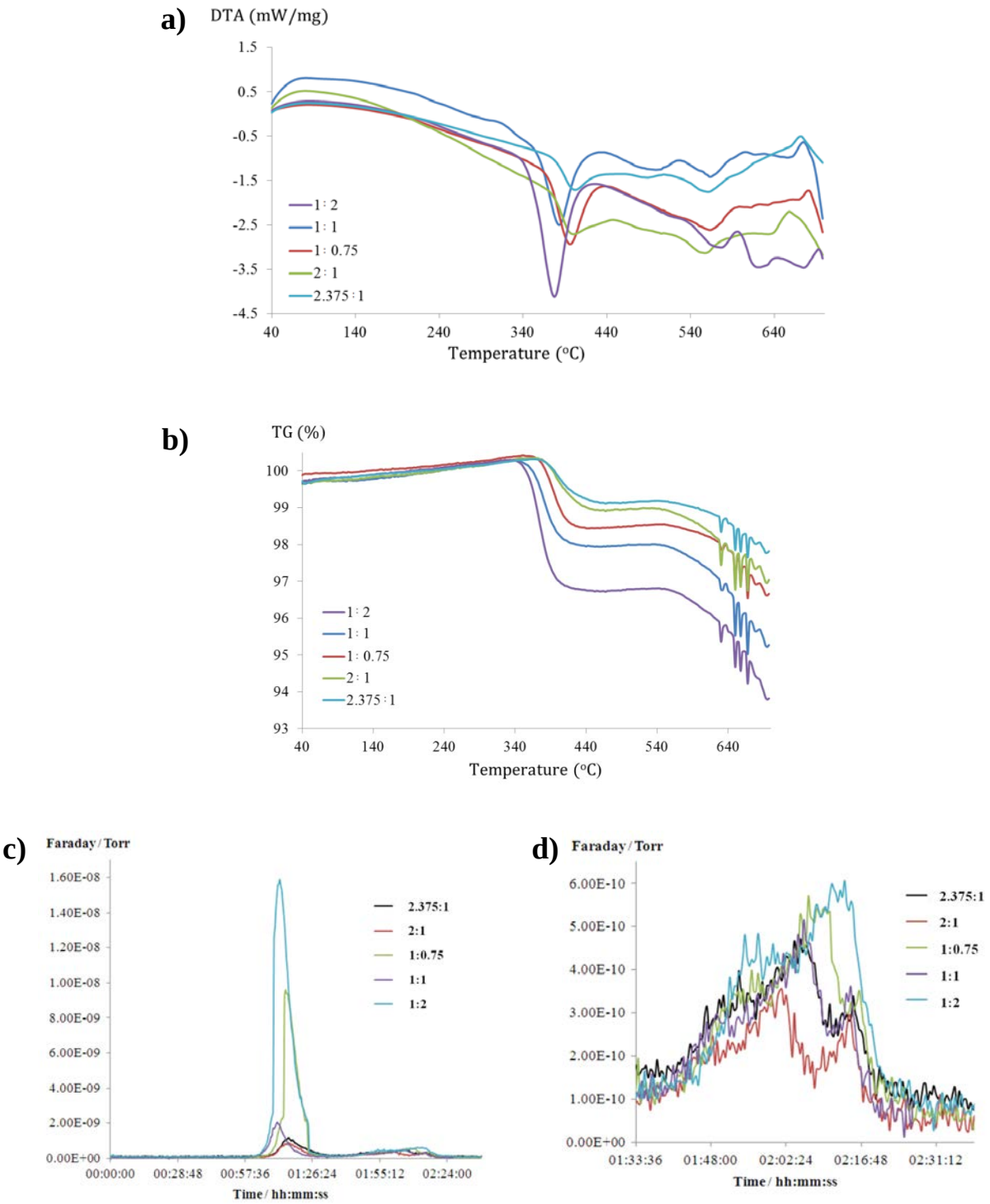

Figure 4-16 a) DTA and b) TG collected at 5 °C/min for samples 39-43, where the CaH_2:MgH_2 ratios are given in the legends. Corresponding MS data for the same samples showing c) full H_2 desorption profile and d) high temperature MS (*m/z* = 2) data.

The peak decomposition temperature (T_{peak}) increases with increasing Ca content (Table 4-15). This may be expected since CaH_2 is more stable than MgH_2, and so the additional Ca may stabilise the ternary phase further. The wt% mass loss decreases with increasing Ca content, which corresponds with the relative increase in formula mass and hence decrease in gravimetric capacity of the composite with increasing proportions of Ca in the system. A

stark contrast in MS signals for H_2 from the excess Ca (*e.g.*, Sample **39**) and excess Mg samples (*e.g.*, Sample **43**) is evident, despite using the same quantity of sample (30 mg) for each analysis, and thus reflects the respective increase in mass loss upon increasing Mg proportions in the ternary phase and *vice versa*.

Table 4-15 Decomposition properties of Sample 39-43.

	DTA		TG	
Sample / CaH_2:MgH_2	T_{onset} / K	T_{peak} / K	TG_{onset} / K	ΔMass / wt%
39 / 2.375:1	651.2	675.2	657.9	1.13
40 / 2:1	651.2	672.2	665.2	1.38
41 / 1:0.75	644.2	668.9	650.8	1.94
42 / 1:1	632.9	655.2	641.1	2.29
43 / 1:2	623.9	650.4	631.4	3.49

The Kissinger plots and relevant data obtained for Samples **39-43** are given in Figure 4-17 and Table 4-16. These show that the activation enthalpy remains relatively similar for these samples.

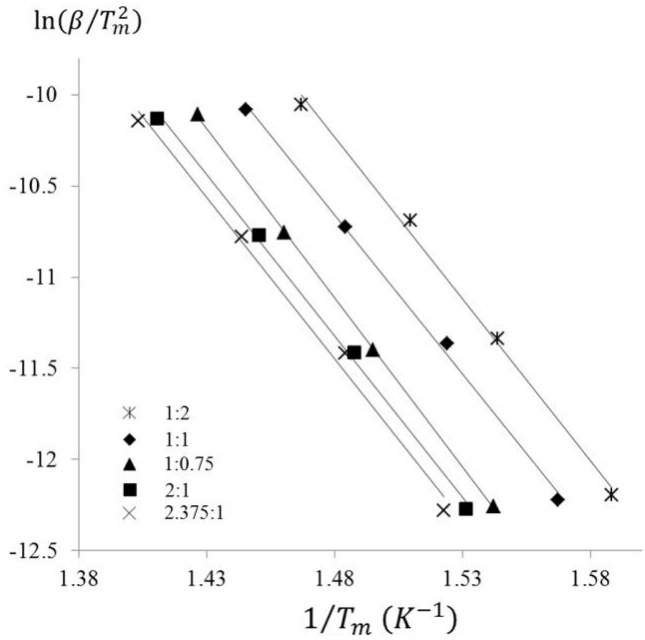

Figure 4-17 Comparison of Kissinger plots of Samples 39-43 where the CaH_2:MgH_2 stoichiometries for each sample are indicated.

Table 4-16 Kissinger plot data for Samples 39-43.

Sample / *CaH_2:MgH_2*	**Trendline Equation**	**R^2**	**E_a (kJ/mol)**
39 / 2.375:1	$y = -17.672x + 14.708$	0.992	146±9
40 / 2:1	$y = -17.683x + 14.848$	0.9977	147±5
41 / 1:0.75	$y = -18.535x + 16.320$	0.9998	154±1
42 / 1:1	$y = -17.45x + 15.169$	0.9975	145±5
43 / 1:2	$y = -17.775x + 16.076$	0.996	147±7

Samples were heated to 523 K, 773 K and 973 K in order to determine the decomposition process in the system. The ternary phase has been previously described to decompose *via* the $Ca_4Mg_3H_{14}$ phase. In each case, respective ternary "$Ca_{19}Mg_8H_{54}$" phases were identified in post STA PXD analysis and therefore had not decomposed upon heating to 523 K (Figure 4-18). At 773 K, very similar patterns were obtained for each sample, where reflections from the binary hydride CaH_2 and Mg metal were identified by PXD and confirmed by Rietveld refinement. (All atomic parameters and temperature factors were fixed to the literature values for each phase, and areas at low 2θ were omitted since no reflections were expected in the region below 15 ^{o}.)

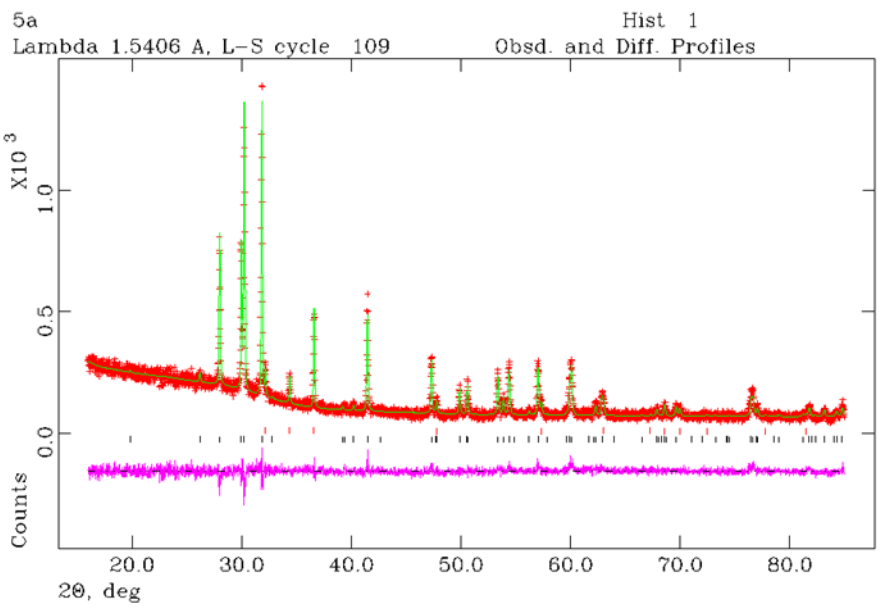

Figure 4-18 Typical PXD pattern collected for samples retrieved after heating to 773 K (Sample 39). (CaH_2 indicated by black tick marks, and Mg indicated by red tick marks). Red crosses show experimental data, the green line is the calculated data and the magenta line is the difference plot.

Using the refinement data of the patterns obtained after heating, it was possible to deduce the relative proportion of CaH_2:Mg after heating to 773 K (Table 4-17). These ratios do not correlate with the original starting ratio of Ca:Mg in each case since the proportion of Mg is lower than expected in each case. Although is it evident that the proportion of Mg increases in the heated sample as a function of the CaH_2:MgH_2 mixture, where Sample **43** has significantly more Mg in the decomposition product than Sample **39**.

Table 4-17 Phase fractions of CaH_2 and Mg from Rietveld refinement of Samples 39-43 collected after heating to 773 K.

	Phase Fractions / %	
Sample	***CaH_2***	***Mg***
39	80.9(4)	19.1(4)
40	82.4(6)	17.6(6)
41	69.1(7)	30.9(7)
42	62(1)	38(1)
43	46.3(4)	53.6(4)

The samples collected after thermal analysis to 973 K indicate the presence of two main phases; CaH_2 and a hexagonal C14-type Laves phase, $CaMg_2$ (Figure 4-19).[77] The presence of $CaMg_2$ in the samples heated to 973 K is likely be the product of the melting feature observed in the DTA above 873 K. (Again, all atomic parameters and temperature factors were fixed to the literature values for each phase, and areas at low 2θ were omitted since no reflections were expected in the region below 15°.) The structure of $CaMg_2$ phase was first described by Witte in 1937, with cell parameters of a = 6.22 Å, c = 10.10 Å.[78] The crystal structure of the Laves phase formed in this work is in excellent agreement with more recent literature values obtained by Gingl and Yvon (Table 4-18, a = 6.2709(5) Å, c = 10.1696(7) Å, volume = 346.3 $Å^3$).[77] (Advanced information about Laves phase formation may be found in reference 79 and in also the relatively more recent two part review by Stein *et al.*[80, 81])

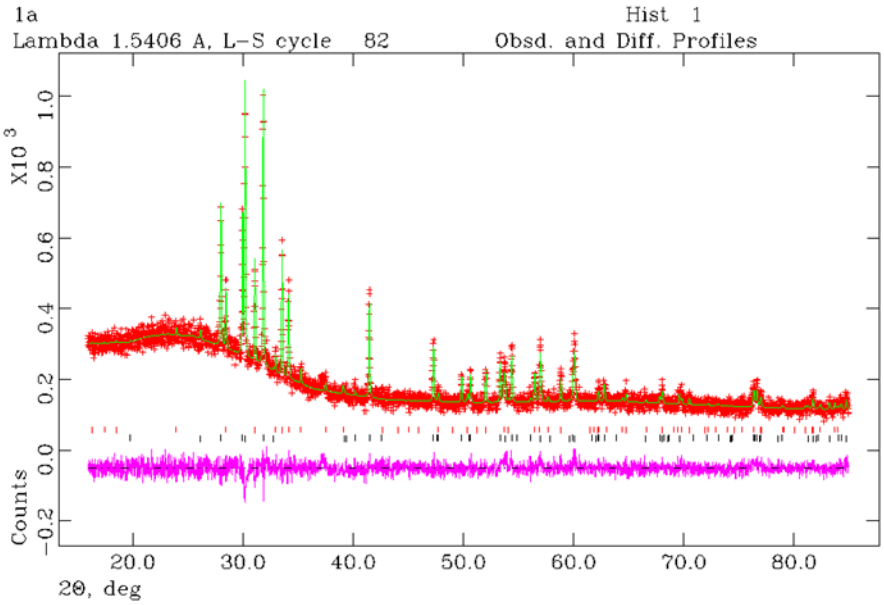

Figure 4-19 Typical PXD pattern collected for sample collected after STA after heating to 973 K (Sample 39). (CaH_2 indicated by black tick marks and $CaMg_2$ indicated by red tick marks). Red crosses show experimental data, the green line is the calculated data and the magenta line is the difference plot.

Table 4-18 Exemplar Rietveld refinement data for samples collected after heating to 773 K and 973 K (data is given for Sample 39).

Temperature / K	***773***		***973***	
Chemical Formula	CaH_2	Mg	CaH_2	$CaMg_2$
Crystal System / Space Group	Orthorh. / *Pnma* (62)	Hexagonal / *P6₃/mmc* (194)	Orthorh. / *Pnma* (62)	Hexagonal / *P6₃mmc* (194)
Z	4	2	4	4
***a* / Å**	5.9581(5)	3.2109(4)	5.9594(4)	6.2723(7)
***b* / Å**	3.6050(3)	*a*	3.6024(2)	*a*
***c* / Å**	6.8019(5)	5.2146(8)	6.1823(5)	10.170(1)
***V* / Å^3**	146.10(3)	46.56(2)	146.25(3)	346.50(9)
Formula Weight / g	168.384	48.610	168.384	354.760
Calculated Density, ρ_x / g cm^{-3}	1.914	1.734	1.912	1.700
Refinement Parameters	29		38	
Data Points	4240		4240	
R_{wp}	9.46		7.70	
R_p	7.37		6.09	
χ^2	1.213		1.154	

Using the phase fraction information obtained from Rietveld refinement of the PXD data collected for samples retrieved after heating to 973 K, the proportion of $CaMg_2$ was shown to increase, with a relative decrease in the CaH_2 phase fraction (Table 4-19). Therefore, the initial CaH_2:Mg_2 ratio has an effect on the conversion of CaH_2 and Mg to $CaMg_2$ at high temperatures, where higher proportions of Mg in the system allow a greater proportion of $CaMg_2$ to be produced. For Sample **42**, Mg was also evident. Attempts to introduce Mg to the refinements of the other samples were made, but the phase fraction of Mg was found to be negligible in all other instances.

Table 4-19 Phase fractions of CaH_2 and Mg from Rietveld refinement of samples collected after heating to 973 K.

	Phase Fractions / %		
Sample	***CaH_2***	***$CaMg_2$***	***Mg***
39	64.9(8)	35.1(8)	-
40	54.9(4)	45.1(4)	-
41	44.3(4)	55.7(4)	-
42	42.3(4)	45.2(4)	12.5(8)
43	39.8(3)	60.2(3)	-

4.3.2.3. Comparison of decomposition properties of selected ternary phases by *in-situ* SXD analysis

To probe the decomposition mechanism further, *in-situ* variable temperature SXD was conducted on two of the samples between 298 - 673 K. Due to time limitations, only two of the five samples could be examined in this way; 2:1 (Sample **40**) and 1:1 (Sample **42**). For Sample **42** the cubic $Ca_{19}Mg_8H_{54}$-type ternary phase remained between room temperature and 573 K, with lattice expansion effects observed due to heating (Figure 4-20). It is clear, however, that a shoulder becomes prominent on the low angle side of the ternary phase peak at 573 K, which is the result of resolution of the $Ca_4Mg_3H_{14}$ phase as the temperature increased.

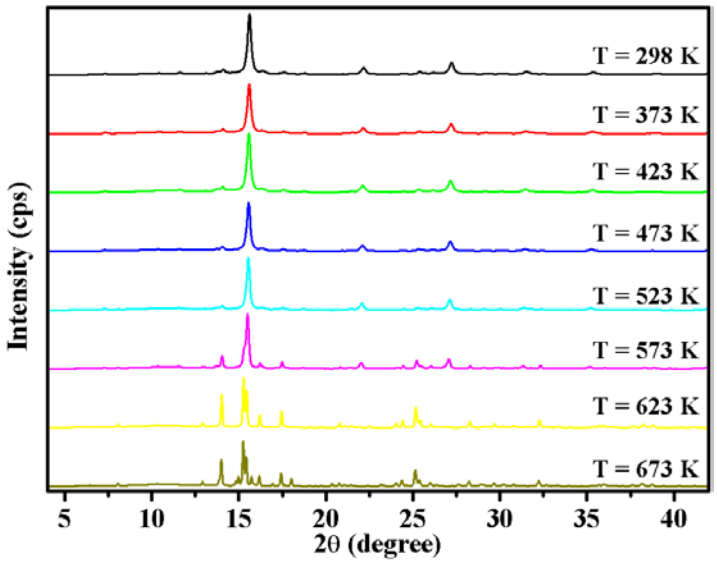

Figure 4-20 SXD patterns collected *in-situ* between 298-673 K for Sample 42.

Figure 4-21 shows the near linear trends obtained for the *a* cell parameter and cell volume of the ternary phase with respect to temperature (up to 573 K) for Sample **42**.

a)

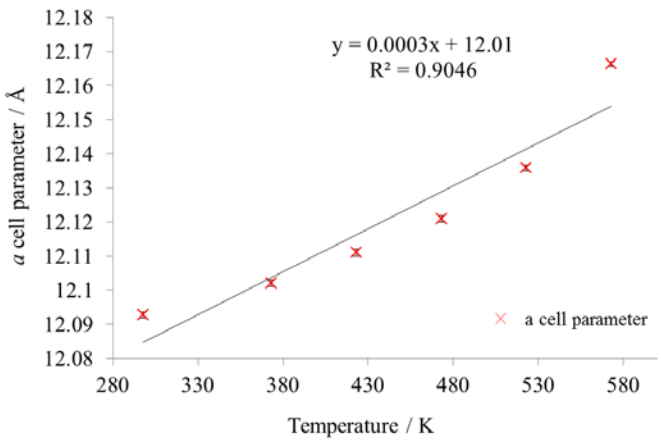

b)

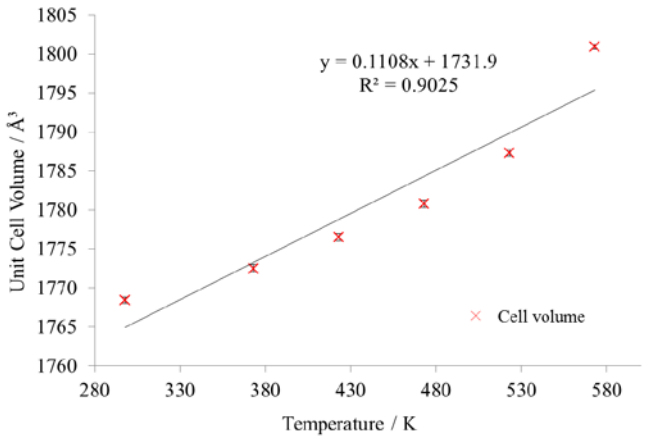

Figure 4-21 Plots of a) *a* cell parameter and b) cell volume for the ternary phase between 298-573 K for Sample 42.

The relative phase fractions of the two ternary phases remain relatively constant until 523 K, with the $Ca_{19}Mg_8H_{54}$-type phase being dominant, *ca.* 80 %. Rietveld refinement of the sample collected at 573 K, however, reveals that the proportion of the $Ca_4Mg_3H_{14}$-type phase is increased relative to the $Ca_{19}Mg_8H_{54}$-type phase (Rietveld refinement data for the diffraction data collected at 573 K are provided in Appendix B, B.21 and B.22). This suggests that the $Ca_{19}Mg_8H_{54}$-type phase has decomposed to the $Ca_4Mg_3H_{14}$-type phase. This is in agreement with the decomposition process suggested previously for $Ca_{19}Mg_8H_{54}$-type phase by Bertheville and Yvon.[53] The observation of this process at 573 K in this work is lower than the temperature quoted previously for the $Ca_{19}Mg_8H_{54}$ phase decomposition (650-700 K).

The $Ca_4Mg_3H_{14}$ phase was revealed as the only crystalline phase present at 623 K. Rietveld refinement showed that the $Ca_4Mg_3H_{14}$-type phase contained slightly more Mg than previously described (Figure 4-22, Table 4-20 and Table 4-21). This was determined by including an additional atom on the Ca 2*e* site since this has the shortest Ca-H length (2.287(4) Å), and allowing the site occupancy to vary. The formula for the hydride found at 623 K could thus be described as "$Ca_{3.93(2)}Mg_{3.07(3)}H_{14}$" (Table 4-20). The lattice parameters are larger than those given by Gingl *et al.* (a = 6.3065(2) Å, c = 6.8820(2) Å), but some contribution towards this is likely from the elevated temperature at which the pattern was collected in this work.[52] (Inclusion of MgH_2 was attempted, but the refinement diverged instantly.)

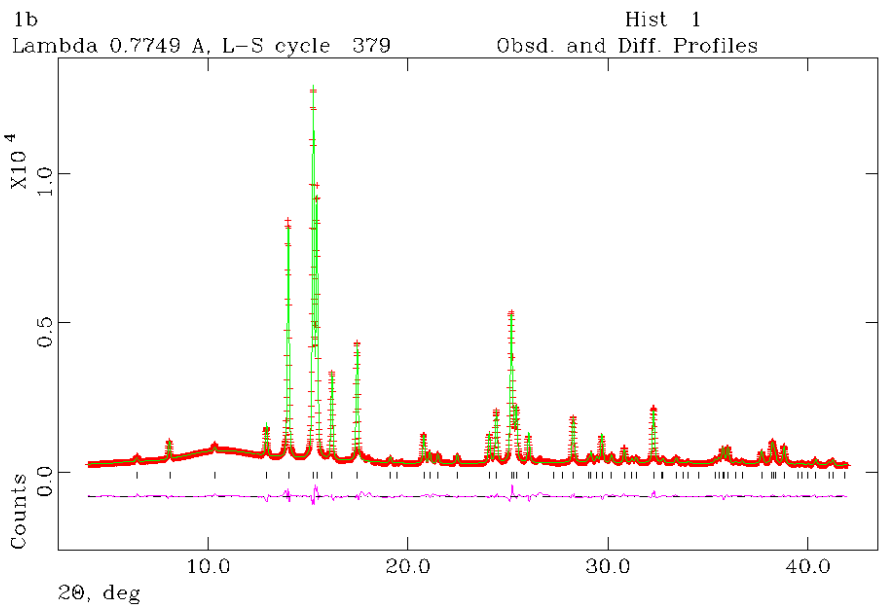

Figure 4-22 SXD pattern of Sample 42 collected after heating *in-situ* 623 K, where the black tick marks represent the "$Ca_{3.93(2)}Mg_{3.07(3)}H_{14}$" phase. Red crosses show experimental data, the green line is the calculated data and the magenta line is the difference plot.

Table 4-20 Rietveld refinement data collected using *in-situ* Synchrotron X-ray Diffraction (623 K) for Sample 42.

Chemical Formula	"$Ca_{3.93(2)}Mg_{3.07(3)}H_{14}$"
Crystal System / Space Group	Hexagonal / $P\bar{6}2m$ (189)
Z	1
***a* / Å**	6.3470(1)
***b* / Å**	*a*
***c* / Å**	6.8787(1)
***V* / Å^3**	239.98(1)
Formula Weight / g	246.264
Calculated Density, ρ_x / g cm^{-3}	1.704
Refinement Parameters	37
Data Points	3999
R_{wp}	5.57
R_p	3.95
χ^2	1.844

Table 4-21 Atomic parameters for $Ca_{3.93(2)}Mg_{3.07(3)}H_{14}$.

Atom	Site	*x*	*y*	*Z*	100xU_{iso} / Å^2	SOF
Ca1	2*e*	0	0	0.2657(2)	2.57(6)	0.966(7)
Ca2	2*d*	$\frac{1}{3}$	$\frac{2}{3}$	$\frac{1}{2}$	2.52(6)	1
Mg1	3*f*	0.5476(3)	0	0	3.47(8)	1
Mg*	2*e*	0	0	0.2657(2)	2.57(6)	0.034(7)
H1	6*i*	0.61282	0	0.2748(2)	2.5	1
H2	3*g*	0.230205	0	$\frac{1}{2}$	2.5	1
H3	*3f*	0.224220	0	0	2.5	1
H4	2*c*	$\frac{1}{3}$	$\frac{2}{3}$	0	2.5	1

N.B. Atomic parameters for H1-4 were fixed to literature positions.

The unit cell structure of the "$Ca_{3.93(2)}Mg_{3.07(3)}H_{14}$" phase identified in the sample heated to 623 K is given in Figure 4-23. The green, pink and blue polyhedra represent the coordination orientations of the Ca-centred 2*d* site, the Mg-centred 3*f* site and the shared Ca/Mg-centred 2*e* site.

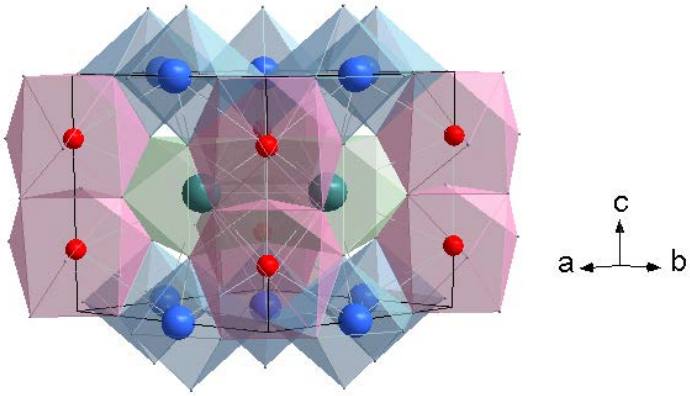

Figure 4-23 Polyhedral representation of the unit cell structure of "$Ca_{3.93(2)}Mg_{3.07(3)}H_{14}$". The green, blue and small light grey spheres represent Ca, Mg, and H atoms respectively. The red spheres represent the shared Ca/Mg 2*e* site.

At 673 K the sample had decomposed further with four phases evident in the sample; a ternary $Ca_4Mg_3H_{14}$-type phase, CaH_2, MgH_2 and Mg, where Rietveld refinement was conducted to determine the phase fractions of the sample (Figure 4-24, Table 4-22). The atomic and temperature parameters of the four phases were fixed to literature values, and the metal site occupancies of the ternary phase were also fixed.

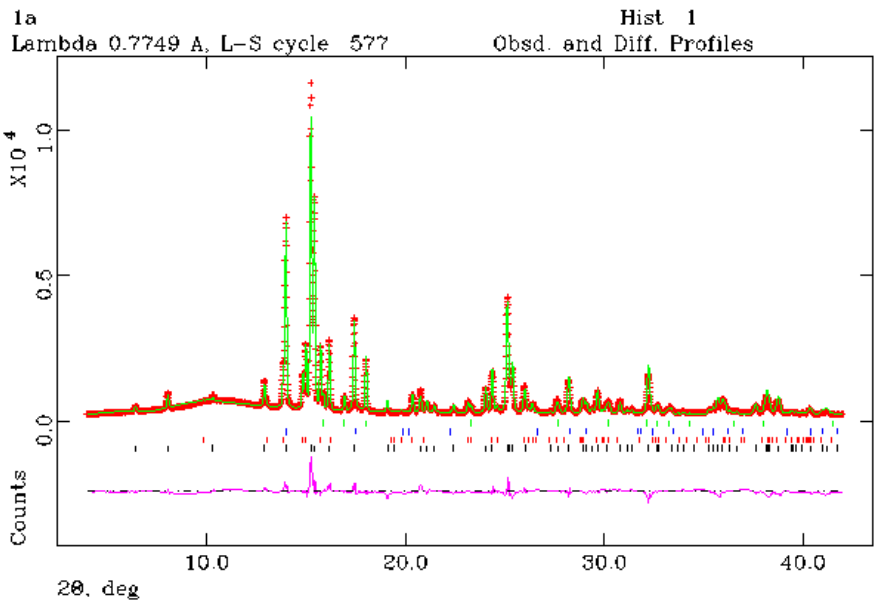

Figure 4-24 SXD pattern of Sample 42 collected after heating *in-situ* 673 K, where the black, red blue and green tick marks represent the $Ca_4Mg_3H_{14}$, CaH_2, MgH_2 and Mg phases, respectively. Red crosses show experimental data, the green line is the calculated data and the magenta line is the difference plot.

Table 4-22 Rietveld refinement data collected using *in-situ* Synchrotron X-ray Diffraction (673 K) for Sample 42.

Chemical Formula	**$Ca_4Mg_3H_{14}$**	**CaH_2**	**MgH_2**	**Mg**
Crystal System / Space Group	Hexagonal / $P\bar{6}2m$ (189)	Orthorh. / *Pnma* (62)	Tetragonal / *P4/mnm*	Hexagonal / *P6₃/mmc*
Z	1	4	2	2
***a* / Å**	6.3553(4)	5.9976(8)	4.489(3)	3.2340(6)
***b* / Å**	*a*	3.6324(5)	*a*	*a*
***c* / Å**	6.8809(4)	6.8324(10)	3.082(9)	5.253(1)
***V* / Å^3**	240.68(4)	148.85(5)	62.1(2)	47.58(2)
Formula Weight / g	233.235	160.320	52.64	48.610
Calculated Density, ρ_x / g cm^{-3}	1.609	1.788	1.414	1.697
Phase Fraction / %	71.4(2)	14.5(2)	3.5(4)	10.6(3)
Refinement Parameters		36		
Data Points		3999		
R_{wp}		9.77		
R_p		7.47		
χ^2		5.622		

The evidence presented here suggests that the $Ca_{19}Mg_8H_{54}$-type phase decomposes to the $Ca_4Mg_3H_{14}$-type phase within a narrower range that previously quoted. The conversion to the $Ca_4Mg_3H_{14}$-type phase occurs between ~573-623 K, and decomposition of the $Ca_4Mg_3H_{14}$-type phase begins at ~673 K. Combination of the SXD information with the PXD data collected at 773 K, the decomposition of the $Ca_4Mg_3H_{14}$-type phase to CaH_2 and Mg may be proposed to occur between ~673-773 K.

Sample **40** was not shown to decompose in the temperature range examined (Figure 4-25a). The diffraction patterns collected up to 400 ^oC were studied by the Rietveld method, and were found to comprise the ternary phase and CaH_2, as was the case at room temperature (Figure 4-25b). The refinements of samples collected between 373-673 K, inclusive, were conducted by fixing the atomic and temperature parameters to the known literature values. The site occupancy factors of the metal atoms in the ternary phase were also fixed.

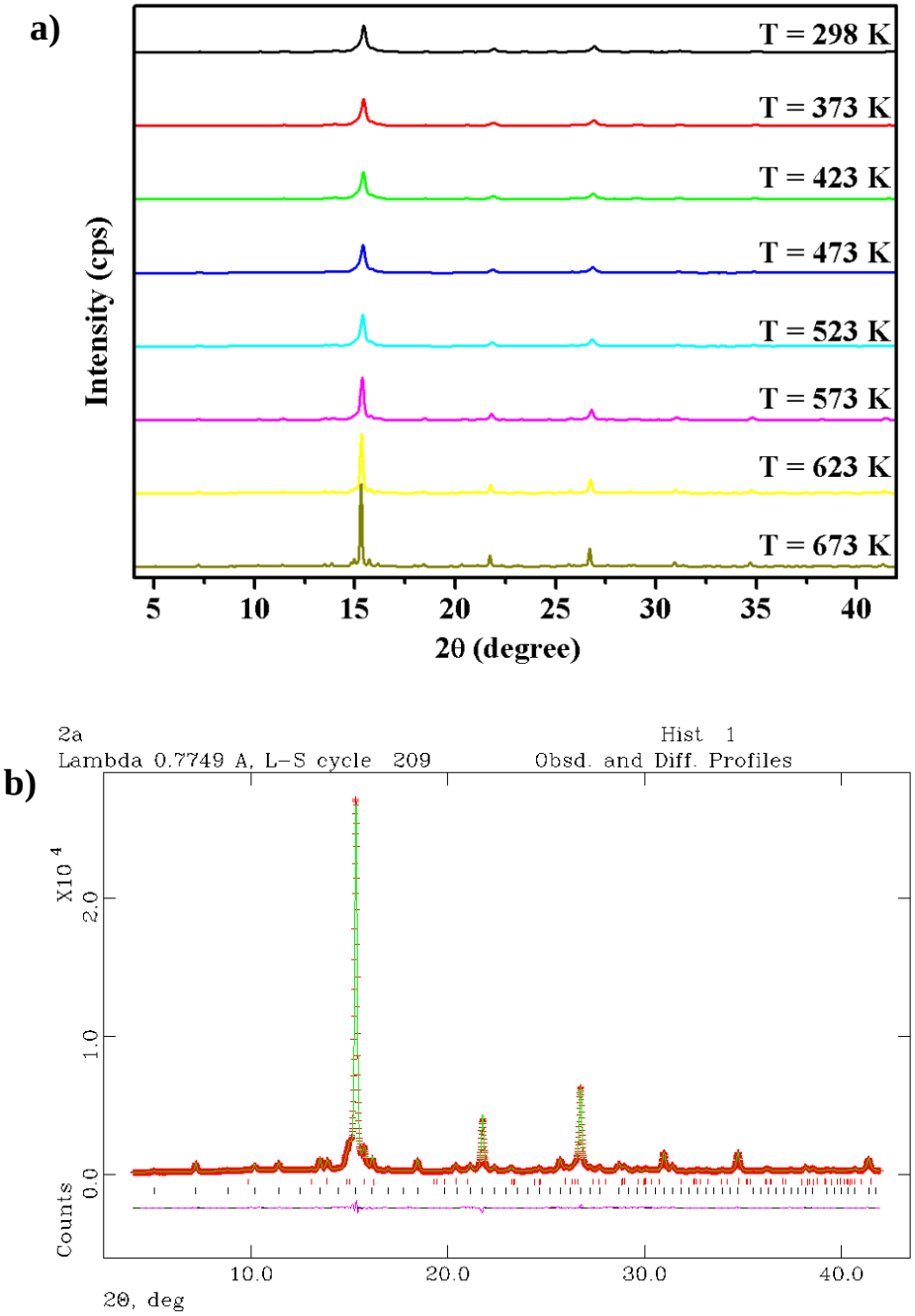

Figure 4-25 a) SXD patterns of Sample 40 collected after heating *in-situ* from 298-673 K. b) Rietveld refinement plot of SXD pattern collected at 623 K. The cubic ternary phase is indicated by black tick marks and CaH_2 is indicated by red tick marks; χ^2 = 1.343 R_p = 3.61 %, R_{wp} = 4.85 %. Red crosses show experimental data, the green line is the calculated data and the magenta line is the difference plot.

As the sample was heated, the ternary phase exhibited significant lattice expansion where the trends in *a* cell parameter and unit cell volume are given in Figure 4-26. These plots show a similar trend is found in both *a* cell parameter and cell volume, where these both increased linearly as the temperature was increased. It is likely that the sample need to be heated to a slightly higher temperature in order to reveal the decomposition process for the

2:1 sample (Sample **40**). This confirms that the reagent stoichiometry employed has a direct effect on the decomposition of the milled sample, where the ternary phase is significantly more stable when more Ca is introduced (Sample **40**) in comparison to samples where excess Mg in incorporated (Sample **42).**

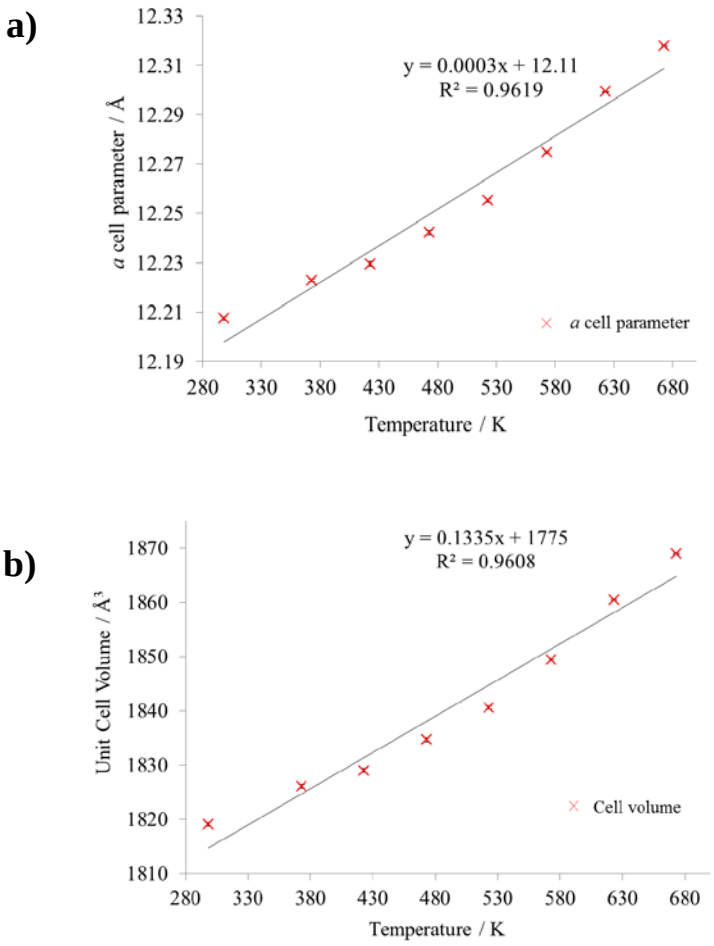

Figure 4-26 Plots of a) a cell parameter *vs.* temperature and b) volume *vs.* temperature for Sample 40 obtained from Rietveld refinement of diffraction data collected by *in-situ* SXD between 298-673 K.

4.3.2.4. Summary

Mechanosynthesis offers considerable opportunities for the preparation of new (and existing) ternary hydrides, as has been demonstrated in this work. It has been shown that under inert environments and by careful selection of the initial binary hydride stoichiometry, the metallic Ca:Mg proportions in the resultant ternary alkaline earth metal hydrides may be tuned effectively. Initially, CaH_2:MgH_2 stoichiometries defined for existing ternary Ca-Mg-H phases (2.375:1 and 1:0.75) were explored. The $Ca_{19}Mg_8H_{54}$-type phase was prevalent and other stoichiometries were then examined. The $Ca_{19}Mg_8H_{54}$-type phase was found in all CaH_2:MgH_2 stoichiometries investigated. The structures of the resultant ternary phases were examined by PXD and SXD and new non-stoichiometric

phases were determined, demonstrating that additional Ca or Mg may be included in the ternary phase by modification of the initial hydride ratio. For the first time, a Group II Ca-Mg-H ternary phase was synthesised as a single phase and was found to be isostructrual to the $Ca_{19}Mg_8H_{54}$ phase previously described, although with a higher Mg content; $Ca_{15.6(3)}Mg_{11.4(3)}H_{54}$. It is unclear why the 1:1 system is a special case in which both the $Ca_{19}Mg_8H_{54}$-type and $Ca_4Mg_3H_{14}$-type phases form, whereas all other samples comprised only the $Ca_{19}Mg_8H_{54}$-type ternary phase.

The decomposition of the as-synthesised ternary hydrides differs as a function of the initial hydride stoichiometry, where incorporation of additional Mg in the ternary phases translates to a ternary phase that gives the lowest decomposition temperature relative to the other phases which contain higher Ca proportions. The gravimetric capacity of all of the ternary hydrides is relatively low, with <5 wt% desorbed in the lowest temperature decomposition event. However, as noted by Bertheville, the high volumetric hydrogen capacity of the ternary $(Ca_{1-x}Mg_xH_2)_n$ type hydrides (~100 g/L) offers a convenient hydrogen storage matrix, despite the gravimetric capacity being less adequate in relation to the binary hydrides.

Hydrogenation of Laves type phases has been covered widely in the literature.[36] Based on the Laves phase $CaMg_2$ alloy obtained here, there is the potential for these materials to store hydrogen reversibly. However, the hydrogenation conditions for $CaMg_2$ would require exposure of the samples to high pressures and temperatures for prolonged periods based on previous evidence in the literature.[36, 52] Further work is required to examine the re-hydrogenation properties of the samples prepared in this work for comparison with existing hydrogenation studies of the $CaMg_2$ Laves phase.

4.4. Conclusions

These ternary hydrides are not only important for understanding how ternary alkaline earth metal hydrides may be synthesised, but they present a convenient building block from which quaternary hydrides may be studied. The work here shows that additional smaller atoms, such as Mg, can be inserted in to the ternary Ca-Mg-H system. Therefore, it would seem prudent to investigate whether other small metallic elements, such as Li or Na, could be included to form a quaternary hydride. By incorporation of Li or Na atoms in to the ternary Ca-Mg-H phase it may be suggested that this would have a destabilising effect, as observed for the inclusion of Na in MgH_2 to form the less stable $NaMgH_3$ ternary phase. Alloys comprising Li-Mg-Ca_x (x=0-15 wt%) have been studied within the past decade, but

hydrogenation of the as-formed pseudo-binary eutectic system was not evaluated.[82] More recent work explored hydrogenation of the Laves type $CaLi_{2-x}Mg_x$ ($0 \leq x \leq 2$) alloys, although no ternary or quaternary hydride phases were determined.[83] Other lightweight Laves type alloys, *e.g.*, $CaLi_xAl_{2-x}$ and $(Ca_{1-x}Mg_x)Al_2$, and ternary Ca-Mg-TM alloys have been studied, but hydrogenation of the alloys did not reveal quaternary hydride phases.[84, 85, 86] It would be interesting to determine whether any quaternary phases incorporating Li or Na could be synthesised from the ternary hydrides produced herein.

Beyond the standalone hydride phases for hydrogen desorption, utilisation of these samples in hydrolysis systems may be a lucrative route to pursue. As described in the introduction of this chapter, inclusion of Ca in the MgH_2 system enhanced the kinetics of the hydrolysis reaction between MgH_2 and water.[62, 63] The close contact of Ca and Mg in these samples may translate to even faster kinetics, and further work in this direction would add to the developing field of hydrolytic hydrogen release systems. This is a rapidly developing field of energy materials research in which CaH_2, MgH_2 and mechanochemistry already play a pivotal role.[64, 87]

From a structure chemistry perspective, further diffraction analysis is required to characterise the hydrogen positions within the ternary phases, and neutron diffraction experiments are expected to be carried out at the UK neutron source facility (ISIS) in the near future. Unfortunately the time constraints of this PhD did not allow this work to be carried out in time for inclusion in this thesis (Appendix E).

---

[1] H. Reardon, N. Mazur and D. H. Gregory, *Progress in Natural Science: Materials International*, 2013, **23**, 343
[2] F. Cheng, Z. Tao, J. Liang and J. Chen, *Chemical Communications*, 2012, **48**, 7334
[3] K. Yvon and B. Bertheville, *Journal of Alloys and Compounds*, 2006, **425**, 101
[4] K. Yvon, *Chimia*, 1998, **52**, 613
[5] "*Hydrides: Solid state transition metal complexes*", K. Yvon and G. Renaudin, *Encyclopaedia of Inorganic Chemistry*, Vol. III, pp. 1814-1846
[6] C. C. Koch and J. D. Wittenberger, *Intermetallics*, 1996, **4**, 339
[7] A. Zaluska, L. Zaluska and J. O. Strom-Olsen, *Journal of Alloys and Compounds*, 1999, **288**, 217
[8] J. Huot, G. Liang and R. Schulz, *Applied Physics*, 2001, **A72**, 187
[9] W. Bronger, *Journal of Alloys and Compounds*, 1995, **229**, 1
[10] A. Zaluska, L. Zaluska and J. O. Strom-Olsen, *Applied Physics*, 2001, **A72**, 157
[11] P. Vajeeston, P. Ravindran, A. Kjekshus and H. Fjellvåg, *Journal of Alloys and Compounds*, 2008, **450**, 327
[12] D. Li, T. Zhang, S. Yang, Z. Tao and J. Chen, *Journal of Alloys and Compounds*, 2011, **509**, 8228
[13] J. P. Bastide, A. Bouamrane, P. Claudy and J. M. Eltoffe, *Journal of the Less-Common Metals*, 1987, **136**, L1
[14] R. Schumacher and A. Weiss, *Journal of the Less-Common Metals*, 1990, **163**, 179
[15] B. Bertheville, T. Herrmannsdörfer and K. Yvon, *Journal of Alloys and Compounds*, 2001, **325**, L13
[16] K. Komiya, N. Moridaku, R. Rong, Y. Takahashi, Y. Shinzato, H. Yukawa and M. Moringa, *Journal of Alloys and Compounds*, 2008, **453**, 157
[17] M. A. Ghebouli, B. Ghebouli, A. Bouhemadou, M. Fatmi and S. Bin-Omran, *Solid State Science*, 2011, **13**, 647

[18] M. Fornari, A. Subedi and D. J. Singh, *Physical Review B*, 2007, **76**, 214118
[19] A. H. Reshak, M. Y. Shalaginov, Y. Saeed, I. V. Kityk and S. Auluck, *Journal of Physical Chemistry B*, 2011, **115**, 2836
[20] Y. Bouhadda, N. Kheloufi, A. Betabet, Y. Doudouma, N. Fenineche and K. Benyalloul, *Journal of Alloys and Compounds*, 2011, **509**, 8994
[21] K. Ikeda, Y. Kogure, Y. Nakamori and S. Orimo, *Scripta Materialia*, 2005, **53**, 319
[22] A. Bouamrane, J. P. Laval, J.-P. Soulie and J. P. Bastide, *Materials Research Bulletin*, 2000, **35**, 545
[23] E. Rönnebro, D. Noréus, K. Kadir, A. Reiser and B. Bogdanovic, *Journal of Alloys and Compounds*, 2000, **299**, 101
[24] H. Wu, W. Zhou, T. J. Udovic, J. J. Rush and T. Yildirim, *Chemistry of Materials*, 2008, **20**, 2335
[25] D. A. Sheppard, M. Paskevicius and C. E. Buckley, *Chemistry of Materials*, 2011, **23**, 4298
[26] D. Pottmaier, E. R. Pinatel, J. G. Vitello, S. Garroni, M. Orlova, M. D. Baro, G. B. M. Vaughan, M. Fichtner, W. Lohstroh and M. Baricco, *Chemistry of Materials*, 2011, **23**, 2317
[27] K. Ikeda, S. Kato, Y. Shinzato, N. Okuda, Y. Nakamori, A. Kitano, H. Yukawa, M. Morinaga and S. Orimo, *Journal of Alloys and Compounds*, 2007, **446-47**, 162
[28] K. Ikeda, Y. Nakamori and S. Orimo, *Acta Materialia*, 2005, **53**, 3453
[29] Y. Li, B. K. Rao, T. McMullen, P. Jena and P. K. Khowash, *Physical Review B*, 1991, 44, 6030
[30] P. K. Khowash, B. K. Roa, T. McMullen and P. Jena, *Physical Review B*, 1997, **55**, 1454
[31] S. Hao and D. S. Sholl, *Applied Physics Letters*, 2008, **93**, 251901
[32] Y. Bouhadda, Y. Boudouma, N. Fennineche and A. Bentabet, *Journal of Physics and Chemistry of Solids*, 2010, **71**, 1264
[33] S. Hao and D. S. Sholl, *Journal of Physical Chemistry Letters*, 2010, **1**, 2968
[34] Y. Bouhadda, N. Fenineche and Y. Boudouma, *Physica B*, 2011, **406**, 1000
[35] A. Klaveness, O. Swang and H. Fjellvåg, *Europhysics Letters*, 2006, **76**, 285
[36] D. Shaltiel, *Journal of the Less-Common Metals*, 1978, **62**, 407
[37] Y. Suzuki, T. Haraki and H. Uchida, *Journal of Alloys and Compounds*, 2002, **330-332**, 488
[38] R.C. King and O. J. Kleppa, *Acta Metallurgica*, 1964, **12**, 87
[39] A. A. Nayeb-Hashemi and J. B. Clark, *Bulletin of Alloy Phase Diagrams*, 1984, **5**, 365
[40] C. W. Bale and A. D. Pelton, *Bulletin of Alloy Phase Diagrams*, 1987, **8**, 125
[41] A. D. Pelton, *Bulletin of Alloy Phase Diagrams*, 1984, **5**, 454
[42] A. D. Pelton, *Bulletin of Alloy Phase Diagrams*, 1985, **6**, 35
[43] A. A. Nayeb-Hashemi and J. B. Clark, *Bulletin of Alloy Phase Diagrams*, 1987, **8**, 58
[44] Y. Tsushio and E. Akiba, *Journal of Alloys and Compounds*, 1998, **269**, 219
[45] F. Gingl, T. Vogt, E. Akiba and K. Yvon, *Journal of Alloys and Compounds*, 1999, **282**, 125
[46] A. Bouamrane, J.-Ph. Soulie and J. P. Bastide, *Thermochimca Acta*, 2001, **375**, 81
[47] P. Vajeeston, P. Ravindran and H. Fjellvåg, *Journal of Chemical Physics*, 2010, **132**, 114504
[48] X. Liu, K. Asano, N. Terashita and E. Akiba, *International Journal of Hydrogen Energy*, 2009, **34**, 1472
[49] K. Nomura, Y. Ishido and S. Ono, *Journal of the Ceramic Association of Japan*, 1978, **86**, 67 (In Japanese)
[50] P. Vajeeston, P. Ravindran and H. Fjellvåg, *Journal of Chemical Physics*, 2010, **132**, 114504
[51] S. F. Matar, M. Nakhl, A. F. Al Alam, M. Zakhour and N. Ouaini, *Solid State Sciences*, 2011, **13**, 569
[52] F. Gingl, F. Bonhomme and K. Yvon, *Journal of Alloys and Compounds*, 1992, **185,** 273
[53] B. Bertheville and K. Yvon, *Journal of Alloys Compounds*, 1999, **290**, L8-L10
[54] S. Sartori, A. Leon, O. Zabara, J. Muller, M. Fichtner, B. C. Hauback, *Journal of Alloys and Compounds*, 2009, **476**, 639
[55] B. Huang, K. Yvon and P. Fischer, *Journal of Alloys and Compounds*, 1992, **190**, 65
[56] D. Lupu, A. Biris, E. Indrea and R. V. Bucur, *International Journal of Hydrogen Energy*, 1983, **8**, 701
[57] J. Bergsma and B. O. Loopstra, *Acta Crystallographica*, 1962, **15**, 92.
[58] C. Ataca, E. Aktürk and S. Ciraci, *Physical Review B*, 2009, **79**, 041406(R)
[59] D. K. Dixit, K. Gandhi and B. K. Dixit, *International Journal of Hydrogen Energy*, 2012, **37**, 3767
[60] C. Ney, H. Kohlmann and G. Kickelbick, *International Journal of Hydrogen Energy*, 2011, **36**, 9086
[61] V. C. Y. Kong, D. W. Kirk, F. R. Foulkes and J. T. Hinatsu, *International Journal of Hydrogen Energy*, 2003, **28**, 205
[62] J. Huot, G. Liang and R. Schulz, *Journal of Alloys and Compounds*, 2003, **353**, L12
[63] J.-P. Tessier, P. Palau, J. Huot, R. Shulz and D. Guay, *Journal of Alloys and Compounds*, 2004, **376**, 180
[64] Y. Xiao, C. Wu, H. Wu and Y. Chen, *International Journal of Hydrogen Energy*, 2011, **36**, 15698
[65] L. Zhu, D. Kim, H. Kim, R. I. Masel and. M. A. Shannon, *Journal of Power Sources*, 2008, **185**, 1334
[66] F. E. Pinkerton, and M. S. Meyer, *Journal of Alloys and Compounds*, 2008, **464**, L1
[67] Y. Zhang, K. Shimoda, H. Miyaoka, T. Ichikawa and Y. Kojima, *International Journal of Hydrogen Energy*, 2010, **35**, 12405
[68] P. P. Yuan, B. H. Liu and Z. P. Li, *International Journal of Hydrogen Energy*, 2011, **36**, 15266
[69] A. C. Larson, R. B. von Dreele, *General Structure Analysis System (GSAS)*; Los Alamos National Laboratory Report LAUR: 86-748, Los Alamos, NM, USA, 1995.

[70] B. H. Toby, *Journal of Applied Crystallography*, 2001, **34**, 210
[71] *Inorganic Crystallographic Structure Database (ICSD)*; http://cds.rsc.org/, accessed 14/05/2014
[72] J. I. Langford and A. J. C. Wilson, *Journal of Applied Crystallography*, 1978, **11**, 102
[73] D. T. Shane, R. L. Corey, R. C. Bowman Jr., R. Zidan, A. C. Stowe, S.-J. Hwang, C. Kim and M. S. Conradi, *Journal of Physical Chemistry C*, 2009, **113**, 18414
[74] M. Ismail, Y. Zhao, X. B. Yu and S. X. Dou, *International Journal of Hydrogen Energy*, 2012, **37**, 8395
[75] J. Šubrt and K. Tobola, *Journal of Thermal Analysis and Calorimetry*, 1976, **10**, 5
[76] X.-D. Kang, J.-H. Luo and P. Wang, *International Journal of Hydrogen Energy*, 2012, **37**, 4259
[77] F. Gingl and K. Yvon, *Zeitschrift für Kristallographie*, 1993, **206**, 313
[78] H. Witte, *Naturwissenschaften*, 1937, **25**, 795
[79] R. L. Berry and G. V. Raynor, *Acta Crystallographica*, 1953, **6**, 178
[80] F. Stein, M. Palm and G. Sauthoff, *Intermetallics*, 2004, **12**, 713
[81] F. Stein, M. Palm and G. Sauthoff, *Intermetallics*, 2005, **13**, 1056
[82] G. S. Song and M. V. Kral, *Materials Characterisation*, 2005, **54**, 279
[83] K. Asano, K. Sakaki, X. Liu and E. Akiba, *Journal of Alloys and Compounds*, 2009, **482**, L18
[84] T. Nobuki, M. Chiba and T. Kuji, *Journal of Alloys and Compounds*, 2007, **447-446**, 152
[85] Q. A. Zhang and G. P. Zhao, *Materials Chemistry and Physics*, 2007, **104**, 373
[86] R. Nesper and G. J. Miller, *Journal of Alloys and Compounds*, 1993, **197**, 109
[87] S.-H. Hong, H.-J. Kim and M. Y. Song, *Journal of Industrial and Engineering Chemistry*, 2012, **18**, 405

5. Synthesis and Structure of Halide Precursors for Tailored Hydride Synthesis *via* Solid State Metathesis Reactions

5.1. Introduction

Metathesis reactions (also known as double decomposition reactions) are defined as "*a bimolecular process involving the exchange of a bond (or bonds) between similar interacting chemical species so that the bonding affiliations in the products are identical (or closely similar) to those in the reactants*".[1] These may be given by the general form:

Equation 5-1

$$AB_{(s)} + CD_{(s)} \rightarrow AD_{(s)} + CB_{(s)}$$

Examples of this type of reaction range from organic synthesis to pure inorganic chemistry, and their exploitation by chemists has resulted in significant developments in both solution and solid state chemistry.[2] Focusing on the solid state method, self-propagating reactions may yield novel products in the form of nanoscale crystallites.[3, 4] The success of these reactions relies on the formation of a thermodynamically stable product, typically an alkali halide salt, and are usually initiated by application of heat. This type of reaction has been termed "self-propagating high-temperature synthesis", or SHS.[5, 6] These exothermic reactions are known to have the potential to occur violently and so controlling the reactivity of the solids can be difficult by this method. Treece *et al.* highlighted that solid-solid reactions involving tailored precursors allows for better control of the reaction, and developments in solid state metathesis, SSM, are wide-ranging.[7] Work in the field of rapid, solvent-free SSM reactions has allowed a plethora of new materials to be discovered by this method, including pnictides, nitrides, carbides, *etc*.[8, 9, 10, 11] Thermal activation is commonly used to assist SSM although in extreme cases they may occur violently at room temperature, even with gentle grinding.

Metathesis reactions present an interesting route towards hydrogen storage materials and have been studied for synthesis of binary hydrides for many decades. Wet-chemistry reactions between magnesium halides and alkali metal hydrides were first reported in the 1950's by Wiberg *et al.*[12] Later, these reactions were developed by Ashby and Schwartz for synthesis of reactive MgH_2 as a catalyst for organic chemistry reactions.[13] Using the wet-chemistry preparatory method, metathesis reactions were shown to take up to four days to proceed under reflux conditions. Synthesis of a wide variety of materials, including

borohydrides and alanates for energy storage, has also been possible using the wet-chemistry metathesis method.[14, 15, 16]

Ball milling is an effective technique that can enable metathesis reactions *via* mechanical activation alone, where hand grinding or thermal means are not sufficient or applicable.[17] Milling results in particle size reduction and significant surface defects without the need for additional thermal initiation or any requirement for solvents.[18] In 2010, solid state metathesis was conducted to generate nanoparticles of magnesium hydride *via* the metathesis mechanism given by Wiberg:[19]

Equation 5-2 $$MgCl_2 + LiH \rightarrow MgH_2 + LiCl \qquad \Delta_f G_{298\,K} = -72.8 \text{ kJ/mol}$$

Sheppard also issued a thermodynamic study establishing the decomposition properties of the hydride as a mixture with the byproduct, *i.e.*, the alkali metal salt, LiCl.[20] They showed that the decomposition enthalpy and entropy of the MgH_2 nano particles synthesized in the solid state were lower than that of the bulk hydride, resulting in a ~6°C drop in the equilibrium temperature at 1 bar. SSM by ball milling has been used to produce a wide range of hydride materials, including lightweight borohydrides[21, 22, 23] and alanates[24,25, 26].

With a focus on metathesis reaction design, the work described in this chapter investigates the mechanochemical synthesis of appropriate inorganic precursors towards the synthesis of hydride materials for hydrogen storage. The chapter is divided in to three sub-sections, in which a halide precursor has been synthesized, followed by investigation of metathesis reactions between the precursor and light metal binary hydrides.

1. Mechanochemical synthesis of $LiAlCl_4$ and subsequent solid state metathesis with NaH towards $LiAlH_4$ synthesis.
2. Conventional and mechanochemical synthesis of $NaMgCl_3$ and subsequent solid state metathesis with LiH/NaH towards $NaMgH_3$ synthesis.
3. Mechanochemical synthesis of $NaAlCl_4$ and subsequent solid state metathesis with LiH towards $NaAlH_4$ synthesis.

Each system will be described, with relevant introductory material followed by results and discussion and conclusions.

5.2. Experimental

Samples were prepared according to the conditions given in Table 5-1.

Table 5-1 Sample ID and reaction conditions for ternary halide synthesis and halide-hydride metathesis reactions.

Sample ID	Reagents	Heating Conditions	Milling Time (h)	b:p
44	$LiCl + AlCl_3$	-	Hand Mixed	-
45	$LiCl + AlCl_3$	-	1	80:1
46	$LiCl + AlCl_3$	-	3	80:1
47	$LiCl + AlCl_3$	-	5	80:1
48	$LiAlCl_4$ (**46**) + 4 NaH	-	5	100:1
49	$NaCl + MgCl_2$	-	Hand Mixed	-
50	$NaCl + MgCl_2$	450 ^oC, 12 h	-	-
51	$NaCl + MgCl_2$	-	1-5	80:1
52	$NaMgCl_3$ (**50**) + 3 NaH	-	5	100:1
53	$NaMgCl_3$ (**51**) + 3 NaH	-	5	100:1
54	$NaMgCl_3$ (**50**) + 3 LiH	-	5	100:1
55	$NaCl + AlCl_3$	-	Hand Mixed	-
56	$NaCl + AlCl_3$	-	5	80:1
57	$NaAlCl_4$ (**56**) + 4 LiH	-	5	100:1

N.B. Starting materials; Anhyd. LiH (95 %), Anhyd. NaH (95 %), Anhyd. LiCl (≥99 %), Anhyd. NaCl (≥99 %), Anhyd. $MgCl_2$ (≥98 %) and Anhyd. $AlCl_3$ (99.99 %), were all purchased from Sigma Aldrich, without further purification.

All milling operations were conducted using stainless steel milling media using stoichiometric quantities of reagents. A 50 ml stainless steel milling jar was used in each case employing 10x 10 mm stainless steel milling balls. Milling was conducted in 5 min milling periods which were followed by 5 min rest periods, and the total experiment time adjusted to meet the milling time requirements.

Samples synthesised by conventional heating were prepared in a glovebox, where the powders were first weighed stoichiometrically and ground with an agate mortar and pestle until thoroughly mixed. The well mixed powders were then transferred to a silica tube and sealed with a Subaseal® septum cap and parafilm. Heating was conducted at the designated temperatures in a bench-top furnace (Figure 2-4) under a constant flow of $Ar_{(g)}$ for the durations noted in Table 5-1 above.

Post-milled and post-thermal analysis samples were investigated by PXD using a Bruker D8 powder diffractometer in transmission geometry with spinning sealed capillaries, this minimized the risk of hydrolysis of the hygroscopic halide products or oxidation of the hydrides. Data were collected between $5 \leq 2\theta / ^{o} \leq 85$ for 1 h for initial characterisation and over $10 \leq 2\theta / ^{o} \leq 110$ for between 10-14 h to obtain higher resolution, higher intensity data (for structure refinement).

All collected diffraction patterns were compared to reference data in the ICDD database using the PANalytical High Score Plus Software package. Rietveld refinement was performed using GSAS/EXPGUI[27, 28] with reference data obtained from the Inorganic Crystal Structure Database (ICSD).[29] Diffraction background was modelled using Function 8 within GSAS; a reciprocal interpolation function. Peak shapes were modelled using the Thompson-Cox-Hastings pV function (Function 2) with asymmetry also being taken into consideration. The unit cell parameters were varied, followed by the atomic and temperature parameters. Where more than one phase was identified, the phase fractions were obtained by refining the scale factors. The atomic positions and temperature factors were refined where possible, and constrained to the values given in literature where significant divergence occurred.

TPD experiments were performed for all samples *via* thermogravimetric-differential thermal analysis-mass spectrometry (TGA-DTA-MS; Netzsch STA 409 coupled to a Hiden HPR20 mass spectrometer). All thermal analysis experiments were conducted within an Ar-filled recirculating glovebox (MBraun UniLab; 0.1 ppm H_2O, 0.1 ppm O_2) using alumina sample pans under a constant flow of $Ar_{(g)}$ at a 5 K min^{-1} heating rate.

SEM-EDX experiments were performed at 20 keV under a nitrogen atmosphere using a Philips XL30 ESEM instrument equipped with an Oxford Instruments X-act spectrometer to determine particle morphology and atomic proportions, respectively. Samples were prepared on carbon tabs under an inert environment. The samples were loaded in a sputter coater and coated with gold at 25 keV. Although exposure of the samples to air was unavoidable during this analysis procedure, it was minimised as much as possible to obtain representative results of the as-prepared samples.

5.3. Mechanochemical Synthesis of $LiAlX_4$ (X = Cl, H).

5.3.1. Introduction

$LiAlCl_4$ has been a key material in the development of fuel cell and battery electrolytes owing to its high ionic conductivity in the molten and solid state.[30, 31, 32, 33, 34] Weppner and Huggins determined the room temperature conductivity to be $1 \times 10^{-6}\Omega^{-1}\,cm^{-1}$, which increased upon heating to 140 ºC to $4\times 10^{-4}\Omega^{-1}\,cm^{-1}$. [35] The work of Behl *et al.* described the enhanced performance of Li-inorganic electrolyte cells comprising the $LiAlCl_4$-$SOCl_2$ electrolyte solution (1.5 M) with carbon black electrodes in comparison to other Li-inorganic cells they studied, giving an energy density of 244 W-hr/lb at a 57 hr discharge rate.[36] $LiAlCl_4$-based electrolytes are now one of the most studied systems for inorganic lithium batteries.[37, 38, 39, 40] The Raman work of Bedfer *et al.* in the 1980s demonstrated that a knowledge of the transformations in chemical structure of the solvated $LiAlCl_4$ electrolyte component throughout the discharge process was critical in understanding the behaviour of Li-inorganic electrolyte batteries.[41, 42] The synthesis of $LiAlCl_4$ is typically *via* heat treatment of a stoichiometric mixture of the corresponding anhydrous salts, LiCl and $AlCl_3$, requiring further purification by addition of lithium metal ($\Delta_f G^o_{solid}$ = -1.16+3.95×10^{-4} $T_{[K]}$ MJ/mol above room temperature).[35, 31] However, more complex and time-consuming methods, such as that described by Behl *et al.*, require $HCl_{(g)}/Cl_{2(g)}$ treatment.[43, 44]

Beyond electrolyte studies, $LiAlCl_4$ could also be exploited as a halide precursor for synthesis of $LiAlH_4$. Early work by Finholt and colleagues[45] showed that the high hydrogen capacity alanate, $LiAlH_4$ ($\Delta_f H^o_{solid}$ = -117.15 kJ/mol[46], 10.64 wt%H), may be formed by the following reaction, where LiCl is the thermodynamically stable by-product ($\Delta_f H^o_{solid}$ = -408.27 kJ/mol[46]; $T_{m.p}$ = 614 ºC[47]):

Equation 5-3

$$4\,LiH + AlCl_3 \xrightarrow{ether} LiAlH_4 + 3\,LiCl$$

The following metathesis reaction was proposed in the early 1990s, but no experimental evidence to show that this has been attempted can be found elsewhere in the literature.[48] The thermodynamically stable by-product being NaCl in this instance ($\Delta_f H^o_{solid}$ = -411.12 kJ/mol[46;] $T_{m.p.}$ = 800.4 ºC[47]).

Equation 5-4

$$LiAlCl_4 + 4\,NaH \rightarrow LiAlH_4 + 4\,NaCl$$

Solid state approaches towards the synthesis of $LiAlH_4$ are also evident in the literature, and the work of Kojima and colleagues showed that the direct synthesis of $LiAlH_4$ by milling LiH and Al under $H_{2(g)}$ was not adequate to form a significant yield of single phase $LiAlH_4$.[49] More recently, synthesis of Ti-doped $LiAlH_4$ by milling LiH and Al in the presence of $TiCl_3$ was studied.[50] By contrast, other additives such as Ti metal, Nb_2O_5 and $NbCl_5$ did not allow formation of the alanate. The investigation of a compatible solvent for rehydrogenation of the dehydrogenated $TiCl_3$ catalysed $LiAlH_4$ composites revealed a hydrogen storage system capable of hydrogen cycling.[51]

The first section in this results chapter looks at mechanochemical synthesis of the ternary halide $LiAlCl_4$ and the subsequent mechanochemical metathesis reaction between the as-prepared halide and a hydride source (NaH). This will not only test the hypothesis that ternary halides may be used for the synthesis of complex hydrides *via* solid state routes, but will also corroborate the metathesis reaction proposed earlier by Chelyukanova and colleagues. The FACTweb software was used to predict the thermodynamics of this system; ΔH = -40.88 kJ, ΔG = -41.28 kJ and ΔS = 13.62 J/K, based on the stoichiometric reaction between the inorganic precursor, $LiAlCl_4$, and NaH in the solid state at 298 K.[52]

5.3.2. Results & Discussion

5.3.2.1. Synthesis and Characterisation of the Halide Precursor, $LiAlCl_4$

After milling, a very pale yellow powder product was collected from the milling jar and stored in a sealed vial under an inert atmosphere. After milling for 1 h only, there was evidence for the complex halide, $LiAlCl_4$, but reflections from the reagents were also evident in the diffraction pattern collected. This suggested that the reaction between LiCl and $AlCl_3$ was incomplete, and the milling time was thus increased to 5 h. The diffraction pattern for the 5 h milled sample revealed significantly broad peaks of $LiAlCl_4$, with a broad background suggesting some amorphization of the product and was likely to be due to the use of over-zealous milling conditions. An intermediate milling time of 3 h was then attempted, and revealed a crystalline product with no additional binary halide phases. The crystalline phase was assigned to $LiAlCl_4$ according to the existing data available from the single crystal work of Mairesse *et el.* (ICSD-1040).[53] The values are also in good agreement with the room temperature data collected in the variable temperature study conducted by Perenthaler and colleagues on single crystals of the halide (a = 7.004(8) Å, b = 6.503(6) Å, c = 12.996(9) Å).[54]

High quality data collected in this work was analysed by the Rietveld method and further structural information for the $LiAlCl_4$ phase synthesised by mechanochemistry was determined (Figure 5-1, Table 5-2 and Appendix C; C.1 & C.2). A small amount of LiCl reagent was found to present from this analysis, but was <1 % and indicates the high purity of the $LiAlCl_4$ product obtained here by the mechanochemical method. This is an interesting development, since the synthesis was not conducted under vacuum, no $HCl_{(g)}$ or $Cl_{2(g)}$ was required, nor further purification by addition of molten Li metal.[35]

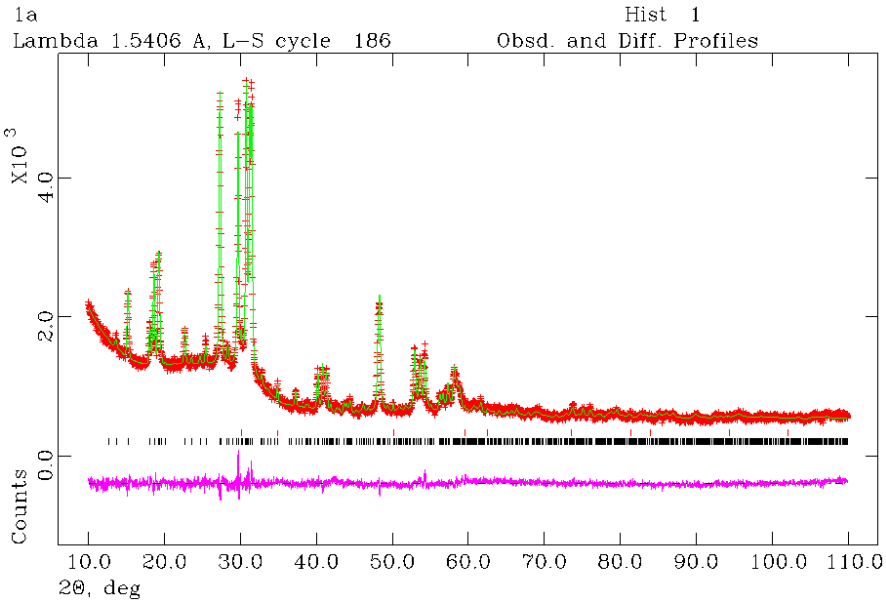

Figure 5-1 Rietveld refinement plot of PXD data for Sample 46. Black tick marks represent the $LiAlCl_4$ phase and the red tick marks indicate the LiCl phase. Red crosses indicate observed data, the green line shows the calculated pattern and the magenta line indicates the difference plot.

Table 5-2 Crystallographic data from Rietveld refinement.

Sample	Literature[53]	Sample 46
Chemical Formula	$LiAlCl_4$	
Crystal System	Monoclinic	
Space Group	$P\ 2_1/c$	
Z	4	
***a* / Å**	7.007(3)	7.0081(3)
***b* / Å**	6.504(4)	6.5136(2)
***c* / Å**	12.995(10)	13.0065(5)
***β*/º**	93.32(5)	93.322(2)
***V* / Å^3**	591	592.71(6)
Formula Weight / g	-	702.940
Calculated Density, ρ_x / g cm^{-3}	1.98	1.969
Phase Fraction		99.09(3)
Refinement Parameters	-	57
Data Points	-	12117
R_{wp}	3.5 %	4.22 %
R_p	2.9 %	3.27 %
χ^2	-	1.633

The $LiAlCl_4$ structure comprises $AlCl_4$ tetrahedra and $LiCl_6$ octahedra. Figure 5-2 a) shows the extended $LiAlCl_4$ structure with Li and Al coordination orientations given in Figure 5-2 b) and c) respectively. The layered structure results from the linkage of pairs of $LiCl_6$ octahedra, which are edge-sharing. The paired octahedra share one corner of a further four octahedron pairs to give a layer of octahedra which exists parallel to the *ac* plane. The layers of octahedra are linked by the $AlCl_4$ tetrahedra, where one octahedra pair shares two edges with each $AlCl_4$ tetrahedron and a further two octahedral units share two corners of the tetrahedron.

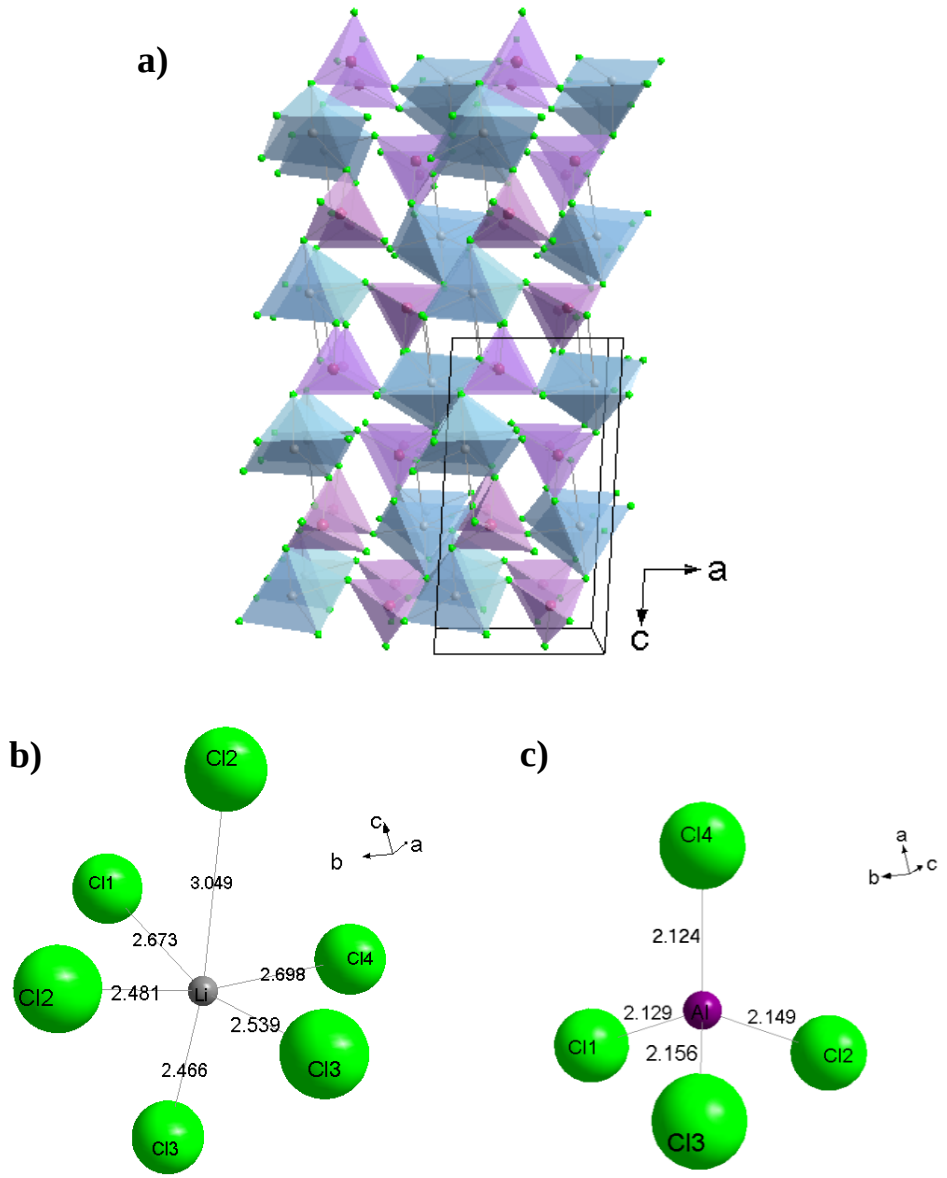

Figure 5-2 a) Expanded structure of mechanochemically synthesised $LiAlCl_4$ (unit cell edges indicated) with tetrahedral representation of $[AlCl_4]^-$ anions given by the blue polyhedra (Li = grey spheres, Al = purple spheres, Cl = green spheres), b) octahedral coordination sphere of Li atoms, and c) tetrahedral coordination sphere of Al atom.

The DTA profiles for hand mixed (Sample **44**) and the milled product (Sample **46**) of LiCl and $AlCl_3$ in stoichiometric proportions are given in Figure 5-3. Both samples exhibited a single endothermic event below 300 °C, where the T_{peak} of the milled mixture occurred at a higher temperature than the hand mixed halide mixture. No other significant thermal features were identified to suggest significant proportions of unreacted binary halide, where the melting points of $AlCl_3$ and LiCl are 194 °C and 614 °C, respectively.[47] The enthalpy of the reaction between LiCl and $AlCl_3$ from the hand-mixed samples, was determined as 11.58 kJ/mol, as determined from analysis of the area of the peak in the DTA trace for Sample **44**. The endothermic event may described as the melting point

($T_{m.p.}$) of the mechanochemically synthesised $LiAlCl_4$ produced in this work, and was found to be 154.4 °C. In addition, it should be noted that the $T_{m.p.}$ of the ternary halide produced by this method is 22 °C higher than that quoted by Morozov and colleagues, 10 °C greater than that described by Kendall *et al.* and 8 °C higher than that quoted by Weppner and Huggins.[43, 55, 31] This could be as a result of the small impurity phase. The sharp peak profile for the complex halide produced here indicates that the purity of the sample is reasonable and is consistent with the high purity suggested for this sample by the phase fraction information obtained by Rietveld refinement. The enthalpy associated with the melting of the $LiAlCl_4$ produced in this work was found to be 19.23 kJ/mol as determined from analysis of the area of the peak in the DTA trace for Sample **46**. There was no associated mass loss with the thermal event in neither the hand-mixed or milled samples, and no evolved gases were observed in the corresponding MS traces.

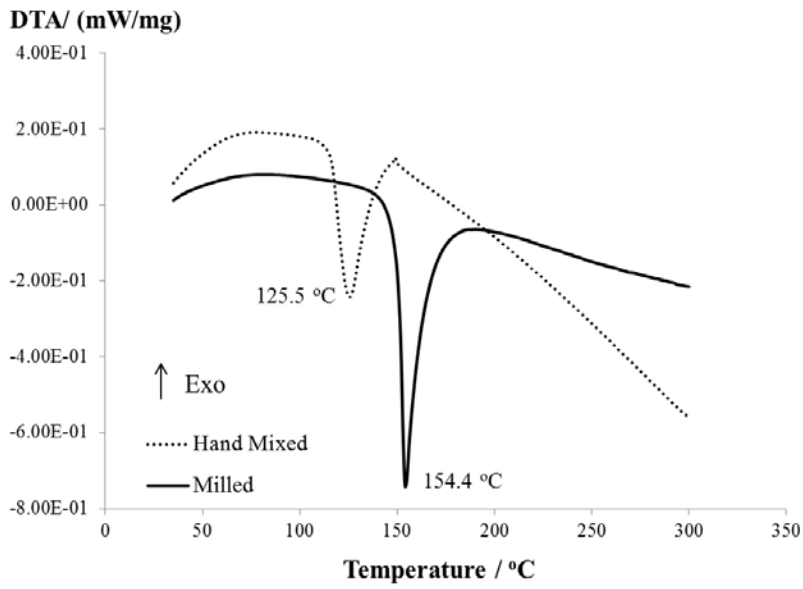

Figure 5-3 Thermal analysis of Sample 44 (dashed line) *vs*. Sample 46 (solid line).

5.3.2.2. Mechanochemical metathesis of halide precursor, $LiAlCl_4$, and hydride donor, NaH.

Stoichiometric proportions of the as-prepared halide (Sample **46**) and NaH (1:4, respectively) were milled and the properties of the resultant mixture examined to establish whether the mechanochemical metathesis reaction was successful in producing $LiAlH_4$ (Sample **48**). This is based on Equation 5-4, described earlier. The SEM image of the as prepared sample (Figure 5-4 a) revealed that the sample is likely to have hydrolysed in the time it was taken to transfer the sample from the sealed vial in to the SEM chamber. This is indicated by the smooth globule-type materials observed in the sample, and highlights the

highly hygroscopic nature of the as-prepared sample. Images of the sample were collected after heating (Figure 5-4 b), and showed an agglomerated material with smooth surfaces, suggesting a melt.

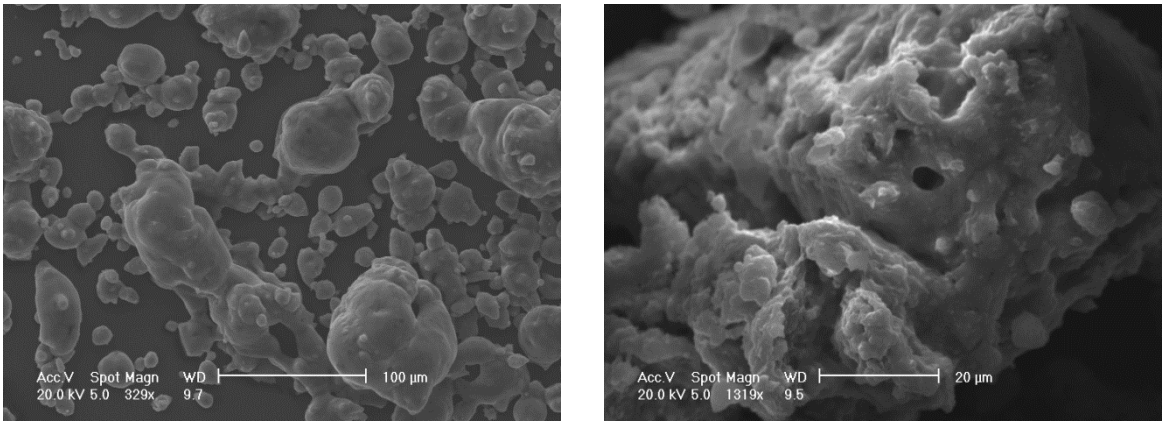

Figure 5-4 SEM images of a) mechanochemical metathesis product (Sample 48, 100 µm) and b) product collected after heating Sample 48 to 300 ºC (20 µm).

PXD revealed the expected thermodynamically stable halide by-product of the metathesis reaction, NaCl, but it also indicates reflections which correspond to Al (Figure 5-5). The presence of the Al phase could be the result of partial decomposition of the complex hydride, $LiAlH_4$, in the mill. As in previous studies involving mechanochemical metathesis of halides and hydrides, the hydride phase was not observed using lab PXD.[19] This could be a result of the small particle size of the hydride formed by this method.

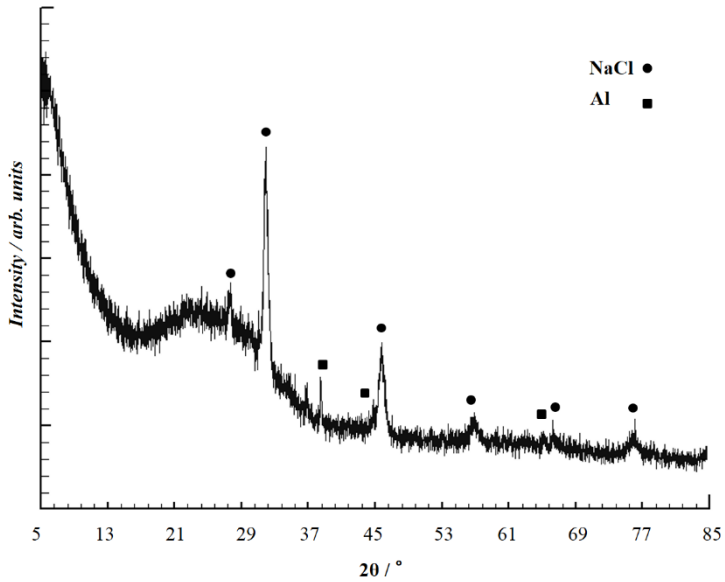

Figure 5-5 PXD pattern of Sample 48.

To confirm whether the thermal behaviour of the as prepared product matched that of $LiAlH_4$, STA was conducted. The sample was analysed to both 300 °C and 500 °C, and these gave consistent thermal analysis results. The DTA and TG profiles between room temperature and 300 °C are given in Figure 5-6 a) and b), and the MS data collected over the whole temperature range (room temperature to 500 °C) is given in Figure 5-6 c).

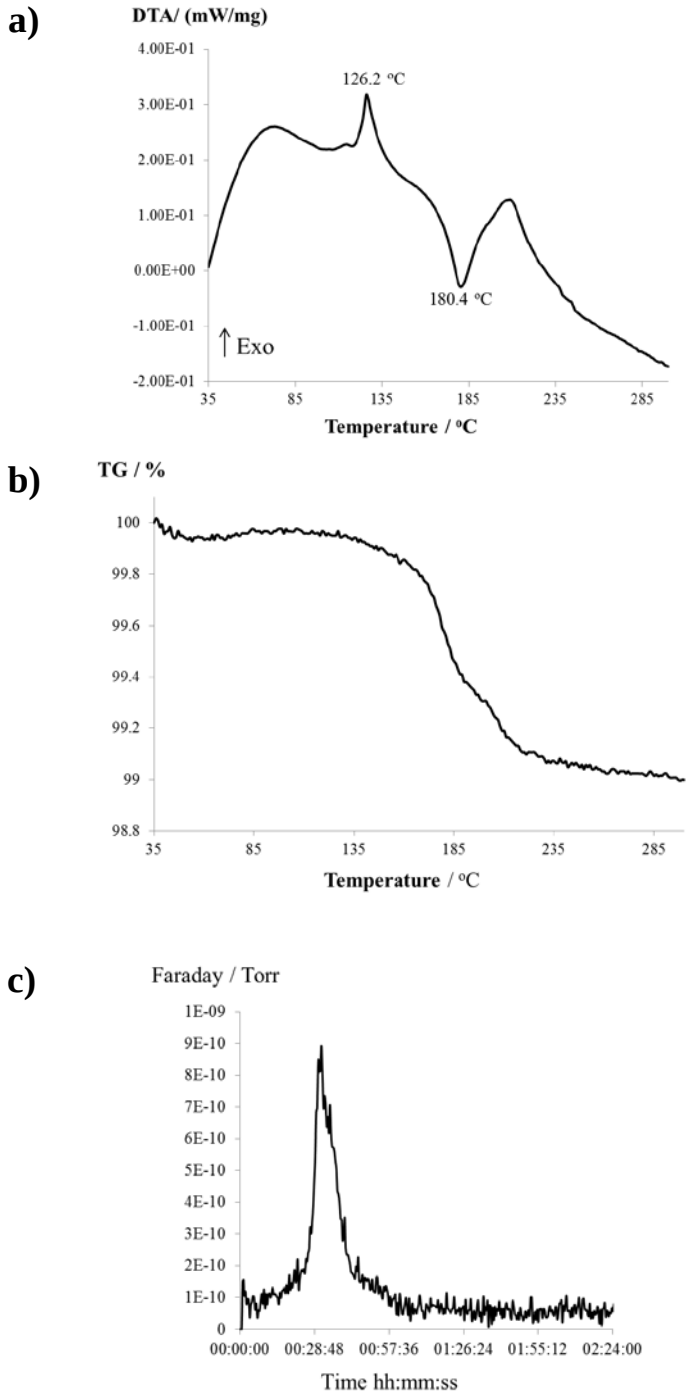

Figure 5-6 a) DTA, b) TG and c) MS data (*m/z* = 2) for Sample 48 heated to 500 ºC using a heating rate of 5 ºC/min.

There were a number of low temperature events identified in the DTA profiles, and these corresponded to a small mass loss (~1 wt%) which could be correlated to the loss of hydrogen from the corresponding MS data. The expected mass loss from the product of the metathesis product is 1.49 wt% based on Equation 5-4. The slightly lower value obtained here suggests that some loss of hydrogen from the sample has occurred as a result of the milling procedure. The low temperature hydrogen desorption is characteristic of the desired $LiAlH_4$ product. The thermal behaviour of $LiAlH_4$ is well documented, and the DTA profile of the sample prepared here matches the previously determined low temperature decomposition profiles given in the literature for $LiAlH_4$ (Equation 5-5 and Equation 5-6).[56] The exo- and endothermic peaks at 126.2 ^{o}C and 180.4 ^{o}C are characteristic of the complex hydride, and correspond to the following two decomposition mechanisms, respectively[57]:

Equation 5-5

$$3\ LiAlH_4 \rightarrow Li_3AlH_6 + 2\ Al + 3\ H_2$$

Equation 5-6

$$Li_3AlH_6 \rightarrow 3LiH + Al + \frac{3}{2} H_2$$

The quoted ranges for these two processes are 150-175 ºC and 180-220 ºC.[56] The results given here indicate that these processes occur at a lower temperature in the mechanochemically synthesised materials relative to the literature values for un-doped and doped $LiAlH_4$ prepared by mechanochemistry. For example, the T_{peak} for the first and second decomposition steps for 5 wt% nano-Fe doped $LiAlH_4$ are 132.1 ºC and 200.2 ºC, respectively.[58] The possibility of this hydrogen evolution being from the hydrogen donor, NaH, can be ruled out as NaH is expected to decompose at a significantly higher temperature from the STA conducted for the as-received NaH material (Appendix C, C.3), where T_{peak} for hydrogen desorption (3.59 wt%) from NaH was determined to be 392.9 ^{o}C and the enthalpy of decomposition for NaH was 48.15 kJ/mol, as determined from analysis of the area of the peak in the DTA trace.

Only reflections for two cubic phases were observed in the diffraction pattern of the sample collected after heating to 300 ºC (Figure 5-7a), these could be attributed to Al/LiH and NaCl, where the diffraction peaks expected for LiH and Al are coincident. The PXD profile of the sample heated to 500 ºC (Figure 5-7 b) indicated reflections attributable to NaCl, Al metal and the LiAl alloy, where the latter two phases are the expected products from the high temperature decomposition events associated with $LiAlH_4$, given by:

Equation 5-7

$$LiH + Al \rightarrow LiAl + \frac{1}{2} H_2$$

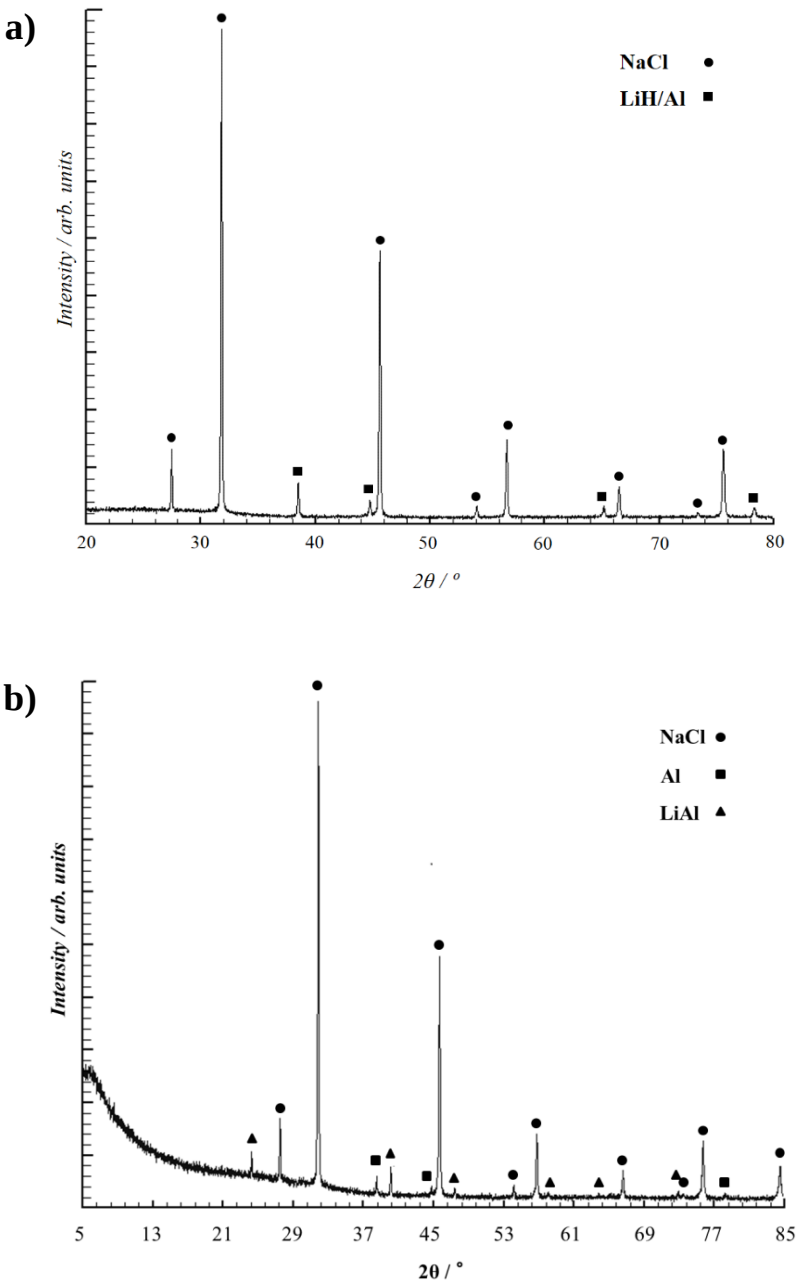

Figure 5-7 X-ray diffraction patterns of samples collected post STA of Sample 48 to a) 300 ºC and b) 500 ºC.

5.3.2.3. Summary

Synthesis of the complex halide, $LiAlCl_4$, was conducted successfully by mechanochemistry, yielding a high purity (>99%) product. This was confirmed by PXD and subsequent treatment of the diffraction data using the Rietveld method. STA data revealed an endothermic event, which which was attributed to the $T_{m.p.}$ of the complex halide, 154.4 ºC. Metathesis between the mechanochemically prepared complex halide and NaH was investigated by solid state mechanochemical reaction. The diffraction results of

the reaction product revealed reflections for the thermodynamically stable by-product, NaCl, and LiH/Al after heating to 300 ºC, and NaCl, LiAl and Al after heating to 500 ºC. The decomposition products are consistent with those expected from the decomposition of $LiAlH_4$. The STA results gave a thermodynamic profile analogous to that of $LiAlH_4$, based on literature data. It may be concluded from this work that the metathesis reaction has proceeded successfully using the ternary halide as the complex hydride precursor. Furthermore, the T_{peak} values for the two low temperature thermal decomposition events for $LiAlH_4$ in this work are at a lower temperature (126.2 ^{o}C and 180.4 ^{o}C) than unmodified and catalyzed $LiAlH_4$, based on literature values.

5.4. Mechanochemical Synthesis of $NaMgX_3$ (X = Cl, H).

5.4.1. Introduction

"The Hydride-Fluoride Analogy" by Maeland and Lahar describes the similarities in structure of the ternary fluorides and hydrides that form the Perovskite structure.[59] There are indeed other examples of structural comparisons between halide and hydride compounds for hydrogen storage, *e.g.*, $Mg_2FeH(D)_6$ has been described with the K_2PtCl_6-type structure.[60, 61] In 2009, Pawelke *et al*. suggested the use of ternary halide precursors as an indirect route to advanced ternary hydrogen storage materials, although their work did not provide further details about how this would be achieved.[62] They prepared Perovskite-type $KM^{II}Cl_3$ (M^{II}=Ti, Cr, Mn, Fe, Co, Ni, Cu, Zn) halides, by mechanochemistry using a high b:p ratio (120:1) and non-stop ball milling for 3 h at 800 rpm, although they state that the reactions are also possible under less energetic conditions using a b:p ratio of 40:1. Based on the knowledge of $NaMgH_3$ from previous chapters, it seemed prudent to investigate whether the same hydride could be formed from a halide precursor, namely $NaMgCl_3$. The NaCl-$MgCl_2$ phase diagram has been studied over a range of binary halide stoichiometries. These demonstrated the eutectic and peritectic features of the NaCl-$MgCl_2$ system, in which two incongruently melting compounds were determined; $NaMgCl_3$ and Na_2MgCl_4.[63, 64, 65, 66] The standard enthalpy of formation for $NaMgCl_3$, however, does not appear to be available in the literature. The diffraction pattern for $NaMgCl_3$ was given by Reddy *et al*. but full crystallographic information for the orthorhombic phase determined in their work was not provided.[67] In fact, they state that the $NaMgCl_3$ structure determined in their work was analogous to that observed in another study by McMurdie *et al.* on $ABCl_3$ compounds, but no reference to the $NaMgCl_3$ compound is given in this latter work.[68] In the work by van Loon on $NaMCl_3$ and Na_2MCl_4 systems (M = Mg, Mn, Fe, Cd), the lattice parameters for $NaMgCl_3$ are given, but no further data is provided in the paper. [69]

This sub-section looks at the synthesis of Perovskite-type halide $NaMgCl_3$ from the binary halides and subsequent reaction with an appropriate hydride *via* the metathesis route. This is in analogy to the concept introduced in the previous section. The following metathesis reaction between $NaMgCl_3$ and LiH or NaH are proposed in this work:

Equation 5-8 $$NaMgCl_3 + 3\ LiH \rightarrow NaMgH_3 + 3\ LiCl$$

Equation 5-9 $$NaMgCl_3 + 3\ NaH \rightarrow NaMgH_3 + 3\ NaCl$$

Both reactions involve the formation of a themodynamically stable by-product, which both have a significantly higher decomposition temperature than the ternary hydride, $NaMgH_3$ ($\Delta_f H^o_{solid}$ = -231±4 kJ/mol[70]), product (see Chapter 4).[47]

5.4.2. Results & Discussion

5.4.2.1. Synthesis and Characterisation of the Halide Precursor, $NaMgCl_3$

The powder products formed by both the thermal method and mechanochemistry were in the form of a white powder. The former had to be scraped from the inside of the silica tube in which it was synthesised as it had formed a solid mass. The latter method formed a loose powder. The highly hygroscopic nature of halide salts make them difficult to handle and analyse and so all sample preparation and retrieval procedures were carried out in an $Ar_{(g)}$ filled glovebox. The SEM images indicate that some degradation may have occurred as a result of the brief exposure to air for the purposes of this analysis. This is evidenced by the melt-like morpohology shown in Figure 5-8 a). The images collected reveal agglomerated particles of the powder product, where higher magnification indicated a porous solid (Figure 5-8 b).

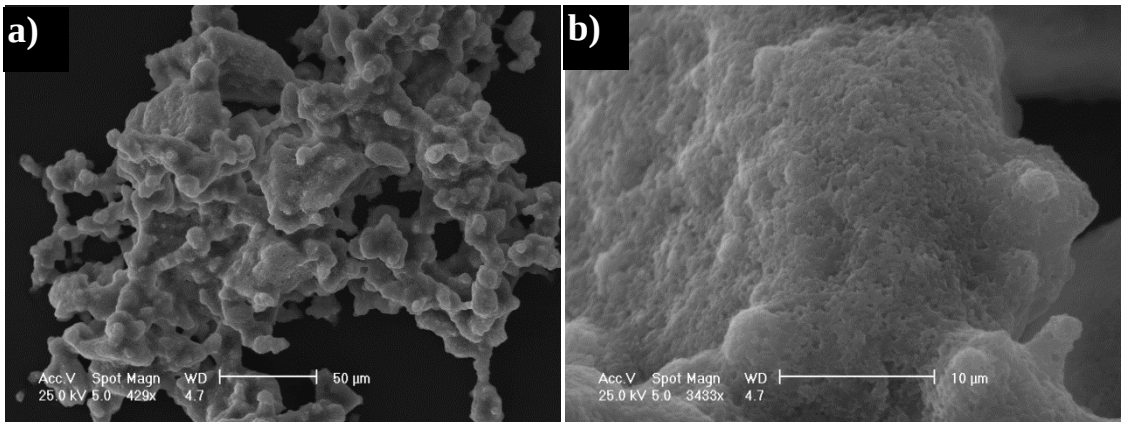

Figure 5-8 SEM micrographs of as prepared $NaMgCl_3$ (Sample 50) using a) low and b) high magnification.

The as synthesised $NaMgCl_3$ (Sample **50**) was determined by PXD to be isostructural to the Perovskite-type $NaMnCl_3$ halide. Using CELREF, the lattice parameters and cell volume could be estimated and compared with values given in literature for $NaMgCl_3$ (Table 5-3).[69] Rietveld refinement allowed determination of the crystal structure of the as-prepared halide (Figure 5-9). The structure of $NaMgCl_3$ has been determined previously, as mentioned, but no structure model was available from the ICSD, therefore the $NaMnCl_3$ structure model was employed (ICSD-2552). The atomic parameters and interatomic distances for $NaMgCl_3$ derived from this work are given in Appendix C, C.4 & C.5.

Table 5-3 Rietveld refinement data for $NaMgCl_3$ and impurity phase (Sample 50).

	$NaMgCl_3$			
Formula	*Literature*[69]	*CELREF*	*Sample **50***	*NaCl*[†]
Crystal System		*Trigonal*		*Cubic*
Space Group		*R-3* (148)		*Fm-3m* (225)
***a* / Å**	6.506(3)	6.49(2)	6.5117(4)	5.6014(5)
***c* / Å**	18.586(7)	18.676(3)	18.584(1)	-
Volume / Å^3	-	681(1)	682.4(1)	175.75(4)
Z		6		4
Formula Weight / g	-	-	1105.722	233.722
Calculated density, ρ_X / g cm^{-3}	-	-	2.690	2.209
Phase Fraction	-	-	86.9(3)	13.1(3)
No of data	-	-	11829	
No of parameters	-	13	40	
R_{wp}	-	-	6.15 %	
R_p	-	-	4.09 %	
χ^2	-	-	1.208	

[†]Impurity phase of Sample **50**.

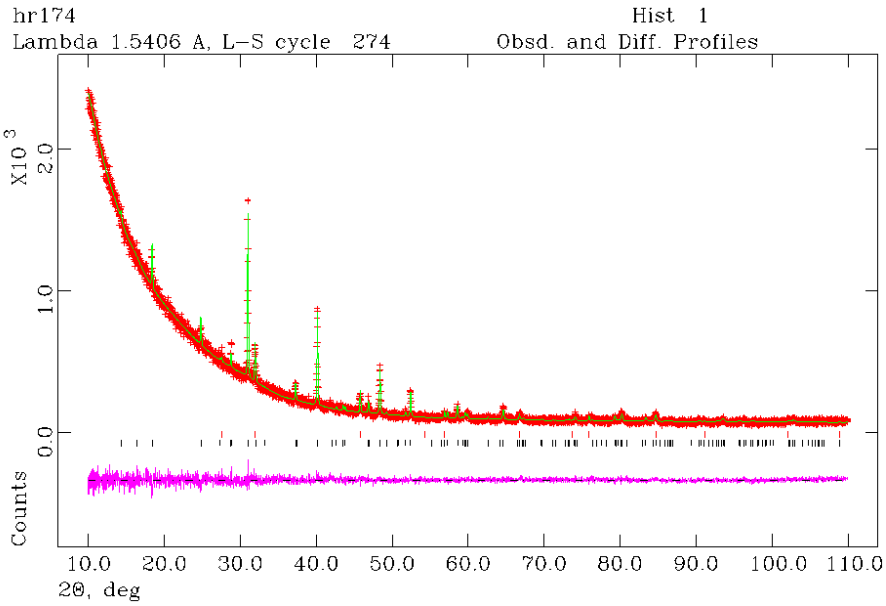

Figure 5-9 Refinement plot of data collected for Sample 50, where black tick marks indicate $NaMgCl_3$, and NaCl impurity are indicated by red tick marks. Red crosses indicate experimental data, and green line indicates the calculated pattern. The magenta line indicates difference plot.

The structure of $NaMgCl_3$ may be described, in analogy to $NaMnCl_3$, as a trigonally distorted hexagonal close-packed lattice, in which alternating layers of Na and Mg cations exist between layers of Cl anions (Figure 5-10 a). The Na and Mg cations form a distorted octahedra with Cl anions on the corners of each octahedron (Figure 5-10 b and c).

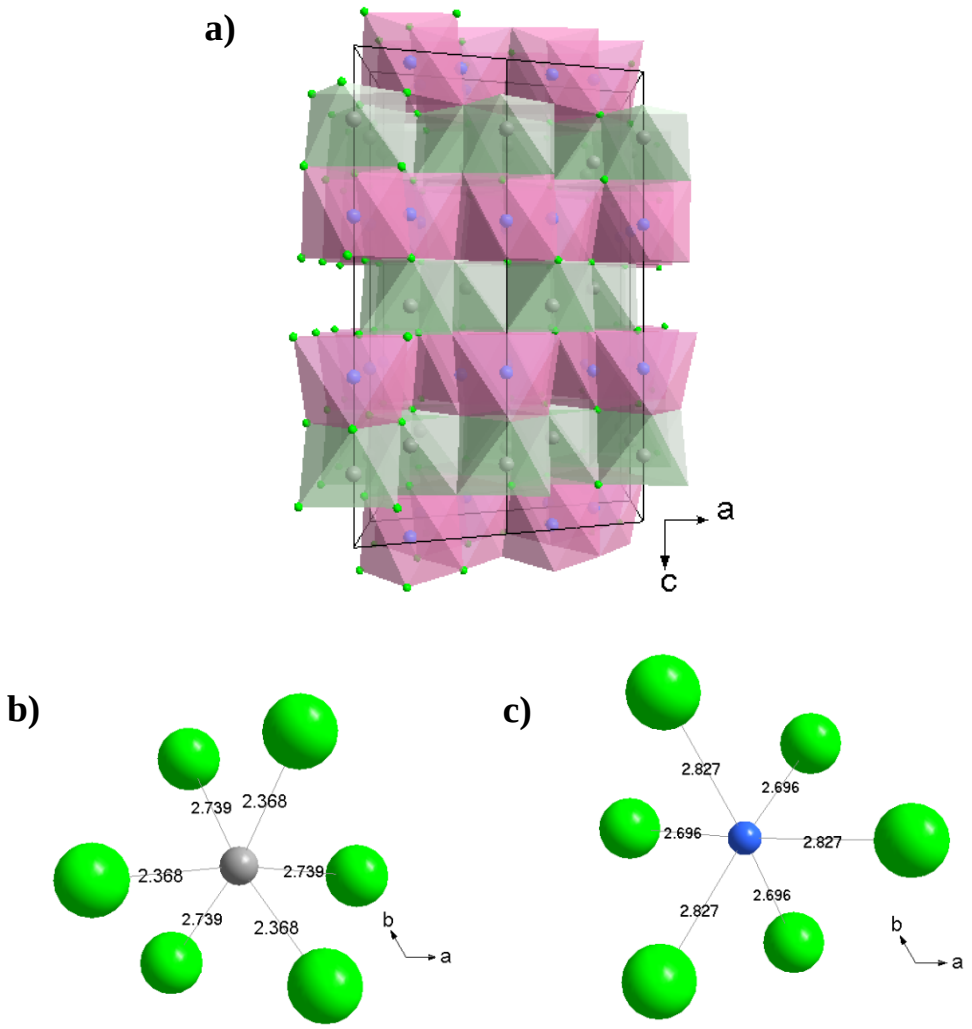

Figure 5-10 a) Structure of $NaMgCl_3$ (Sample 50) showing alternating layers of Na centred octahedra (green) and Mg centred octahedral (pink). Coordination orientation of the b) Na octahedral and c) Mg octahedral. (Mg = blue spheres, Na = grey spheres, Cl = green spheres.)

Synthesis of $NaMgCl_3$ was also investigated by the mechanochemical method (Sample **51**), and the effect of milling time is shown in Figure 5-11. The ternary halide $NaMgCl_3$ phase is evident after only 2 h of milling, although minor reflections of a second ternary halide phase are also evident, which is consistent with evidence given in phase diagram studies where the two phases exist. This result is surprising given that previous work on the mechanochemical synthesis of Na-Mg-Cl type phases by the mechanochemical method were unsuccessful.[71] The work of Solinas and Lutz used milling times of up 100 h employing a 2:1 ratio for Na_2MgCl_4 synthesis, although no further milling conditions for the NaCl-$MgCl_2$ systems studied in their work is provided. Based on the observations from this work, it may be possible that the milling conditions used in the study by Solinas and Lutz were too vigorous and the halides thus became amorphous.

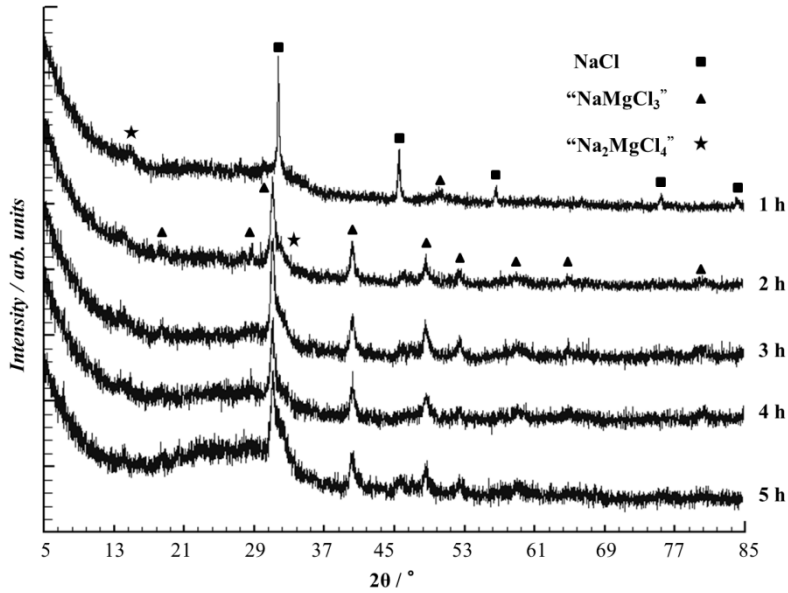

Figure 5-11 Effect of milling time on the synthesis of $NaMgCl_3$ from a stoichiometric 1:1 mixture of NaCl and $MgCl_2$ (Sample 51).

The thermal properties of mechanochemically synthesised $NaMgCl_3$ were probed by STA and also by *in-situ* high temperature PXD between room temperature and 500 ºC. The STA of the 1:1 molar mixture of NaCl:$MgCl_2$ prepared by hand-mixing, and mechanochemistry are compared in Figure 5-12. This shows similar DTA profiles, but the temperatures of the main features occur at a lower temperature in the milled sample in comparison to the hand-mixed sample. The main endothermic feature at ~460 °C may be ascribed to the eutectic point of the 1:1 molar mixture, and is in close agreement to the values obtained in previous work (462 °C).[65] For the milled sample (Sample **51**), there is a small mass loss (~2.5 wt%) associated with the low temperature feature at 216 °C, and a further mass loss associated with the eutectic event. This occurs at 260 °C for the hand mixed sample (Sample **49**), but the mass appears to increase again this event. It is not clear what this small mass loss is associated with in either of the samples, as no evolution of water or other species could be detected in the mass spectrometry data.

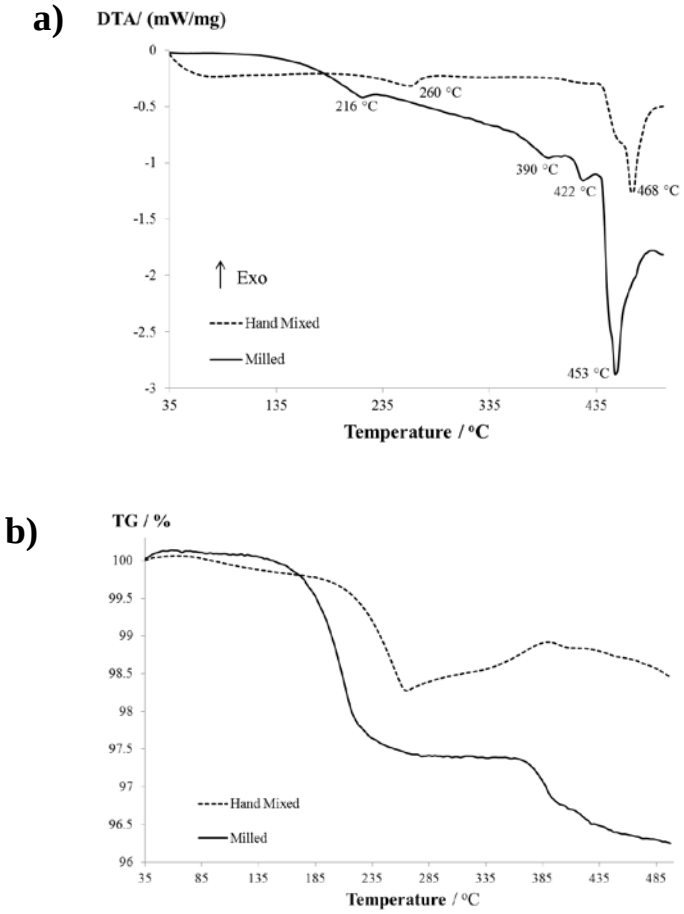

Figure 5-12 STA data comparison for Samples 49 and 51, showing a) DTA and b) TG data, respectively.

PXD data was collected for Sample **51** (5 h milled) heated to 300 °C to establish the structure of the material obtained after the low temperature event at 216 °C. A ternary phase was identified, which was isostructural to $Na_2Mn_3Cl_8$ (ICSD-1846, Figure 5-13).[69, 72]

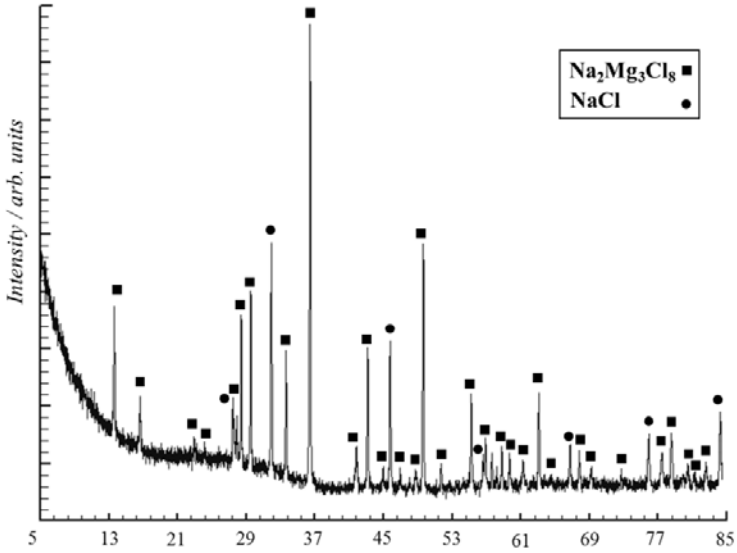

Figure 5-13 X-ray diffraction pattern of product collected after heating Sample 51 to 300 °C (5 °C/min in a flow of $Ar_{(g)}$).

Indexing was conducted using CELREF software to determine the lattice parameters of the ternary phase produced here relative to the known $Na_2Mg_3Cl_8$ structure data given by van Loon *et al*. The structure data was found to be in good agreement with the literature values (Table 5-4). The Rietveld method was then used to determine further structure information about the $Na_2Mg_3Cl_8$ observed at 300 ºC using $Na_2Mn_3Cl_8$ (ICSD-1846) as a structure model (Figure 5-14 and Table 5-4). The atomic parameters for $Na_2Mg_3Cl_8$ derived from this work are given in Appendix C, C.6.

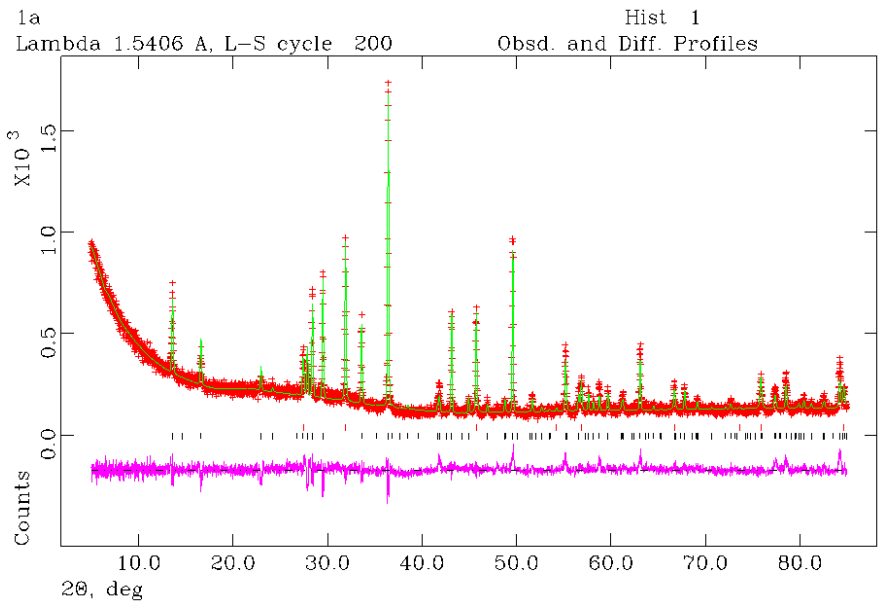

Figure 5-14 Rietveld plot for product of Sample 51 heated to 300 ºC. Black tick marks represent the $Na_2Mg_3Cl_8$ phase and red tick marks represent NaCl. Red crosses indicate experimental data, and the green line indicates the calculated pattern. The magenta line indicates difference plot.

Table 5-4 Rietveld refinement data for product of Sample 51 heated to 300 ºC.

Formula		**$Na_2Mg_3Cl_8$**		**NaCl**[†]
Source	***Literature***[69]	***CELREF***	***Sample 51***	
Crystal System		Trigonal		Cubic
Space Group		$R\bar{3}m$ (166)		$Fm\bar{3}m$ (225)
***a* / Å**	7.355(6)	7.351(2)	7.3444(5)	5.6038(4)
***c* / Å**	19.51(1)	19.5039(4)	19.499(2)	-
Volume / Å^3	-	917.8(3)	910.9(2)	175.98(4)
Z		3		4
Formula Weight / g	-	-	1207.557	233.722
Calculated density, ρ_X / g cm^{-3}	-	-	2.201	2.206
Phase Fraction	-	-	86.9(3)	13.1(3)
No of data	-	-	4846	
No of parameters	-	30	44	
R_{wp}	-	-	9.32 %	
R_p	-	-	6.96 %	
χ^2	-	-	1.868	

[†]Impurity phase of Sample **51**.

The structure of $Na_2Mg_3Cl_8$ is analogous to the $Na_2Mn_3Cl_8$ structure, where the Mg atoms are octahedrally coordinated with Cl, and the Na atoms are coordinated in a trigonal prism configuration (Figure 5-15). This gives rise to a mixed lattice comprising both close-packed and hexagonal stacking layers of equal quantity.

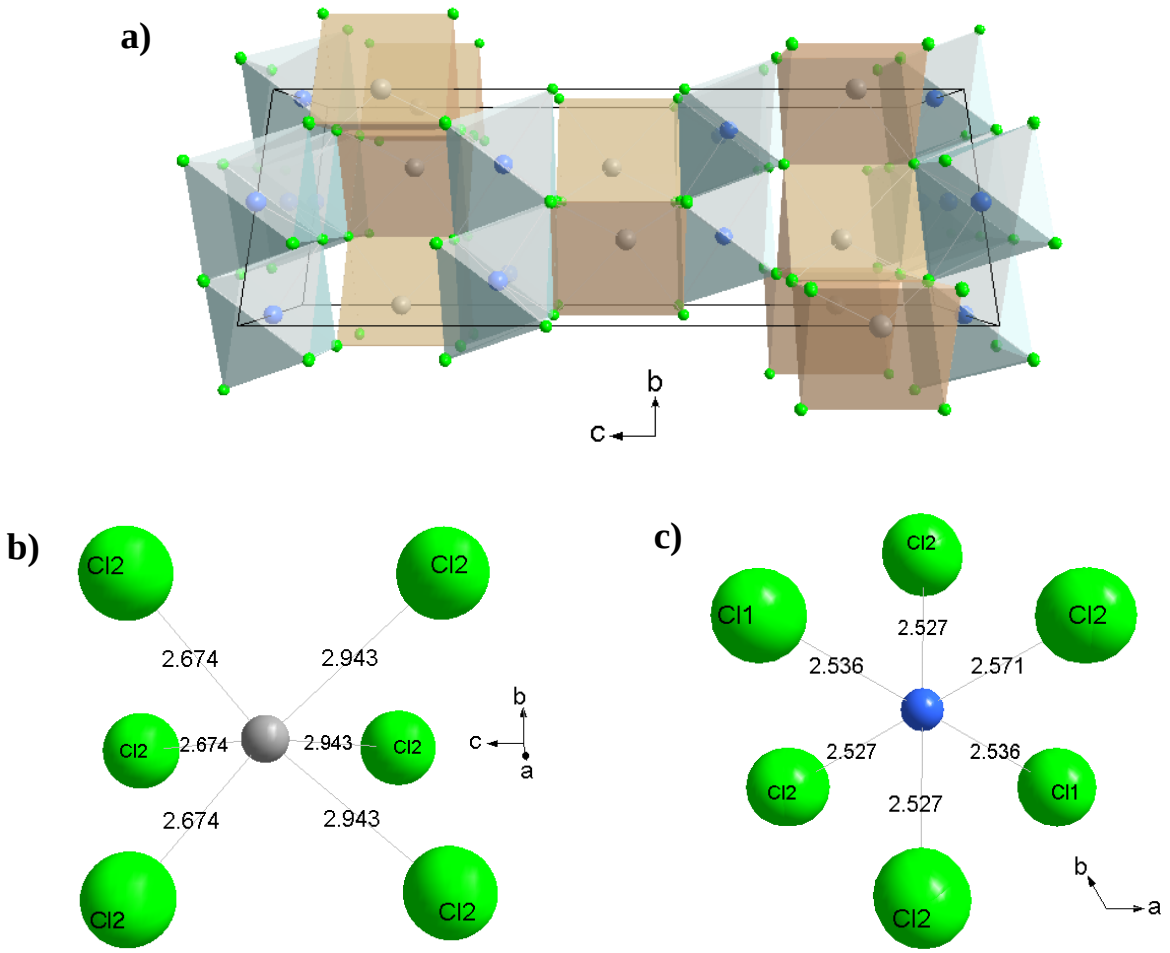

Figure 5-15 a) Structure of $Na_2Mg_3Cl_8$ (Sample 51 heated to 300 °C) showing alternating layers of Na centred trigonal prisms (beige) and Mg centred octahedra (blue). Coordination orientation between Cl anions and the b) Na cation and c) Mg cation. (Mg = blue spheres, Na = grey spheres, Cl = green spheres.)

The *in-situ* PXD revealed the phase transformations upon heating Sample **51** (Figure 5-16). Even after heating to only 100 °C, the reflections for NaCl and the Na_2MgCl_4 phase become evident. The patterns recorded at room temperature and 50 °C indicated reflections for the $NaMgCl_3$ phase and are not shown here for brevity. At 100 °C, it is clear that the sample has begun to change based on the emergence of another reflection at a higher angle relative to the main reflection for the $NaMgCl_3$ phase. The ternary $Na_2Mg_3Cl_8$ phase begins to emerge at 150 ºC. Between 150-300 ºC, the sample is a biphasic system comprising $Na_2Mg_3Cl_8$ and NaCl, which is consistent with the observations for the product collected after heating Sample **51** to 300 ºC described previously. The $Na_2Mg_3Cl_8$ phase remains evident at 350 ºC, but decomposition occurs at 400 ºC with the formation of the binary halides, NaCl and $MgCl_2$. This is consistent with the onset of the eutectic melting point observed by STA from phase diagram information.[52]

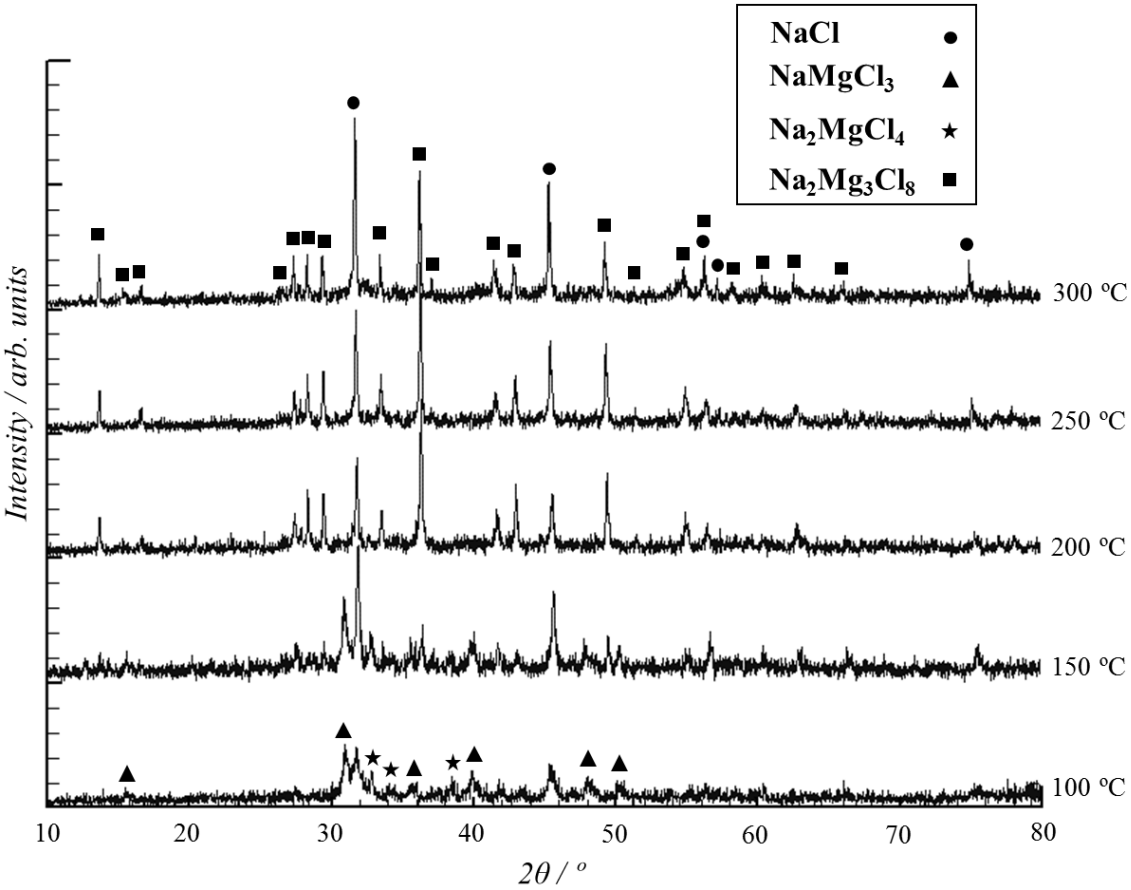

Figure 5-16 Comparison of diffraction patterns collected by *in-situ* PXD analysis between room temperature and 300 ºC (Sample 51).

5.4.2.2. Metathesis Reaction between Perovskite Halide Precursor, $NaMgCl_3$, and LiH/NaH

With a knowledge of the structure and thermal properties of the halide prepared by both thermal and mechanochemical methods, the metathesis reactions were conducted using the thermally synthesised material in the first instance and then using the mechanochemically synthesised precursor for comparison.

Sample **50** was reacted with stoichiometric proportions of NaH by milling for 5 h (Sample **52**). The resultant grey powder product contained only one crystalline phase, NaCl, as determined from PXD (Figure 5-17). The absence of reflections from $MgCl_2$ or the original ternary halide suggests that the reaction was successful. Further, the absence of reflections from any hydride phase, such as the hydride source (NaH) or the expected hydride product ($NaMgH_3$) should be noted. Based on previous work on hydride synthesis by this route, lab PXD is not sufficient to show the hydride has formed. This is likely to be the result of a combined effect from the small crystallite size of the hydride product and hence broad

Bragg reflections, also low scattering. The broad band between 13-30 º may also suggest some contribution from an amorphous material.

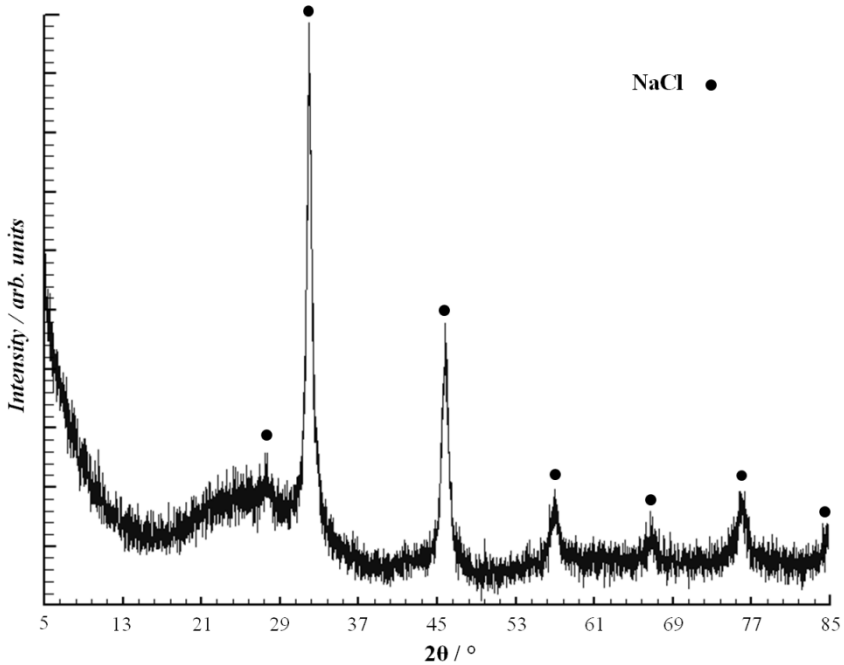

Figure 5-17 PXD pattern of Sample 52.

To establish whether the reaction had successfully formed $NaMgH_3$, STA was conducted using the metathesis product (Figure 5-18). The sample was heated to 500 ºC (5 ºC/min), to cover the temperature range in which $NaMgH_3$ decomposes. The DTA trace shows a two-step decomposition process. The observed loss of hydrogen from the sample is <1 wt% H_2, which is less than the expected loss of hydrogen from the as-prepared composite which should be 1.34 wt% when allowing for the mass of the other components in the metathesis product.

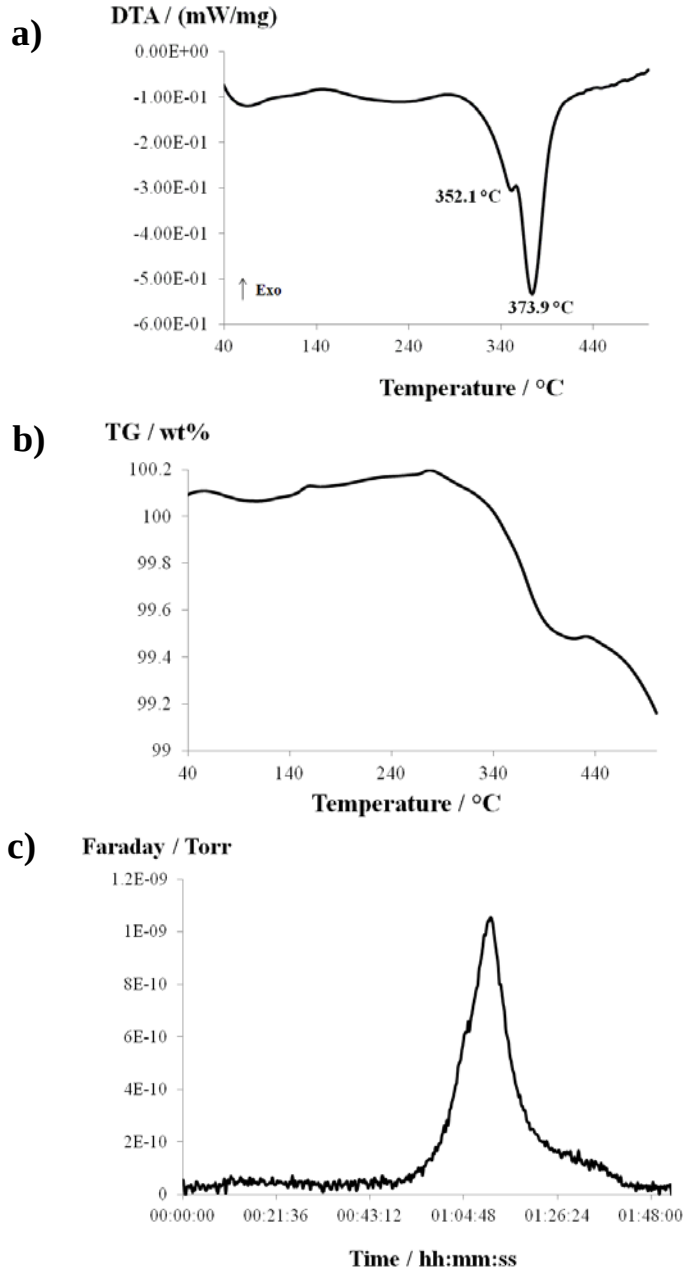

Figure 5-18 STA data for Sample 52 heated from room temperature to 500 °C at 5 °/min; a) DTA, b) TG and c) MS (*m/z* = 2).

The asymmetry in the DTA trace suggests that the decomposition has occurred *via* a two-step process as indicated by the DTA trace. The expected decomposition products of the ternary hydride would comprise Na, Mg (See Chapter 4) and the expected halide by-product for this reaction, NaCl, would remain unchanged. The PXD pattern of the post STA product is shown in Figure 5-19, and indicates reflection from the two metallic phases and NaCl, as predicted.

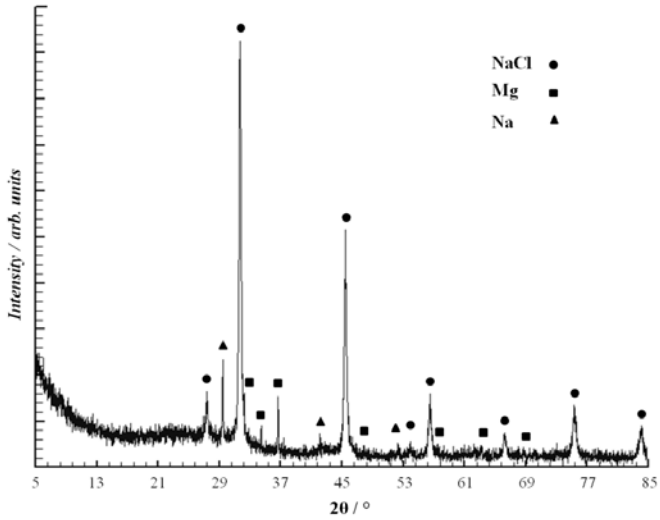

Figure 5-19 PXD pattern of sample collected after STA.

The absence of $MgCl_2$ suggests that the ternary halide did not decompose to the respective binary halides during the metathesis reaction or during the thermal analysis. The presence of Na and Mg metal phases suggests that the decomposition was from a hydride containing both Na and Mg which is likely to be $NaMgH_3$, however, decomposition from NaH and MgH_2 cannot be categorically ruled out.

For comparison, the metathesis reaction was conducted using stoichiometric proportions (1:3) of the halide precursor, Sample **51**, and NaH as the hydrogen donor (Sample **53**) to establish whether the halide synthesis method had an impact on the metathesis reaction. The post metathesis product revealed only the NaCl by-product from PXD (Figure 5-20), and is consistent with the previous results given for the metathesis reaction conducted using the halide produced *via* the conventional thermal method.

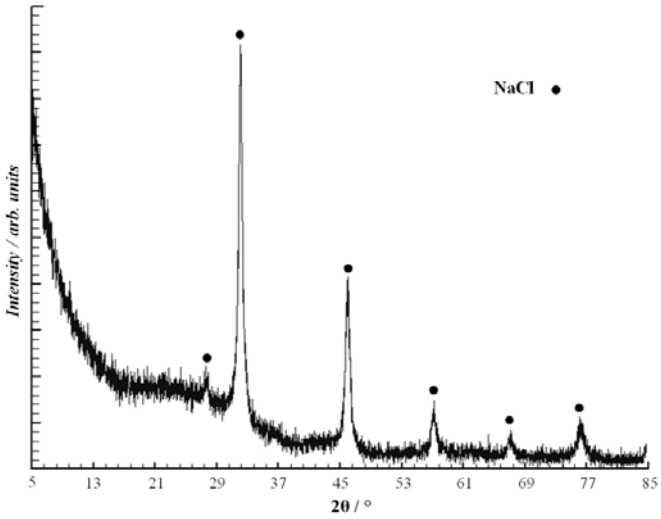

Figure 5-20 PXD of post milled metathesis product (Sample 53).

Thermal analysis showed very similar results to that observed previously, where a two-step endothermic decomposition process was observed by DTA and the asymmetry in the hydrogen release profile recorded by MS reflects this (Figure 5-21). The TG once again shows a <1 wt% mass loss associated with the release of hydrogen, which is slightly less than the theoretically expected mass loss (1.34 wt%).

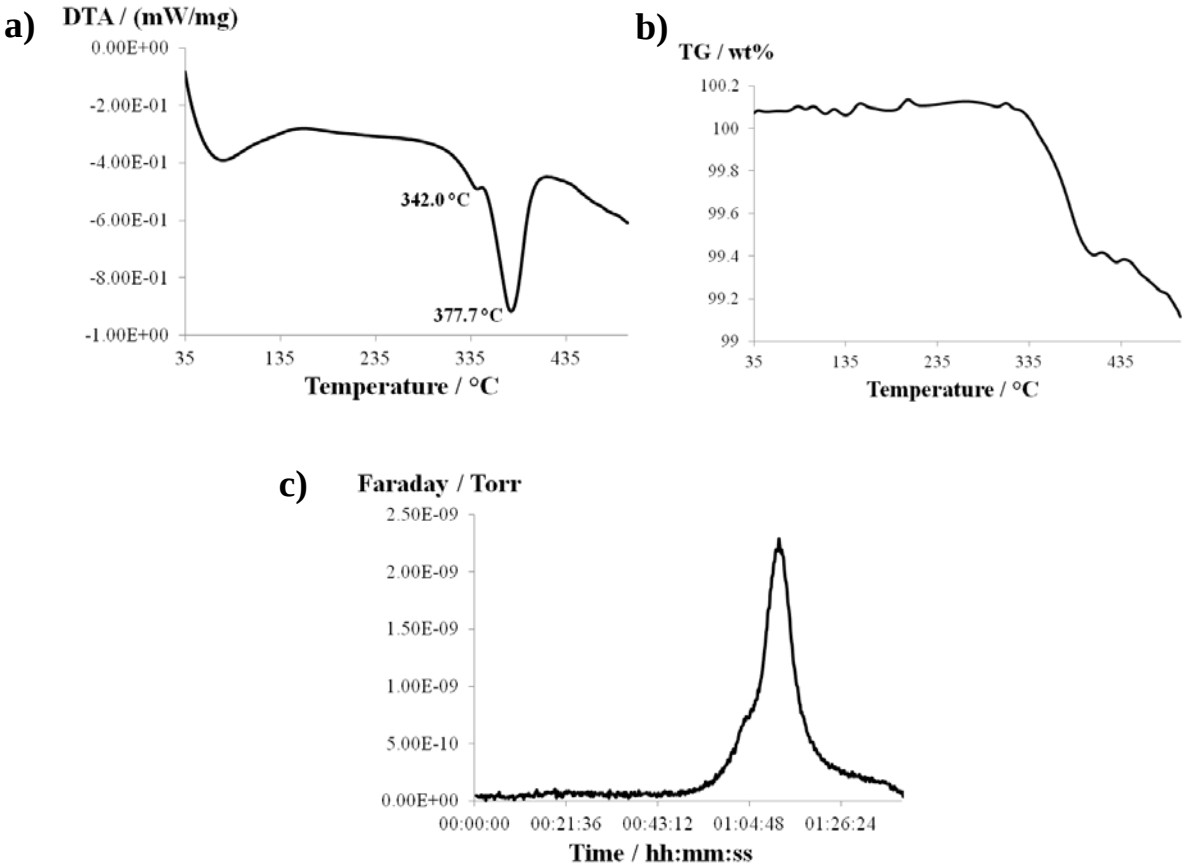

Figure 5-21 STA data for the Sample 53 heated to 500 °C at 5 °/min; a) DTA, b) TG and c) MS (*m/z* = 2).

The product collected after thermal analysis was analogous to that observed for the product collected previously, where reflections for Na, Mg and NaCl were observed. This suggests that the mechanochemically prepared halide precursor gives the same metathesis results as with the thermally prepared precursor.

Since the precursor and hydride donor contained Na cations, the possibility of the NaCl by-product coming from the precursor could not be ruled out. Therefore, attempts were made to investigate the use of LiH as a hydride source for this system, Sample **54**, *via*:

Equation 5-10

$$NaMgCl_3 + 3\ LiH \rightarrow NaMgH_3 + 3\ LiCl$$

This was expected to show that the H^- and Cl^- ions were interchanged as a result of this process, and that the NaCl observed as the by-product was not simply NaCl from decomposition of the ternary halide precursor. (Sample **50** was used as the halide precursor to form Sample **52**.) The SEM images of the post metathesis reaction product indicated that the sample may have been affected upon exposure to air but images collected at higher magnification reveal that the sample is comprised of smaller, agglomerated particles amongst the smooth portions of the sample (Figure 5-22).

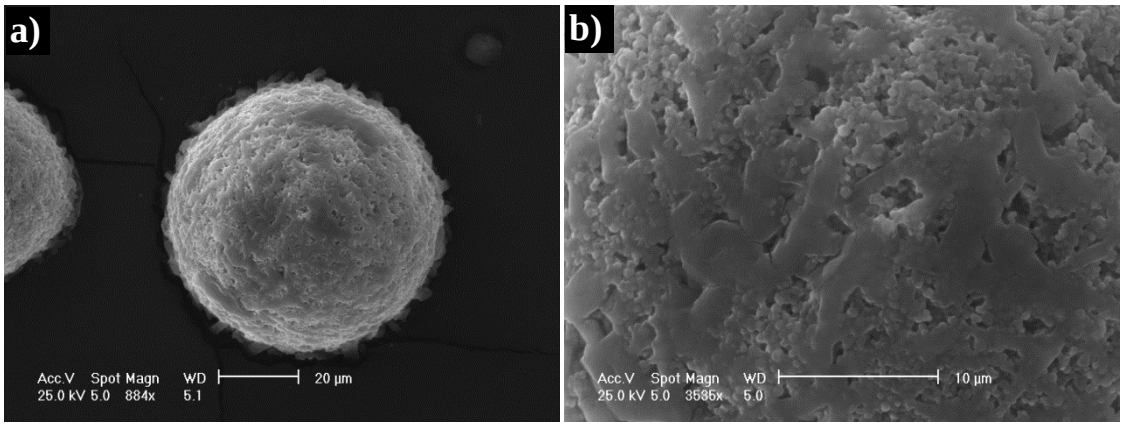

Figure 5-22 SEM images of Sample 54; a) low (20 µm) and b) high (10 µm) magnifications.

However, the PXD results of the post metathesis product, a pale grey powder, showed reflections for the expected by-product, LiCl, and also NaCl (Figure 5-23).

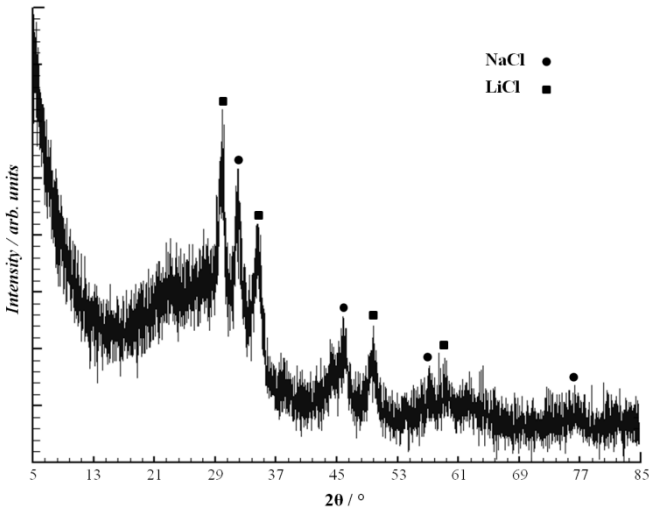

Figure 5-23 PXD pattern of post metathesis product; Sample 54.

It may suggest that the ternary halide has decomposed to its respective binary halides, where the following reaction scheme driven by the mechanical action in the mill may be considered:

Equation 5-11 $NaMgCl_3 + 3LiH \rightarrow NaCl + MgCl_2 + 3LiH \rightarrow MgH_2 + LiH + NaCl + 2\ LiCl$

However, no reflections from LiH or $MgCl_2$ appear evident from the PXD data. An alternative suggestion for this would be that a competing contemporaneous reaction is taking place where there is the potential for two thermodynamically stable salt products; LiCl and NaCl. The STA results indicate a thermal event at 316.6 ^{o}C which is associated with hydrogen release (Figure 5-24). This is well below that expected for LiH (680 ºC), NaH (392.9 ºC), $NaMgH_3$ (365 ºC) or MgH_2 (424.5 ºC) (T_{peak} values given from data collected using 5 ºC/min heating rate) suggesting that another material within the milled metathesis product is releasing hydrogen at this temperature.

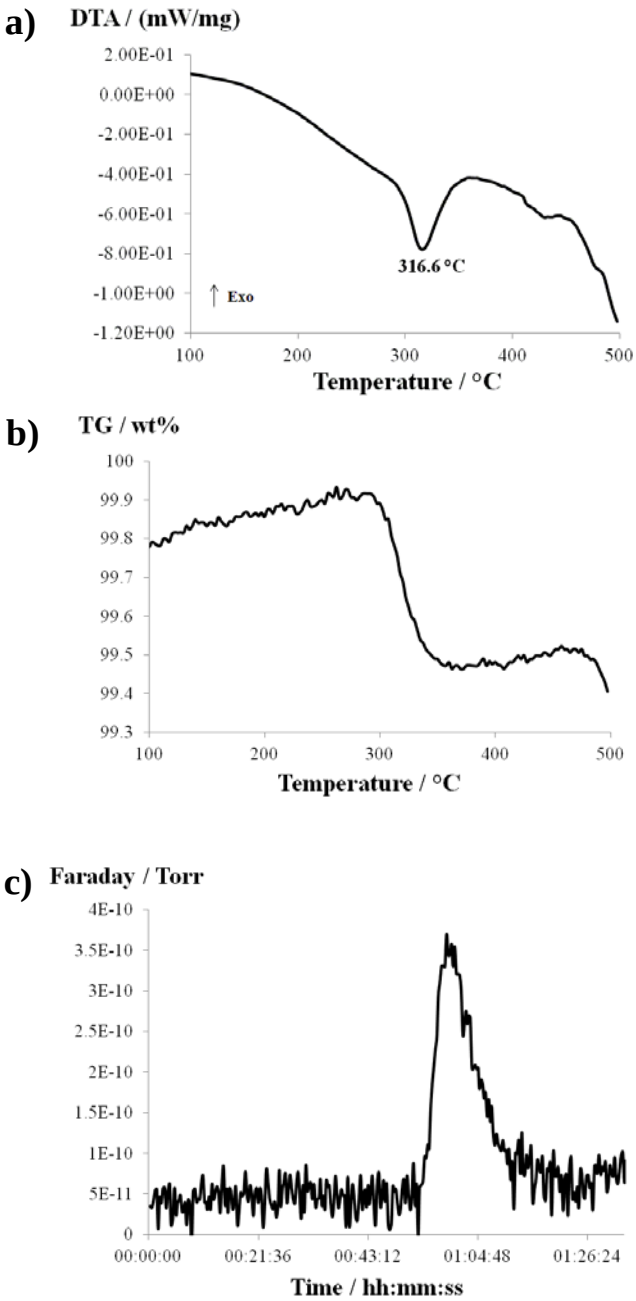

Figure 5-24 STA data collected Sample 54; a) DTA, b) TG and c) MS (*m/z* = 2).

The PXD data of the black powder sample collected after heating showed reflections from NaCl and LiCl as in the metathesis product, and a third phase identified as the "LiMg" alloy described by Levinson.[73] CELREF was used to index the cubic lattice parameter of this phase which was found to be a = 3.518(2) Å, volume = 43.5(2) Å^3. Rietveld refinement allowed structural information to be derived using the literature model for the three phases and the results are given in Figure 5-25 and Table 5-5. The cell parameter determined for the LiMg phase by Rietveld refinement is consistent with the indexing conducted by CELREF, however, the cell parameter is slightly larger than that given in literature for "LiMg"; a = 3.5137(3) Å *vs.* 3.484(1) Å. This suggests that the Li:Mg ratio in the alloy phase derived here may not be 1:1. Attempts to refine the SOF parameters for Li and Mg were attempted but were unsuccessful, causing the refinement to diverge significantly.

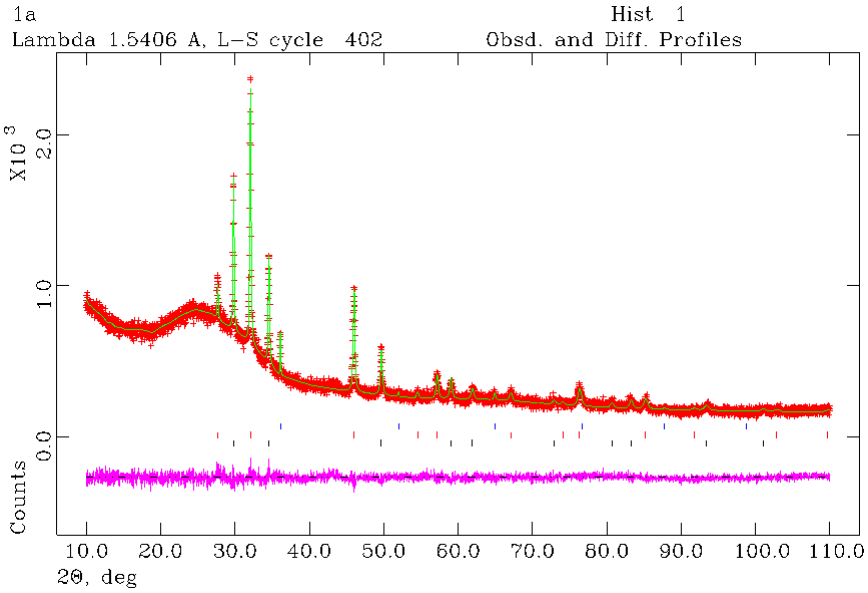

Figure 5-25 Rietveld refined of the post STA product collected for Sample 54 showing the LiMg alloy phase indicated by blue tick marks (Phase 1), NaCl in red tick marks (Phase 2) and LiCl in black tick marks (Phase 3). Experimental and calculated data are indicated by red crosses and the green continuous line, respectively. The lower magenta line indicates the difference plot.

Table 5-5 Rietveld data for sample collected after heating Sample 54 to 500 ºC.

Phase	1	2	3
Chemical Formula	"LiMg"	NaCl	LiCl
Crystal System		Cubic	
Space Group	$Im\bar{3}m$ (229)	$Fm\bar{3}m$ (225)	$Fm\bar{3}m$ (225)
***a* / Å**	3.5137(3)	5.5724(3)	5.1833(3)
Phase Fraction / %	3.7(1)	55.8(1)	40.5(1)
Volume / Å^3	43.38(1)	173.3(3)	139.26(2)
Z	1	4	4
Formula Weight / g	62.492	233.722	169.576
Calculated density, ρ_X / g cm^{-3}	2.392	2.243	2.022
No of data		11774	
No of parameters		46	
R_{wp}		5.62	
R_p		4.26	
χ^2		1.200	

This result suggests that the hydrogen release from the metathesis product resulted from a hydride from which the LiMg alloy was derived. "$LiMgH_3$", however, has previously eluded researchers in the field of hydrogen storage. It is not possible, however, to say with certainty whether this phase was formed during the mechanochemical metathesis reaction or during heating in the STA. The absence of reflections from either elemental Mg or Na suggests that other competing metathesis reactions towards the synthesis of MgH_2 or NaH do not occur. The theoretical hydrogen capacity for $LiMgH_3$ is 8.84 wt%, although less than 1 wt% H_2 is evolved from the sample prepared in this work and is likely to be the result of the additional halide by-product phases.

The first synthesis of $LiMgH_3$ was reported by Ashby and Goel using wet-chemistry involving reaction of $LiMgPh_3$ with $LiAlH_4$ in diethyl ether.[74] Attempts to synthesis this lightweight hydride experimentally from Li-Mg alloys have been made but were unsuccessful.[75] Theoretical chemistry methods have been employed to establish information about the thermodynamics of this hydride. [76, 77, 78]

The most thermodynamically feasible reaction for formation of the ternary hydride, $LiMgH_3$, is given below, and this sheds light on the potential decomposition process involved during heating of the metathesis product.

Equation 5-12

$$LiMg + \frac{2}{3}H_2 \rightarrow LiMgH_3$$

Pfrommer *et al.* also determined the ternary hydride to be a thermodynamically stable material (ΔG_0 = -1.07 eV/Mg atom, under standard temperature and pressure). Based on the known $LiBeMg_3$ phase, Li *et al.* proposed the $LiMgH_3$ phase to exist in a Perovskite-type structure.[79] More recent work has shown that the $LiMgH_3$ phase may be more akin to the trigonal $LiTaO_3$-type structures, which was estimated from the theoretical studies (Table 5-6).

Table 5-6 Comparison of theoretical values for the $LiMgH_3$ structure (R3c (167), Z = 6) and formation thermodynamics based on Equation 5-12.

Reference	*a* / Å	*c* / Å	Formation Enthalpy / kJ/mol
Vajeeston *et al.* [77]	4.958	13.337	ΔH^a = -147.5
Li *et al.*[78]	4.9226	13.2106	$\Delta G^{300\ K}$ = -129.7

[a]Temperature effects not considered.

The thermodynamic calculations conducted by Vajeeston *et al.* suggest that the reason why the $LiMgH_3$ phase cannot be synthesised by the combination of the binary hydrides (LiH and MgH_2) in analogy to the $NaMgH_3$ phase is because the reaction between the two binary hydrides is exothermic.

Therefore the possibility of this mechanochemical metathesis method being a novel route to $LiMgH_3$ is exciting due to the facile nature of the method. The desorption temperature recorded for the metathesis product here is consistent with a trend in observations made for ternary hydrides formed in the work of this thesis. Inclusion of alkali metals in ternary hydride phases with Mg, such as $NaMgH_3$, result in a lower desorption temperature relative to milled commercial MgH_2. While heavier alkaline earth metals, such as Ca, increase the desorption temperature. The $LiMgH_3$ desorption temperature may be expected to be lower than the $NaMgH_3$ system, and the thermal decompositon results obtained for the suspected $LiMgH_3$ phase here are consistent with this hypothesis since the T_{peak} of the metathesis product compared with mechanochemically synthesised $NaMgH_3$ is lower; 316 ºC *vs.* 365 ºC.

5.4.2.3. Summary

The synthesis of the ternary halide, $NaMgCl_3$, from stoichiometric quantities of the binary halides, NaCl and $MgCl_2$, was studied by both thermal and mechanochemical methods. The ternary phase was successfully synthesised by both methods, and comparisons in

structural data were made with existing information in the literature. The thermal characteristics of the mechanochemically prepared sample was probed by both STA and by *in-situ* PXD, and the structure of the $Na_2Mg_3Cl_8$ phase obtained at 300 ºC was described relative to literature data. The halide precursor obtained by the thermal method was used to conduct mechanochemical metathesis reactions with both LiH and NaH hydride donors. The results of the latter demonstrated that the expected product for a successful metathesis reaction towards $NaMgH_3$ was possible, but it was not possible to verify the presence of such a phase in this work. Similar results were obtained when the $NaMgCl_3$ precursors synthesised by the mechanochemical method were employed in the metathesis experiment. The experiment employing LiH as a hydride donor is very interesting, since the metathesis reaction revealed two salt by-products, inferring that a competing reaction was occurring. The thermal analysis revealed an endothermic event which was accompanied by hydrogen evolution. The PXD pattern of the product collected after heating revealed the presence of a LiMg phase, suggesting that a Li-Mg-H phase may be responsible for the hydrogen release event.

5.5. Mechanochemical Synthesis of $NaAlX_4$ (X = Cl, H).

5.5.1. Introduction

In order to probe the results given in the previous section further, another simple metathesis reaction was devised in which only alkali metal cations would participate. Considering the first section of this chapter involving the synthesis of $LiAlH_4$ from $LiAlCl_4$ and NaH, a similar reaction for the synthesis of $NaAlH_4$ from its respective halide precursor, $NaAlCl_4$ ($\Delta_f H^o_{solid}$ = -117±2 kJ/mol[80]), may be proposed (Equation 5-13).

Equation 5-13

$$NaAlCl_4 + 4\ LiH \rightarrow NaAlH_4 + 4\ LiCl$$

However, the following metathesis reaction involving the products of the above reaction may also be described, which is known to proceed *via* wet chemistry in THF[81, 82]:

Equation 5-14

$$NaAlH_4 + LiCl \rightarrow LiAlH_4 + NaCl$$

Therefore if these reactions are occurring simultaneously then one might expect both LiCl and NaCl phases in the post metathesis product since an excess of LiCl will be available from the first reaction (Equation 5-14). This hypothesis was tested experimentally.

5.5.2. Results & Discussion

5.5.2.1. Synthesis and Characterisation of the Halide Precursor, NaAlCl4

The halide, $NaAlCl_4$ ($\Delta_f H^o_{solid}$ = -1139.45 ±1.20 kJ/mol[83]), was synthesized from a stoichiometric mixture of the corresponding binary halides, NaCl and $AlCl_3$, *via* the mechanochemical method (Sample 56, Table 5-1). Rietveld refinement was conducted for the white powder product, where convergence between the experimental data and the model data (Baenziger *et al*.) was achieved swiftly.[84] Attempts were made to include NaCl in the refinement to establish if the binary halide reagent remained, but this caused significant divergence. The refined plot and structure data of the as-prepared ternary halide are given in Figure 5-26 and Table 5-7, respectively. The atomic parameters and interatomic distances derived for $NaAlCl_4$ in this work are given in Appendix C, C.7 & C.8.

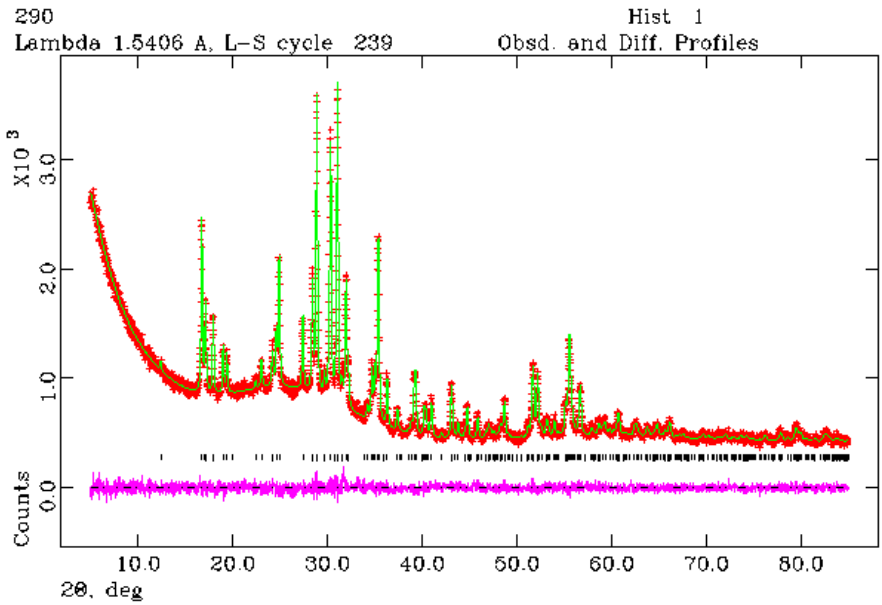

Figure 5-26 Rietveld plot of mechanochemically prepared $NaAlCl_4$ (Sample 56); black tick marks indicate the $NaAlCl_4$ phase. Red crosses indicate experimental data, and green line indicates the calculated pattern. The magenta line indicates the difference plot.

Table 5-7 Crystallographic data from Rietveld refinement for mechanochemically synthesised $NaAlCl_4$, Sample 56, compared with literature data (ICSD-30611).

Chemical Formula	***$NaAlCl_4$***	
Source	**Literature[84]**	**Sample 56**
Crystal System, Z	Orthorh., 4	
Space Group	$P2_1\ 2_1\ 2_1$ (19)	
***a*/Å**	10.36	10.3358(8)
b/ Å	9.92	9.8886(8)
c/ Å	6.21	6.1709(5)
Volume/Å^3	638.21	630.7(1)
Formula Weight/g	765.486	767.136
Calculated density, ρ_X/g·cm^{-3}	2.03	2.020
No of data	-	4846
No of parameters	-	52
R_{wp}	3.9 %	3.79
R_p	2.5 %	2.90
χ^2	-	1.148

The extended structure of mechanochemically synthesised $NaAlCl_4$ is given in Figure 5-27, along with the Na and Al cation bonding orientations and metal-chloride bond lengths.

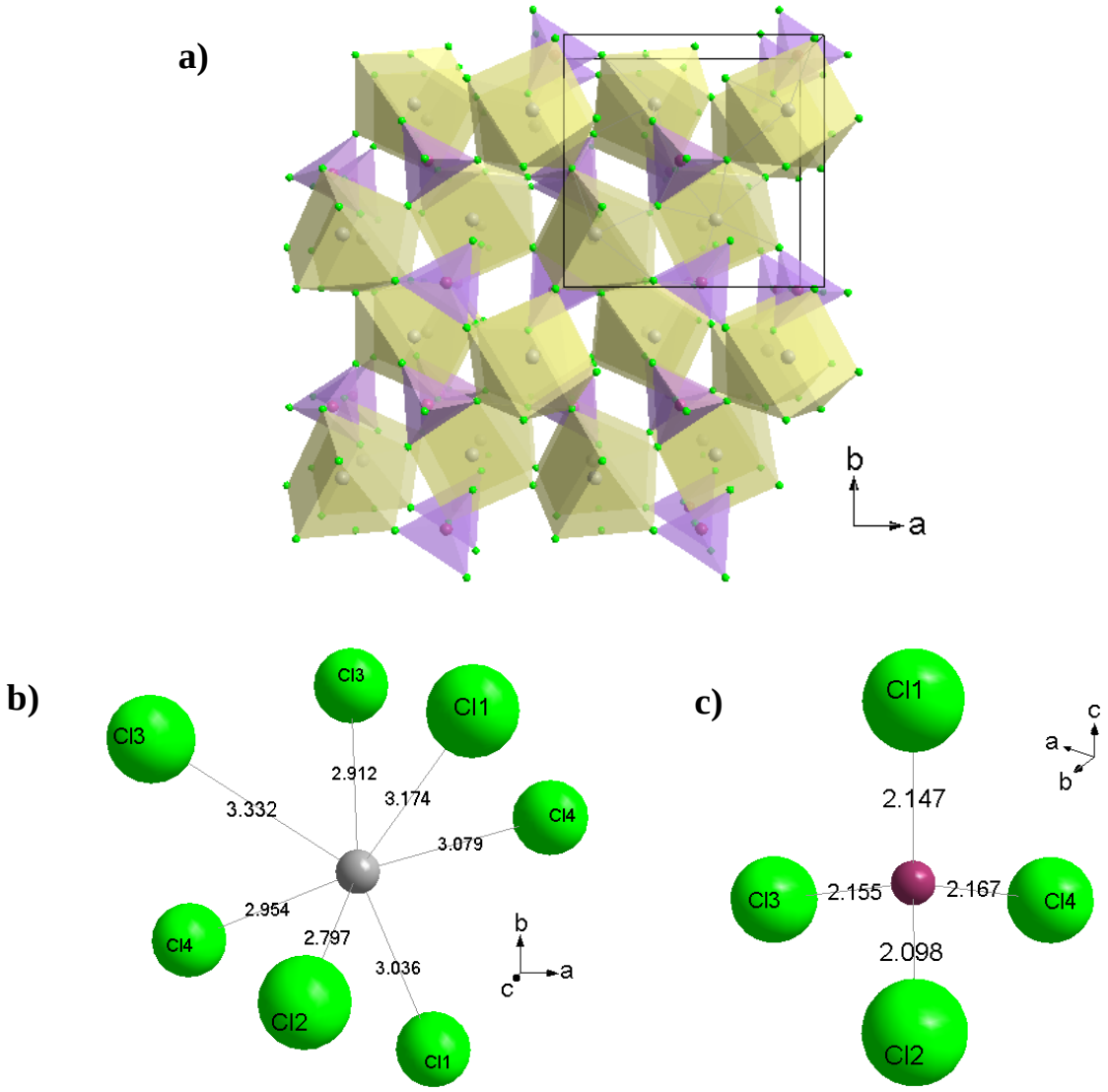

Figure 5-27 a) Extended structure of mechanochemically synthesized $NaAlCl_4$ (Sample 56) and the coordination orientations of Cl anions to the b) seven coordinate Na cations (yellow polyhedra) and c) Al tetrahedra (purple polyhedra). (Al = purple spheres, Na = grey spheres, Cl = green spheres.)

Thermal analysis was conducted for the hand mixed and mechanochemically prepared samples, **55** and **56** (Figure 5-28). A single, sharp endothermic event was recorded for the as-synthesised halide (T_{peak} = 159.3 ºC), and is consistent with the incongruent melting point of $NaAlCl_4$ given in previous studies.[55,85] The endothermic event observed for Sample **55** is less defined and occurs at a temperature lower (121.5 ºC) than that of the melting feature observed for the complex halide product. From information collated by Levin *et al.*, this may be described as the eutectic point for the 1:1 NaCl-$AlCl_3$ system. No mass loss was detected for Samples **55** or **56** from the corresponding MS analysis.

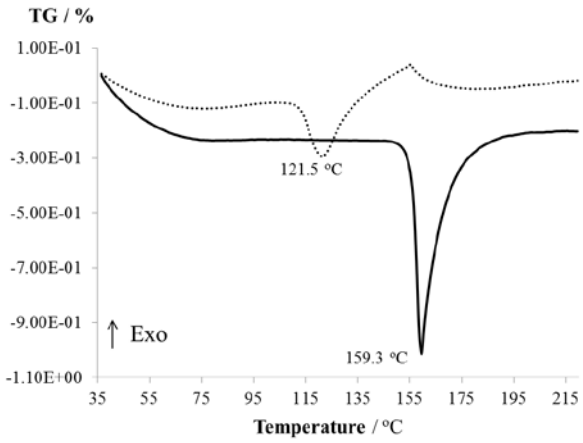

Figure 5-28 DTA profiles of Sample 55 (dashed line) *vs.* Sample 56 (solid line).

5.5.2.2. Mechanochemical Metathesis between Halide Precursor, $NaAlCl_4$, and LiH.

The metathesis reaction was carried out in the same way as previously, employing stoichiometric proportions of the hydrogen donor, LiH (Sample **57**). PXD of the reaction products revealed that a reaction had proceeded since reflections to suggest the presence of the starting materials were not evident. As predicted in the event of a simultaneous metathesis reaction (Equation 5-13 and Equation 5-14), NaCl is present in the products. The PXD pattern also shows that the desired complex hydride, $NaAlH_4$, has formed as a result of the milling procedure.[86] (A small peak at ~48° may be assigned to LiH, but no other reflections for this phase were evident)

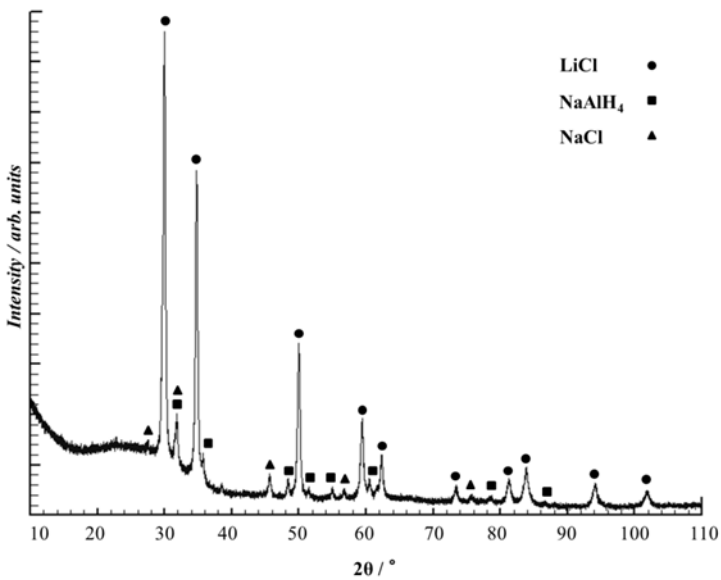

Figure 5-29 PXD pattern or sample collected after metathesis reaction between $NaAlCl_4$ and LiH (Sample 57).

The DTA and MS profiles obtained from STA, however, show a DTA trace and mass loss which closely resemble that of $LiAlH_4$ (Equation 5-14). The early release of hydrogen and corresponding endo- and exothermic features present at 126 ^{o}C and 181.3 ^{o}C, respectively, correspond well with that observed previously in this work. This may be the result of the as-formed $NaAlH_4$ reacting with the LiCl in the post-milled product during the heating experiment or it may be that it was present in the post metathesis product where no reflections were evident, as in the previous work towards $LiAlH_4$ synthesis described earlier. A third event at 218 °C is also evident, and from the change in slope of the TG data and the distinct second peak shown in the MS data (Figure 5-30 c) it is associated with release of hydrogen, although very small (~0.2 wt%). This could be due to decomposition of residual unreacted $NaAlH_4$, which is the product from Equation 5-13.

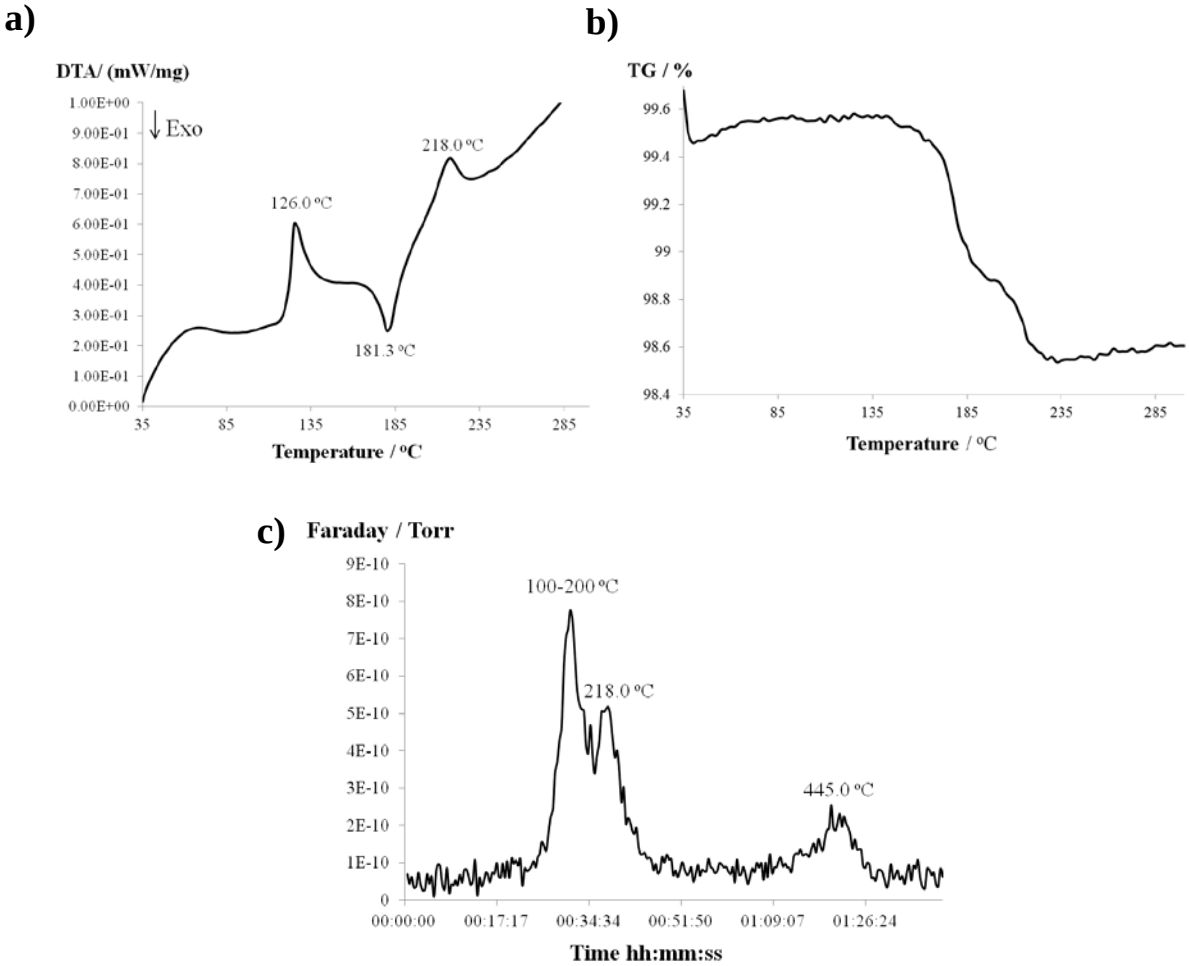

Figure 5-30 STA data for Sample 57; a) DTA, b) TG and c) MS (*m/z* = 2).

The sample retrieved after STA to 300 °C reveals reflections for the binary halides, NaCl and LiCl, and also the reflections expected for LiH/Al (Figure 5-31). Again, the evidence for LiH/Al is consistent with the expected products after the low temperature decomposition of $LiAlH_4$, according to Equation 5-14. The sample retrieved after STA to 500 °C shows the presence of a LiAl alloy, which is expected to be the high temperature

dehydrogenation product of $LiAlH_4$, and would imply that reaction to lithium alanate has either occurred in the mill or during the heating experiment. The presence of LiCl is likely to be as a result of excess LiCl produced in the metathesis reaction (Equation 5-13).

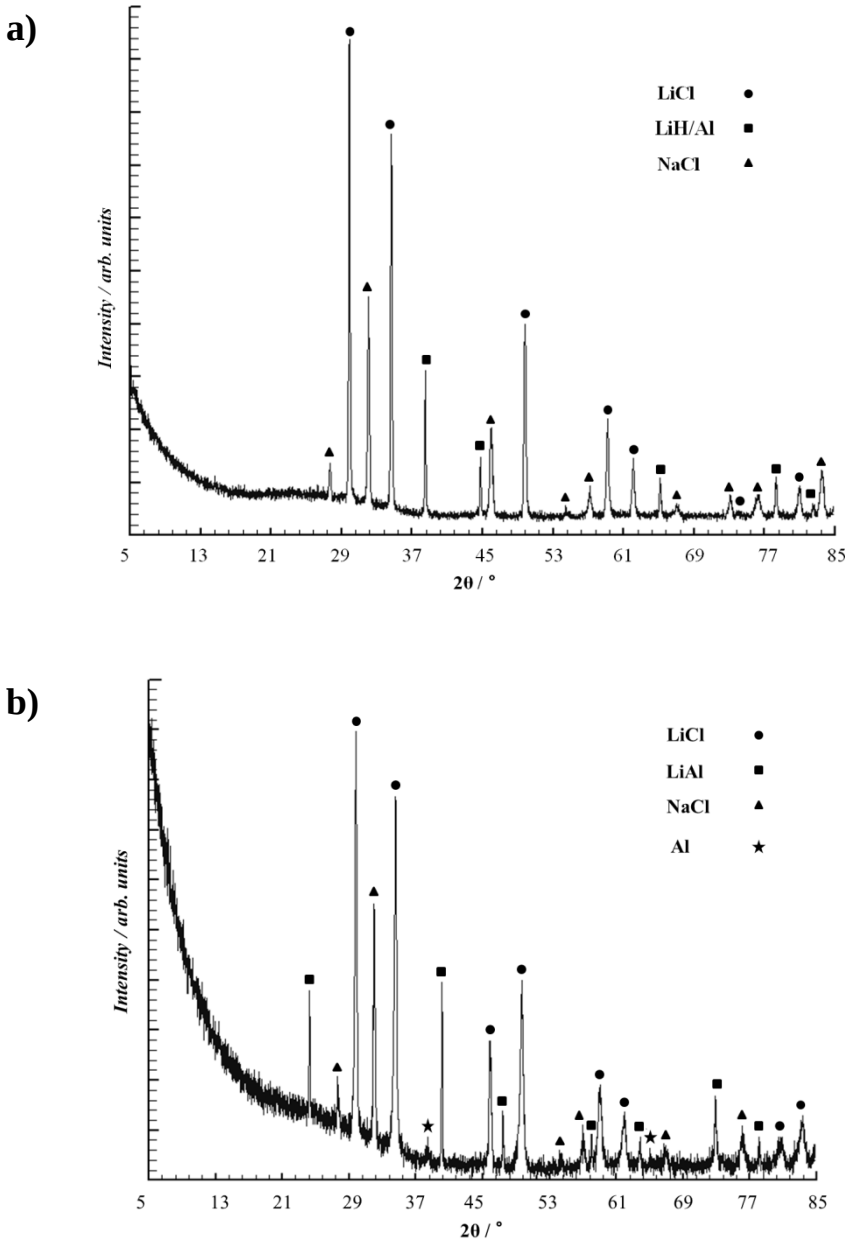

Figure 5-31 PXD patterns of the samples collected post STA for Sample 57 to a) 300 °C and b) 500 °C.

5.5.2.3. Summary

Based on the evidence provided experiment above, it may be suggested that the reaction described above proceeds *via* a pair of metathesis reactions which involve:

1. exchange of H^- and Cl^- anions, *and*
2. exchange of Li^+ and Na^+ cations.

This work suggests that the mobility of all these species can be facilitated by mechanical action alone, but further work is required to establish the full thermodynamic profile of these systems. It may be proposed that both of the metathesis reactions described in Equation 5-13 and Equation 5-14 occur simultaneously within the mill under the conditions employed in this work. The marginally higher thermodynamic favourability (based on $\Delta_f H^o_{solid}$) of NaCl *vs.* LiCl (-411.12 *vs.* -408.27 kJ/mol) suggests that Equation 5-14 will occur rapidly once the products in Equation 5-13 start to form.

On this premise, it may be also be suggested that pair of metathesis reactions for the $NaMgCl_3$ metathesis scenario may proceed based on the similarities observed in the metathesis products and the LiMg alloy obtained after heating (Equation 5-15 and Equation 5-16).

Equation 5-15 $$NaMgCl_3 + 3\ LiH \rightarrow NaMgH_3 + 3\ LiCl$$

Equation 5-16 $$NaMgH_3 + LiCl \rightarrow LiMgH_3 + NaCl$$

Once again, the thermodynamic stability of the NaCl product would appear to be the thermodynamic driver for these reactions to occur simultaneously, where the reaction in Equation 5-16 begins as soon as the reaction products in Equation 5-15 are formed. This process of determining the most thermodynamically stable product to yield a desired product is by no means a new concept, as stated at the start of this chapter, but the approach considered here suggests that there is more exploratory experimental work to be done in the field of mechanochemistry towards developing new materials.

5.5.2.4. Conclusions

This work demonstrates that metal halides are fundamental to developments in solid state hydrogen storage research. The synthesis and understanding of many hydride materials has only been made possible by metathesis reactions between halides and hydrides and this work contributes to the determination of facile routes to ternary halides and hydrides by mechanochemistry. Three halide precursors were synthesised by the mechanochemical method from their respective binary halides; $LiAlCl_4$, $NaMgH_3$ and $NaAlCl_4$. Using the halide precursors, a number of mechanochemical metathesis reactions were studied to examine the possibility of new routes to hydride materials from bespoke halide precursors. Transformation of ternary halide precursors to the corresponding ternary hydride using mechanical action alone involved understanding the thermodynamic drivers for the

reactions involved. The formation of a thermodynamically stable halide by-product was fundamental to the success of these metathesis reactions.

Using mechanochemically prepared $LiAlCl_4$, formation of $LiAlH_4$ *via* the metathesis reaction between NaH and $LiAlCl_4$ was studied. The thermodynamically stable salt by-product, NaCl, was obtained and suggested that the reaction was successful. Based on the thermal profiles obtained for the metathesis product and the diffraction patterns obtained for the samples retrieved after heating, the reaction appears to have formed $LiAlH_4$.

A study on the Perovskite halide, $NaMgCl_3$ was then conducted, and the halide was synthesised by both the thermal and mechanochemical methods, the latter of which has not been successfully conducted prior to this work. Subsequent reactions involving a hydride donor, LiH/NaH, were then conducted, and revealed interesting results. The $NaMgCl_3$-NaH system revealed results to suggest the success of the metathesis reaction, indicating the thermodynamically expected by-product, NaCl, and thermal analysis results consistent with the formation (and decomposition) of $NaMgH_3$. The $NaMgCl_3$-LiH system was then developed, and proposed to proceed *via* two contemporaneous metathesis reactions in which both anion and cation exchange took place. This was the result of the thermodynamic driving forces associated with the halide by-products involved. A further example was then given to confirm that the interchange of anions and cations was possible within one system when two competing metathesis reactions were involved. The results from this work showed that this could potentially provide an alternative solid state route to $LiMgH_3$; a hydride which has significant potential in the field of hydrogen storage owing to its reasonably high hydrogen capacity (8.84 wt%), but which has proven difficult to synthesise.

The challenge that remains for this work is the separation of the desired hydride from the halide by-product. Due to time constraints, this could not be explored further but will be discussed in the Further Work section of this thesis (Chapter 7).

---

[1] IUPAC. Compendium of Chemical Terminology, 2nd ed. (the "Gold Book"). A. D. McNaught and A. Wilkinson. Blackwell Scientific Publications, Oxford (1997). XML on-line corrected version: http://goldbook.iupac.org (2006-) created by M. Nic, J. Jirat, B. Kosata; updates compiled by A. Jenkins. ISBN 0-9678550-9-8. doi:10.1351/goldbook.

[2] "*Nobel Prize in Chemistry 2005*", Y. Chauvin, R. H. Grubbs and R. R. Schrock; http://www.nobelprize.org/nobel_prizes/chemistry/laureates/2005/

[3] J. B. Wiley and R. B. Kraner, *Science*, 1992, **255**, 1093

[4] R. G. Blair and R. B. Kraner, *ChemFiles*, 2005, **5**, Article 13

[5] R. W. Cahn, *Advanced Materials*, 1990, **2**, 314

[6] H. C. Yi and J. J. Moore, *Journal of Materials Science*, 1990, **25**, 1159

[7] R. E. Treece, E. G. Gillan and R. B. Kraner, *Comments on Inorganic Chemistry: A Journal of Critical Discussion of the Current Literature*, 1995, DOI: 10.1080/02603599508035775
[8] I. P. Parkin, *Transition Metal Chemistry*, 2002, **27**, 569
[9] I. P. Parkin, *Chemical Society Reviews*, 1996, **25**, 199
[10] A. M. Nartowski, I. P. Parkin, M. Mackenzie, A. J. Craven and I. MacLeod, *Journal of Materials Chemistry*, 1999, **9**,1275
[11] A. M. Nartowski, I. P. Parkin, M. Mackenzie and A. J. Craven, *Journal of Materials Chemistry*, 2001, **11**, 3116
[12] E. Wiberg and R. Bauer, *Zeitschrift für Naturforschung B*, 1951, **6**, 171
[13] E. C. Ashby and R. D. Schwartz, *Inorganic Chemistry*, 1971, **10(2)**, 355
[14] H. Hagemann and R. Černý, *Dalton Transactions*, 2010, **39**, 6006
[15] L. H. Rude, T. K. Nielsen, D. B. Ravnsbæk, U. Bösenberg, M. B. Ley, B. Ruchter, L. M. Arnbjerg, M. Dornheim, Y. Filinchuk, F. Besenbacher and T. R. Jensen, *Physica Status Solidi A*, 2011, **208(8)**, 1754
[16] K. Koyima, N. Morisaku, Y. Shinzato, K. Ikeda, S. Orimo, Y. Ohki, K. Ttsumi, H. Yukawa and M. Morinaga, *Journal of Alloy and Compounds*, 2007, **446-447**, 237
[17] L. Takacs, *Progress in Materials Science*, 2002, **47**, 355
[18] B. Paik, I. P. Jones, A. Walton, V. Mann, D. Book and I. R. Harris, *Journal of Alloys and Compounds*, 2010, **492**, 515
[19] D. A. Sheppard, M. Paskevicius, and C. E Buckley, *Journal of Alloys and Compounds*, 2010, **492**, L72-L74
[20] M. Paskevicius, D. A. Sheppard and C. E Buckley, *Journal of the American Chemical Society*, 2010, **132**, 5077
[21] Y. Nakamori, H.-W. Li, M. Matsuo, K. Miwa, S. Towata and S. Orimo, *Journal of Physics and Chemistry of Solids*, 2008, **69**, 2292
[22] R. Liu, D. Reed and D. Book, *Journal of Alloys and Compounds*, 2012, **515**, 32
[23] A. Bateni, S. Scherpe, S. Acar and M. Somer, *Energy Procedia*, 2012, **29**, 26
[24] Y. Kim, E.-K. Lee, J.-H. Shim, Y. W. Cho and K. B. Yoon, *Journal of Alloys and Compounds*, 2006, **422**, 283
[25] H. Kabbour, C. C. Ahn, S.-J. Hwang, R. C. Bowman Jr. and J Graetz, *Journal of Alloys and Compounds*, 2007, **446-447**, 264
[26] C. Li, X. Xiao, L. Chen, K. Jiang, S. Li and Q. Wang, *Journal of Alloys and Compounds*, 2011, **509**, 590
[27] A. C. Larson, R. B. von Dreele, *General Structure Analysis System (GSAS)*; Los Alamos National Laboratory Report LAUR: 86-748, Los Alamos, NM, USA, 1995.
[28] B. H. Toby, *Journal of Applied Crystallography*, 2001, 34, 210
[29] *Inorganic Crystallographic Structure Database (ICSD)*; http://cds.rsc.org/, accessed 14/05/2014
[30] W. Weppner and D. A. Huggins, *Physics Letters A*, 1976, **58(4)**, 245
[31] W. Weppner and D. A. Huggins, *Solid State Ionics*, 1980, **1**, 3
[32] G. T.-K. Fey, *Journal of Power Sources*, 1991, **35**, 153
[33] R. Hartl, R. Neueder and H. J. Gores, *Acta Chimica Slovenica*, 2009, **56**, 109
[34] "*Advanced Batteries: Materials Science Aspects*", R. A. Huggins, 2009, Springer e-ISBN:978-0-387-76424-5
[35] W. Weppner and D. A. Huggins, *Journal of the Electrochemical Society*, 1977, **124**, 35
[36] W. K. Behl, J. A. Christopulos, M. Ramirez and S. Gilman, *Journal of the Electrochemical Society*, 1973, **120(12)**, 1619
[37] G. T.-K. Fey, W.-K. Liu and Y.-C. Chang, *Journal of Power Sources*, 2001, **97-98**, 602
[38] L. Zinck, M. Borck, C. Ripp and G. Hambitzer, *Journal of Applied Electrochemistry*, 2006, **36**, 1291
[39] R. Hartl, R. Neueder and H. J. Gores, *Acta Chimica Slovenica*, 2009, **56**, 109
[40] R. Hartl, M. Fleischmann, R. M. Gschwind, M. Winter and H. J. Gores, *Energies*, 2013, **6**, 4448
[41] Y. Bedfer, J. Corset, M. C. Dhamekubcourtm F. Wallart and P. Barbier, *Journal of Power Sources*, 1983, **9**, 267
[42] M. C. Dhamekubcourtm F. Wallart and P. Barbier, C. Mairesse and P. Descroix, *Journal of Power Sources*, 1985, **14**, 77
[43] A. I. Morozov, V. G. Kuznetsov and S. I. Moksimova, *Russian Journal of Inorganic Chemistry*, 1971, **16**, 1773
[44] S. Anderson, 'Method of preparing purified lithium aluminium chloride', US 3761578, 1973
[45] A. E. Finholt, A. C. Bond and H. I. Schlesinger, *Journal of the American Chemical Society*, 1947, **69**, 1199
[46] *National Institute of Standards and Technology*; http://webbook.nist.gov/; accessed 07/05/2014
[47] "*Perry's Chemical Engineers Handbook*", D. W. Green and R. H. Perry, 8th Edition, 2008, McGraw-Hill
[48] S. V. Chelyukanova, T. D. Nanina, N. K. Efimov and A. V. Konov, *Koordinatsionnay Khimiya*, 1992, **18(5)**, 549
[49] Y. Kojima, Y. Kawai, T. Haga, M. Matsumoto and A. Koiwai, *Journal of Alloys and Compounds*, 2007, **441**, 189

[50] X. Liu, H. W. Langmi, S. D. Beattie, F. F. Azenwi, G. S. McGrady and C. M. Jensen, *Journal of the American Chemical Society*, 2011, **133**, 15593
[51] X. Liu, G. S. McGrady, H. W. Langmi and C. M. Jensen, *Journal of the American Chemical Society*, 2009, 131, 5032
[52] C. W. Bale, E. Bélisle, P. Chartrand, S. A. Decterov, G. Eriksson, K. Hack, I. H. Jung, Y. B. Kang, J. Melançon, A. D. Pelton, C. Robelin and S. Petersen, *FactSage Thermochemical Software and Databases - Recent Developments*, Calphad, vol. 33, pp 295-311, 2009 <www.factsage.com>
[53] G. Mairesse, P. Barbier and J.-P. Wignacourt, *Acta Crystallographica B*, 1979, **35**, 1573
[54] E. Perenthaler, H. Schulz and A. Rabenao, *Zeitschrift für Anorganische und allgemeine Chemie*, 1982, **491**, 259
[55] J. Kendall, E. D. Crittenden and H. K. Miller, *Journal of the American Chemical Society*, 1923, **45**, 963
[56] "*Renewable Hydrogen Technologies*", R. A. Varin, Z. S. Wronski, Elsevier, 2013, Chapter 13 pp. 293-332
[57] H. W. Brinks, B. C. Hauback, P. Norby and H. Fjellvåg, *Journal of Alloys and Compounds*, 2003, **531**, 222
[58] R. A. Varin and R. Parviz, *International Journal of Hydrogen Energy*, 2012, **37**, 9088
[59] A. J. Maeland and W. D. Lahar, *Zeitschrift für Physikalische Chemie*, 1993, **179**, 181
[60] K. Yvon, *Journal of the Less-Common Metals*, 1984, **103**, 53
[61] S. S. S. Raman, D. J. Davidson, J.-L. Bobet and O. N. Srivastava, *Journal of Alloys and Compounds*, 2002, **333**, 282
[62] R. H. Pawelke, M. Flederhoff, C. Weidenthaler, B. Bogdanovíc and F. Schüth, *Zeitschrift für anorganische allgemeine Chemie*, 2009, **635**, 265
[63] W. Klemm and P. Weiss, *Zeitschrift für anorganische und allgemeine Chemie*, 1940, **245**, 279
[64] W. Klemm,K. Beyersdorfer and J. Oryschkewitsch, *Zeitschrift für anorganische und allgemeine Chemie*, 1948, **256**, 25
[65] K. Grjothem, J. L. Holm and M. Røtnes, *Acta Chemica Scandinavica*, 1972, **26**, 3802
[66] R. Kanno, Y. Takeda, K. Murata and O. Yamamoto, *Solid State Ionics*, 1990, **39**, 233
[67] B. K. Reddy, K. Somiah and V. H. Babu, *Journal of Materials Science Letters*, 1987, **6**, 847
[68] H. F. McMurdie, J. de Groot, M. Morris and H. E. Swanson, *Journal of Research of the National Bureau of Standards – A. Physics and Chemistry*, 1969, **73A**, 621
[69] C. J. J. van Loon and D. J. W. Ijdo, *Acta Crystallographica*, 1975, **B31**, 770
[70] A. Bouamrane, C. de Brauer, J.-P. Soulié, J. M. Létoffeé and J. P. Bastide, *Thermochimica Acta*, 1999, **326**, 37
[71] I. Solinas and H. D. Lutz, *Journal of Solid State Chemistry*, 1995, **117**, 34
[72] P. Villars, K. Cenzual, J. Daams, R. Gladyshevskii, O. Scherban, V. Dubenskyy, N. Melnichenki-Koblyuk, O. Pavlyuk, I. Savysyuk S. Stoyko and L. Sysa, *Landolt-Brnstein – Group III Condensed Matter*, 2007, **43A5**, 655
[73] D. W. Levinson, *Acta Metallurgica*, 1955, **3**, 294
[74] E. C. Ashby and A. B. Goel, *Inorganic Chemistry*, 1978, **17**, 322
[75] A. Fischer, H. Köstler and L. Schlapbach, *Journal of the Less-Common Metals*, 1991, **172-174**, 808
[76] B. Pfrommer, C. Elsässer and M. Fähnle, *Physical Reviews B*, 1994, **50**, 5089
[77] P. Vajeeston, p. Ravindran, A. Kjekshus and H. Fjellvåg, *Journal of Alloys and Compounds*, 2008, **450**, 327
[78] D. Li, T. Zhang, S. Yang, Z. Tao and J. Chen, *Journal of Alloys and Compounds*, 2011, **509**, 8228
[79] Y. Li, B. K. Rao, T. McMullen, P. Jena and P. K. Khowash, *Physical Reviews B*, 1991, **44**, 6030
[80] P. Claudy, J.-M. Letoffe, G. Chahine and B. Bennetot, *Thermochimica Acta*, 1984, **78**, 323
[81] "*Process for the preparation of lithium aluminium hydride*", T. L. Rathman, J. A. Schindeman, E. J. Granger and S. B. Smith, US 5730952, 1998
[82] "*Hydrogen Storage Technology: Materials and Applications*", 2013, CRC Press, L. Klebanoff, p 138
[83] L. J. Rogers, *Journal of Chemical Thermodynamics*, 1980, **12**,51
[84] N. C. Baenziger, *Acta Crystallographica*, 1951, **4**, 216
[85] E. Levin, J. F. Kinney, R. D. Wells and J. T. Benedict, *Journal of Research of the National Bureau of Standards – A. Physics and Chemistry*, 1974, **78a**, 505
[86] J. W. Lauher, D. Dougherty and P. J. Herley, *Acta Crystallographica*, 1979, **B35**, 1454

6. Conclusions

In this work, mechanochemistry has been employed as a simple, solid-state, solvent free method to modify and synthesise metal hydrides for hydrogen storage. Magnesium may be seen as the building block for the materials synthesised herein and modification or synthesis of Mg based compounds provides the theme for this work.

It is evident from Chapter 3 that mechanical milling of MgH_2 is a simple way of reducing the hydrogen desorption temperature of MgH_2 and that non-oxide catalysts provide a route to MgH_2 which more closely meets the thermodynamic demands of a real system. However, further work is necessary to fully establish the interactions between the hydride and additives employed in this work under both mild and harsh milling conditions.

Modification of MgH_2 by the inclusion of other alkali or alkaline earth metal cations was explored in Chapter 4, where ternary hydrides were successfully synthesised by mechanical alloying of binary hydrides. The simplicity of this method was highlighted in the preliminary $NaMgH_3$ work. Then, by using a number of different binary hydride stoichiometries, a series of $(Ca_{1-x}Mg_xH_2)_n$-type hydrides were discovered and characterised, which demonstrated that the mechanochemical synthesis of ternary hydrides in this system was tuneable.

The final chapter, Chapter 5, is exploratory in nature. It reveals that selection of suitable ternary or complex halide precursors can provide new routes to hydrides *via* thermodynamically feasible metathesis routes. Using mechanical activation, rather than direct heating to propagate the metathesis reaction, these routes enable formation of hydrides with low temperature hydrogen release properties, which is likely to be the result of the formation of nanocrystallites of the hydride by the SSM route, but further verification that this is indeed the case is required. This is likely to involve the careful separation of the hydride product from the halide by-product using an appropriate anhydrous solvent, such as THF.

7. Further Work

To identify the kinetics and cyclability of the MgH_2-*x* wt% SiC:graphite system, pressure-composition isotherms are necessary. XPS may also assist in identifying the interactions at the interface between the SiC:graphite catalyst system and MgH_2. To determine whether the two-step hydrogen release anomaly is indeed a combined polytype-particle size effect, the doped hydrides will be considered in an up-coming SANS (small angle neutron scattering) experiment, to be conducted on the NIMROD beamline at the ISIS research centre (STFC (Science and Technology Facilities Council) Rutherford Appleton Laboratory). (See accepted proposal attached in Appendix D.)

The hypothesis that the high dispersion of graphite in smaller hydride particles is the reason for enhanced hydrogen desorption from MgH_2 would require further corroboration. This is likely to require hydrogen cycling experiments, *e.g.*, analysis by PCT (Pressure-Composition-Temperature) or IGA (Intelligent Gravimetric Analyser). Results from this advanced thermal analyses would provide developed information on the kinetic behaviour of the SiC:graphite doped hydride, and establish the hysteresis effects observed upon cycling *via* compilation of Van't Hoff plots. In addition, the effect on equilibrium pressure relative to dopant loading would also be obtained, and would provide a thorough knowledge of the sorption characteristics of these composites relative to other doped MgH_2 systems. This thermodynamic and kinetic data would ultimately determine whether the composite materials produced in this work would be a significant contender for commercial use. In addition, *in-situ* SANS investigations of the particles prepared at mild milling conditions may yield interesting results to indicate the structure and dispersion of the graphite involved at the Mg-graphite layer interface. The surface chemistry of the composites could be further probed using XPS, TEM and SAED (Selected Area Electron Diffraction) techniques. Furthermore, these would also help to establish whether the dispersion of the additive throughout the sample remains consistent upon cycling experiments, and thus establish whether agglomeration (and size increase) of Mg/MgH_2 particles after cycling was prevented by inclusion of this additive composite.

The hydrogen positions of the $(Ca_{1-x}Mg_xH_2)_n$-type hydride series could not be accurately determined from lab or synchrotron diffraction, therefore neutron beamtime on the POLARIS powder diffraction beamline at ISIS has been sought, including *in-situ* measurements to verify the decomposition process. The proposed neutron experiment has

been accepted and will be conducted in due course. (See accepted proposal attached in Appendix E.)

Investigation of the potentially promising route to $LiMgH_3$ *via* mechanochemical metathesis should be investigated further. Analysis will likely require the removal of the halide by-product matrix, which will require careful consideration of the moisture sensitivity of the hydride and solubility of the halide by-product. Neutron diffraction would be useful for determining the Li and H atomic positions and coordination of the metals in $LiMgH_3$, where experiments could be conducted on the as-prepared metathesis product, and also with the isolated hydride alone if successfully separated without decomposition or modification.

Appendix A.

A.1. Data derived from STA analysis for commercial MgH2.

	DTA		TG	
Heating Rate / °C/min	**T_{onset} / °C**	**T_{peak} / °C**	**Mass Loss T_{onset} / °C**	**Mass Loss / wt%**
2	392.8	403.2	395.5	7.07
5	410.7	424.5	414.3	7.05
10	424.5	442.7	429.2	7.01
20	439.5	464.3	449.4	6.79

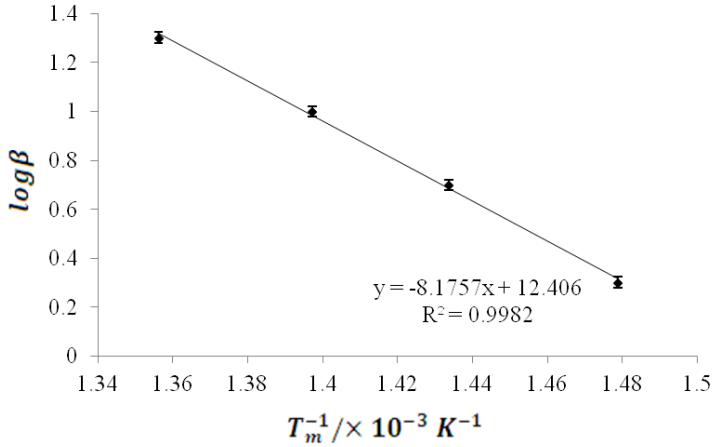

A.2. Ozawa plot of commercial MgH_2.

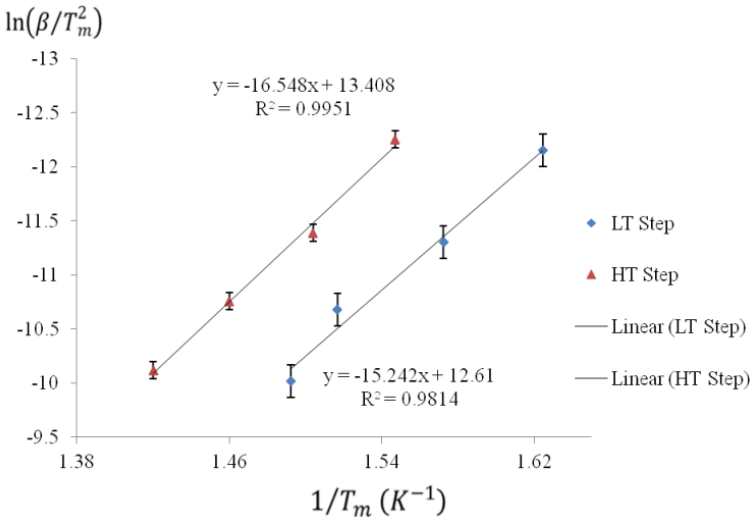

A.3. Kissinger plots for Sample 2.

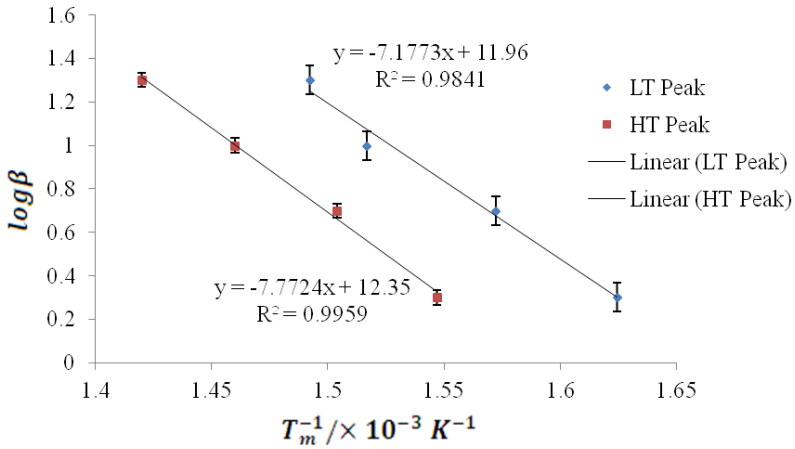

A.4. Ozawa plots Sample 2.

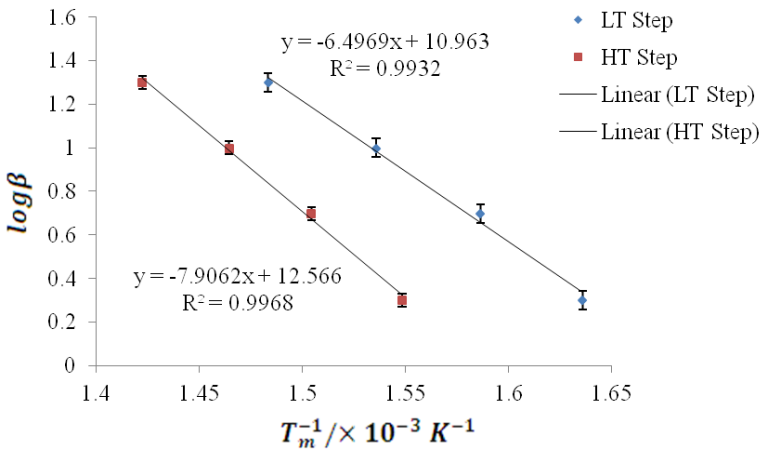

A.5. Ozawa plots for Sample 3.

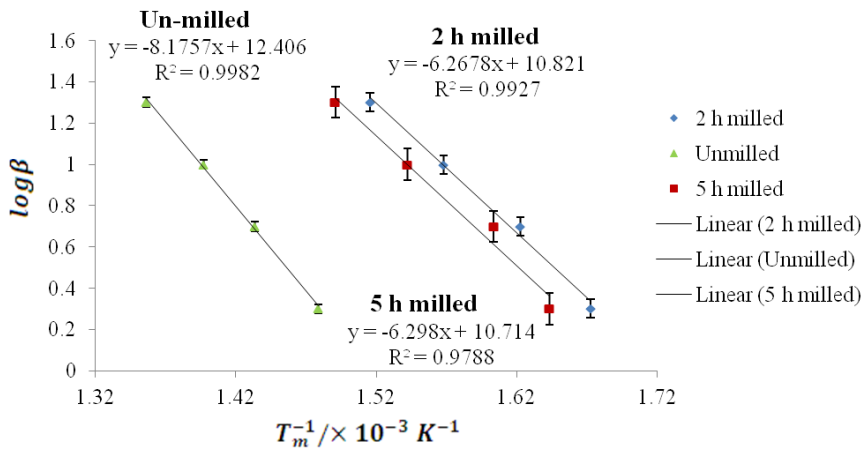

A.6. Ozawa plot overlay comparing commercial un-milled MgH_2 with Samples 11 and 12.

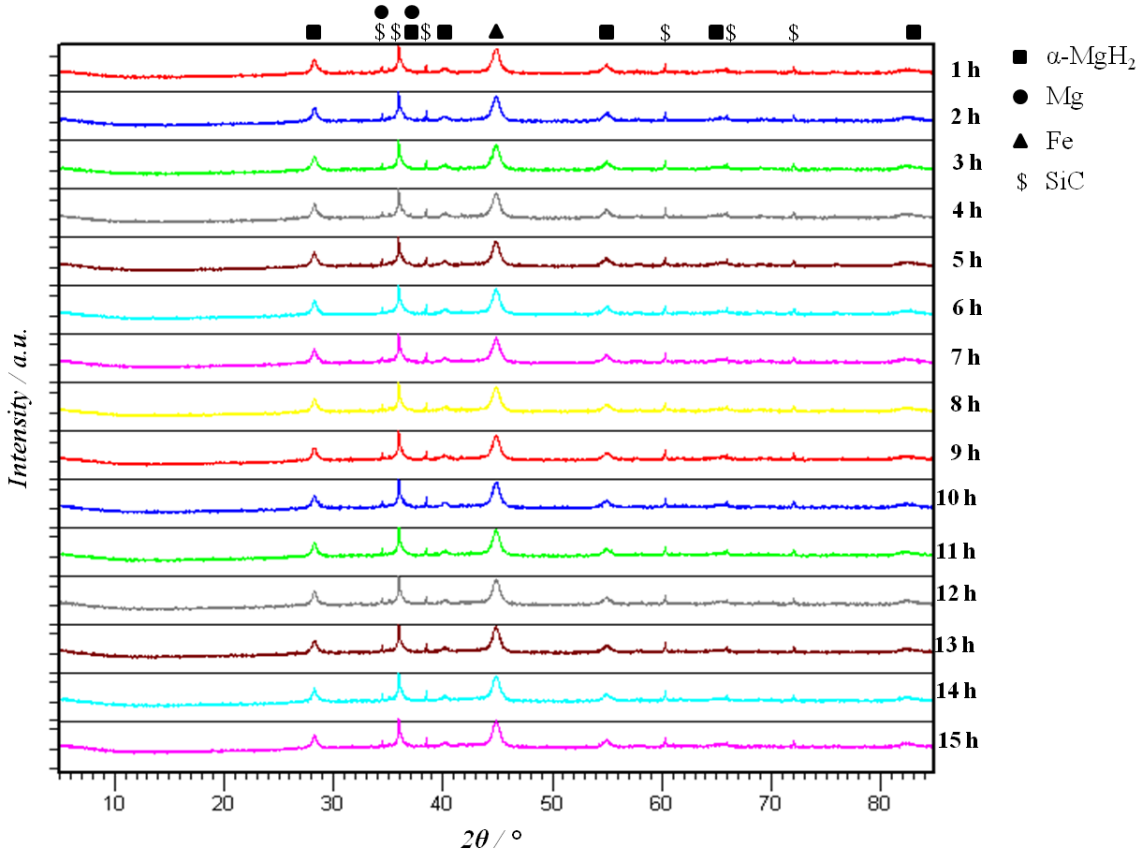

A.7. Time resolved PXD of MgH_2-20wt%SiC-graphite (Sample 30).

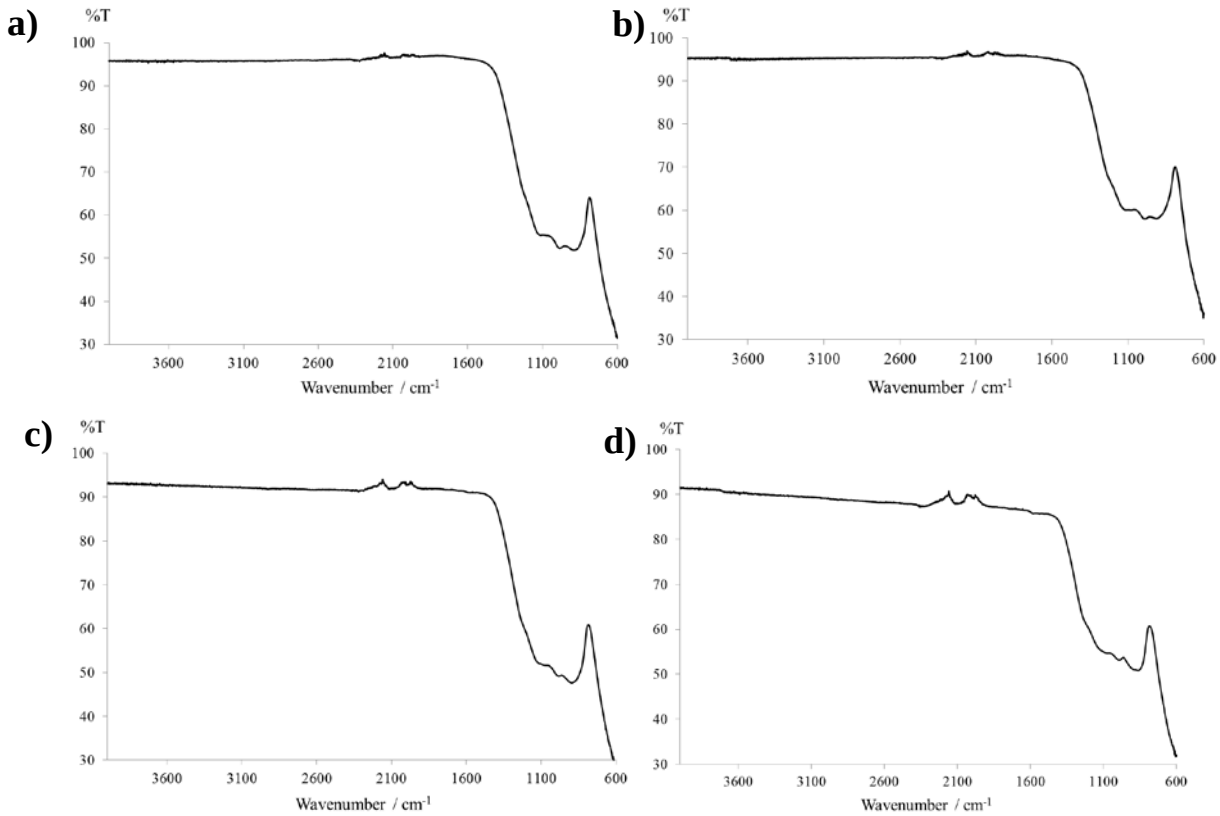

A.8. FTIR spectra of SiC-graphite doped MgH_2, a-d) Samples 29-32, respectively.

a)

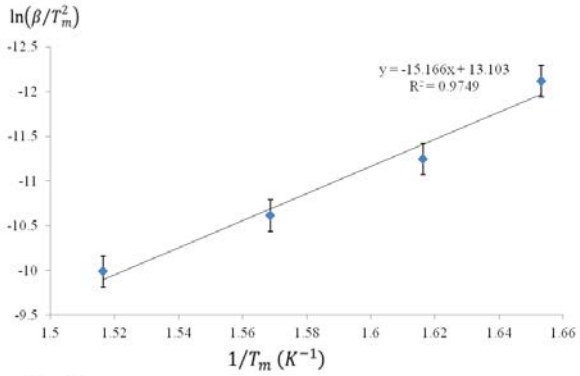

b)

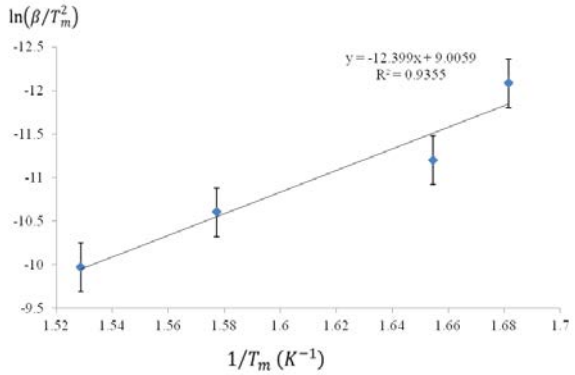

c)

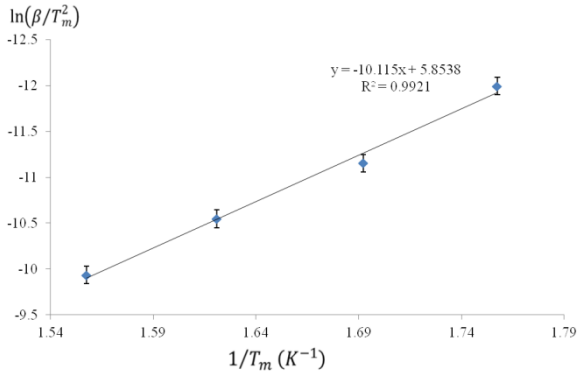

d)

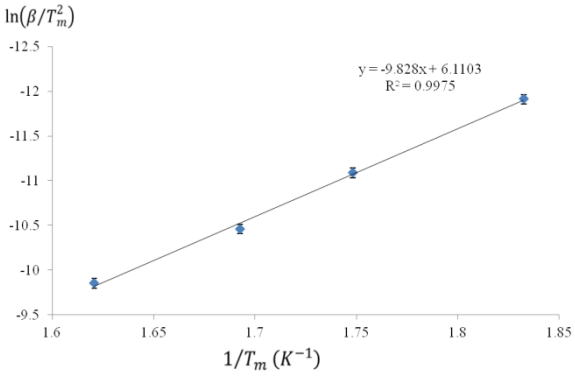

A.9. Kissinger plots of a-d) Samples 29-32, respectively, showing error bars.

a)

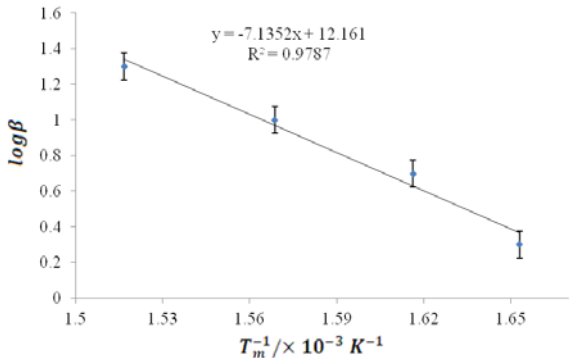

b)

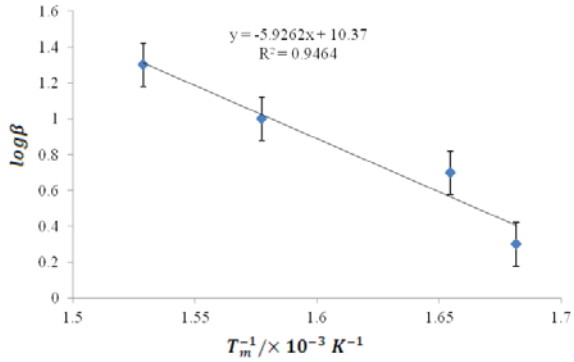

c)

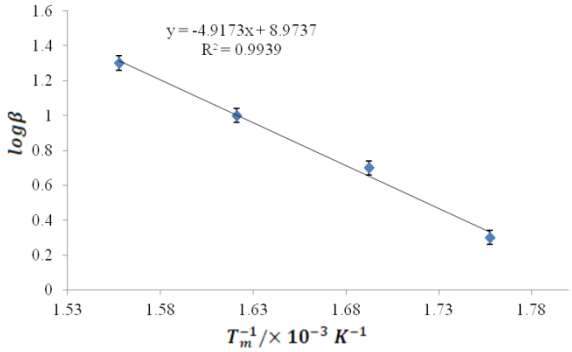

d)

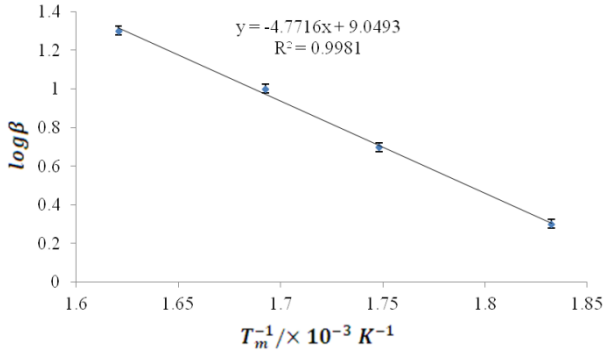

A.10. Ozawa plots of a-d) Samples 29-32, respectively, showing error bars.

Appendix B.

a)

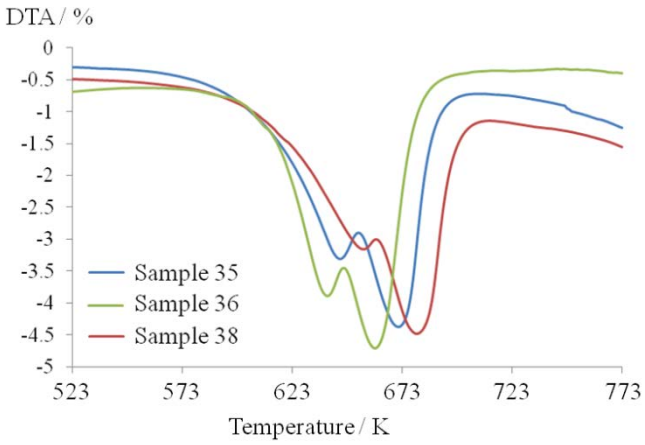

b)

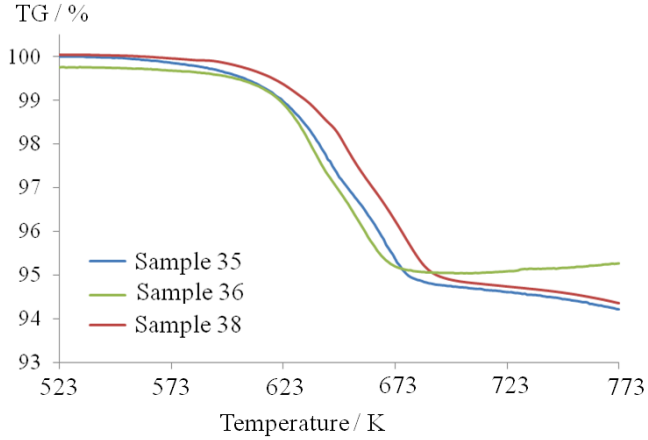

B.1. **The a) DTA and b) TGA profiles of $NaMgH_3$ samples prepared by milling for 5h under a low b:p ratio (Sample 35), intermediate b:p (Sample 36) and high b:p (Sample 38).**

B.2. **Table of DTA-TG data collected for $NaMgH_3$ prepared under various b:p ratios.**

Sample	35	36	38
T_{peak1} (K)	644.7	639.0	655.3
T_{peak2} (K)	671.3	660.5	679.6
Total Mass Loss (wt%)	5.36	4.71	5.20

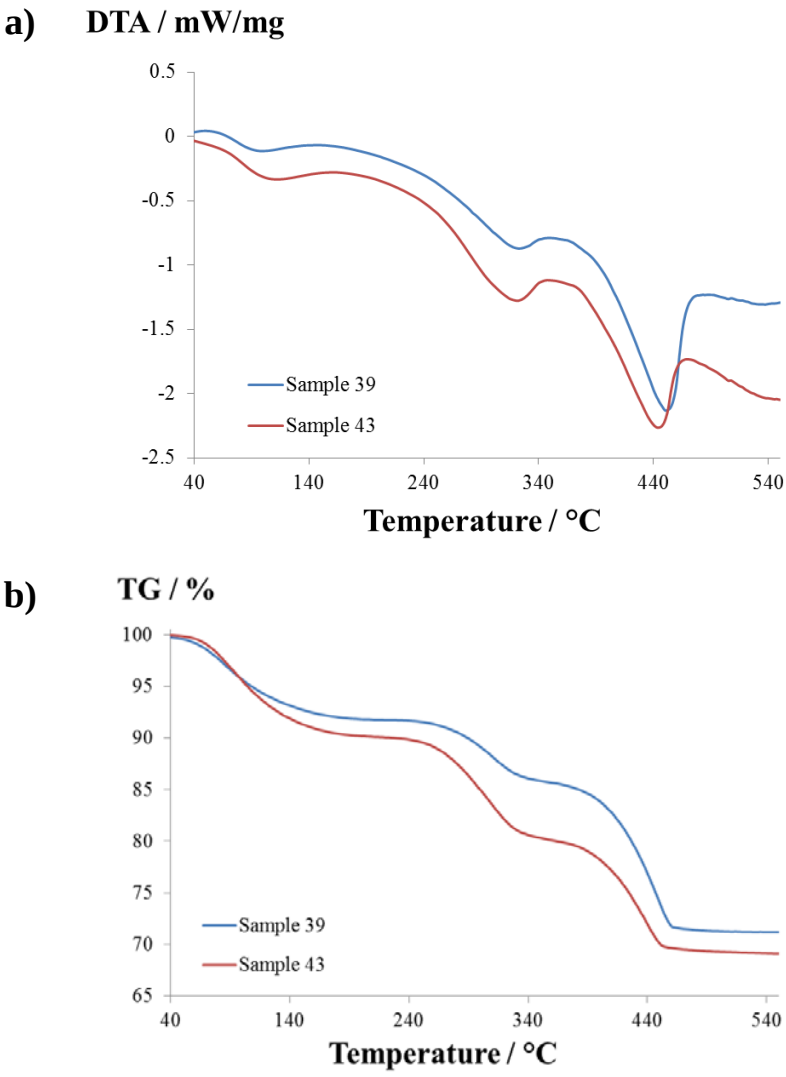

B.3. DTA-TG data for Sample 39 and 43 after air exposure.

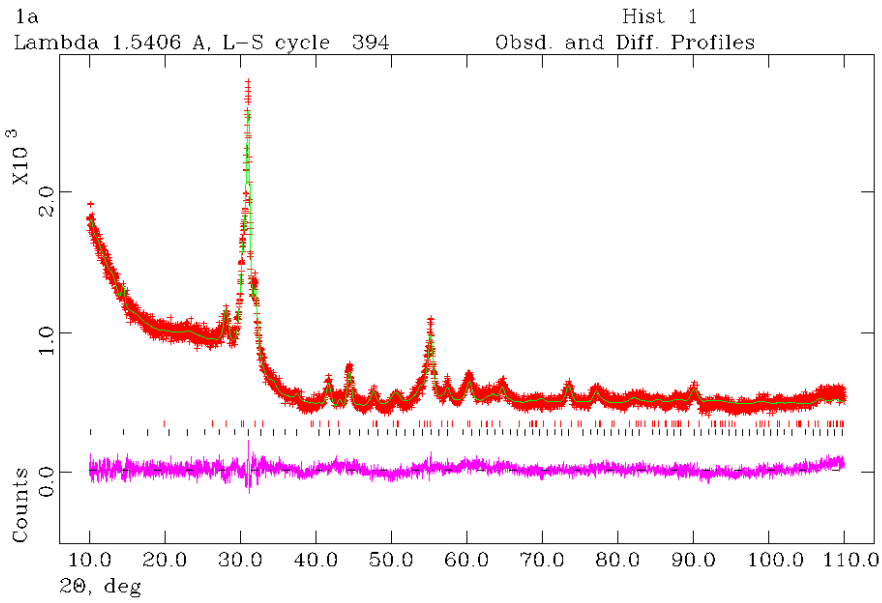

B.4. **Rietveld plot for Sample 39 showing the ternary phase (black tick marks) and CaH_2 (red tick marks). Red crosses indicate observed data, the green line shows the calculated pattern and the magenta line indicates the difference plot.**

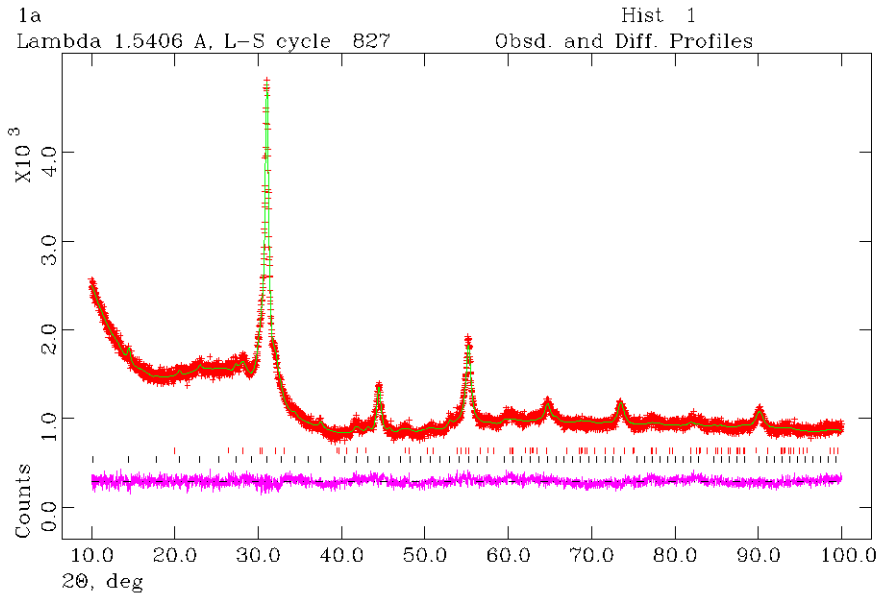

B.5. **Rietveld plot for Sample 40 showing the ternary phase (black tick marks) and CaH_2 (red tick marks). Red crosses indicate observed data, the green line shows the calculated pattern and the magenta line indicates the difference plot.**

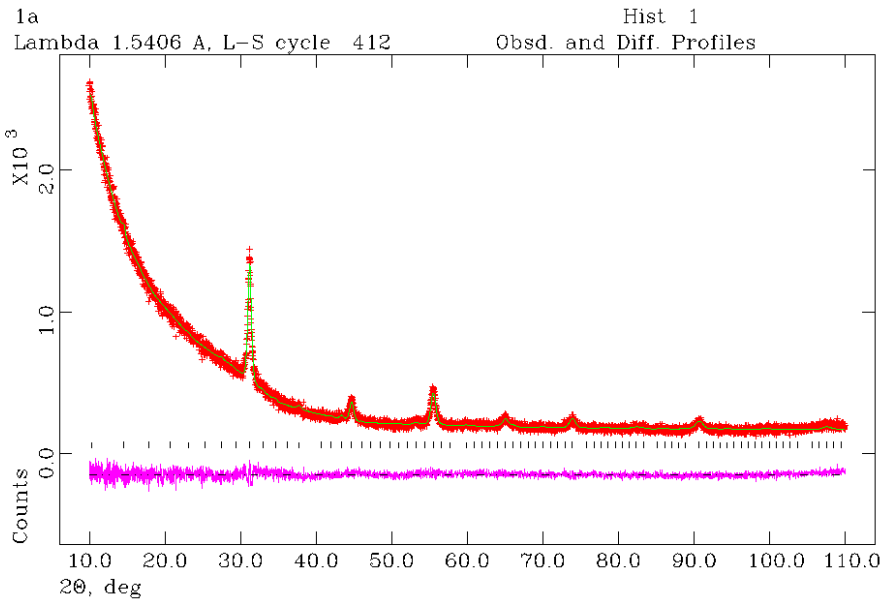

B.6. **Rietveld plot for Sample 41 showing the ternary phase only (black tick marks). Red crosses indicate observed data, the green line shows the calculated pattern and the magenta line indicates the difference plot.**

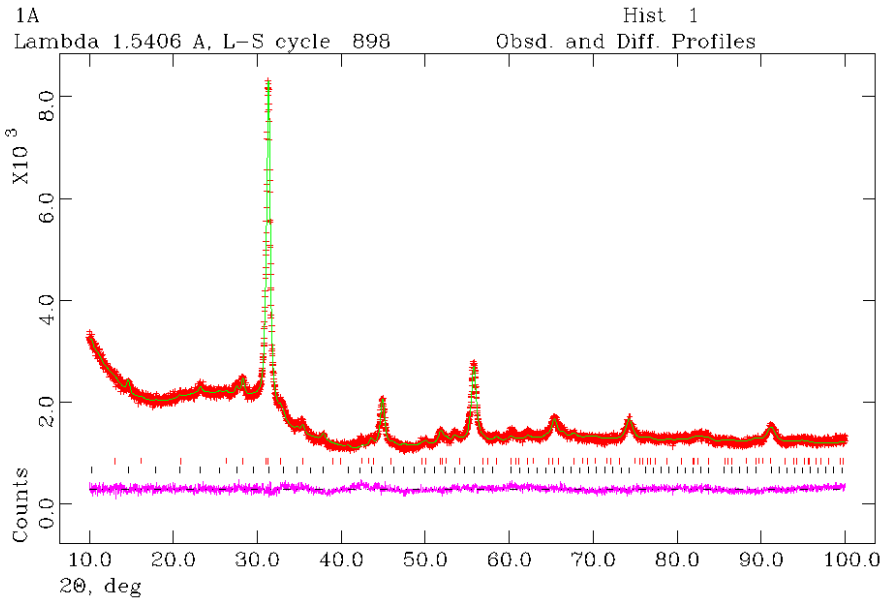

B.7. **Rietveld plot for Sample 42 showing the ternary phase (black tick marks) and $Ca_4Mg_3H_{14}$ (red tick marks). Red crosses indicate observed data, the green line shows the calculated pattern and the magenta line indicates the difference plot.**

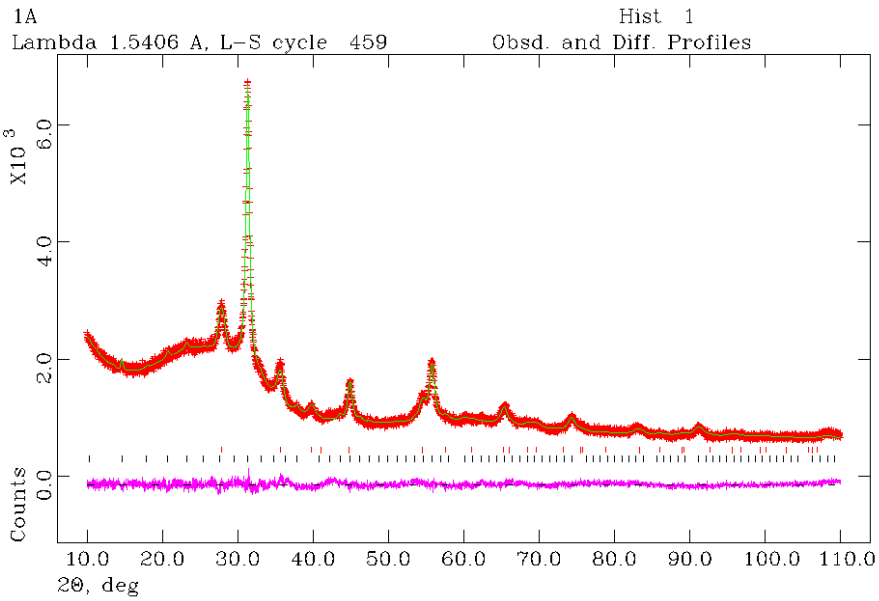

B.8. **Rietveld plot for Sample 43 showing the ternary phase (black tick marks) and MgH_2 (red tick marks). Red crosses indicate observed data, the green line shows the calculated pattern and the magenta line indicates the difference plot.**

B.9. **Table of lab PXD refinement data for additional phases.**

Sample / *CaH_2:MgH_2*	**39 / *2.375:1***	**40 / *2:1***	**42 / *1:1***	**43 / *1:2***
Chemical Formula	CaH_2	CaH_2	$Ca_4Mg_3H_{14}$	MgH_2
Crystal System / Space Group	Orthorh. / *Pnma* (62)		Hexagonal / $P\bar{6}2m$ (189)	Tetragonal / *P4/mnm* (136)
Z	4		1	2
***a* / Å**	4.917(2)	5.904(7)	6.307(2)	4.5185(8)
***b* / Å**	3.5912(8)	3.582(2)	-	-
***c* / Å**	6.750(2)	6.751(8)	6.777(4)	3.0289(7)
***V* / Å^3**	143.42(6)	142.8(1)	233.4(1)	61.84(2)
Formula Weight / g	168.384	168.384	247.347	52.64
Calculated Density, ρ_x / g cm^{-3}	1.950	1.958	1.760	1.414
Phase Fractions	52.8(4) %	40.7(8) %	17.2(8) %	30.1(6) %

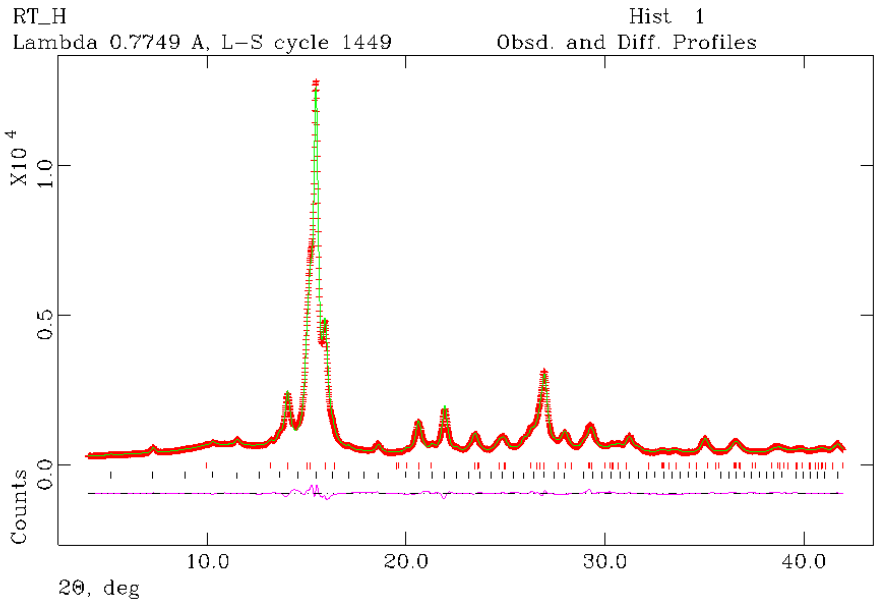

B.10. **Rietveld plot for Sample 39 showing the ternary phase (black tick marks) and CaH_2 (46.9(2) %, red tick marks). Red crosses indicate observed data, the green line shows the calculated pattern and the magenta line indicates the difference plot.**

B.11. **Atomic parameters for $Ca_{21.4(3)}Mg_{5.6(3)}H_{54}$ (Sample 39)**

Atom	Site	*x*	*Y*	*Z*	$100xU_{iso}$ / Å^2	SOF
Ca1	24*g*	0	0.3151(2)	0.3438(2)	2.73(6)	1
Ca2	12*d*	0.3364(4)	0	0	2.73(6)	1
Ca3	2*a*	0	0	0	2.73(6)	1
Ca*	16*f*	0.1588(4)	0.1588(4)	0.1588(4)	10.7(3)	0.30(2)
Mg1	16 *f*	0.1588(4)	0.1588(4)	0.1588(4)	10.7(3)	0.70(2)

N.B. H atoms were fixed to values given in literature for $Ca_{19}Mg_8H_{54}$.

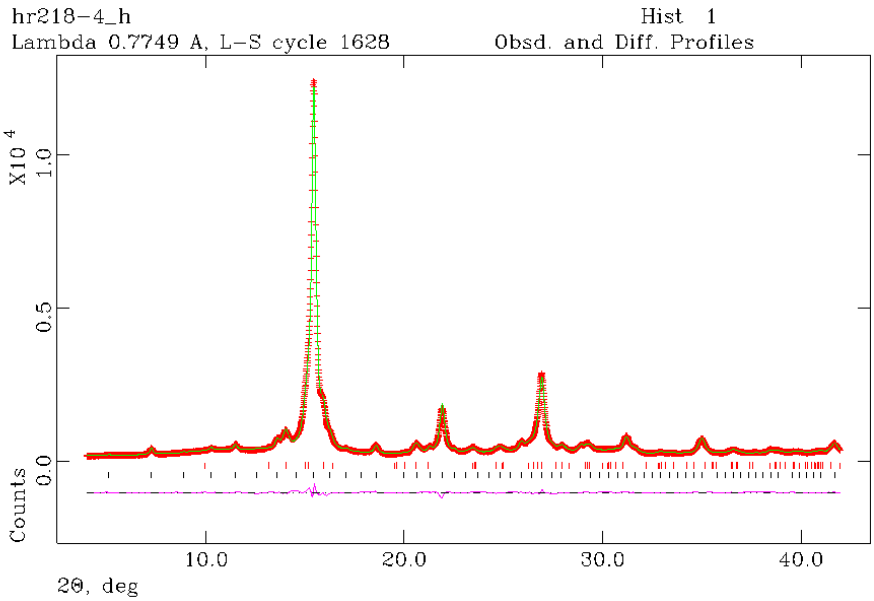

B.12. **Rietveld plot for Sample 40 showing the ternary phase (black tick marks) and CaH_2 (21.0(1) %, red tick marks). Red crosses indicate observed data, the green line shows the calculated pattern and the magenta line indicates the difference plot.**

B.13. **Atomic parameters for $Ca_{21.6(1)}Mg_{5.1(1)}H_{54}$ (Sample 40)**

Atom	Site	*x*	*y*	*Z*	$100xU_{iso}$ / Å^2	SOF
Ca1	24*g*	0	0.3161(1)	0.3429(1)	2.13(4)	1
Ca2	12*d*	0.3380(2)	0	0	1.69(4)	1
Ca3	2*a*	0	0	0	7.58(4)	1
Ca*	16*f*	0.1609(2)	*x*	*X*	10.9(2)	0.320(9)
Mg1	16 *f*	0.1609(2)	*x*	*X*	10.9(2)	0.680(1)

N.B. H atoms were fixed to values given in literature for $Ca_{19}Mg_8H_{54}$.

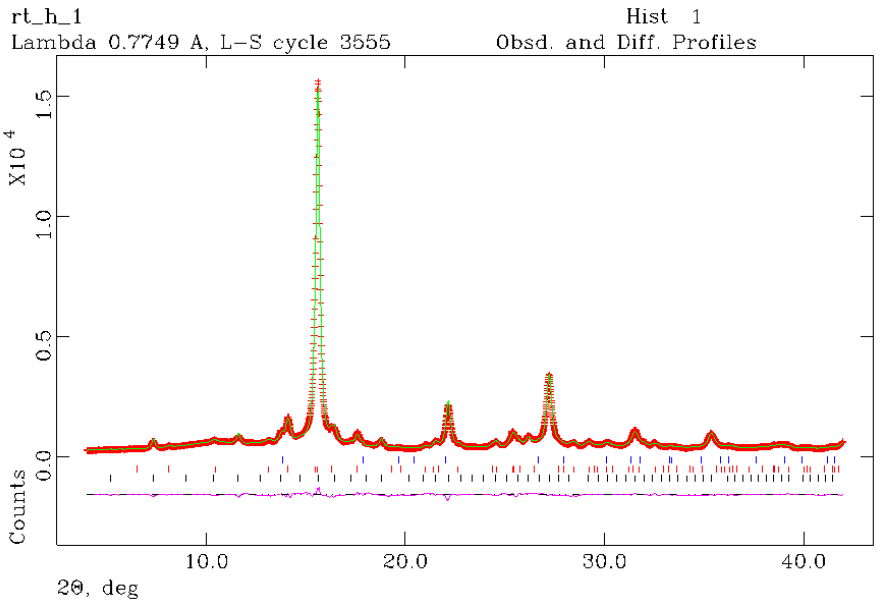

B.14. **Rietveld plot for Sample 42 showing the cubic ternary phase $Ca_{15.2(2)}Mg_{11.8(2)}H_{54}$, $Ca_4Mg_3H_{14}$, and MgH_2 (black, red and blue tick marks, respectively). Red crosses indicate observed data, the green line shows the calculated pattern and the magenta line indicates the difference plot.**

B.15. **Atomic parameters for $Ca_{15.2(2)}Mg_{11.8(2)}H_{54}$ (Sample 42)**

Atom	Site	*x*	*Y*	*Z*	$100xU_{iso}$ / Å^2	SOF
Ca1	24*g*	0	0.3123(2)	0.3455(3)	3.17(3)	0.68(2)
Ca2	12*d*	0.3353(4)	0	0	1.9(1)	1
Ca3	2*a*	0	0	0	3.99(4)	1
Mg1	16*f*	0.1624(4)	*x*	*X*	3.6(2)	1
Mg*	24*g*	0	0.3123(2)	0.3455(3)	3.17(3)	0.32(2)

N.B. H atoms fixed to values given in literature for $Ca_{19}Mg_8H_{54}$.

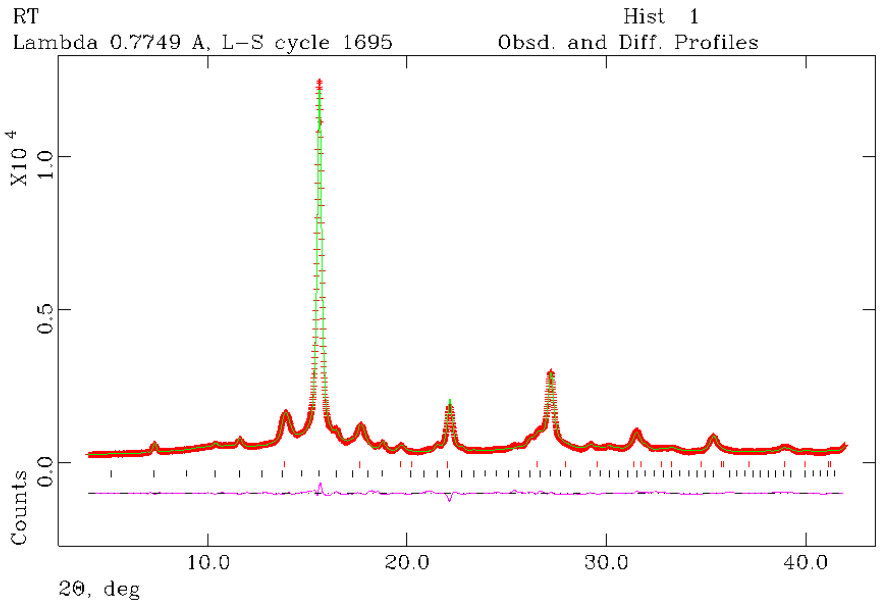

B.16. **Rietveld plot for Sample 43 showing the ternary phase (black tick marks) and MgH_2 (red tick marks). Red crosses indicate observed data, the green line shows the calculated pattern and the magenta line indicates the difference plot.**

B.17. **Atomic parameters for $Ca_{13.3(8)}Mg_{13.8(8)}H_{54}$ (Sample 43)**

Atom	Site	*x*	*y*	*z*	$100xU_{iso}$ / Å^2	SOF
Ca1	24*g*	0	0.3140(3)	0.3413(4)	2.7(2)	0.53(3)
Ca2	12*d*	0.3334(4)	0	0	3.1(2)	1
Ca3	2*a*	0	0	0	6.4(7)	1
Mg1	16*f*	0.1527(3)	*x*	*x*	2.8(2)	1
Mg*	24*g*	0	0.3140(3)	0.3413(4)	2.7(2)	0.48(3)

N.B. H atoms were fixed to values given in literature for $Ca_{19}Mg_8H_{54}$.

B.18. **Interatomic distances for ternary phases containing excess Ca (denoted Ca*) as determined from SXD analysis.**

	Length / Å	
Interatomic Distance	**Sample 39 / *2:375:1***	**Sample 40 / *2:1***
Ca(1)-H(1) ×2	2.2263(26)	2.2348(16)
Ca(1)-H(1) ×2	2.4878(9)	2.4831(16)
Ca(1)-H(2) ×2	2.2732(25)	2.2829(15)
Ca(1)-H(2) ×1	2.2000(21)	2.1855(14)
Ca(1)-H(4) ×1	2.3045(32)	2.2951(20)
Ca(2)-H(1) ×4	2.5371(6)	2.5404(4)
Ca(2)-H(2) ×2	2.3700(16)	2.3645(10)
Ca(2)-H(3) ×2	2.403(4)	2.4207(25)
Ca(2)-H(4) ×2	2.462(4)	2.4467(24)
Ca(3)-H(3) ×12	2.50185(10)	2.50263(12)
Mg(1)/Ca*-H(1) ×3	1.955(4)	1.9371(18)
Mg(1)/Ca*-H(3) ×3	2.035(6)	2.0648(30)

B.19. **Interatomic distances for ternary phases containing excess Mg (denoted Mg*) as determined from SXD analysis.**

	Length / Å	
Interatomic Distance	**Sample 42 / 1:1**	**Sample 43 / 1:2**
Ca(1)/Mg*-H(1) x2	2.1843(26)	2.1883(30)
Ca(1)/Mg*-H(1) x2	2.4792(10)	2.4652(13)
Ca(1)/Mg*-H(2) x2	2.2362(31)	2.276(4)
Ca(1)/Mg*-H(2) x1	2.2132(30)	2.157(4)
Ca(1)/Mg*-H(4) x1	2.3120(33)	2.301(4)
Ca(2)-H(1) x4	2.5125(6)	2.5076(5)
Ca(2)-H(2) x2	2.3528(17)	2.3577(14)
Ca(2)-H(3) x2	2.371(4)	2.350(4)
Ca(2)-H(4) x2	2.450(4)	2.4658(35)
Ca(3)-H(3) x12	2.47912(15)	2.47670(19)
Mg(1)-H(1) x3	1.9070(31)	1.9932(30)
Mg(1)-H(3) x3	2.065(5)	1.932(4)

B.20. Table of Rietveld refinement data for additional phases in SXD patterns collected at room temperature.

Sample / CaH_2:MgH_2 ratio	**39 / 2.375:1**	**40 / 2:1**	**42 / 1:1**		**43 / 1:2**
Chemical Formula	CaH_2	CaH_2	$Ca_4Mg_3H_{14}$	MgH_2	MgH_2
Crystal System **Space Group**	Orthorhombic *Pnma* (62)	Orthorhombic *Pnma* (62)	Hexagonal $P\bar{6}2m$ (189)	Tetragonal *P4/mnm* (136)	Tetragonal *P4/mnm* (136)
Z	4	4	1	2	2
a / Å	5.9168(5)	5.920(1)	6.301(1)	4.535(1)	4.526(1)
b / Å	3.5851(3)	3.5820(6)	-	-	-
c / Å	6.7363(6)	6.738(1)	6.771(2)	2.983(1)	3.0338(1)
V / Å^3	142.89(2)	142.87(5)	232.8(1)	61.37(4)	62.16(4)
Formula Weight / g	168.384	168.384	261.431	52.642	52.642
Calculated Density, ρx / g cm^{-3}	1.957	1.957	1.865	1.424	1.406
Phase Fraction / %	46.9(2)	21.0(1)	17.0(2)	0.7(4)	17.0(5)

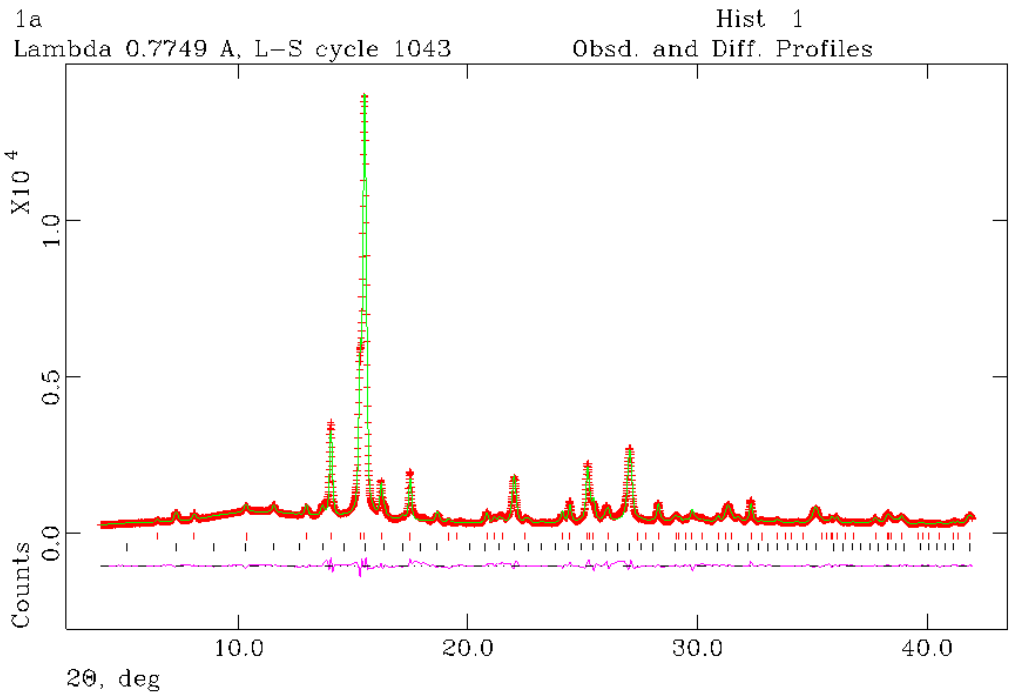

B.21. **Rietveld plot for SXD data of Sample 42 heated to 573 K showing the cubic $Ca_{19}Mg_8H_{54}$ ternary phase (black tick marks) and $Ca_4Mg_3H_{14}$ (red tick marks). Red crosses indicate observed data, the green line shows the calculated pattern and the magenta line indicates the difference plot.**

B.22. Rietveld refinement data for *in-situ* SXD analysis of Sample 42 heated to 573 K.

Sample / *CaH_2:MgH_2*	**42 / *1:1***	
Chemical Formula	$Ca_{19}Mg_8H_{54}$	$Ca_4Mg_3H_{14}$
Crystal System / Space Group	Cubic / $Im\bar{3}$ (204)	Hexagonal / $P\bar{6}2m$ (189)
Z	2	1
***a* / Å**	12.1663(6)	6.3346(3)
***b* / Å**	*a*	*a*
***c* / Å**	*a*	6.8538(4)
***V* / Å^3**	1800.9(3)	238.17(3)
Formula Weight / g	1911.920	233.235
Calculated Density, ρ_x / g cm^{-3}	1.763	1.626
Phase Fractions	52.6(2)	47.4(2)
Refinement Parameters	47	
Data Points	3999	
R_{wp}	6.33	
R_p	4.61	
χ^2	2.544	

N.B. All atomic positions and site occupancies were fixed to literature values for $Ca_{19}Mg_8H_{54}$.

Appendix C.

C.1. Comparison of interatomic distances for $LiAlCl_4$ (Sample 46).

Interatomic Distance	Literature Values /Å	Length / Å
Li-Cl1 ×1	2.4536	2.669(31)
Li-Cl2 ×1	2.7094	2.48(4)
Li-Cl2 ×1	2.8228	3.045(31)
Li-Cl3 ×1	2.6101	2.470(32)
Li-Cl3 ×1	2.7787	2.540(31)
Li-Cl4 ×1	2.5135	2.70(4)
Al-Cl1 ×1	2.1269	2.140(6)
Al-Cl2 ×1	2.1461	2.109(6)
Al-Cl3 ×1	2.1454	2.125(5)
Al-Cl4 ×1	2.1229	2.143(6)

C.2. Atomic parameters for mechanochemically synthesised $LiAlCl_4$ (Sample 46).

Atom	Site	*x*	*y*	*z*	100x U_{iso} / $Å^2$
Li	4*e*	0.112(6)	0.984(5)	0.352(3)	8(1)
Al	4*e*	0.7078(6)	0.3238(8)	0.8987(3)	4.6(2)
Cl1	4*e*	0.6951(6)	0.1846(6)	0.0472(3)	2.2(2)
Cl2	4*e*	0.8096(7)	0.6248(6)	0.9260(4)	2.6(2)
Cl3	4*e*	0.9285(7)	0.1847(7)	0.8176(4)	4.4(2)
Cl4	4*e*	0.4372(7)	0.3161(7)	0.8131(4)	4.0(2)

N.B. Site occupancy factors for all atomic positions were fixed to 1.

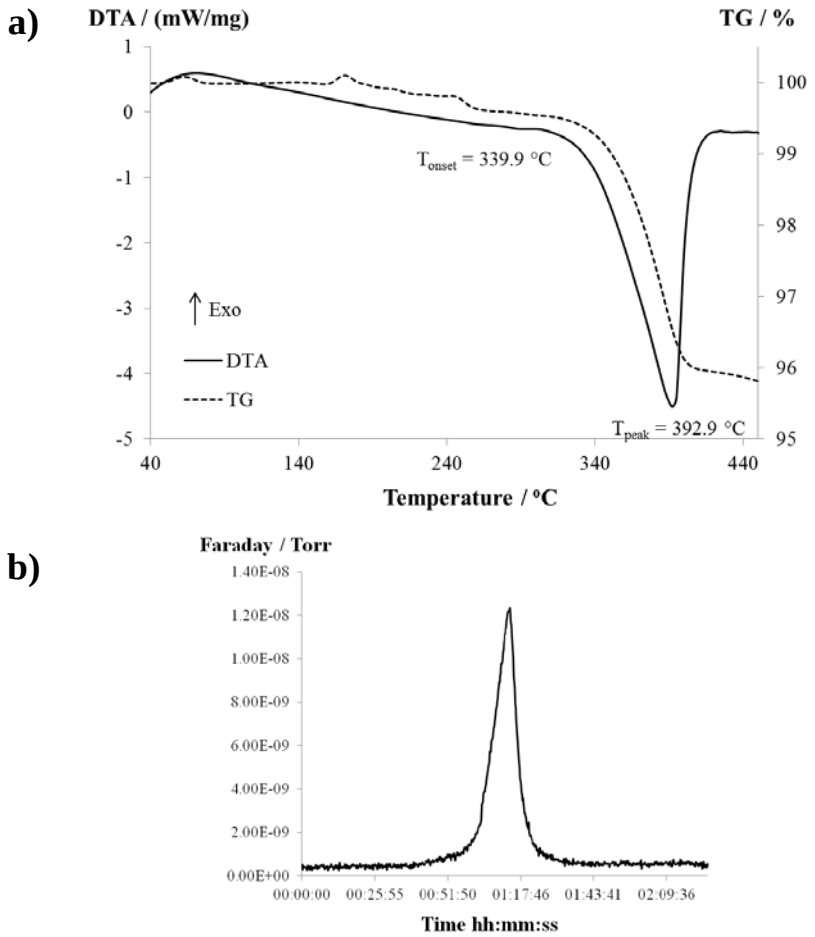

C.3. **a) STA data and b) corresponding MS data for NaH used in this work.**

C.4. **Interatomic distances and bond angles for $NaMgCl_3$ (Sample 50).**

Interatomic Distance	Length / Å	Bond Angles	Angle / °
Mg-Cl ×3	2.833(7)	Mg-Cl-Na	137.63(29)
Mg-Cl ×3	2.692(9)	Mg-Cl-Na	82.34(33)
Na-Cl ×3	2.367(10)	Na-Cl-Na	96.93(21)
Na-Cl ×3	2.737(14)	Cl-Mg-Cl	82.18(34)
Mg-Na ×1	3.574(18)	Cl-Na-Cl	100.2(5)
Na-Na ×3	3.828(7)	Cl-Na-Cl	83.07(21)
		Cl-Na-Cl	95.05(24)

C.5. Atomic parameters for mechanochemically synthesised $NaMgCl_3$ (Sample 50).

Atom	Site	*x*	*y*	*z*	100x U_{iso} / Å^2
Na	6*c*	0	0	0.147(1)	6.7(8)
Mg	6*c*	0	0	0.3400(6)	8.6(5)
Cl	18*f*	0.339(1)	0.0362(8)	0.0881(3)	0.2(1)

N.B. Site occupancy factors for all atomic positions were fixed to 1.

C.6. Atomic parameters for product of Sample heated to 300 ºC; $Na_2Mg_3Cl_8$.

Atom	Site	*x*	*y*	*z*	100x U_{iso} / Å^2
Na	6*c*	0	0	0.1561(7)	2.4(4)
Mg	9*e*	$\frac{1}{2}$	0	0	2.5[a]
Cl1	6*c*	0	0	0.4047(5)	2.5 [a]
Cl2	18*h*	0.4958(5)	0.5042(5)	0.4059(2)	2.5 [a]

N.B. Site occupancy factors for all atomic positions were fixed to 1. [a]Isotropic temperature factors fixed.

C.7. Interatomic distances for the $[AlCl_4]^-$ tetrahedron in mechanochemically synthesised $NaAlCl_4$ (Sample 56).

Interatomic Distance	Literature	Length / Å
Al-Cl1 ×1	2.16	2.147(5)
Al-Cl2 ×1	2.11	2.155(6)
Al-Cl3 ×1	2.13	2.084(9)
Al-Cl4 ×1	2.12	2.152(8)

C.8. Atomic parameters for mechanochemically synthesised $NaAlCl_4$ (Sample 56).

Atom	Site	*x*	*y*	*z*	100x U_{iso} / Å^2
Na	4*a*	0.1232(8)	0.2153(8)	0.689(1)	7.3(4)
Al	4*a*	0.0392(6)	0.4838(9)	0.2063(9)	4.0(3)
Cl1	4*a*	0.0319(4)	0.4918(7)	0.5537(6)	3.7(2)
Cl2	4*a*	0.1464(6)	0.3156(6)	0.1104(8)	3.7(2)
Cl3	4*a*	0.3467(3)	0.0252(5)	0.9270(8)	3.1(2)
Cl4	4*a*	0.3751(6)	0.3357(5)	0.5744(9)	4.6(2)

N.B. Site occupancy factors for all atomic positions were fixed to 1.

Appendix D.

Understanding the Two-step Decomposition of Milled Magnesium Hydride by Neutron Scattering; Part II: In-situ SANS

Hazel Reardon & Duncan H. Gregory; School of Chemistry, University of Glasgow, G12 8QQ.

Summary: By contrast to untreated hydride, when processed under relatively mild milling conditions, MgH_2 exhibits a *two-step* thermal decomposition process, where loss of hydrogen is associated with each endothermic event. To date, no causal link between the two thermal events and the material has been established and no absolute description of the mechanism involved in the two hydrogen desorption steps has been determined. To unravel the decomposition mechanism of the milled hydride, we propose two neutron experiments using small angle scattering and diffraction respectively to decouple the effects of microstructure and phase behaviour in the dehydrogenation of MgH_2. In the experiment described here we will determine the particle surface properties of intermediate partially hydrogenated (MgH_{2-x}) phases that evolve during the "low temperature" (LT) and "high temperature" (HT) endotherms *via in-situ* small angle neutron scattering (SANS) measurements.

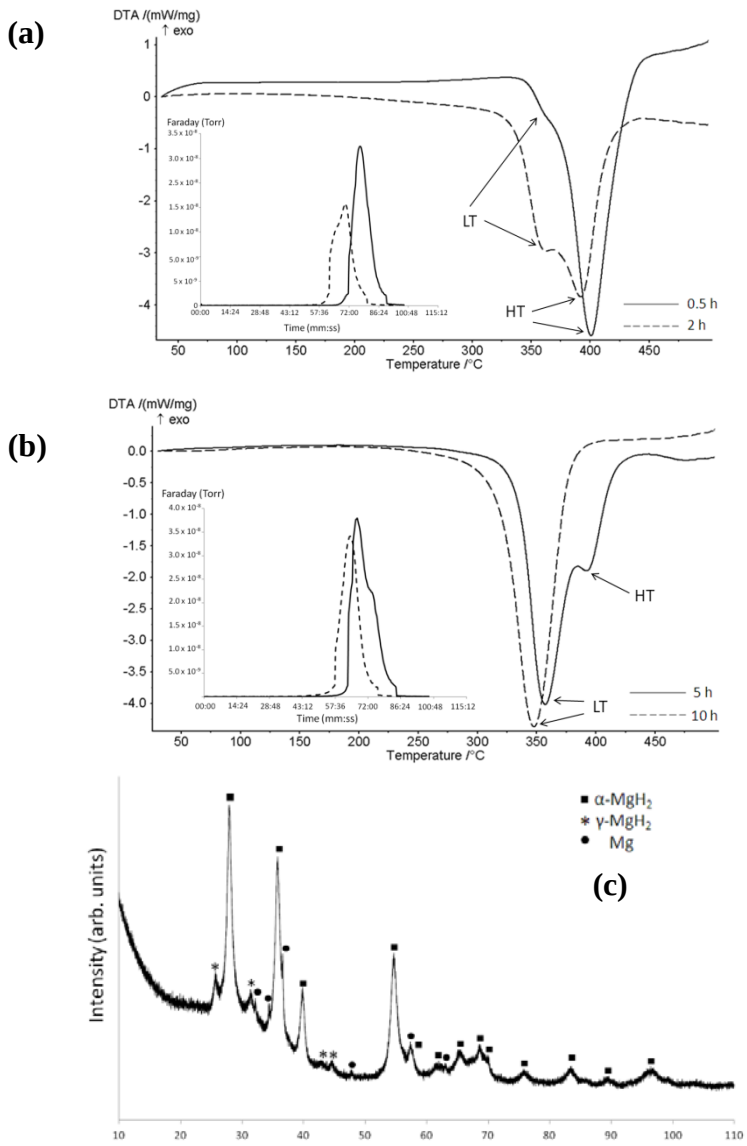

Fig. 1 *– DTA & mass spectrometry (MS) data (inset) for MgH_2 milled at a) low and b) high milling times to reveal the two-step decomposition and c) PXD data for 10 h milled MgH_2.*

<u>Background & Aims:</u> Magnesium hydride already finds application in commercial hydrogen storage units (such as those manufactured by McPhy, for example), where mechanical treatment of MgH_2 is the most common method employed to optimise its hydrogen storage performance. The technique is known to reduce particle size and introduce surface defects and therefore can modify the kinetics (and in some cases, the thermodynamics) of dehydrogenation. Milling MgH_2 is also capable of producing the high pressure gamma phase (γ-MgH_2) under relatively mild conditions, but never as a single phase.[1] In some instances, milling appears to induce a two-step decomposition process (*e.g.* seen as double maxima in the differential thermal analysis (DTA) profiles) and

despite many efforts to identify the reasons for this additional step, ambiguity remains over its origin. The modification was originally proposed as a result of the sequential decomposition of γ-MgH_2 particles prior to α-MgH_2 particles.1 ,2 Many studies have since questioned this theory, attributing the split to particle size and stress effects[3], oxide interfaces formed with/without oxide catalysts[4,5] or to successive decomposition of smaller (γ-)MgH_2 particles followed by larger (α-)MgH_2 particles, implying a synergistic particle size-polytype effect.[6] This study is therefore comprised of two investigations using neutrons; (1) determination of the phases involved in the two-step mechanism using powder neutron diffraction, and (2) SANS experiments to obtain information regarding surface structure and microstructure as a function of time and temperature. Hence by adopting this dual approach for the first time, we aim to establish whether these effects are both extant and intrinsically linked.

Use of SANS for MgH_2 studies have only emerged in the last decade, with a focus on particle dimensions and the power-law exponent.[7] [8] These investigations were driven by information required about the impact of specific catalysts (Cr_2O_3 & FeF_3) for MgH_2 milling and sorption properties. Fractal geometries were identified in milled 5 mol% FeF_3-MgH_2, where structural modifications and variance in scattering characteristics were observed upon heating, which were measured by changes in α relative to Porod's Law.[9] This was attributed to sintering and volume shrinkage and Deladda *et al.* suggested that the catalyst employed may impact upon the power-law type scattering observed in MgH_2. No detailed examination of surface scattering has been conducted to probe the synergistic particle size-polytype effects described for the two-step decomposition in MgH_2. We seek to use SANS to identify information about the crystallite and particle structure (a) after milling and (b) during the two-step dehydrogenation of MgH_2 by conducting both room temperature *ex-situ* and variable temperature *in-situ* SANS experiments respectively. This will allow us to examine the surface scattering characteristics which may be linked to the two distinct thermal processes.

Thermal analysis, SEM-EDX, spectroscopic techniques (Raman & IR) and lab PXD have been crucial for our investigations of MgH_2 milled for different times, with all other milling variables kept constant, *i.e.*, rotation speed, ball:powder ratio, mill-rest periods (*Fig. 1*). Thermal analysis reveals that the LT peak emerges even after short milling periods (0.5 h) then becomes more prominent as the milling time is increased (2 h). At higher milling times (10 h), however, the split is no longer evident which suggests the

phase responsible for the LT peak is dominant. In our PXD studies of the as-milled hydride, we see the emergence of minor, broad reflections that correspond to γ-MgH_2 with relatively mild peak broadening of the α-MgH_2 after only 2 h of milling. At higher milling times, all diffraction peaks are significantly broadened, and reflections corresponding to γ-MgH_2 are more defined. We have examined the milled hydride sample which exhibits the highest separation (ΔT_{peak}) of the two events measured from DTA profiles, *i.e.*, 5 h mill (ΔT_{peak} = 34.3 ^{o}C), to establish any intermediate phases but, as in previous work, only residual α-MgH_2 and Mg metal are observed by PXD. The poor scattering capabilities of hydrogen using lab PXD limit the information we can obtain about the structures involved, and only using neutrons can we more accurately determine the transient H(D) particle characteristics and their effect on particle configuration of these samples.

Beyond undoped, milled MgH_2, we have also been able to enhance the ΔT_{peak} in the DTA, showing that it can be modified and controlled using different additives (*Fig. 2a*). Using 10 wt% SiC:graphite-MgH_2 composites, we have separated the thermal events to a greater degree (ΔT_{peak} = 48.9 ^{o}C), with respect to the 5 wt% composite (Fig *2b*). We see significantly higher surface coarsening with higher additive loadings, but it is unclear how the surface characteristics are related to the impact on the two-step DTA profile. Here, the use of SANS will provide unique information about how the surface characteristics of MgH_2 can be tailored to enhance the low temperature feature for commercial applicability and will be of significant interest in the field of hydrogen storage research. Inclusion of additives in archetypal hydride systems (such as Mg-H) remains essentially a “dark art” and minimal information exists as to the catalytic action or otherwise of such materials. Due to the distinct (discrete) nature of the two thermal features that we observe and the repeatable temperatures of the peak maxima that we record (combined also with consistent thermogravimetic (TG) and d(TG)/dt data), we believe that a reproducible synergic dehydrogenation mechanism linking structure, composition and microstructure is manifest.[10] To date, no studies provide firm evidence for the origins of the two events in milled, undoped MgH_2 or for the mechanism of the two-step decomposition. A combined diffraction-SANS approach provides a powerful opportunity to evidence the link between structure and microstructure ***in-situ*** for the first time. Further, this study will assist in the tailored design of catalysed MgH_2 for commercial applications.

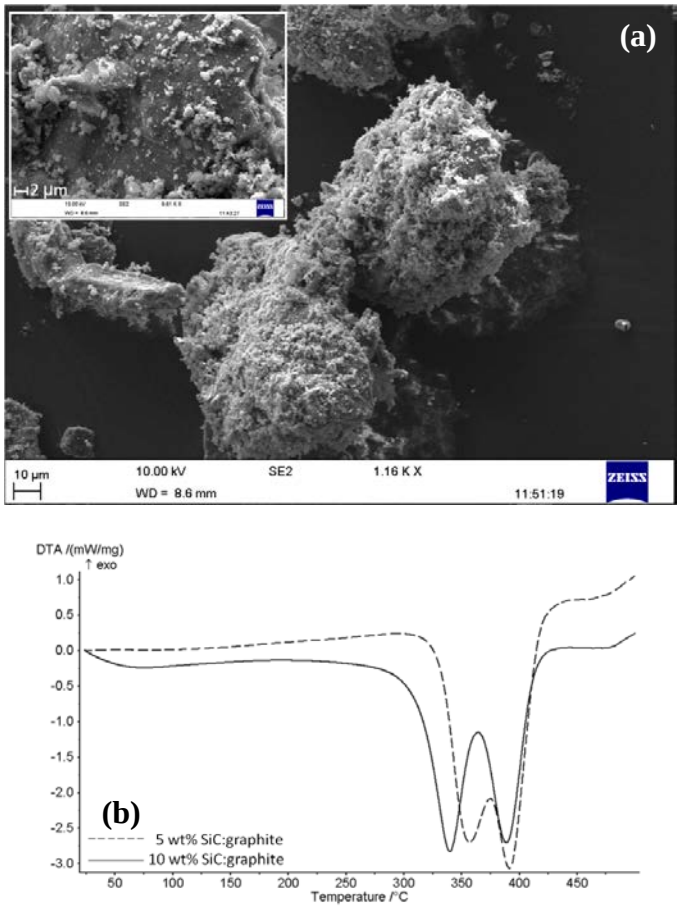

Fig. 2 *– a) Typical SEM images of SiC:graphite doped MgH_2 at 10 µm (Inset: higher magnification image at 2 µm). b) DTA-MS data for 10wt% SiC:graphite doped MgH_2 5 h milled. c) PXD data for the sample heated to 350 ^{o}C.*

Beamtime Request: After discussion with relevant experts and beamline scientists at ISIS, the NIMROD beamline is ideal for these RT and *in-situ* SANS experiments. The wide *Q*-range ($0.01 < Q < 50$ Å^{-1}) of NIMROD will not only allow surface scattering information to be acquired, but we will also be able to conduct PDF-style measurements. (A complementary proposal has also been submitted for more developed powder diffraction data at wider angles to ensure a thorough investigation of the emerging MgH_{2-x} phases.) We will synthesise deuterated samples due to the better signal-to-noise of D relative to H, and propose the following experiments:

1. Analysis of two as-milled MgD_2 samples (2 h and 5 h milling times) over temperatures spanning RT-500 °C (heating rates: 5 °C between RT-250 °C, 2 °C/min 250-400 °C, then 5 °C/min 400-500 °C) to establish the surface scattering profiles and local structure of undoped MgD_{2-x} materials.

2. Investigation of doped MgD_2 samples (5 & 10 wt% SiC:graphite loading in MgD_2) over the same temperature range in order to examine the effect on the stability of the intermediate phases as a result of the additive inclusion.

Samples will be loaded in the furnace assembly sample holder at ISIS from which evolved H2 will be vented, and sample air exposure will be minimised by use of a glovebox/glovebag. Measurements will be acquired at RT, 250, 300, 325, 350, 375, 400 & 500 °C, and we anticipate 12 h per sample will be sufficient to perform static and ramped temperature measurements over the range of interest (48 h total). Taking into account time for background runs, sample loading/changes, and heating-cooling times, we request a total of 3 days on NIMROD.

---

[1] J. Huot, G. Liang, S. Boily, A. V. Neste and R. Schulz, J. Alloys Comp., **293-295**, 1999, 495.
[2] R. Schulz, J. Huot, G. Liang, S. Boily, G. Lalande, M. C. Denis and J. P. Dodelet, Mater. Sci. Eng. A, **267**, 1999, 240.
[3] F. C. Gennari, F. J. Castro and G. Urretavizcaya, J. Alloys Comp., **321**, 2001, 46.
[4] R. A. Varin, S. Li, Ch. Chiu, L. Guo, O. Morozova, T. Khomenko and Z. Wronski, J. Alloys Comp, **404-406**, 2005, 494.
[5] A. Borgschulte, U. Bösenberg, G. Barkhordian, M. Dornheim and R. Bormann, Catal. Today, **120**, 2007, 262.
[6] R. A. Varin, T. Czujko, Ch. Chiu and Z. Wronski, J. Alloys Comp., **424**, 2006, 356.
[7] P. K. Pranzas, M. Dornheim, D. Bellmann, K.-F. Aguey-Zinsou, T. Klassen and A. Schreyer, Physica B, **385-386,** 2006, 630.
[8] S. Deladda, M. Vennstrom, A. Borissova, A. R. Yavari and G. Fragneto, Rev., Adv. Mater. Sci., **18**, 2008, 616.
[9] P. W, Schmidt, J. Appl. Cryst., **24**, 1991, 414.
[10] H. Gijs Schimmel, J. Huot, L. C. Chapon, F. D. Tichelaar and F. M. Mulder, JACS, **127**, 2005, 14348.

Appendix E.

Structure and decomposition of ternary alkaline earth hydrides; $(Ca_{1-x}Mg_xH(D)_2)_n$

Hazel Reardon and Duncan H. Gregory; C3-13, School of Chemistry, University of Glasgow, G12 8QQ

Summary: Ternary hydrides comprising alkaline earth metals, Mg and Ca, have been synthesised by a simple mechanochemical reaction between the corresponding binary hydrides without the use of high pressure H_2. From analysis of both conventional lab powder X-ray diffraction (PXD) and synchrotron XRD (SXD) data, a cubic structure persists over a number of Ca:Mg ratios. The decomposition mechanisms for these hydrides have been explored by thermal analysis, but complete determination of the dehydrogenation pathway has not been possible using X-ray techniques. The purpose of this application for neutron beam time is two-fold: (1) to determine the room temperature structure of the hydrides prepared at various Ca:Mg ratios and (2) to perform *in situ* measurements to establish the dehydrogenation pathway of single phase Ca-Mg-H(D) hydride.

Background & Aims: The $Yb_{19}Mg_8D_{54}$ structure has been proposed previously for $Ca_{19}Mg_8H_{54}$, (a = 12.1457(6) Å, Z=2, $Im\bar{3}$, 100.9 g/l H_2). The ternary hydride was prepared under high H_2 pressure at high temperature starting from a 2:1 ratio of CaH_2:MgH_2, but was not synthesised as a single phase; the sample also contained CaH_2, MgH_2 and MgO.[1] Nevertheless powder neutron diffraction (PND) data allowed a refined structure to be determined. The cubic Ca-Mg-H phase (or phases) has (have) subsequently been apparently observed within multiphase mixtures, although the structure and properties of these reported compounds have never been determined.[2] Using relatively mild milling conditions (ball: powder ratio 76:1, 450 rpm, 5 h), we have synthesised hydrides of different nominal stoichiometries from commercial CaH_2 and MgH_2. Our results indicate that a cubic ternary hydride forms at all of the CaH_2:MgH_2 ratios examined. *Figure 1a* shows the lab PXD pattern of the nominal 1:1 sample. The data could be fit to a structure isotypic to $Ca_{19}Mg_8H_{54}$. Milled samples have characteristically poor diffraction profiles owing to particle size reduction (and microcrystalline strain) which results in peak broadening and masking of weak reflections. Therefore, to obtain better quality diffraction

data for structure solution, we collected SXD data at NSRRC (Taiwan), using the 01C2 powder SXD beamline. SXD patterns revealed the low angle and weak reflections characteristic of the $Ca_{19}Mg_8H_{54}$ phase.

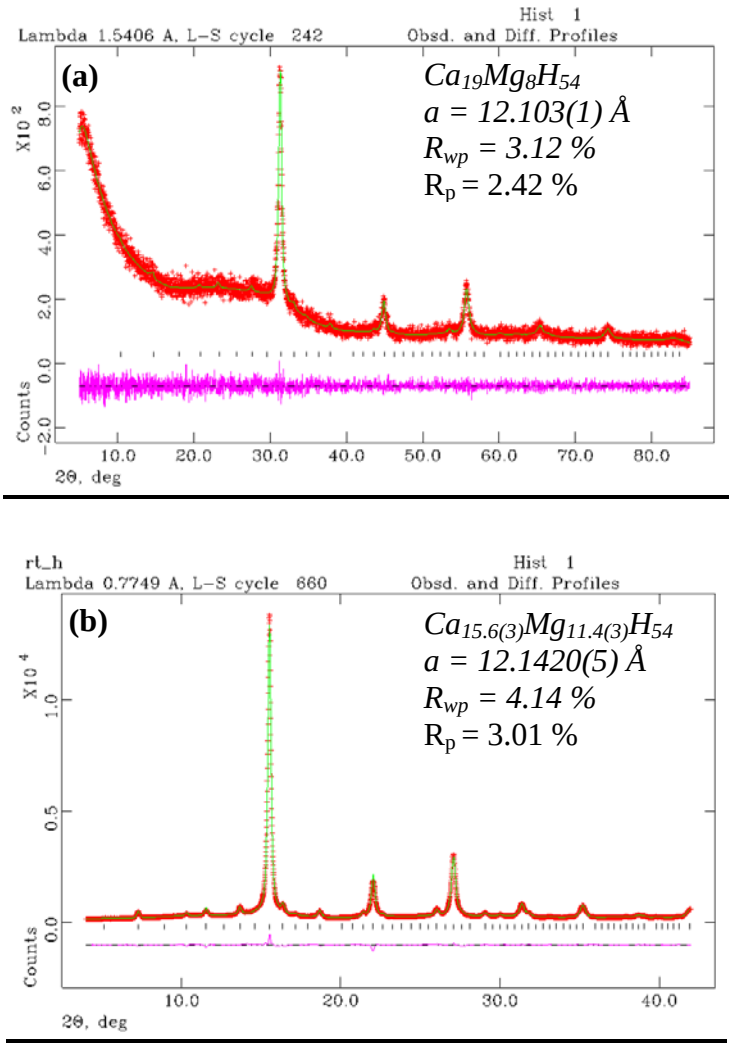

Figure 1 – a) *Rietveld plot of lab PXD data for 1:1 Ca:Mg, and* ***b)*** *Rietveld plot of Synchrotron XRD data for 4:3 Ca:Mg; "$Ca_{15.6(3)}Mg_{11.4(3)}H_{54}$".*

Diffraction data shown in *Figure 1b* provides strong evidence for a structure seemingly identical to $Ca_{19}Mg_8H_{54}$ prepared by the conventional high pressure-high temperature route. However the cubic unit cell volume varies as a function of metal content and therefore new non-stoichiometric $(Ca_{1-x}Mg_xH_2)_n$ structures are suggested from the diffraction data collected thus far. (*e.g.*, refining site occupancies for the 1:0.75 Ca:Mg sample shown in *Fig 1b*, a stoichiometry for the hydride was deduced as $Ca_{15.6(3)}Mg_{11.4(3)}H_{54}$, with partial substitution of Mg on the Ca 24*g* site). Although structures have been obtained from SXD Rietveld refinements conducted using fixed

hydrogen positions based on the model proposed by Bertheville & Yvon1, full characterisation of these non-stoichiometric phases requires accurate determination of the hydrogen atom positions and the identification of possible vacancies on the hydride sublattice. Therefore, we seek PND data to determine the positions and occupancies of the hydride anions accurately and to confirm the metal site positions and distributions from SXD models. We will prepare deuterated samples, to exploit the superior coherent scattering from D over H given scattering lengths of b = 6.671 *vs*. -3.7390 fm respectively and the lower inelastic cross section of ^{2}D relative to ^{1}H by several orders of magnitude (0.000519 *vs.* 0.3326 barn).

Having prepared several Ca-Mg-H compositions, we have studied the dehydrogenation behaviour of these materials under flowing $Ar_{(g)}$ using thermogravimetric-differential thermal analysis coupled to mass spectrometry (TG-DTA-MS) followed by PXD of resultant products. Bertheville and Yvon had suggested the decomposition of the hydride (under 5 bar H_2) to follow a two-step mechanism: first *via* decomposition to CaH_2 and $Ca_4Mg_3H_{12}$ at 650-700 K, followed by subsequent formation of Mg and CaH_2 at 750 K. No evidence at that time or since has substantiated this result. Thermal analysis in our lab yields a 2-step process (*Figure 2a*) but, contrary to the mechanism proposed by Yvon, lab PXD data demonstrate decomposition *via*, CaH_2 and Mg at 773 K with the loss of ~2 wt% H_2. Upon further heating to 973 K, $CaMg_2$, CaH_2, and Mg remain, even after a subsequent hydrogen loss. No evidence of Ca is observed, therefore the second hydrogen loss may be attributed to the partial decomposition of CaH_2 to form $CaMg_2$ with Mg. We seek to conduct an *in-situ* neutron experiment to examine the ternary hydride decomposition *via* accurate measurement of the dehydrogenation products as they form. This should provide evidence to rationalise reversibility of hydrogen sorption in the single phase sample and the prospects of manipulating reversibility (cyclability) by control of Ca and Mg stoichiometry.

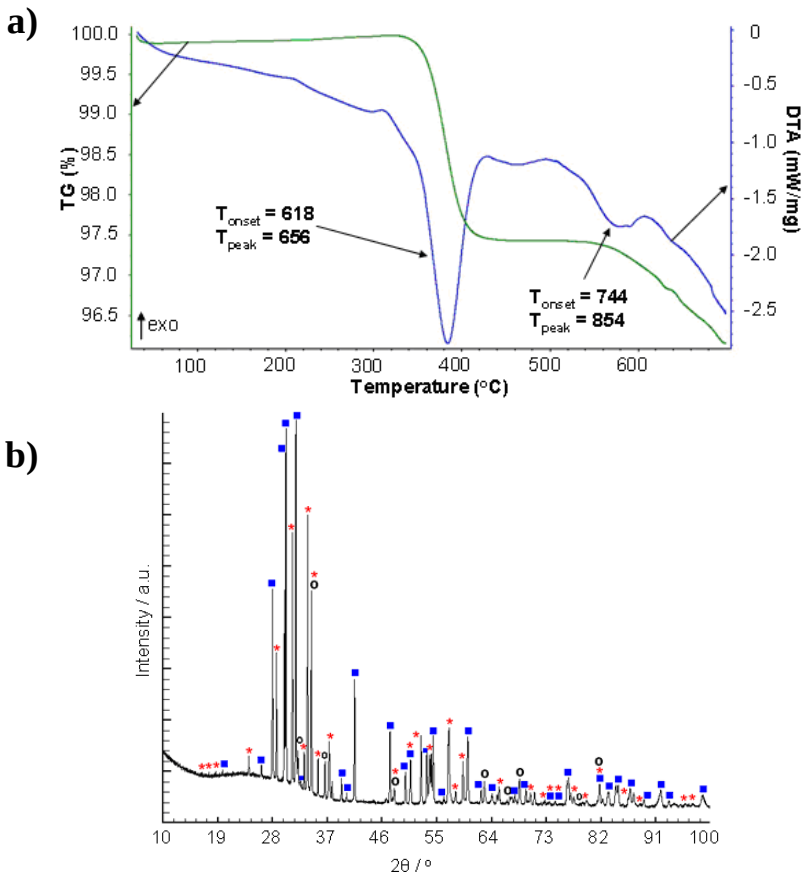

Figure 2 (a) *STA profile showing decomposition thermodynamics (DTA) and mass loss (H_2), and* ***(b)*** *Lab PXD data obtained after TPD analysis to 973 K (red stars = $CaMg_2$, blue squares = CaH_2 and open circles = Mg).*

Experimental: After obtaining advice from relevant experts and beamline scientists at ISIS, the POLARIS beamline is the ideal choice for these experiments owing to its high count rate and wide *Q* ranges. Proposed experiments:

- Determination of the D atom positions to understand structural variance in the Ca-Mg-D samples prepared at different Ca-Mg ratios. This requires analysis of 5 x Ca-Mg-D samples prepared at 1:0.75, 1:1, 1:2, 2:1 and 2.375:1 Ca: Mg ratios to determine definitive room temperature structures.

- *In-situ* dehydrogenation of the single phase Ca-Mg-D hydride is required to draw conclusions about the dehydrogenation mechanism. One sample will be used for this *in-situ* decomposition study, *i.e.*, the 4:3 (Ca: Mg) sample, and measurements will be conducted under flowing Ar (or similar inert gas) and the sample holder vented to remove hydrogen as it evolves. The sample will be heated at 2 ^{o}C/min to 200 ^{o}C, where

measurements will be recorded at RT, 200, 250, 300, and 350 ^{o}C. Thereafter, a slower heating rate will be used (~0.5 ^{o}C/min) and measurements taken at 375, 400, 425, 450, 500, 525, 550, 600, 650, 700 ^{o}C to elucidate the phases evident upon hydrogen evolution. Hence 15 in situ datasets will be collected. (The incident and scattered beam will be collimated to 90° in order to omit scattering observed from the steel container.)

Room temperature measurements will be made using quartz capillaries, and the sample for *in-situ* measurements will be loaded in a bespoke steel can (currently being commissioned at ISIS). Due to the air sensitive nature of these materials, all sample handling will be conducted under inert conditions using a glovebox. Based on a measurement time of 1 h (**1 h x 20** measurements), taking sample preparation and changeover into account and including the heating/cooling times required for the *in-situ* experiment, we request a total beamtime of **3 days** for this study**.**

---

[1] B. Bertheville and K. Yvon, J. Alloys Comp., **290,** 1999, L8-L10.
[2] S. Sartori, A. Leon, O. Zabara, J. Muller, M. Fichtner and B. C. Hauback, J. Alloys Comp., **476**, 2009, 639.

Appendix F.

F.1. Table of Samples – Chapter 3

Sample ID	Components	Milling Duration	b:p	No. Milling Balls
1	Commercial MgH_2	0.5	40:1	2
2	Commercial MgH_2	2	40:1	2
3	Commercial MgH_2	5	40:1	2
4	Commercial MgH_2	10	40:1	2
5	Commercial MgH_2	20	40:1	2
6	Commercial MgH_2	40	40:1	2
7	Commercial MgH_2	0.5	40:1	8
8	Commercial MgH_2	2	40:1	8
9	Commercial MgH_2	5	40:1	8
10	Commercial MgH_2	0.5	80:1	8
11	Commercial MgH_2	2	80:1	8
12	Commercial MgH_2	5	80:1	8
13	MgH_2 - 1 wt% graphite	5	40:1	2
14	MgH_2 - 5 wt% graphite	5	40:1	2
15	MgH_2 - 10 wt% graphite	5	40:1	2
16	MgH_2 - 20 wt% graphite	5	40:1	2
17	MgH_2 - 5 wt% graphite	2	80:1	8
18	MgH_2 - 5 wt% graphite	5	80:1	8
19	MgH_2 - 1 wt% SiC	5	40:1	2
20	MgH_2 - 5 wt% SiC	5	40:1	2
21	MgH_2 - 10 wt% SiC	5	40:1	2
22	MgH_2 - 20 wt% SiC	5	40:1	2
23	MgH_2 - 5 wt% SiC	2	80:1	8
24	MgH_2 - 5 wt% SiC	5	80:1	8
25	MgH_2 - 1 wt% SiC:graphite	5	40:1	2
26	MgH_2 - 5 wt% SiC:graphite	5	40:1	2
27	MgH_2 - 10 wt% SiC:graphite	5	40:1	2
28	MgH_2 - 20 wt% SiC:graphite	5	40:1	2

Sample ID	Components	Milling Duration	b:p	No. Milling Balls
29	MgH_2 - 1 wt% SiC:graphite	2	80:1	8
30	MgH_2 - 5 wt% SiC:graphite	2	80:1	8
31	MgH_2 - 10 wt% SiC:graphite	2	80:1	8
32	MgH_2 - 20 wt% SiC:graphite	2	80:1	8

F.2. Table of Samples – Chapter 4

Sample ID	Components	Milling Duration	b:p	No. Milling Balls
33	NaH:MgH_2 (1:1)	1	70:1	10
34	NaH:MgH_2 (1:1)	2	70:1	10
35	NaH:MgH_2 (1:1)	5	47:1	10
36	NaH:MgH_2 (1:1)	5	70:1	10
37	NaH:MgH_2 (1:1)	5	85:1	10
38	NaH:MgH_2 (1:1)	5	100:1	10
39	CaH2:MgH_2 (2.375:1)	5	76:1	10
40	CaH2:MgH_2 (2:1)	5	76:1	10
41	CaH2:MgH_2 (1:0.75)	5	76:1	10
42	CaH2:MgH_2 (1:1)	5	76:1	10
43	CaH2:MgH_2 (1:2)	5	76:1	10

F.3. Table of Samples – Chapter 5

Sample ID	Components	Heating Conditions	Milling Duration	b:p	No. Milling Balls
44	$LiCl + AlCl_3$	-	Hand Mixed	-	-
45	$LiCl + AlCl_3$	-	1	80:1	10
46	$LiCl + AlCl_3$	-	3	80:1	10
47	$LiCl + AlCl_3$	-	5	80:1	10
48	$LiAlCl_4$ (**46**) + 4 NaH	-	5	100:1	10
49	$NaCl + MgCl_2$	-	Hand Mixed		
50	$NaCl + MgCl_2$	450 ^{o}C, 12 h	-	-	10
51	$NaCl + MgCl_2$	-	1-5	80:1	10
52	$NaMgCl_3$ (**50**) + 3 NaH	-	5	100:1	10
53	$NaMgCl_3$ (**51**) + 3 NaH	-	5	100:1	10
54	$NaMgCl_3$ (**50**) + 3 LiH	-	5	100:1	10
55	$NaCl + AlCl_3$	-	Hand Mixed		
56	$NaCl + AlCl_3$	-	5	80:1	10
57	$NaAlCl_4$ (**51**) + 4 LiH	-	5	100:1	10